Novel Excitations in Driven Vortex Channels in a Superconductor, and Solitary Waves of Light and Atoms in Photonic Crystal Fibres

by

Jack Anthony Gartlan

A thesis submitted to
The University of Birmingham
for the degree of
DOCTOR OF PHILOSOPHY

Theoretical Physics Group
School of Physics and Astronomy
The University of Birmingham

October 31, 2019

Abstract

This is a thesis in two parts. In Part I, we will study the shear response of confined vortices. In Part 2, we will study light and matter interactions in photonic crystal fibres. Whilst the approaches of each are completely different, they both have the same central theme: solitons.

In the first part of this thesis we study the static and dynamic properties of vortices within a Type-II superconductor, confined within a channel. The channel comprises a collection of pinned vortices, which form the perfect triangular lattice in the boundary, and rows of "free" particles which are driven via an external force. We provide two main results within this system. First we calculate the potential stemming from the boundary, and derive (under certain approximations) the phenomenologically accepted result for the critical shear dependence on the system width. We then study a novel system in which a defect is placed in a deformable potential; specifically a system comprised of two channels where one or both channels have a defect. This system provides a mechanism for the proliferation of kink/kink and anti-kink/anti-kink pairs as the defect binds to a local excitation in the form of a "breather". We observe and explain what appears to be an action at a distance style interaction between excitations.

In Part II, we will utilise the nonlinear effects of a Bose condensate and the unique optical properties of a photonic crystal fibre to demonstrate there are nonlinearly stable configurations which exist in the vicinity of an optical mode with a cut-off. These are solitary waves, whose relative composition of atoms and photons may be changed via altering the detuning of light from an atomic transition and Feshbach resonances.

Acknowledgements

In many ways this is the most important section of this thesis. The last four years have been mentally exhausting, and without the continual love and support of those mentioned below I wouldn't be writing this today.

To my supervisors, Professor Mike Gunn and Professor Nicola Wilkin, thank you for all you have done for me during my PhD. I would also like to thank Dr Martin Long for always showing an interest in my work and providing useful guidance.

To all the research students I have had the pleasure to work beside, we had many laughs and I thank you for it. A special mention to Matt Hunt and Rory Whelan, some of my fondest problems solved during my PhD were red routes with you.

To my lads' WhatsApp group, the insightful discussions on *Mourinho - In or Out?* provided a much needed distraction. I thank you for it!

To the world best Godmother, Tara, thank you for always believing in me and buying me that lab coat all those years ago.

To my girlfriend, Niamh, thank you for keeping me motivated and supporting me through the many, many late nights (and for teaching me that the purpose of a comma isn't to give me a break from typing). By the time this is printed we will be Dr & Dr!

To my good friend, Rich Mason, your natural enthusiasm for physics and calming demeanour helped turn what seemed like an insurmountable task back into pure enjoyment. Words alone cannot describe how much you have helped me over the last year and a half, thank you! Additionally, I would like to thank Jon Watkins, you two formed quite the double act and I look forward to listening to your hit podcast in the future, though maybe wait until after recording to open a bag of crisps.

To my Nan, thank you for always lighting candles for me, I hope to one day balance this carbon footprint. To my siblings, Sean and Grace, I am so very proud of both of you. I feel exceptionally grateful to be part of your lives.

My final and most important thank you extends to my Parents. To my Mum, our daily phone calls have kept me sane over the last four years. The love and support you have shown me has been invaluable, thank you so much! To my Dad, your infamous two word texts have continually made me laugh. I think I am ready to finally stop being a student and join the real world of work.

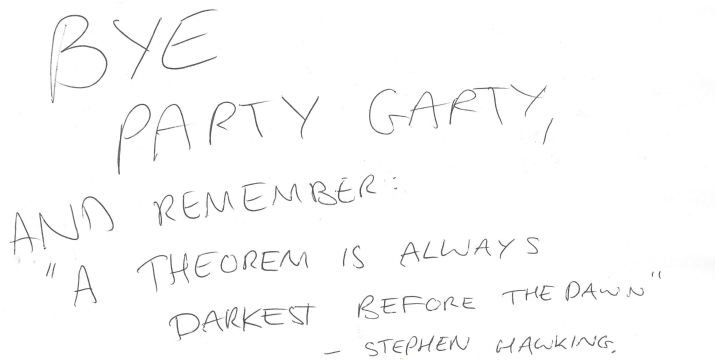

Contents

List of Figures

Part I

Shear Flow in Superconducting Channels

Chapter 1

Introduction to Part I

Motivation

The strength of crystalline materials is of paramount importance. The structure of a material greatly impacts its elastic and plastic response to external forces, such as shearing. The effects become more pronounced on the microscopic level. We try to understand shearing, and the motion of defect on a fundamental level. We identify novel dynamics in the shear response of crystalline vortex structures confined in a narrow superconducting channel [1].

Historically, it was long known that materials had much lower shear modulus than was theoretically expected, and so there is great interest in the response of materials to shear [11]. The basic question is, when a shear force is applied to, for example, a crystal lattice, what are the mechanisms that allow the system to respond? First considered in the context of dislocation motion in metals [12], the phenomena is now studied in a host of physical systems including 2π rotations in coupled pendula [13], crowdion motion within lattice structures [14] and fluxon mobility in Josephson junctions [15, 16].

In Part I of this thesis, we study the dynamics of defects within sheared lattice geometries. More specifically, we investigate the changes to defect motion in the presence of a mobile neighbouring chain. While the mechanism for shear in bulk systems is understood, we are concerned with systems where the defect is placed into a *deformable* potential. The interplay between deformations in the potential and the defect itself provide a rich physical picture. We identify a novel regime in which a defect self-localises. The range of this localisation is dependent on the shearing force applied to the underlying lattice. This work was originally motivated by understanding the "slip" mechanism of sheared neighbouring chains with different densities [17, 18] or with a position dependent force [19, 20].

Both P. H. Kes *et al.* [17] and R. Besseling *et al.* [18] consider the the shear response of a mobile lattice with variable density within a modulated confining potential. They both consider the point at which the "free" lattice becomes mobile against a "fixed" background; the so-called critical shear point. Both observe sharp peaks in the critical shear, as a function of density, when the density matches that of the modulated potential. The sharp peaks in the shear response of driven channels in [18] are found by R. Besseling *et al.* to occur when the channel density is commensurate with the substrate potential. The authors also relate the value of these critical shear peaks, $\mathrm{F}_w^{\mathrm{C}}$, to the phenomenologically accepted equation

$$\mathrm{F}_w^{\mathrm{C}} = \frac{2Ac_{66}}{w}, \tag{1.1}$$

where w is the channel width, A encapsulates the microscopic details of the system and c_{66} is the is the shear modulus as defined in [21]. D. V. Tkachenko *et al.* numerically studied the dynamics of colloids in two-dimensional narrow channels with a nonuniform shearing force [19]. Among other things, the authors identified that the transition between the elastic (or rigid-body) and plastic regimes of mo-

tion occurred at higher driving forces when the relative density of each chain was closer matched. Similarly, C. Reichhardt *et al.* study the rigid body to plastic transition when only one chain experiences a driving force [20]. The decoupling of each chains is found to occur at higher drives for chains with commensurate densities. In this thesis, we investigate the "slip" mechanism which occurs in the plastic regime.

These numerical studies, [17–20], primarily focus on the integrated properties of each chain, with motivation from the experimental results. The integrated properties of a chains dynamics can be inferred from experimental measurements, for example the mobility of a superconducting chain of vortices can be inferred from resistance measurements as shown by C. F. Hempstead and Y. B. Kim [22]. The recent real-time observation of microscopic colloidal dynamics by M. P. N. Juniper *et al.* [23] has opened up the studying the underlying mechanisms of defects in confined channels.

The theoretical backdrop to this work is the Frenkel-Kontorova (FK) model. In this thesis we provide an overview of the FK model so that the non-trivial deformable background potential system may be *partially* cast within that framework. This remarkably simple model is commonly used to study the static and dynamical properties of excitations in discrete one-dimensional systems with competing length scales. In this thesis, we use it to understand the "slip" mechanism. An additional benefit of the FK model is that in the continuum limit it transforms into the sine-Gordon equation, as was shown by [24]. The sine-Gordon equation has exact solutions which can be related to the excitations observed in discrete systems.

The specific physical system in which we study the FK model is a narrow type II superconducting channel, displayed in figure 1.1. Not only is the narrow su-

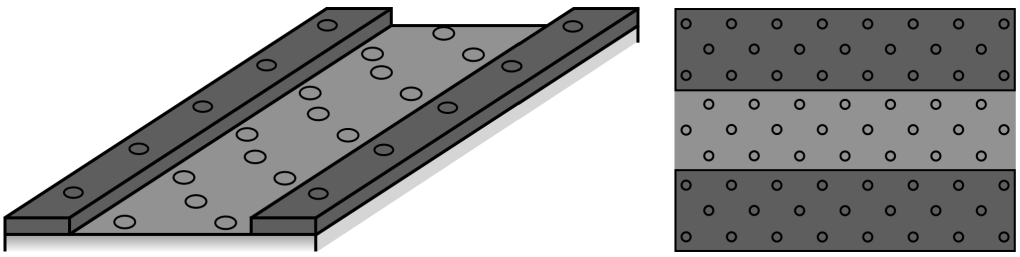

Figure 1.1: Schematic plot of the the narrow superconducting channel geometry, both a three dimensional (left) and two dimensional (right) representation. The circles represent vortices, and the light/dark grey shading indicates different superconductors. The applied magnetic field acts out of the plane. The pinned channel edges have been aligned with the **a** lattice vector. A similar channel geometry was experimentally studied in [1].

perconducting channel an FK-type system in the classical limits we consider but its versatility means the channel can be geometrically tailored to the specific requirements [1]. One can tune the channel density by varying the externally applied magnetic field. The pinned vortices which confines the mobile channel can also be fabricated to a host of designs [25].

These systems are expensive to study experimentally. We therefore use molecular dynamics to model the type II superconducting channels, in which the repulsive vortices are treated like point-like particles. This gives us access to long term molecular simulations at the cost of observing phenomena such as vortex/anti-vortex annihilation. Determining the confining force from the channel edges becomes numerically taxing in large systems. To reduce this, we employ Poisson summation to find an alternative representation for the potential stemming from the channel edges.

Originally motivated by the reduction in simulation time, the rapid convergence of the Fourier form of the substrate potential allows us to perform some analytical calculations on *registered* channels, where each well contains exactly one particle, channel systems. We are able to derive equation 1.1 for the registered, which is phenomenologically accepted by most experiments. We also use the Fourier form to

investigate the onset of shearing in registered channels and compare the profile of the transverse confining potential to a commonly applied discrete boundary with imposed cut-off length to the interaction force, as used in [26]. The rapid convergence also means we can verify the applicability of the FK model for the superconducting channel. Previous experiments have accepted this form without identifying its applicability analytically [18].

After studying and approximately analytically solving the registered system as a function of width, we move on to more complex systems. We first summarise the existing literature (illustrated with our own numerics) on a single defect in a fixed potential, before we move on to study a defect within a deformable potential. With an exact solution and good background from simpler systems, we are able to understand an "action at a distance" style interaction which first motivated our interest in this system.

Overview

In Part I of this thesis we investigate the dynamics of kinks within the FK model. To do so we numerically model a narrow superconducting channel. Chapters 2 and 3 discuss the relevant background material required for us to model this system. The specifics of the simulation are discussed in Chapter 4. Chapters 5 and 7 are a combination of a literature review with novel results within. Chapters 6 and 8 contain original material.

In Chapter 2 of Part I, we present the Frenkel-Kontorova model which underpins this thesis. Following the methods in [2], we present this model and review some of the applications, as well as the extensions considered such as impurities, long-range

interaction and transverse motion. We then discuss the continuum limit solution, the sine-Gordon equation, and define the form of two of the excitations it supports, the kink and the breather. We go on to introduce the different types of ground state phases observed in these channels; the commensurate and incommensurate structures as well as channels with discommensurations (kinks). As kinks play a significant role in this thesis, we review some of their known features such as energy and interaction.

Type II superconductors are the subject of the Chapter 3. Among other things, we review the Ginzburg-Landau approach in order to determine the properties of the narrow superconducting channel. We present the numerical implementation of the superconducting channel in Chapter 4, the methods in this chapter have been verified by previous work within this group: J. S. Watkins [27] and A. A. Tomlinson [28]. Also in Chapter 4 we outline methods used to reduce the simulation time.

Motivated from both a mathematical and numerical standpoint, in Chapter 5 we employ Poisson summation to determine an alternative representation for the potential stemming from a pinned Abrikosov lattice. Originally believed to be novel work, we later found that this had already been achieved by T. Dröse *et al.* [29].

We apply the Fourier form of the boundary potential to derive the critical shear in registered channels. Our novel approach allows us to derive the phenomenologically accepted formula 1.1. The deviation of the $1/w$ dependence of the critical shear on the channel width employs three approximations (detailed later). When these approximations are not employed (via either exact numerical investigations or analytics), we identify a small, but finite, correction term to the phenomenological equation. To the best of our knowledge, this contribution has gone unnoticed both

experimentally and numerically.

The use of the Fourier boundary provides an excellent representation of the boundary, allowing us to perform more precise molecular dynamics (MD) than before, along with exact calculations. We go on to show that the velocity profile of the critical shear, which is derivable for a one-dimensional chain in the FK model, is scale invariant. Additionally we qualitatively discuss the impact of including temperature and transverse motion on the critical shear, as observed from our simulations.

The primary objective of this thesis is to study the properties of defects in wide channels, as presented in Chapter 8. In order to deduce the phenomena observed in wide channels, we first complete a rigorous study of the static and dynamical properties of defects in single channels, in Chapter 7, with the support of an extensive literature. Finally, we investigate the response to the shear of defects in superconducting channels in a deformable potential, which in this context amounts to a channel system with two free rows, one of which contains a defect. We observe a novel self-localising mechanism in which the defect is bound to a finite region of the channel. We identify that this effect is caused by the perturbations the defect induces in the neighbouring chain, where the perturbation experiences drive dependent asymmetry. We use this mechanism to explain the interaction of defects in separate chains, originally motivated by "action at a distance".

Chapter 2

The Frenkel-Kontorova Model

In this chapter, we outline the key features of the Frenkel-Kontorova model that underpin the research in this thesis. For a more detailed presentation of this model see [2] and [30]. We begin by motivating the Frenkel-Kontorova model as a useful tool in evaluating the critical shear of a bulk lattice. We then discuss some of the other physical systems in which it has proven to be useful. In section 2.2, we derive the equation of motion for the Frenkel-Kontorova model and solve it for low amplitude displacements. In section 2.3 we discuss the continuum limit form of the Frenkel-Kontorova model, which is applicable for strong interactions. We explicitly state the known expressions for the excitations of the continuum limit as they will be useful in later chapters. The ground state structure of the Frenkel-Kontorova has an extensive set of phases, these phases are discussed in section 2.4. As we investigate the dynamics of defects in this thesis, considerable attention is paid to discussing decommensurate phases.

2.1 Introduction

In the early 1900s, experiments investigating the shear response of various crystals identified a common characteristic, plastic deformation increased the shear strength of the crystal [31]. This could not be explained by shearing one lattice plane uniformly with respect to another under stress. Uniform shearing would not strengthen a crystal and predicts a shear modulus many orders of magnitude different to experimental measurements [30].

An explanation for shear strengthening was proposed by G. I. Taylor [11] in 1934 based on the experimental observations of sheared salt crystals by A. F. Joffe [32]. Taylor explained that shearing does not occur uniformly but is mediated by localised defects, which he defined as dislocations. Using the lattice model proposed by Dehlinger [33], predecessor of the Frenkel-Kontorova model, Taylor found that the cost of breaking a finite number of bonds was energetically favourable to uniform shear. As real crystals often contain "misfits" or dislocations which can be removed by shearing, Taylor was also able to explain the increased shearing strength. Additionally, when commenting on the interaction between nearest neighbours Taylor stated that “the whole macroscopic phenomenon of gliding must be regarded as the integrated effect of individual jumps” [11].

Four years after Taylor’s seminal paper, a similar model to Dehlinger’s for interacting particles on a one-dimensional periodic substrate was independently proposed by Y. Frenkel and T. Kontorova [34, 35]. Initially employed to study dislocations in metals [12], the Frenkel-Kontorova (FK) model now has applications spanning a broad range of physical systems. The applications include classical systems such as coupled pendula [13] to quantum system such as Josephson Junctions [15, 16].

2.2 The Frenkel-Kontorova Model

In this section, we derive the intuitively simple FK model. We consider a one dimensional chain of harmonically interacting particles on a sinusoidal landscape, as depicted in figure 2.1. The nearest neighbour interaction has elastic constant g and an interparticle spacing of a_{bulk} in equilibrium. The sinusoidal landscape has an amplitude of ϵ_s and periodicity a_{CE} where CE denotes the channel edge.

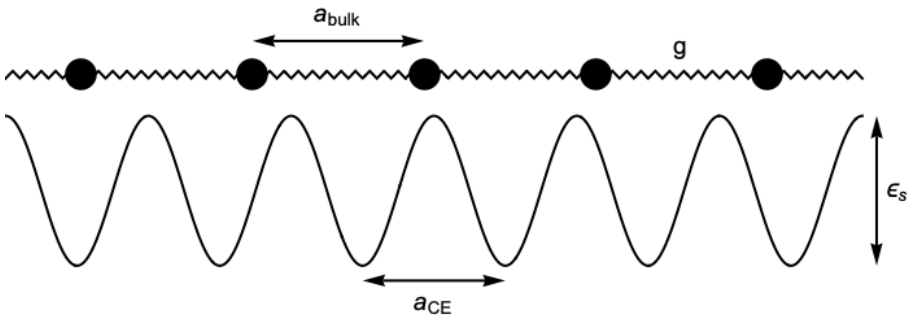

Figure 2.1: Schematic plot of the FK model. A chain of particles with natural spacing a_{bulk} and elastic constant g situation on a substrate potential with period a_{CE} and amplitude ϵ_s. Adapted from Fig. 1.1 in [2]

The Hamiltonian for the model depicted in figure 2.1 is comprised of the kinetic energy

$$\mathcal{K} = \frac{m}{2} \sum_n \left(\frac{dx_n}{dt} \right)^2 , \tag{2.1}$$

where m and x_n are the mass and position of the n^{th} particle, we assume all particles are identical. The potential energy has two contributing factors; one from the position of the particles on the potential landscape and the other from the separation of nearest neighbours away from equilibrium.We can express this as

$$\mathcal{U} = U_{sub} + U_{int} = \sum_n \left[\frac{\epsilon_s}{2} \left(1 - \cos \left(\frac{2\pi x_n}{a_{\text{CE}}} \right) \right) + \frac{g}{2} \left(x_{n+1} - x_n - a_{\text{bulk}} \right)^2 \right] , \tag{2.2}$$

where ϵ_s is the potential amplitude and a_{bulk} is the substrate periodicity. The elastic constant is defined to be the second differential of the interaction potential at the equilibrium interparticle separation, $g = U''_{int}(a_{\text{bulk}})$ [36]. The equilibrium separation, a_{bulk}, can be an inherent length scale of the potential, such as particles joined by springs. Such potentials, which have both an attractive and repulsive branch, can be used to study "free-end" chains [23]. Alternatively, for a convex interaction potential ($U''_{\text{int}}(x) > 0$ for all $x > 0$), such as the interaction of superconducting vortices [18], one considers a "fixed-density" FK chain. The length of a_{bulk} is set by fixing the number of particles N in a given length of chain L.

Combining equation 2.1 and equation 2.2 and then dedimensionalising, one arrives at the Hamiltonian

$$H = \frac{2\mathcal{H}}{\epsilon_s} = \sum_n \left[\frac{1}{2} \left(\frac{d\tilde{x}_n}{d\tilde{t}} \right)^2 + (1 - \cos(\tilde{x}_n)) + \frac{\tilde{g}}{2} (\tilde{x}_{n+1} - \tilde{x}_n - \tilde{a}_{\text{bulk}})^2 \right], \qquad (2.3)$$

where we have rescaled the following length scales to be defined with respect to the periodic landscape:

$$\tilde{a}_{\text{bulk}} = \left(\frac{2\pi}{a_{\text{CE}}} \right) a_{\text{bulk}}, \quad \tilde{x}_n = \left(\frac{2\pi}{a_{\text{CE}}} \right) x_n, \quad \tilde{t} = \left(\frac{2\pi}{a_{\text{CE}}} \right) t \left(\frac{\epsilon_s}{2m} \right)^{1/2} \qquad (2.4)$$

for the interparticle spacing in equilibrium, the particle position and the time dimensions respectively. The dimensionless coupling constant is

$$\tilde{g} = \left(\frac{a_{\text{CE}}}{2\pi} \right)^2 g \left(\frac{\epsilon_s}{2} \right)^{-1}. \qquad (2.5)$$

The associated equation of motion is therefore

$$\frac{d^2x_n}{dt^2} + \sin(x_n) - g(x_{n+1} + x_{n-1} - 2x_n) = 0, \tag{2.6}$$

where we have dropped the tilde for the dimensionless variables. For low temperatures and with no external force applied, the mobile particles can only be displaced a small amount. In this limit we can linearise the equations of motion by making a change of variables to $x_n = na_{\mathrm{CE}} + u_n$ where $|u_n| \ll a_{\mathrm{CE}}$ when the density is approximately one particle per well. Applying this variable change and Taylor expanding to lowest order gives

$$\frac{d^2u_n}{dt^2} + u_n - g(u_{n+1} - u_{n-1} - 2u_n) = 0. \tag{2.7}$$

The solution of which, $u_n(t) \propto e^{\mathrm{i}\omega_{ph}(k)t - \mathrm{i}kn}$, describes phonon modes along the chain with dispersion relation $\omega_{ph}^2(k) = 1 + 2g[1 - \cos(k)]$. One can identify a minimum phonon frequency, which in this normalised expression is $\omega_{ph}(k = 0) = 1$. Additionally the maximum phonon frequency is $\omega_{ph}(k = \pi) = \sqrt{1 + 4g}$. This linearised form is sufficient as long as the displacement remains small in comparison to periodicity. For larger displacement nonlinear effects are crucial.

The impact of phonon modes depends on the damping strength. In the underdamped regime, defect motion can be suppressed by phonon radiation. J. F. Currie *et al.* [37] found, through numerical investigation, that the defect oscillations, as it travels over the potential landscape, causes phonon radiation which reduce the defects energy. Our work is focused in the overdamped limit in which phonons can be neglected [2]. We return to the dynamics of driven channels in Chapter 6.

The generalised FK model given in equation 2.6 is the most simplified form of the model. Extensions to the generalised model have been the subject of many investigations [2], two prominent contributors to this field are O. M. Braun, Yu. S. Kivshar [38, 39]. We now briefly summaries some of the observations from the extended FK model.

Equation 2.6 assumes harmonic interactions in one dimension between neighbouring particles which are indistinguishable. O. M. Braun, Yu. S. Kivshar investigated the impact to defect dynamics in the FK model with long range interaction [40], transverse motion [41], impurities [38] as well as the impact on diffusion an anharmonic particle interaction at different densities [39].

O. M. Braun, Yu. S. Kivshar numerically compare the kinks characteristics of the standard FK model with nearest neighbour interactions with long range Coulomb and dipole interactions [40]. Whilst the general properties of the defects remain the same the specific form of their shape is altered. This in turn changes the form of the mass, potential energy and interaction between defects. Introducing anharmonicity into the interaction potential breaks the symmetry in defect motion, chains with interstitial atoms have a greater response to shearing than an equivalent chain with vacancies [39].

Impurities can be included in the FK model by manipulating the properties of a particle within the chain, i.e. its mass or interaction strength. O. M. Braun, Yu. S. Kivshar investigated the defect dynamics in a discrete chain containing an impurity. They found that the defect-impurity interactions can lead to a change in the transport properties and induce scattering, the change in transport properties depends on the nature of interactions (i.e. attractive or repulsive).

Just like the inclusion of anharmonic interactions, O. M. Braun, Yu. S. Kivshar demonstrate that a transverse degree of freedom in the FK model causes a break in the symmetry of defect motion [41]. The authors determine the critical region in which zig-zag defects form, they conclude that an effective anharmonicity is induced by the coupling of the transverse and longitudinal degrees of freedom.

O. M. Braun, Y. S. Kivshar and A. M. Kosevich analytically investigated the interaction between two very weakly coupled one dimensional FK chains [42]. They demonstrated that the interaction of two slow kinks in neighbouring chains causes a bound state to be formed. This system can be used to model stacked superconductors such as BSCCO [43]. The binding effect has been observed in the highly discrete limit by P. Woafo [44] in which the slow moving kinks had a width similar to the lattice spacing.

Additionally, one can consider the effects of perturbing the sinusoidal substrate potential. In the context of superconducting vortex channels, where the substrate potential is induced by the pinned channel edge. R. Besseling *et al.* found that shearing one channel edge with respect to the other caused an abrupt change in the shearing dynamics of the interacting chain [18]. Replacing the periodic channel edge with one with disorder, R. Besseling *et al.* discovered the nucleation of defects which mediated the shear [45].

Despite its simplicity, the one-dimensional FK model has been applied to many physical systems including crowdions, where an interstitial atom is played within an ordered lattice. This was investigated by A. S. Kovalev *et al.* [14], the authors considered the lattice line containing the crowdion as a one-dimensional interact-

ing tube within a substrate potential. Similarly, A. C. Scott derived an equivalent expression to equation 2.6 for a chain of pendula coupled by torsional springs [13]. The coupled pendula model has since been applied by S. W. Englander *et al.* to the denaturation in DNA [46]. We now use the pendula model to arrive at the continuum limit solution.

2.3 The Continuum Limit Approximation

In the limit of strong torsional coupling, the angular deviation between neighbouring springs is small, as such the evolution of the angle along the chain can be approximated as a continuous variable. In the continuum limit, equation 2.6 becomes

$$\frac{d^2u}{dt^2} - d^2\frac{d^2u}{dx^2} + \sin(u) = \frac{a_{\mathrm{CE}}^2}{12}\left[\frac{\partial^4 u}{\partial^2 x \partial^2 t} + \left(\frac{\partial u}{\partial t}\right)^2 \sin(u) - \frac{\partial^2 u}{\partial x^2}\cos(u)\right], \qquad (2.8)$$

where $u(x,t)$ is the continuum limit position variable and $d = a_{\mathrm{CE}}\sqrt{g}$ [2]. The continuum limit expression of the FK model was first shown by P. Rosenau when investigating the nonlinear dynamics of mass-spring chains [24]. Assuming the contributions from the discreteness of the chain are negligible then we can set the right hand side of the equation to zero. After rescaling the spatial variable by d we are left with the sine-Gordon (sG) equation.

$$\frac{\partial^2 u}{\partial t^2} - \frac{\partial^2 u}{\partial x^2} + \sin(u) = 0. \qquad (2.9)$$

The sG equation was the first to show solitonic properties [2], the existence of long time stable waves which can evolve with constant profile. One such solution to the continuum limit equation, referred to as a kink, is expressed as

$$u(x,t) \propto \tan^{-1}\left[\exp\left(-\sigma\frac{x-vt}{\sqrt{1-(\frac{v}{c})^2}}\right)\right], \tag{2.10}$$

where v is the velocity of the kink and σ is the topological charge which has a value of $+1(-1)$ for a (anti-) kink [2]. A plot of this function, for $\sigma = 1$, is given in figure 2.2. A kink forms when an excess particle is placed in the chain, a kink can be formed within a chain of coupled pendula by inducing a complete rotation of a pendula [13]. The anti-kink occurs when a particle is removed from the chain, or when a pendula is completely rotated in the opposite direction.

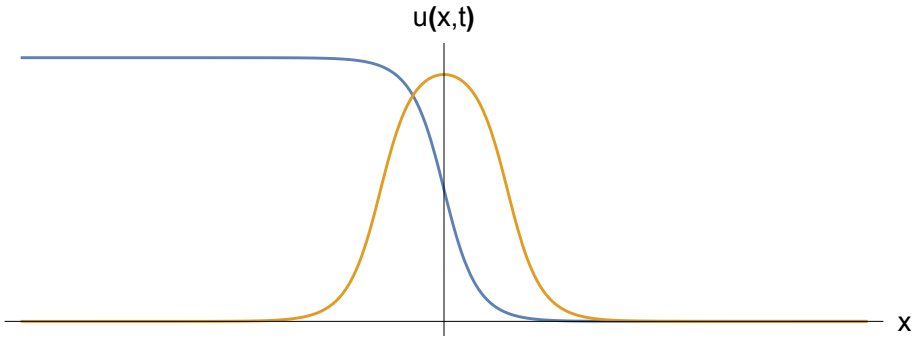

Figure 2.2: Schematic plot of equation 2.10 (blue) and 2.11 for the arbitrary parameters $\sigma = 1,\ u = 0,\ \Omega = 0.1,\ t = 5\pi$.

The final excitation which can occur in this model are known as breathers and they have zero topological charge. In the FK model, breathers are described by

$$u(x,t) \propto \tan^{-1}\left[\left(\frac{\sqrt{1-\Omega^2}}{\Omega}\right)\frac{\sin(\Omega t)}{\cosh\left(x\sqrt{1-\Omega^2}\right)}\right], \tag{2.11}$$

The breather describes a localised oscillation, its magnitude oscillates in t with internal frequency $\Omega < \omega_{ph}(k = 0)$ [2]. The profile at an arbitrary time is given in figure 2.2. As discussed in Chapter 8, the breathers observed in the superconducting channel take a different form to the one given in equation 2.11. We classify ours as

breathers as they are a local excitation which has zero topological charge.

The continuum limit kink solution has been shown to approximately model the kink excitation in discrete system, in the strong coupling limit of $g \gg 1$, up to an "adiabatic dressing" [2]. Whilst the dressing only perturbs the continuum limit solution, in the limit of strong interaction, it can have a significant impact on the properties of the excitations. The profile of the sG kink given in equation 2.10 is translationally invariant. In the discrete case, however, the kink experiences a, reduced, potential barrier. This is referred to as the Peierls-Nabarro (PN) Barrier after its namesakes who independently studied the critical shear of dislocations [47] and [48] respectively.

Fluxons in Josephson junctions (JJs) are an example of a system which can be studied in both the continuum [15] and discrete [16] limit. A JJ is comprised of two superconductors separated by an insulating layer. Supercurrents circulate between the two superconductors about the fluxon which exists within this insulating layer [5]. D. W. McLaughlin and A. C. Scott demonstrated that the long JJ can be modelled using a perturbed sG equation [15]. The fluxon in their model can be treated as a kink in the continuum limit. Alternatively, A. V. Ustinov *et al.* consider a model similar to that of the discrete FK model given in equation 2.6 when investigating the fluxon dynamics in periodic array of discrete JJs [16].

2.4 Ground State Structure

We have introduced the FK model, its continuum limit counterpart the sG equation and reviewed some studies of kink properties in the presence of alterations to the generalised FK model. The ground state study of the FK model has applications in adsorbed atoms (or adatoms) on the surface of crystals where the bulk and sub-

strate lattice parameter can vary significantly [49]. In fixed-density systems one can quantify the discrepancy in a number of ways, with the optimum method depending on the system considered.

For a chain of particles connected by springs, the preferential parameter to use when quantifying the discrepancy is the associate natural length scale of the bulk a_{bulk} and substrate a_{CE}. The relative density is often considered when investigating vortices in superconductors [18] as it can be altered using an external magnetic field [5]. Alternatively, one can use the relative number of particles N and potential wells M within the periodic unit of length L. These relative parameters can be expressed via the dimensionless coverage parameter

$$\theta = \frac{a_{\text{CE}}}{a_{\text{bulk}}} = \frac{N}{M}. \tag{2.12}$$

As the coverage parameter, θ, of the FK model changes, the ground state transitions through a number of different states [2]. The ground state structure is dependent upon both the coverage parameter and the relative strengths of the interaction and substrates. Solving for such a ground state can be cumbersome process as it requires solving N coupled ODEs. One method suggested by Griffiths and Chou [3], involves a minimisation eigenvalue approach for an effective potential.

Using the minimisation eigenvalue approach, Marchand *et al.* numerically determined the phase space of a simplified version of the FK model with non-convex interaction potential [4], shown in figure 2.3. The phases are shown as a function of the difference in lattice parameter $\delta = a_{\text{CE}} - a_{\text{bulk}}$ and the relative interaction strength $\text{K} = \frac{U^0_{\text{int}}}{U^0_{\text{sub}}}$. The tongues in figure 2.3 are labelled by their winding number, as defined in [3]. Marchand *et al.* found that there is "usually" [4] a continuous

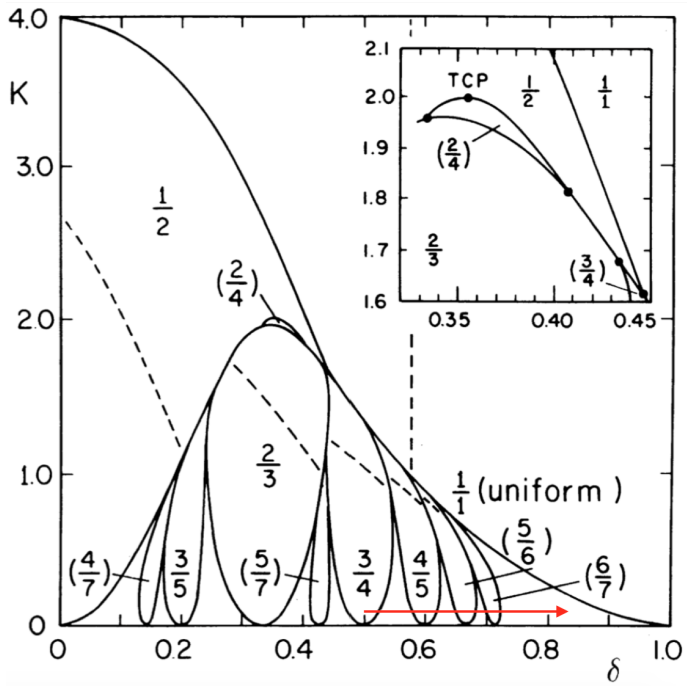

Figure 2.3: Phase space of the FK model showing the commensurate states (or tongues) as a function of relative interaction K and difference in lattice parameters δ. Each state is labeled by its winding number as defined in [3]. Results were obtained numerically by Marchand *et al.* [4]. Overlaid red arrow is related to equation 2.14 and not part of the original figure displayed in Fig. 3 in [4]

second order transition from the state labelled $1/1 \rightarrow s/q$ where s and q are integers and typically a first order transition between all other states.

As the interaction strength decreases, $K \rightarrow 0$, one can see, from figure 2.3, an increases in the density of phases. Marchand *et al.* noted that the winding number of a given state was found by adding the numerators and denominators of the neighbouring tongues. For example, at $K = 1.0$ in figure 2.3 the $\frac{2}{3}$ tongue is bounded by the $\frac{3}{5}$ and $\frac{3}{4}$ tongues, adding the numerator and denominator of these neighbouring tongues returns $\frac{3+3}{5+4} = \frac{2}{3}$. For this reason Marchand *et al.* proposed that for an infinite chain there is a devils staircase of phases [4]. These states can be categorised by commensurate, incommensurate and decommensurate.

2.4.1 Commensurate Ground States

For any value of $\theta = \frac{s}{q}$, where $s,\ q$ are coprimes, there exists a commensurate structure. The simplest case is when $s = q = 1$ which is the registered state in which each potential well contains exactly one particle. An alternative commensurate state is achieved when $\theta = \frac{1}{2}$, which has an associated winding number $\omega = 2$, where every second well is occupied, inverting this coverage gives $\theta = 2$ ($\omega = \frac{1}{2}$) would result in an equilibrated state in which each well is doubly occupied. These are just two of an infinite number of possible ground states. For $\theta = \frac{1}{p}$ where p is an integer, the ground state is formed by equally spacing the particles with one situated at the minima of every pth well. The translational invariance of the $\theta = \frac{1}{p}$ states means that the response to shearing in a one dimensional system is independent of p [2].

Figure 2.4: Ground state arrangement for $\theta = 3/5$ where 3 particles are located within a periodic region of length $5a_{\mathrm{CE}}$. Figure taken directly from Fig. 5.3 in [2].

For all other commensurate values of θ the ground state structure is comprised of a repeated period structure of length sa_0 consisting of q particles, the lattice spacing (and particle deviation u_n) is no longer constant throughout the chain. The ground state for $\theta = 3/5$ is displayed in figure 2.4, note how the periodic unit of width $5a_{\mathrm{CE}}$ contains three particles.

2.4.2 Incommensurate Ground States

When θ cannot be expressed as a rational number the resulting structure is referred to as incommensurate, these states can only occur in infinitely long system. To numerically study the ground state structure of an infinite length system of fixed density, periodic boundary conditions are often implemented. Such a system has a fixed number of wells, M, and particles, N, within the periodic unit of length L, as such a rational value of θ always exists and it is impossible to simulate a truly incommensurate state.

One can overcome the simulation limitations by selecting an appropriate choice for N and M. One such option is to pick successive numbers from the Fibonacci sequence (FS), e.g $N = 89,\ M = 144$. This approach was taken by L.M. Floría and F. Falo when investigating the response of incommensurate structures to an alternating driving force [50]. The ratio of these values closely approximates the irrational Golden ratio (GR). For comparison, the coverage parameters of the GR and FS are

$$\theta_{GR} = \frac{\sqrt{5}-1}{2} \approx 0.61803 \quad \text{and} \quad \theta_{FS} = \frac{89}{144} \approx 0.61806. \tag{2.13}$$

The incommensurate state has no regular structure, in the infinite limit a particle exists at every height in the well including the maxima. S. Aubry found that there is an abrupt transition in the behaviour of the incommensurate structure as the interaction parameter passes through a critical point, defined g_{Aubry} [51]. For $g < g_{\text{Aubry}}$ the incommensurate structure is pinned to the substrate potential, above the Aubry transition the structure is in the sliding mode.

2.4.3 Decommensurate Ground State

We have outlined the key ground state features for both a commensurate and incommensurate coverage parameter. Now we ask what happens when a periodic unit of M wells contains $N = M \pm m$ particles where $M \gg m \in \{1,\ 2,\ 3, ...\}$. In this limit the ground state structure which forms is that of the commensurate state $\theta = \frac{N}{M} = 1$ but with m equally spaced kinks (or anti-kinks if $m < 0$). One can also have kinks at other filling factors $\theta = s/q$ where $q > 1$, where each the kink contains σ/q additional atoms. In this thesis, we only consider the simplest case of $q = 1$. These kinks have well defined profile, mass and energy [2]. As these decommensurations are a pivotal part of the coming research, an overview of their ground state properties will now be given.

We simulate a periodic unit of length $L = N_c a_{\mathrm{CE}}$. One might wonder why a periodically evolving structure with $\omega = (N_c - 1)/N_c$ where both are coprimes is not the natural ground state when one particle is removed from the registered chain. As the lattice parameter discrepancy increases from $\delta = 0.5$ for $K \ll 1$, the ground state transitions through a series of phases starting with a winding number of $\omega = \frac{3}{4}$, shown by the red arrow in figure 2.3. The average particle spacing approaches unity via

$$\omega = \frac{3}{4} \to \frac{4}{5} \to \frac{5}{6} \to \frac{6}{7} \to \frac{n-1}{n}. \tag{2.14}$$

As n increases, the size of the associated tongue in phase space reduces. In the limit $n \to \infty$, it becomes energetically favourable to form the registered state with decommensuration. When a decommensuration is introduced, a finite region of the periodically ordered chain is perturbed. In section 2.2 we defined $u_n = x_n - n a_{\mathrm{CE}}$ as

the displacement of each particle, we can therefore quantify the impact of a defect by the accumulated impact of each particles displacement

$$\Delta u = u_{-\infty} - u_{\infty} = \sigma. \tag{2.15}$$

which is equal to the topological charge for the system. Figure 2.5 provides an example the local deformations in the presence of an (a) anti-kink (b) kink, the particle positions, in this schematic, are located at the intersection of the continuum limit solution (dashed black line) and the substrate potential (solid blue line).

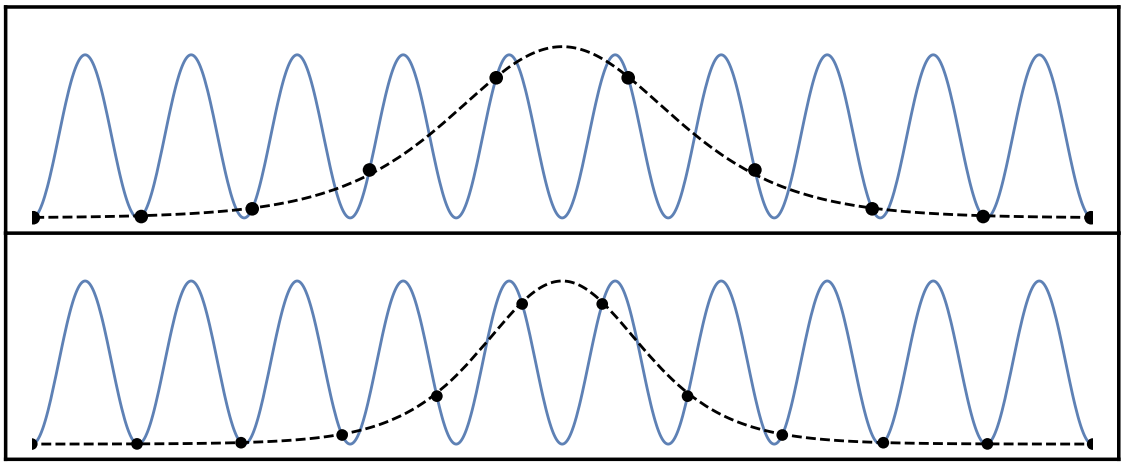

Figure 2.5: Schematic arrange of particles in the presence of an anti-kink (top) and a kink (bottom). The particles (black) are situated at different heights in their respective potential wells (blue), the dashed black line emphasises the continuum limit solution. Far from the centre of the defect particles are situated at the potential minima.

Whilst only one well can physically contain the interstitial (or vacancy), the particles in the neighbouring wells dilate (or contract) in order to minimise the overall potential energy contributions from both the substrate and interaction. Independent of the topological charge, both defects are identifiable by a localised excitation which exponentially decays.

The extent of the distribution, i.e. the kinks size, has been shown in the continuum limit to be

$$d_{\text{eff}} = d\left[-\mathrm{V}''_{\text{sub}}(x_m)\right]^{-1/2}, \tag{2.16}$$

where x_m is the location of the maximum substrate potential and $d = a_{\text{CE}}\sqrt{g}$ [39]. We can see from this formula that as the substrate potential increases in magnitude, the kinks width decreases. This is because the curvature of each well increases and so displacing a particle from the equilibrium by the same amount now costs much more. Furthermore, from the continuum limit we understand that the mass of a kink/anti-kink is given by

$$m_a = \frac{1}{4\pi^2\sqrt{g}} \int_{x'_0}^{x''_0} d\phi \sqrt{2\mathrm{V}_{\text{sub}}(\phi)}, \tag{2.17}$$

where x'_0, x''_0 are the positions of two adjacent minima. When considering multiple defects, one must ensure that the system length $L \gg \sigma d_{\text{eff}}$ is sufficiently long such that each defect can be resolved. For two kinks one requires that $x_d^{(2)} - x_d^{(1)} \gg d_{\text{eff}}$, where x_d is the location of the defects centre of mass. Away from a defect ($x \gg x_d + d_{\text{eff}}$) the chain returns to the registered state.

When a kink (anti-kink) forms, there is an aggregation (dispersion) of interacting particles. The net effect of this is an increase (decrease) in the local charge. Therefore, much like the particles forming it, decommensurations also interact. Whether they attract or repel each other depends on their relative topological charge.

For an exponentially decaying particle interaction, the interaction energy between

two static kinks, which are sufficiently separated, was shown by Y. Hsu to be given by

$$v_{int}(R) \propto \sigma_1 \sigma_2 \sqrt{g} e^{-\frac{R}{d}}, \tag{2.18}$$

where σ_i is the topological charge, d is the kinks width and R is the separation. The interaction between two solitons is caused by the overlap in their tails. We can see from equation 2.18 that a static kink and anti-kink would attract whilst a kink-kink pair would repel. The equation also shows that one can always treat the interactions of kinks as a two body problem.

2.5 Concluding Remarks

- The Frenkel-Kontorova model can be used to describe one dimensional systems with a competing length scale between the interaction and substrate potential.
- In the over-damped limit, one can neglect phonon modes which impact the dynamics of excitations.
- In the limit of strong interaction, one can consider the continuum limit in which the FK model transforms into the sG equation.
- Stable excitations to the sG equation exist which allow for the evolution of topological charge along the chain.
- The sG model also supports breather modes. The profile of these, however, is different to the kind observed in our investigation.
- The discreteness of physical systems can have a perturbative effect on the structure of the excitations, known as the adiabatic dressing [2].
- The ground state structure of a harmonically interacting chain of particles on a sinusoidal substrate depends on the relative potential strength K and coverage parameter θ.
- The periodicity of the structure in the commensurate phase depends on the coverage parameter. As $\theta \to 1$ the energetically favourable state is an isolated defect in an otherwise registered chain.
- The static properties of kinks have known mass, width and interactions which depend on the microscopic details, such as the potential strength K.

Chapter 3

Superconductivity

The system we have chosen to consider for our investigation of the dynamics in the presence of competing length scales is Type-II superconductors. More specifically, we consider the mixed phase of a narrow superconducting channel comprised of layered superconductors. In this chapter, we provide the system relevant background required in this thesis for modelling these system. More detail, than presented in this section, can be found by combined reading of [5] and [6].

We begin, in section 3.1, by motivating our investigation of superconducting channels. An overview of Type-I and Type-II superconductors is presented in section 3.2. We then introduce both London and Ginzburg-Landau theory, in sections 3.3 and 3.4 respectively. These theories introduce the crucial concepts of our model. One such concept is the superconducting vortex. These flux tubes are the building blocks of all of our simulations, section 3.5 details their properties. The dynamics and interaction are quantified and an account of the limits considered are given. We conclude this chapter by discussing the design of our superconducting vortex channel in section 3.6.

3.1 Introduction and Motivation

By definition, superconductivity is the phenomenon of zero electrical resistance and either the complete or partial expulsion of a magnetic field below a critical temperature, T_c [5]. The advent of a material with zero resistance has many promising real world applications, such as in particle accelerators [52]. One of the major limitations, however, are the critical temperatures currently achieved. Despite increasing two orders of magnitude since its discovery in 1911 [53], the recorded values are still far below room temperature. One of the highest critical temperatures achieved at ambient pressure to date was in a cuprate known as $HgBa_2Ca_2Cu_3O_{8+\delta}$, with a record value of 135K [54]. These significantly higher temperatures and magnetic fields are, in part, due to the existence of the mixed phase in which the zero resistance state is prolonged by the formation of flux tubes [6].

More recently, experiments involving hydrides such as H_3S and LaH_{10} have achieved temperatures of 203K and 250K respectively [55]. These experiments, however, were performed at extremely high pressure, of order $\mathcal{O}(10^2\text{GPa})$. However, temperature and pressure are not the only limitation these superconductors face. Manufacturing superconductors is also made difficult by their brittle nature. For example, cuprate superconductors are extremely brittle [56]

An upper bound to the achievable critical temperature still remains elusive, with a complete explanation for the phenomena lacking. As we shall discuss in the coming sections, the flux tubes which extend the range of superconductivity can introduce a resistance when in motion. There has been significant interest in studying the dynamics of the flux tubes, with the motivation of reducing their mobility [45].

3.2 Type-I and -II Superconductors

Superconductors exhibit the phenomena of zero resistance and the complete expulsion of a magnetic field when the temperature is below a critical value. Different types of superconductors can be differentiated by how this state breaks down. In the coming few sections we shall review two of the phenomenological theories behind superconductivity and explain in more detail how these two types of superconductor differentiate. First, we qualitatively describe the key features of Type-I and -II superconductors, emphasising the main differences.

The names Type-I and Type-II refer to the number of critical fields; a Type-I superconductor has only one critical field below which the magnetic field is completely expelled from the bulk of the superconductor. This transition was show by Halperin, Lubensky and Ma to be first order [57]. The Type-II superconductor, however, has two critical fields. It too exhibits complete magnetic expulsion, known as the Meissner effect, below its lower critical field, H_{c1} in figure 3.1, and a partial expulsion below its upper critical field, H_{c2} in figure 3.1, with a continuous (second order) transition between the two critical field strengths. This phenomena is explained by the existence of flux tubes which distribute themselves throughout the bulk, which we shall discuss in greater detail in section 3.5. A schematic depiction of the magnetic induction is given in figure 3.1

The type of materials that exhibit Type-I superconductivity include pure metals and metalloids, such as Mercury and Aluminium [58]. In 1992, U. Gottlieb *et al.* discovered that the alloy $TaSi_2$ displayed characteristics of Type-I superconductivity [59]. Type-I superconductors are often referred to as low temperature superconductors as they commonly have critical temperatures below 10K [58].

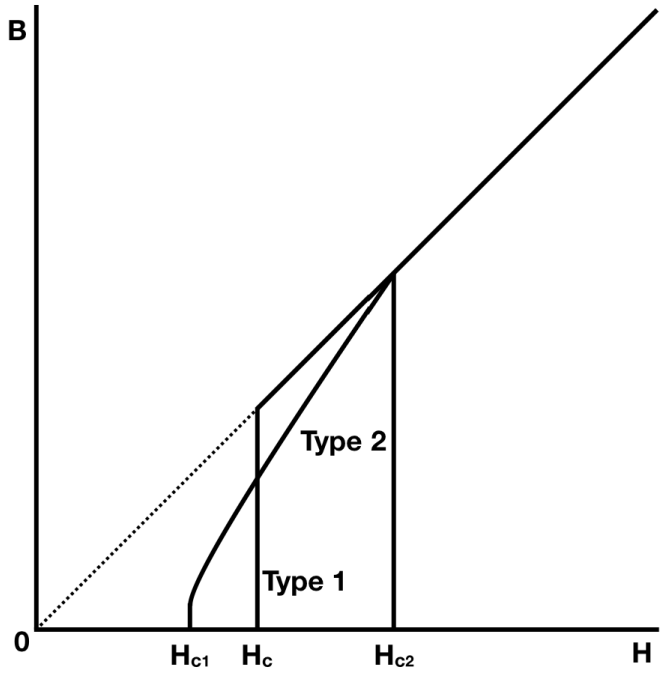

Figure 3.1: Schematic plot depicting the difference in the flux penetration (magnetic induction) B as a function of applied external magnetic field H for Type-I and Type-II superconductors. The critical fields of each type of superconductor are also displayed. This figure is reproduced from Fig. 1.5 in [5].

Type-II superconductors, however, tend to have a much more complex composition. Common materials include metal alloys such as NbN and Nb_3Ge with associated transition temperatures of 16K and 23.2K respectively. Another type of Type-II superconductors are the cuprate compounds. They are often referred to as high temperature superconductors (HTSCs) as their transition temperature is above the boiling point of liquid nitrogen. Examples of these compounds include $YBa_2Cu_3O_{7-\delta}$ (YBCO) [60] and $Bi_2Si_2CaCu_2O_8$ (BSCCO) [61], both of which are multilayered compounds containing layers of CuO_2. The transition temperatures of these cuprates are 93K and 96K respectively, much larger than that of Type-I superconductors as well as Type-II metal alloys. More recently other metallic compounds have shown high temperature superconductivity such as iron-based compounds [62].

3.3 London Theory

We now give an overview the London theory of superconductivity. The earliest formalism of superconductivity was produced by F. and H. London in 1935 [63]. The brothers proposed two equations, relating the microscopic properties of the electric, $\mathbf{E}$, and magnetic, $\mathbf{B}$, fields to the superconducting current density $\mathbf{J_s}$ via

$$\mathbf{E} = \frac{m^*}{n_s e^{*2}} \frac{\partial \mathbf{J_s}}{\partial t}, \tag{3.1}$$

$$\mathbf{B} = -\frac{m^*}{n_s e^{*2}} \boldsymbol{\nabla} \times \mathbf{J_s}, \tag{3.2}$$

where n_s is the density of superconducting charge carriers with mass m^* and charge e^*. Equation 3.1 shows that an electric field causes the superconducting charge carriers to accelerate. Comparing this expression to Ohm's law $\mathbf{J} = \sigma \mathbf{E}$ which describes the fixed current induced by an electric field. We can identify that equation 3.1 describes a current which increases with time $\mathbf{J_s} \propto \mathbf{E}t$. This is the first key feature of superconductors, perfect conductivity.

We now turn our attention to the second London equation. Employing both Ampere's law, $\boldsymbol{\nabla} \times \mathbf{B} = \mu_0 \mathbf{J}$, and Gauss' law for magnetism, $\boldsymbol{\nabla} \cdot \mathbf{B} = 0$, one can remove the current density dependence from equation 3.2. Readily arriving at

$$\nabla^2 \mathbf{B} = \frac{1}{\lambda^2} \mathbf{B}. \tag{3.3}$$

To appreciate the power of this equation, one should consider a semi infinite superconductor extending from $x = 0$ to $x = -\infty$ with a constant magnetic field applied

parallel to the surface. Solving equation 3.3 for the magnetic field profile within the superconductor, one simply finds $\mathbf{B}(x) = \mathbf{B_0}\mathrm{e}^{-x/\lambda}$. The magnetic field decays exponentially within the superconductor, with a decay length of

$$\lambda = \sqrt{\frac{m^*}{n_s e^{*2} \mu_0}}. \tag{3.4}$$

Equation 3.3 therefore describes the second key feature of superconductivity, the Meissner effect - the exclusion of a magnetic field from the bulk of a superconductor by screening currents. This phenomena was discovered by W. Meissner and R. Ochsenfeld two years before the London brothers published their findings [64]. The decay constant λ, better known as the London penetration depth, is the distance an external magnetic field penetrates the superconductor. The London penetration depth is material dependent with $\lambda \approx 50$nm in Nb and $\lambda \approx 190$nm in $YBa_2Cu_3O_{7-\delta}$ [58].

3.4 Ginzburg-Landau Theory

Similar to the London theory, the Ginzburg and Landau (GL) theory is a phenomenological approach to describing superconductivity. However, it can be applied to both Type-I and Type-II superconductors. Whilst the BCS theory offers a more in depth understanding of the microscopic effects of the superconductor, the phenomenological approaches of both the London brothers and Ginzburg-Landau contain all the necessary features for the system explored in this thesis. Additionally, it has been shown, by L. Gor'kov in 1959 [65], nine years after the GL theory and seven years after BCS, that the GL theory is a generalised form of the 1972 Nobel prize winning BCS theory [66], which is beyond the scope of this thesis.

Whilst the pseudo-wavefunction theory was postulated by Ginzburg and Landau, many others made significant contributions. Along with L. Gor'kov, who associated the GL parameters with the microscopic theory [65], A. Abrikosov first used the GL theory to explain the features of Type-II superconductors [67]. In this section, we shall review the GL theory following the derivation presented in [6] and [5]. Then use it to quantify the difference between Type-I and Type-II as well as explain some of the pertinent phenomena of Type-II superconductors introduced in section 3.1.

The GL theory is based upon the theory of second-order phase transitions, published by L. Landau in 1937. The ethos of this theory is that in the vicinity of criticality one can expand the free energy, F, in powers of the complex pseudo-wavefunction ψ, where each of the powers in the expansion has a dependence on the temperature where ψ is small. This pseudo-wavefunction is related to the superconducting electron density via $n_s = |\psi|^2$, which is zero in the normal phase. This is associated to the density of Cooper pairs in the BCS theory [66]. Near the critical

temperature T_c, one can Taylor expand the free energy as

$$F = a_0 + a_1\psi + a_2\psi^2 + a_3\psi^3 + a_4\psi^4, \tag{3.5}$$

where $a_i = a_i(T)$ are the temperature-dependent coefficients, in the absence of any fields or gradients. As $\psi = 0$ for $T > T_c$, the constant $a_0 = F_n$ is equal to the free energy of the normal phase. At any given temperature, the equilibrium state is associated with a minimum in the free energy. One therefore requires that $a_1 = 0$ for all T. Similarly, as $F \in \mathbb{R}$ one also requires $a_3 = 0$ for all T. This reduces the free energy expansion of a homogeneous material at zero magnetic field to

$$F = F_n + a_2\psi^2 + a_4\psi^4. \tag{3.6}$$

The coefficients a_2 and a_4 in equation 3.6 are more commonly denoted as $\alpha(T)$ and $\frac{1}{2}\beta(T)$ respectively. Ginzburg and Landau considered the temperature dependence of these two coefficients, by considering the location of the minimum free energy which occurs at $\psi_0 = 0$ and $\psi_0 = \pm\alpha/\beta$. In the vicinity of the critical point, we require β to be a positive constant. The temperature dependence is then encoded within $\alpha \propto \tau$ where τ is the reduced temperature. The variation in the free energy as a function of the pseudo-wavefunction is given in figure 3.2

From figure 3.2, it is evident that below the transition temperature, the energy is minimised by a finite density of superconducting electrons. The density increases linearly as the temperature is reduced below T_c. Including both magnetic fields and gradient terms, the full expansion of the free energy density may be expressed as

$$F = F_n + \alpha|\psi|^2 + \frac{\beta}{2}|\psi|^4 + \frac{1}{2m^*}\left|\left(\frac{\hbar}{\mathrm{i}}\boldsymbol{\nabla} - \frac{e^*}{c}\mathbf{A}\right)\psi\right|^2 + \frac{\mathrm{B}^2}{2\mu_0}, \tag{3.7}$$

where $\mathbf{A}$ is the vector potential. A consequence of incorporating the "kinetic energy" term is a variation in the wavefunction causes an increase in the free energy. These consequences are more readily understood from the Ginzburg-Landau equations

$$\alpha\psi + \beta|\psi|^2\psi + \frac{1}{2m^*}\left(-\mathrm{i}\hbar\boldsymbol{\nabla} - \frac{e^*}{c}\mathbf{A}\right)^2\psi = 0, \tag{3.8}$$

$$\mathbf{J_s} = \frac{e^*}{m^*}|\psi|^2\left(\hbar\boldsymbol{\nabla}\varphi - \frac{e^*}{c}\mathbf{A}\right) = e^*|\psi|^2\mathbf{v_s}, \tag{3.9}$$

where $\psi(\mathbf{r}) = |\psi(\mathbf{r})|\mathrm{e}^{\mathrm{i}\varphi(\mathbf{r})}$ and $\mathbf{v_s}$ is the superconducting electron velocity. These are found by minimising the GL free energy with respect to both ψ and $\mathbf{A}$ [5]. By setting $\mathbf{A} = 0$ in equation 3.8 and normalising with respect to the $\psi_\infty^2 = -\alpha/\beta$ one finds

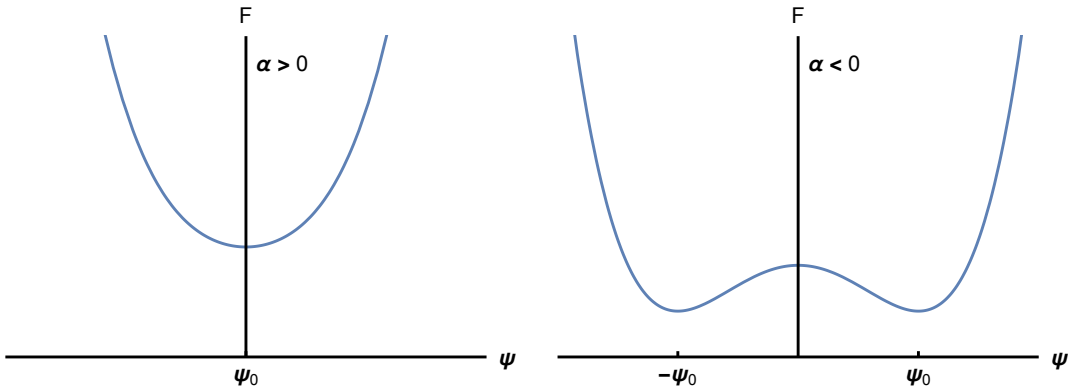

Figure 3.2: Schematic plot of the free energy functional above (left) and below (right) the critical temperature T_c, ψ_0 highlights the equilibrium positions. This figure is reproduced based on Fig. 8.3 in [6].

$$\xi^2 \frac{d^2\tilde{\psi}}{dx^2} + \tilde{\psi} - \tilde{\psi}^3 = 0, \tag{3.10}$$

in one dimension where $\tilde{\psi} = \psi/\psi_\infty$. The parameter ξ in equation 3.10 defines the natural length scale over which ψ varies, more commonly known as the coherence length. This is defined as

$$\xi(T) = \sqrt{\frac{\hbar^2}{2m^*|\alpha(T)|}}. \tag{3.11}$$

As one approaches T_c, the scale over which ψ varies diverges. So far we have introduced two characteristic length scales. The first defines the decay of the applied magnetic field, λ, and the second is the characteristic length scale of the variation, ξ, of the pseudo-wavefunction ψ. Both characteristic length scales are dependent on the specific superconductor in question, with $\xi = 39$nm in Nb and $\xi = 2$nm in $YBa_2Cu_3O_{7-\delta}$ [58]. By considering the ratio of the two length scales associated with a superconductor, one arrives at the Ginzburg-Landau parameter

$$\kappa = \frac{\lambda}{\xi}. \tag{3.12}$$

The consequences of this ratio are profound. Through numerical integration of equation 3.10, Ginzburg and Landau studied the behaviour of the surface energy between the normal and superconducting phase. They found that its contribution to the free energy changes from positive to negative as one increases through the critical value $\kappa_c = \frac{1}{\sqrt{2}}$. They also justified how the Type-I superconductors have $\kappa < \kappa_c$, which was experimentally verified at $\kappa = 0.03$ and $\kappa = 0.11$ in the Type-I superconductors of Al and In, respectively.

In 1957, A. Abrikosov went on to study the impact of a negative surface energy [67]. He found that the free energy is minimised by maximising the domain wall area through subdividing the normal regions. Naively, however, this suggests a run-away effect in which the free energy can be reduced further by the continual subdivision of the regions. Whilst increasing the domain wall area reduces the free energy, the contribution from the gradient term in equation 3.7 increases as the state sub-divides.

A. Abrikosov found that the optimum domain size for these evenly distributed normal regions was of the order $\mathcal{O}(\xi)$, which we know as the vortex lattice, see section 3.5. Abrikosov also found that instead of the abrupt breakdown of superconductivity observed in Type-I superconductors, two critical fields exists within which the flux penetrating gradually increases. In the mixed state, between the lower (H_{c_1}) and upper (H_{c_2}) critical fields, the field enters the superconductor via an increasing density of quantised vortices, also referred to as flux tubes.

The mixed state provides a useful toy model for simulating a Frenkel-Kontorova type system. The next section is dedicated to applying the theory discussed in this section to derive the relevant parameters of our model. Only required background is highlighted.

3.5 The Superconducting Vortex

In the previous section, we established that in the mixed phase of a Type-II superconductor the magnetic flux penetrates through normal domains called vortices. Through a free energy optimisation, A. Abrikosov found that the optimum size of each domain is of the order $\mathcal{O}(\xi)$. In this section, we take a closer look at the vortex. Following the methods presented in [6] and [5], we show the flux carried by each vortex, how they interact, the natural ground state arrangement and the dynamical response to internal and external forces.

3.5.1 Vortex-Vortex Interaction

Like the suppression of the magnetic field by supercurrent flow at the boundaries of a Type-I superconductor, each vortex has a supercurrent circulating around it. In a similar fashion to London's evaluation of the flux, Φ, contained within the core of a superconducting ring, one can integrate the magnetic field within an isolated circular surface of radius $r \gg \xi$ which is far away from the vortex that the enclosing $\mathbf{v}(r) = 0$. This gives

$$\Phi = \int \mathbf{B} \cdot d\mathbf{S} = \oint \mathbf{A} \cdot d\mathbf{l} \tag{3.13}$$

using Stoke's Theorem. Combining this with equation 3.9, the line integral along the closed circular path at a radial distance of r from the vortex core yields when going around any closed path

$$\Phi = \Phi_0 = \frac{h}{2e}, \tag{3.14}$$

as the wavefunction remains single valued. In contrast, had the integration loop included n vortices, then the total flux would have been $\Phi = n\Phi_0$. The quantisation of the fluxoid, suggested by F. London, was experimentally verified using a thin walled cylinder by W. A. Little and R. D. Parks in 1964 [68]. One should note that it is the fluxoid and not the flux which is conserved, far from the vortex core, however, where the screening currents are zero the two are indistinguishable.

For a given magnetic flux, B, penetrating the superconductor, there will be $n = \mathrm{B}/\Phi_0$ vortices. We now consider their interaction, and deduce from this the ground state lattice structure. We also determining the total flux around an isolated vortex, we can also determine the magnetic field profile at $r \gg \xi$. We consider a modified form of equation 3.3, from London theory, which accounts for the vortex core.

$$\nabla^2\mathbf{B} - \frac{1}{\lambda^2}\mathbf{B} = -\frac{\Phi_0}{\lambda^2}\delta_2(\mathbf{r})\hat{\mathbf{z}}. \tag{3.15}$$

where $\delta_2(\mathbf{r})$ is the two-dimensional delta function, for convenience the vortex is situated at the origin. Equation 3.15 has known solution for $r \gg \xi$ given by

$$\mathrm{B}(r) = \frac{\Phi_0}{2\pi\mu_0\lambda^2} K_0\left(\frac{r}{\lambda}\right) \tag{3.16}$$

where $\mathrm{B}(r)$ is the magnitude of the magnetic field at a radial distance r from the vortex. The modified Bessel function of the second kind, $K_0(r)$, diverges logarithmically as $r \to 0$. The interaction between two vortices can be determined by calculating the free energy contribution from the combination of the fields from two vortices situated at $\mathbf{r_1}$ and $\mathbf{r_2}$, respectively as derived in [5]. They find

$$V_{12} = \frac{\Phi_0^2}{2\pi\mu_0\lambda^2} K_0\left(\frac{r_{12}}{\lambda}\right). \tag{3.17}$$

for the interaction between vortices with Euclidean separation $r_{12} \gg 2\xi$. The interaction increases the free energy and, as such, the vortices have a repulsive interaction with a force of magnitude

$$\mathrm{F}_{12} = \frac{\Phi_0^2}{2\pi\mu_0\lambda^3} K_1\left(\frac{r_{12}}{\lambda}\right), \tag{3.18}$$

which acts in the radial direction between $\mathbf{r_1}$ and $\mathbf{r_2}$. So far, we have identified that due to the fluxoid quantisation the vortex density of the mixed phase is set by the external magnetic field. These vortices are repulsive and so favour maximal separation. The arrangement which offers maximum separation at a given density is the triangular lattice with lattice vectors

$$\mathbf{a} = a_{\mathrm{bulk}}\hat{\mathbf{x}} \tag{3.19}$$

$$\mathbf{b} = a_{\mathrm{bulk}}\left(\frac{1}{2}\hat{\mathbf{x}} + \frac{\sqrt{3}}{2}\hat{\mathbf{y}}\right) \tag{3.20}$$

where $a_{\mathrm{bulk}}^2 = 2/\sqrt{3}n$ is the lattice spacing. In the context of superconducting vortices, the triangular lattice is more often referred to as Abrikosov lattice, despite its namesake incorrectly predicting a square lattice arrangement. The vortex lattice was first imaged ten years after Abrikosov's prediction by Essman and Träuble using magnetic decoration [69]. We shall discuss this observation method in greater detail (see section 6.3.2). In the presence of boundaries or inhomogeneities in the

underlying material, the Abrikosov lattice is distorted to minimise the free energy. Whilst bulk lattice defects are not of primary interest in this thesis, we shall discuss some of the methods for identifying them in section 4.4.

3.6 Superconducting Narrow Channel

Thus far, we have reviewed the theoretical groundwork of superconductivity, with a particular focus on the mixed state of Type-II superconductors. We now discuss how one can create a driven superconducting lattice within a confining channel geometry.

First presented by A. Pruymboom *et al.* in 1988 [1], the superconducting narrow channel (SCNC) has had enormous amounts of interest [18, 70–73], with its adaptability being one of its main drawing points. We begin by outlining the general composition of a SCNC. While our focus is on a single isolated channel, experiments often produce an array of around 200 narrow channels from one sample. This allows the measurements of bulk properties. Our focus is on dynamics and so we focus on a single channel.

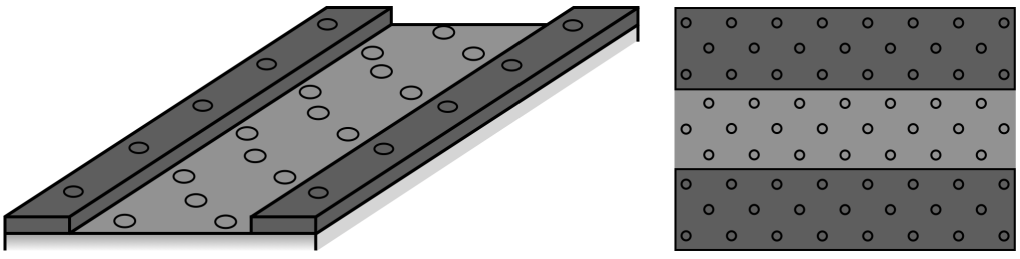

Figure 3.3: Schematic plot of the the narrow superconducting channel geometry, both a three dimensional (left) and two dimensional (right) representation. The circles represent vortices, and the light/dark grey shading indicates different superconductors. The applied magnetic field acts out of the plane. The pinned channel edges have been aligned with the **a** lattice vector.

Figure 3.3 depicts a schematic example of one of the narrow superconducting channels of the experiments of A. Pruymboom *et al.* [1]. The channel is produced by layering two different superconductor's, and etching away a channel region from the upper layer to reveal the lower layer. Pruymbooms device consisted of a $d_1 = 50$nm thick layer of NbN on top of a $d_2 = 550$nm thick layer of amorphous Nb_3Ge. Conventionally, channel geometries are long and thin, however, alternative geometries can be imagined, for example A. A. Tomlinson has proposed an alternative fabrication which would mimic periodic boundaries by etching a large hexagon from a pinned Abrikosov lattice [28]. An alternative channel etching, with diamond constrictions rather than straight boundaries was investigated by K. Yu *et al.* [73]

Before we justify the design of figure 3.3, we first comment on the thickness of the "thin" superconductor. It is well documented that a superconductor's properties can drastically change in the thin limit. Namely the loss of the Meissner effect and Pearl's solution for the vortex-vortex interaction [6]. The quantities derived in section 3.5 however were for a "thick" superconductor. The compound Nb_3Ge has a coherence length of $\xi = 3$nm and a London penetration depth of $\lambda \approx 90$nm, as one can see $d_2 \gg \lambda \gg \xi$. By "thin", therefore, we are referring to the structural properties of the vortex tube. We assume that the samples are sufficiently thin that the vortex remains straight and free of entanglement, permitting us to model it as a two dimensional system as justified by A. Pruymboom *et al.* [1].

The Abrikosov lattice can deform in the presence of inhomogeneities in the underlying superconductor. These random defects in the crystalline structure cause a local reduction in the local order parameter [74]. If the size of a defects is of the order $\mathcal{O}(\lambda)$ then it is energetically favourable for a vortex to align with it. One is not limited to randomised pinning sites, as by employing ionising radiation one can

fabricate a specific pinning geometry, such as conformal arrays [25].

Not only do these pinning sites limit the thermal motion of vortices, but they can also restrict motion from transport currents. When an external current, **J**, is applied across a superconductor, it induces a Lorentz force which acts in the direction perpendicular to both the external current and magnetic flux. This can be described by

$$\mathbf{F_D} = \mathbf{J} \times \frac{\Phi_0}{c}. \tag{3.21}$$

Alternatively, one could have considered the Lorentz force from the screening currents to derive the vortex-vortex interaction. At finite temperatures with an applied current, the pinned vortices may undergo discontinuous motion known as flux creep. As these pinning sites can help minimise vortex motion, which introduces a resistance, there is a significant amount of research dedicated to understanding and manipulating the effects of pinning [75]. Pinning plays a crucial role in the layered geometry depicted in figure 3.3 in which the NbN layer has a significantly higher pinning strength than the underlying Nb_3Ge layer. By etching out a channel geometry, a region of the low pinning superconductor is exposed.

For finite drive, vortices in an isolated NbN sample remain motionless whilst the vortices in an isolated Nb_3Ge sample would flow almost unimpeded by pinning sites [1]. By layering the superconductors, those vortices located underneath the NbN layer will be locked into place through the strong attraction. Those vortices located in the exposed region will be in a state of motion for sufficient drive. As we shall see, however, there is an artificial pinning imposed on the exposed superconductor with the ordered channel edge acting as the substrate potential in the FK model.

As the mobile portion of the superconducting lattice flows, it accumulates a viscous drag force proportional to the velocity of the vortex $\mathbf{F_{drag}} = -\eta \mathbf{v_v}$. The viscous drag coefficient η was found by Bardeen and Stephenson to be

$$\eta = B\frac{\Phi_0}{\rho_f c^2} \tag{3.22}$$

where $\rho_f \propto B$ is the flow resistivity, meaning the viscous drag coefficient is independent of the magnetic field. As we shall see, the dynamics of the vortices beyond the critical shear in superconducting channels is challenging to resolve. By enhancing the viscous drag one could conceivably improve the resolution of the vortex dynamics without impacting the critical driving forces. M. Danckwerts *et al.* [76] has shown that by coupling the superconductor to a nearby two dimensional electron gas, the vortex motion can be further suppressed by induced Eddy currents.

3.7 Concluding Remarks

- Type-II superconductors experience a mixed phase, in which magnetic flux penetrates the superconductor in the form of discrete vortices. This phase is not observed in Type-I superconductors
- The vortex carries a quantum of flux, Φ_0 within its core. The core radius of a vortex is of the order $\mathcal{O}(\xi)$ where ξ is the coherence length.
- In the mixed phase, away from the upper critical magnetic field, the separation between vortices is much greater than the core radius, $a_{\text{bulk}} \gg \xi$. One can, therefore, consider the vortices to be point-like.
- The repulsive vortex-vortex interaction is the modified Bessel function of the second kind, to maximise separation the vortices arrange into the Abrikosov lattice at zero temperature.
- A vortex can be pinned to an inhomogeneity in the underlying superconductor where there is a reduction in the local order parameter. The pinning sites can be natural or fabricated.
- Confining channels of pinned and "free" vortices can be created by layering superconductors with different pinning strengths. The vertical alignment causes "free" vortices which reside under the strong pinning material to also be pinned.
- Considering thin superconductors means we can treat the flux tubes as straight. These tubes experience a viscous drag force when driven by a Lorentz force.

Chapter 4

Numerical Model for SCNC

In Chapter 3 we introduced relevant required properties of Type-II superconductors for this thesis. In this chapter, we now explain how these physical features can be reproduced in numerical simulations. In section 4.2, we present a detailed account of the overdamped Langevin equation. We discuss each component of this equation in turn, identifying both how this equation can model a superconducting channel and possible methods of optimising each component. Further optimisation techniques such as tabulating the interaction force, cell decomposition and the periodic corrector method are described in section 4.3. For a detailed study of the optimisation methods and appropriateness of the simulated thermostat, we refer the reader to previous work within this group: J. S. Watkins [27] and A. A. Tomlinson [28] respectively. With a vortex lattice simulation established, we conclude this section by determining the melting temperature of an infinite Abrikosov lattice. This allows us to verify our simulation and set the scale for annealing.

4.1 Introduction

The generalisations of the FK model detailed, in section 2.2, are not analytically tractable. We simulate numerically with C++ and analyse with Mathematica. Simulating many body systems over long time periods is computationally intensive, they are sensitive to noise and require averaging over many runs. It is for this reason that a discussion of optimisation techniques is presented.

When simulating the mixed state of Type-II superconductors one is presented with a choice: one can numerically solve the Ginzburg-Landau equation directly and simulate a limited number of vortices as one is constrained by the computational intensity, or, one can model the pancake vortices of a thin Type-II superconductor as point particles with zero mass interacting in a flat two dimensional plane. The benefit of treating the vortices as point particles as the computational simplicity means that the number of vortices which can be simulated increases dramatically. The cost, however, is that one loses the ability to study the creation and annihilation of vortex/anti-vortex pairs. As the average spacing between vortices is much larger than the vortex core, $a_{\text{bulk}} \gg \xi$, we treat the vortex cores as point like.

Although it is possible to experimentally study Type-II superconductors in a lab, there are many benefits to employing numerical techniques. Experiments are expensive, whilst simulations are, in general, cheap. When simulating, one can readily perform a parametric sweep of phase space. The accessibility of the phase space in simulations can, however, be a double edged sword. As experiments require more effort to run, greater attention is often paid beforehand to determine appropriate parameters.

4.2 The Overdamped Langevin Equation

In this thesis, we numerically solve for the static and dynamical behaviour of a collection of N interacting vortices under the influence of external constraints. There are a number of techniques which can be applied to tackle many body systems, each of which have their own benefits and constraints. One is the Monte Carlo method. Whilst this approach is useful when trying to find the ground state of a system, it offers limited applicability when studying dynamics [77]. The work presented in this thesis needs to incorporate the flow of vortices, we opt instead to employ Langevin dynamics. The method discussed in this section applicable for many physical systems including superconducting vortices and repulsive particle's. We, therefore, introduce the generalised equation of motion and then outline how it can be realised for superconducting vortices.

Langevin dynamics simplifies the treatment of a system by allowing one to neglect the treatment of microscopic interactions in place of a continuum. The time scales of the macroscopic vortex dynamics and the motion of the microscopic Cooper pairs are very disparate. This means that the specific details of the interactions can be replaced with a stochastic force, $\boldsymbol{\chi}(t)$, and a viscous drag, $-\eta\dot{\boldsymbol{r}}$ where η is the flux flow defined in the last section. Such techniques are common place when studying Brownian motion. The equation of motion for a particle is

$$m\ddot{\boldsymbol{r}} = \mathbf{F} + \boldsymbol{\chi}(t) - \eta\dot{\boldsymbol{r}}, \tag{4.1}$$

where m is the particle mass, $\ddot{\boldsymbol{r}}$ is the particle's acceleration and $\mathbf{F}$ encapsulates all of the additional forces the particle experiences.

We now isolate each term and discuss its role in narrow superconducting channels and how it can be optimised. Firstly, the viscous drag acting on the vortex is significantly greater than the inertia. In this overdamped limit one can treat the vortex as massless ($m = 0$), leaving behind a first order differential equation known as the overdamped Langevin equation.

The power of employing Langevin dynamics is the adaptability of the model. Take the force acting on the vortex $\mathbf{F}$; this can include interaction with other mobile vortices $\mathbf{F}_{vv}$, with a confining pinned lattice $\mathbf{F}_{vp}$, with pinning sites within the channel $\mathbf{F}_p$ or with an external driving force $\mathbf{F}_D$. Furthermore each of these components can be varied to meet the specific needs of the experiment. In our simulations we consider the interaction of superconducting vortices derived in the previous chapter, one could however consider repulsive magnetic colloids instead by setting the interaction force as $\mathbf{F}_{vv} \propto r^{-3}$ [40].

The mobile vortices are confined in the homogeneous channel by a lattice of pinned vortices in a triangular arrangement. Pinning sites can be simulated in a number of ways [18, 78, 79]. H. J. Jensen *et al.* [79] considered weak pinning sites when conducting a phase space investigation of two-dimensional flux flow as a function of driving force and pinning strength. A similar study was later produced by H. Fangohr *et al.* [78]. In our investigation, we consider infinite strength pinning sites in the channel edges and no pinning in the channel, similar to that of [18]. The current required to induce flux motion (see equation 3.21) is 2×10^4 times bigger in NbN than in amorphous Nb_3Ge [1]. This approximation is, therefore, appropriate for modelling narrow superconducting channel, as depicted in figure 3.3.

The final component of the force is the externally applied force. Here we consider a

constant Lorentz force discussed in the previous chapter. F. Peeters *et al.* studied the flow profiles of vortices in wide channels with a variety of position dependent driving forces when investigating the relative chain velocities in wide channels [19]. Beyond inhomogeneous forces, time dependent forces such as an AC driving force are commonly implemented when investigating synchronisation [23].

To approximate temperature, one requires a model for a thermostat. The stochastic behaviour in our system is simulated with the Anderson thermostat [80], this simulates a canonical ensemble (NVT) with temperature T, number of vortices N and volume, V. This thermostat requires that the thermal kinks from the underlying continuum are uncorrelated between both time and vortices, which is expected due to the disparate time scales. The Anderson thermostat assumes that the kicks should produce the Boltzmann distribution of the vortices energies and have a time average of zero. One can represent this as

$$\langle \chi_i(t) \rangle = 0, \tag{4.2}$$

$$\langle \chi_i(t)\chi_j(t') \rangle = 2Tk_B\eta\delta_{ij}\delta(t-t'), \tag{4.3}$$

where $k_B = 1$ is the Boltzmann constant and δ is the Kronecker delta function. We implement this by assigning each vortex in the system a probability of being kicked. To simulate this, we let

$$\boldsymbol{\chi_i}(t) = \sqrt{\frac{2k_BT\eta}{p\Delta t}}\gamma_i(t)\Theta(p - q_i(t))\left[\cos(\theta_i(t))\hat{\mathbf{x}} + \sin(\theta_i(t))\hat{\mathbf{y}}\right], \tag{4.4}$$

where Δt is the iterated time step. This must be held constant throughout the simulation as varying it would also vary the magnitude of the kick. The Θ is the

Heaviside function and permits a kick when the randomly generated probability, $q_i(t)$, from the uniform real distribution $U(0,1)$ is less than the probability of a kick occurring $p = 0.01$. An appropriate value of p was previously investigated by A. Tomlinson [28].

As the system is 2D, the angular direction of the kick $\theta_i(t)$ was also evaluated using a randomly generated probability from the uniform real distribution $U(0, 2\pi)$. As we require a distribution of kick sizes, $\gamma_i(t)$ was a randomly selected number from the normal distribution with a mean of 0 and a variance of 1. To generate pseudo-random numbers we used the c++ package *#include <random >*.

Beyond simulating stochastic dynamics, the advantage of having a thermostat is the ability to anneal. Annealing involves increasing and subsequently decreasing the temperature in order to release a system from a meta-stable state. These stochastic kicks can free a system from an excited state in which it is trapped. When employed correctly, annealing can dramatically reduce the time required to obtain the ground state.

To anneal the system one must first thermally excite the vortices by increasing the temperature to $T < T_m$ where T_m is the melting temperature determined in section 4.4. Holding the vortices at the desired temperature below the melting allows the system to escape metastable states. We maintain this temperature for a prescribed period of time and then slowly reducing the temperature back to zero, lowering the temperature must be performed slowly as to avoid quenching. Reducing by T^{-1} as this was found to be most effective. We anneal the vortices across multiple cycles.

With each term in equation 4.1 discussed, we now justify how the vortices posi-

tions are updated. Rearranging equation 4.1

$$\mathbf{r}_i(t+\Delta t) = \mathbf{r}_i(t) + \int_t^{t+\Delta t} \delta t \left(\mathbf{F}(\mathbf{r}(t), t) + \boldsymbol{\chi}(t)\right). \tag{4.5}$$

There are a range of integration techniques which can be used, depending on the nature of the PDE. The stochastic nature of Langevin dynamics, however, means that many of the conventional techniques cannot be employed. For example, the predictor-corrector method assumes knowledge of previous states which is forbidden by equation 4.3. Instead we employ the simple Euler technique of

$$\mathbf{r}_i(t+\Delta t) = \mathbf{r}_i(t) + \Delta t \left(\frac{\mathbf{F}(\mathbf{r}(t), t) + \boldsymbol{\chi}(t)}{\eta}\right). \tag{4.6}$$

The final parameter to be determined is an appropriate value for the time step, Δt. The error of the position at a given time, when using the Euler method, is proportional to the time step. A larger time step also increases the risk of vortices becoming too close and experiencing unnaturally large interaction forces, this sets a limit on the maximum time step [77]. On the other hand, choosing a time step which is too small makes observing long term dynamics significantly harder. An extensive analysis of an appropriate choice of Δt was conducted by J. Watkins [27]. In accordance with his analysis, we set $\Delta t = 0.0125$. This value ensures that the displacement of any one particle $|\boldsymbol{\delta}\mathbf{r}| \ll \frac{a_{\text{bulk}}}{50}$.

4.3 Further Optimisation

As with any numerical investigation, optimisation is key. Simulating the long time dynamics of a many body system over a range of phase space is numerically taxing. In this section, we introduce the techniques implemented in our simulation and discuss why they were chosen over alternative forms. For a detailed analysis of the numerical techniques presented in this section, we refer the reader to [27]. Aside from computational improvements, one can reduce the human inefficiencies by first reducing the phase space studied as well as implementing a bash script for sweeping over this space. This script allowed a list of desired simulations to be iterated through without user input between simulations, saving valuable time.

When simulating many body dynamics the most computationally intensive contribution to the simulation time is determining the interactions; both the vortex-vortex interaction as well as the vortex-pin interaction. At every time step the forces need to be recalculated in order to update positions, for N mobile and M pinned vortices the interaction is an order $\mathcal{O}(N^2 + NM)$ process. We now address a number of methods which can be implements to improve the performance of this calculation.

The interaction between vortices, as derived in Chapter 3, is the modified Bessel function of the second kind. This is a numerically taxing function as one has to access external libraries such as the Boost library. The Bessel function reduces in magnitude as its argument grows. As such, the contribution to the interaction force from far away vortices is negligible when compared with those close by. It is therefore sensible to implement a cut-off distance beyond which the contributions are neglected, for which $r_c = 6\lambda$ is a commonly used [26].

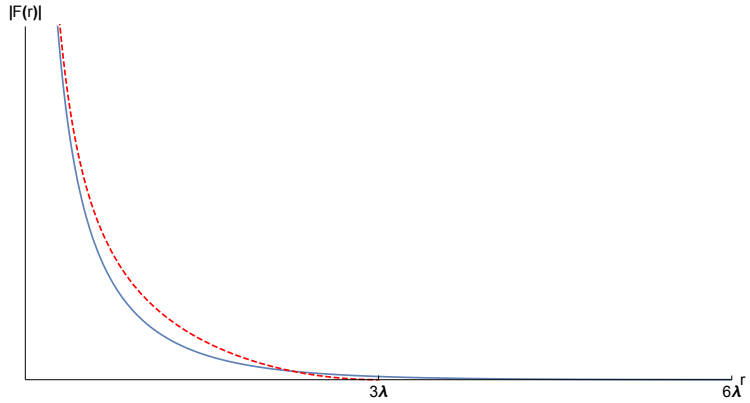

Figure 4.1: Plot of the magnitude of the interaction force as a function of separation. The form of the interaction given in equation 3.18 is displayed in blue, the approximate form given in equation 4.7 with a cut off radius of $r_c = 3\lambda$ is displayed in red.

Accessing the Boost library still accumulates a significant amount of time, even with a cut-off distance in place. For $r_c = 6\lambda$ one still has to access the library $A_{r_c}/A_{\text{cell}} \propto \mathcal{O}(10^2)$ times, as shown in figure 5.2. An approach taken by A. E. Koshelev and V. M. Vinokur [81] was to apply an approximate form of the interaction force,

$$F_{vv}(r) = F_{vp}(r) = \left(\frac{1}{r}\right)\left(1 - \frac{r^2}{r_c^2}\right)^2, \tag{4.7}$$

for $r \leq r_c$. Whilst this does have the beneficial property of being equal to zero at the cut-off radius, it is evident from figure 4.1 that the profile of the approximate force represents a softer interaction compared to true vortex interaction. As the asymmetry of the Bessel function plays a crucial role in the dynamics we instead tabulate the Bessel function at every $r = ih$ and use

$$f(r^*) = \begin{cases} f(h) & h < r^*, \\ f(r_-) + [f(r_+) - f(r_-)]\left(\frac{r^* - r_-}{h}\right) & h \leq r^* < r_c, \\ 0 & r_c \leq r^* \end{cases} \tag{4.8}$$

the magnitude of the force at r^* which is situated between the list elements $i_- = r_-/h$ and $i_+ = r_+/h$. Note that the interaction force is truncated here to $f(h)$, as $\Delta r \gg h$ this does not present any issues. We let $h = r_c/60000 = 0.0001$ as determined by J. Watkins [27]. The approximate interaction force of A. E. Koshelev and V. M. Vinokur was found to be almost two times faster than the tabulated force [27]. In this thesis, we implement the tabulated force. Although it is not the most efficient method presented, it is more representative of the true force. In Chapter 5 we show that by keeping the Bessel form of the boundary interaction, we can construct an alternative representation of the boundary potential which both improves the simulations efficiency and permits some exact calculations.

Whilst implementing a cut-off radius significantly reduces the number of force calculations, one still has an order $\mathcal{O}(N^2 + NM)$ process in determining whether a given vortex is within the cut-off distance. One way to overcome this is to discretise the space, determine which cell each vortex is located in and then only include nearby cells in the iteration. This process is called cell decomposition.

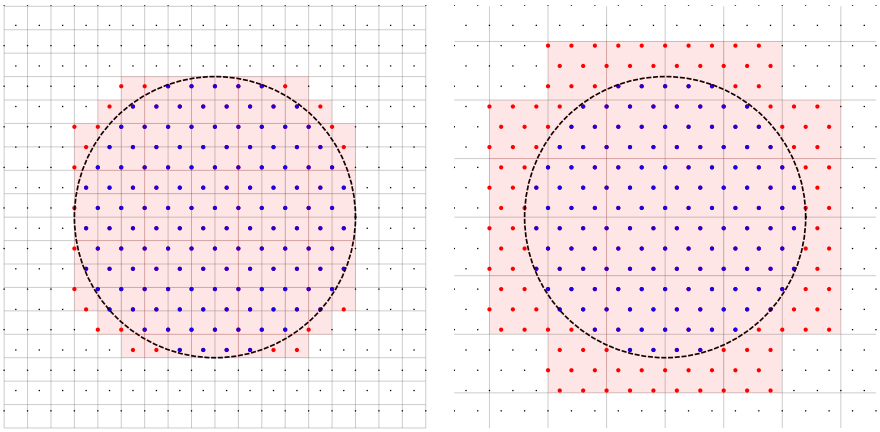

Figure 4.2: Plot of a Abrikosov lattice with parameter $a_{\text{bulk}} = 1$ shown in black, the vortices within a cut-off radius of a given point (black dashed line) are displayed in blue. The vortices within the linked grid elements are displayed in red. The left and right figure have a cut-off of $r_c = 6$ and box width $w = a_{\text{bulk}}$ and $w = 2.5a_{\text{bulk}}$ respectively.

When discretising the space into individual cells an appropriate cell size must be determined. If the cells size is too large, one evaluates many null contributions which is inefficient. As the cell size is reduced the connections become more complex and the number of empty cells increases. An optimum dimension is of the order $\mathcal{O}(a_{\text{bulk}})$, an example of an optimum and inefficient cell decomposition is displayed in figure 4.2 respectively. For the set up shown in figure 4.2, a box dimension of $w = a_{\text{bulk}}$ gives an efficiency of 85.3% whilst a dimension of $w = 2.5a_{\text{bulk}}$ gives an efficiency of 55.4%. Although the efficiencies are subject to position, one can identify an improvement.

In the FK model one can employ Middleton's no passing rule [82], in which the ordering in the channel remains constant, instead of cell decomposition. This technique can be applied when simulating both registered wide channels and incommensurate single chain channels under constant drive. As we are concerned with the "slip" mechanism between neighbouring chains in this thesis, we do not apply this.

There are two commonly used approaches to implementing periodic boundary conditions. The first method is to apply ghost cells. Whilst these cells are not physically present, they are included in the force calculations. When invoking cell decomposition one has to also keep a record of neighbouring cells which are through the periodicity. We however opt for the far more efficient approach of periodic correction. As $L \gg r_c$, for a horizontal separation $\Delta x > L/2$ one can instead apply

$$\Delta x \to \Delta x - \frac{\Delta x}{|\Delta x|} L. \tag{4.9}$$

Combining these methods leads to a significant improvement in simulation efficiency. In the next chapter, we shall revisit the boundary interaction and show how the efficiency can be vastly improved when the contribution is expressed.

4.4 Melting an Infinite Vortex Lattice

We now determine the melting temperature of the infinite vortex lattice. This both verifies the simulation and sets a scale for annealing. The expected ground state of an infinite plane of repulsive vortices is the triangular lattice, referred to as the Abrikosov lattice for a superconducting vortex lattice. Once melted, the state loses all triangular order. As such, one can use the hexatic order parameter to determine the location of the melting temperature. The hexatic order parameter is given by

$$\psi_6 = \left| \left\langle \frac{1}{N_p} \sum_{i=0}^{N_p} \frac{1}{z_i} \sum_{j=0}^{z_i} \mathrm{e}^{\mathrm{i}6\theta_{ij}} \right\rangle \right|^2, \tag{4.10}$$

where θ_{ij} is the angle between the ith vortex and its jth neighbouring vortex, z_i is the coordination number of the ith vortex and $\langle\rangle$ are a time average. To maximise the number of vortices included in the analysis, ghost cells were applied during the Delaunay triangulation to determine the coordination numbers. As we are simulating an infinite system we expect for there to be an impact on the sharpness of the melting transition due to finite sized effects. To determine a melting temperature from the broad transition we select the intersection of the hexatic order parameter ψ_6 and the defect ratio N_v, defined as

$$N_v = 1 - \frac{1}{N_p} \sum_{i=0}^{N_p} \delta_{6,z_i}, \tag{4.11}$$

where δ_{6,z_i} is the delta function which gives 0 if the coordination number is anything other than 6. There are many alternative methods for identifying the melting temperature, one such example is the Lindemann criteria which is given by

$$T_m = \frac{4\pi m \nu c a_{\mathrm{bulk}}^2}{k_B}, \tag{4.12}$$

where m is the atomic mass, ν is the kick frequency, a_{bulk} is the atomic spacing. This method is subjective, one must first define an appropriate value for the Lindemann criterion c. A typical value of the Lindemann criterion is $c = 0.2$.

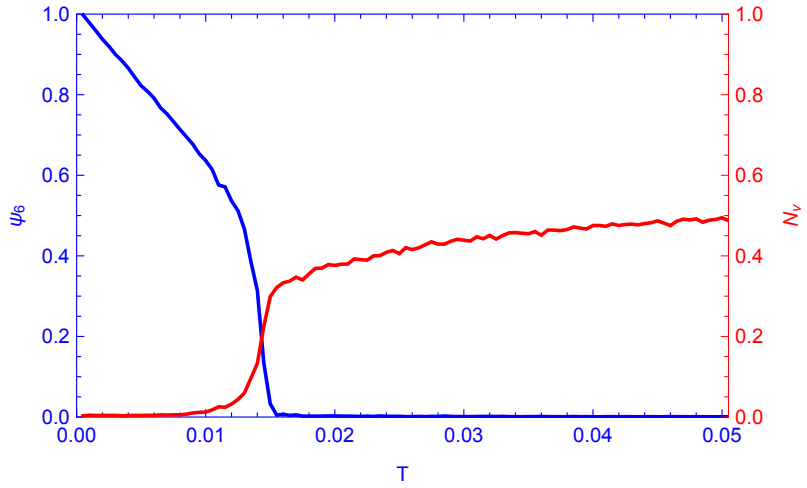

Figure 4.3: Plot of ψ_6 (blue) and N_v (red) as a function of temperature T for a doubly periodic unit cell of dimensions $a_{\text{bulk}}L \times \sqrt{3/4}a_{\text{bulk}}L$ containing $n = 1296$ vortices.

The simulation was initiated at $T = 0$ with $N_p = 1296$ arranged in the Abrikosov lattice within a periodic unit with dimensions $a_{\text{bulk}}L \times \sqrt{3/4}a_{\text{bulk}}L$ at $T = 0$. The temperature is increased by $\Delta T = 0.0005$ every $N_t = 20000$ time steps. The incrementation in temperature is not abrupt, instead each change was implemented by increasing the temperature by an amount $\delta T = \frac{\Delta T}{100}$ until the desired temperature is achieved. At each temperature, the positional data was sampled every 100 time steps. Figure 4.3 displays the averaged results of many repeats of this simulation, from which one finds $T_m \approx 0.0143$.

The melting temperature of the confined channel may differ from that of the infinite system. We, however, only require an estimate to set an upper bound when annealing. As a final verification, we annealed $N_p = 1296$ randomly ordered vortices. Perfect order was found after three cycles of the annealing method discussed above, with a maximum applied temperature of $T = 0.003575 \ll T_m$.

4.5 Concluding Remarks

- Many of the experimental concepts discussed in Chapter 3 can be transferred over to numerical simulations.
- Computational simulations can provide a fast and effective method of sweeping phase space as well as accessing states which are difficult to achieve experimentally.
- Langevin dynamics is an appropriate model which can be adapted to investigate many different effects, the cost of using such techniques for superconductors is that one loses the ability to observe some phenomena.
- We model the mixed phase of superconductivity, away from the upper critical magnetic field. In this limit the vortices can be treated as point-like.
- Additionally, we consider the limit in which the viscous drag acting on the vortex is significantly greater than the inertia. In this limit we use the overdamped Langevin equation.
- A host of different optimisation techniques have been employed to make the simulations more efficient. These include a radial cut-off length, tabulating the force and the periodic corrector method.
- The melting temperature for an infinite two dimensional superconducting vortex lattice, $T_m \approx 0.0143$, shall be used as a scale for the annealing process.

Chapter 5

Fourier Representation of Channel Potential

In this chapter, we use Poisson summation to determine an alternative expression for the potential stemming from an infinite periodic array of vortices. Initially believing this to be a novel result, we later found that it had already been achieved by T. Dröse *et al.* [29]. We, however, have reproduced it independently. In section 5.1 we outline the analytical techniques employed in this chapter, the techniques are presented in greater detail in section 5.2 were we derive the form of the potential experienced by a single point within an infinite lattice. In section 5.3, we determine the potential stemming from a half infinite vortex lattice in section, briefly commenting on its convergence compared to the infinite lattice potential. In section 5.4, we determine an alternative expression for the potential stemming from the confining walls of a narrow superconducting channel. For the channel system, the new form is compared to the original summation - both in convergence and accuracy. We conclude this chapter by comparing the Fourier form with a discrete sum of pinned sites with an imposed cut-off length.

5.1 Introduction

In Chapter 4, we discussed some of the many techniques employed to improve the efficiency of the simulation. By applying these standard techniques we improved our numerical efficiency at the cost of accuracy. In this chapter we employ Poisson summation to determine an alternative expression for the potential stemming from the channel edge, which is comprised of a pinned lattice of vortices. We refer to this alternative expression as the Fourier form of the potential.

It was noted, in Chapter 4, that the most significant contributor to the computational time is the calculation of the interaction force. Whilst the Bessel function is not long-range, decaying exponentially at long range, the potential at a point within the channel has contributions from many lattice sites. As we are dealing with a narrow channel, the number of particles in the boundary, M, is far greater than contained in the channel, N. As such the dominant contribution to the simulation time is from calculating the force from the pinned boundary.

5.1.1 Summary of Analytical Procedure

Here we outline the technique we apply to re-write the potential stemming from the pinned boundary. We consider the potential $V_T(|\mathbf{r}|)$ which has the following properties. The potential is comprised of a sum over an infinite lattice $\mathbf{\Lambda}$, with periodicity a. This requires

$$V_T(\mathbf{r}') = \sum_{\mathbf{r}\in\mathbf{\Lambda}} V(|\mathbf{r}-\mathbf{r}'|). \tag{5.1}$$

The potential stemming from each site $V(|\mathbf{r}|)$ must be integrable, meaning it does not have any uncontrolled singularities. When singularities are present one can employ Ewald summation [83]. For this method to be most effective, the potential $V(|\mathbf{r}|)$ must decay slowly. We first Fourier transform the potential in equation 5.1,

$$\tilde{V}_T(|\mathbf{k}|) = \mathcal{F}\left[V_T(|\mathbf{r}|)\right](|\mathbf{k}|) = \sum_{\mathbf{r}\in\mathbf{\Lambda}} \mathrm{e}^{-\mathrm{i}\mathbf{k}\cdot\mathbf{r}} \int d\mathbf{r}' \mathrm{e}^{\mathrm{i}\mathbf{k}\cdot\mathbf{r}'} V(|\mathbf{r}'|). \tag{5.2}$$

We now inverse Fourier transform to find the potential in real space again

$$V_T(|\mathbf{r}|) = \mathcal{F}^{-1}\left[\tilde{V}_T(|\mathbf{k}|)\right](|\mathbf{r}|) = \int \frac{d\mathbf{k}}{\Omega} \mathrm{e}^{-\mathrm{i}\mathbf{k}\cdot\mathbf{r}} \sum_{\mathbf{r}'\in\mathbf{\Lambda}} \mathrm{e}^{\mathrm{i}\mathbf{k}\cdot\mathbf{r}'} \tilde{V}(|\mathbf{k}|), \tag{5.3}$$

$$= \int \frac{d\mathbf{k}}{\Omega} \mathrm{e}^{-\mathrm{i}\mathbf{k}\cdot\mathbf{r}} \frac{1}{\Omega_w} \sum_{\mathbf{\Lambda}_\mathbf{k}} \delta(\mathbf{k}-\mathbf{\Lambda}_\mathbf{k}) \tilde{V}(|\mathbf{k}|), \tag{5.4}$$

where $\mathbf{\Lambda}_\mathbf{k}$ is the reciprocal lattice and we have used the identity for the Fourier series representation of a sum of delta-functions over a lattice, and Ω is the volume for the Fourier transform in d-dimensions and Ω_w is the volume term for Poisson summation.

The potential is therefore given by

$$V_T(|\mathbf{r}|) = \frac{1}{\Omega\Omega_w} \sum_{\mathbf{k}\in\mathbf{\Lambda_k}} \mathrm{e}^{-\mathrm{i}\mathbf{k}\cdot\mathbf{r}} \tilde{V}(|\mathbf{k}|), \tag{5.5}$$

which is a sum over reciprocal space, $\mathbf{\Lambda_k}$. For the particular potential here the algebraic details mean we go through the derivation in detail, but the basic idea is encapsulated purely in equation 5.5 up to constants. We simply calculate the Fourier transform of our potential, and sum over it with appropriate phases, over the reciprocal lattice. For some lattice geometries, some of these sums will be analytically tractable which is the power of the technique.

5.2 The Infinite Rectangular Lattice

The potential experienced at the point (x, y) (where $x \neq 0$ and $y \neq 0$) within in an infinite pinned vortex lattice, shown in figure 5.1, is defined to be

$$V_\infty(x,y) = \sum_{n,m=-\infty}^{\infty} \mathrm{K}_0\left(\frac{\sqrt{(x+a_x n)^2 + (y+a_y m)^2}}{\lambda}\right), \tag{5.6}$$

where K_0 is the modified Bessel function of the second kind, $a_{x,y}$ are the horizontal/vertical lattice parameters (for a square lattice $a_x = a_y$) and λ is the penetration depth.

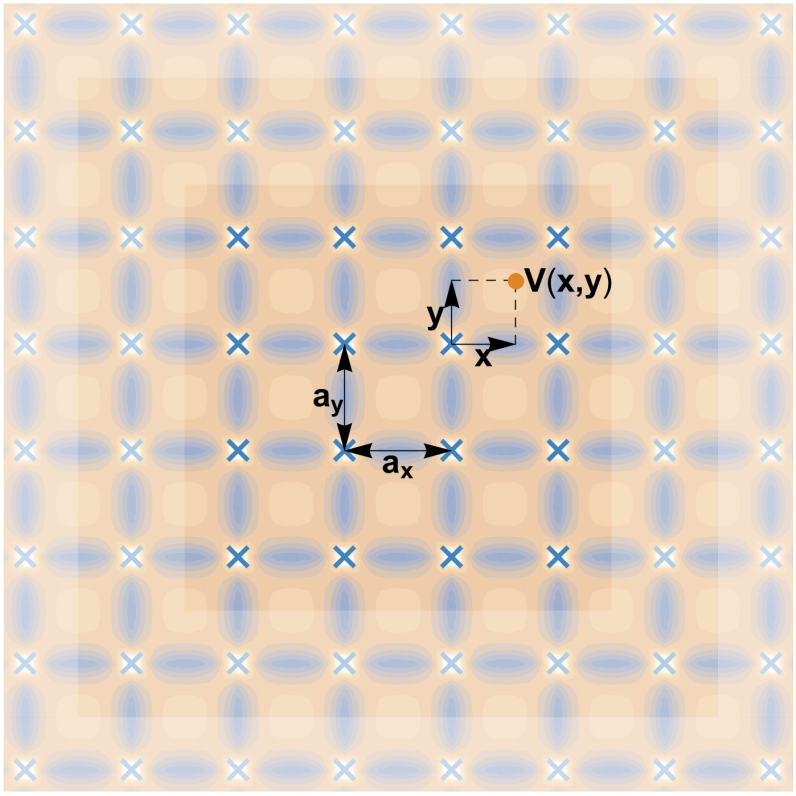

Figure 5.1: Schematic plot of the infinite rectangular lattice (blue crosses) with associated potential landscape shown in the overlaid contour plot. A reference point is defined along with the horizontal and vertical lattice parameters, $a_{x,y}$ respectively. Lattice sites are located at $\mathbf{\Lambda} = na_x\hat{\mathbf{x}} + ma_y\hat{\mathbf{y}}$ where the integers $n \in (-\infty, \infty)$ and $m \in (-\infty, \infty)$. To form the Abrikosov lattice one can set $a_x = 1$, $a_y = \sqrt{3}$ and then superimpose $V_\infty(x, y)$ and $V_\infty(x + a_x/2, y + a_y/2)$.

The equation 5.6 defines the potential through a two-dimensional real space summation over a lattice. The modified Bessel function of the second kind, asymptotically, is exponentially convergent, given by

$$\mathrm{K}_0 \sim \frac{\mathrm{e}^{-z}}{\sqrt{z}}, \tag{5.7}$$

in the large z limit [84]. The real space sum is also, therefore, a convergent one. However, the scale over which the Bessel function becomes exponential can be quite large (the $\lambda \to 0$ limit is particularly troublesome). We essentially apply Poisson summation to carry out parts of the summation. In the full infinite lattice this does not improve convergence, It does, however, improve the convergence for the potential stemming from a superconducting channel edge, which is the focus of this thesis.

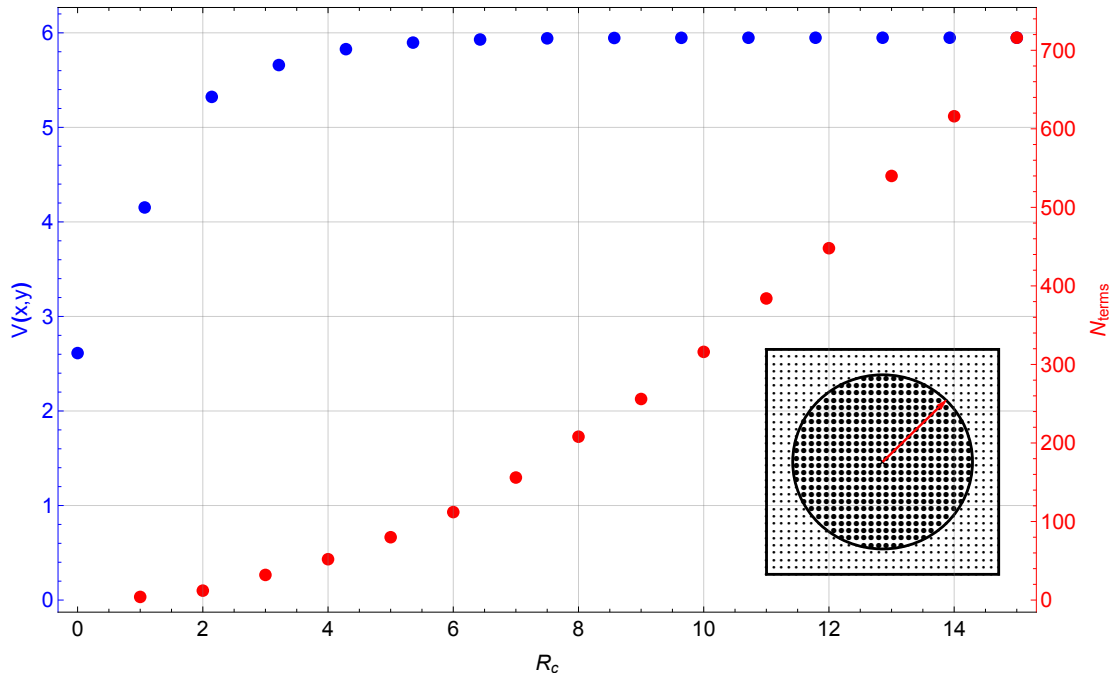

Figure 5.2: Plot of the potential $V_\infty(x, y)$ and number of included lattice sites N as a function of cut-off radius R_c, with $\lambda = 1$. The inset shows the selected particles from a point (x, y) for a given R_c.

In figure 5.2, both the value of the potential $V_\infty(x,y)$ and the number of lattice points included are plotted as a function of cut of radius, R_c for a square lattice. The potential at $R_c \geq 6\lambda$, a commonly used cut-off value in simulations, is converged to $< 1\%$ its true value. From figure 5.2 we can identify that a minimum of $N = 100$ lattice points are included for this choice of cut-off. As the Bessel function is computationally taxing to evaluate, reaching significant precision requires a long simulation time - especially for large system sizes. In order to return to the potential, we must apply inverse Fourier transforms to equation 5.8.

$$\tilde{V}_\infty(k_x,k_y) = \sum_{n,m=-\infty}^{\infty} \int_{-\infty}^{\infty} \frac{dx'}{\sqrt{2\pi}} \int_{-\infty}^{\infty} \frac{dy'}{\sqrt{2\pi}} \mathrm{e}^{\mathrm{i}k_x x' + \mathrm{i}k_y y'} \times \mathrm{K}_0\left(\frac{\sqrt{(x'+a_x n)^2 + (y'+a_y m)^2}}{\lambda}\right). \tag{5.8}$$

We note that the zeroth order modified Bessel function of the second kind has an integral representation given by

$$\mathrm{K}_0(z) = \frac{1}{2}\int_0^\infty \frac{dt}{t} \mathrm{e}^{-t-\frac{z^2}{4t}}, \tag{5.9}$$

where $\lambda z = \sqrt{(x'+a_x n)^2 + (y'+a_y m)^2}$ [84]. Using this representation, as well as the variable changes $\lambda\bar{x} = x' + na_x$ and $\lambda\bar{y} = y' + ma_y$ one arrives at

$$\tilde{V}_\infty(k_x,k_y) = \frac{1}{2}\sum_{n,m=-\infty}^{\infty} \mathrm{e}^{-\mathrm{i}k_x n a_x - \mathrm{i}k_y m a_y} \int_0^\infty \frac{dt}{t}\mathrm{e}^{-t} \times \int_{-\infty}^{\infty} \frac{d\bar{x}}{\sqrt{2\pi}} \mathrm{e}^{\mathrm{i}k_x\bar{x} - \frac{\bar{x}^2}{4\lambda^2 t}} \int_{-\infty}^{\infty} \frac{d\bar{y}}{\sqrt{2\pi}} \mathrm{e}^{\mathrm{i}k_y\bar{y} - \frac{\bar{y}^2}{4\lambda^2 t}}, \tag{5.10}$$

where the order of integration has been changed. It is now evident that the integrals in both $\bar{x}$ and $\bar{y}$ are standard Gaussian integrals of the form

$$I_1 = \int_{-\infty}^{\infty} \frac{dz}{\sqrt{2\pi}} \mathrm{e}^{-\frac{z^2}{a}+bz} = \sqrt{\frac{a}{2}} \mathrm{e}^{\frac{ab^2}{4}}, \tag{5.11}$$

where we require that $a \in \mathbb{R}$. One is then left with a final integral over t which can be readily solved, yielding

$$\tilde{V}_\infty(k_x, k_y) = \sum_{n,m=-\infty}^{\infty} \frac{\mathrm{e}^{-\mathrm{i}k_x n a_x - \mathrm{i}k_y m a_y}}{\lambda^{-2} + k_x^2 + k_y^2}. \tag{5.12}$$

In order to retrieve the infinite potential, we transform back. The infinite potential is therefore given by the double summation

$$V_\infty(x, y) = \frac{2\pi}{a_x a_y} \sum_{n,m=-\infty}^{\infty} \frac{\mathrm{e}^{-\frac{2\pi i n x}{a_x} - \frac{2\pi i m y}{a_y}}}{\frac{1}{\lambda^2} + (\frac{2\pi n}{a_x})^2 + (\frac{2\pi m}{a_y})^2}. \tag{5.13}$$

We have utilised the Fourier series for a Dirac comb

$$\sum_{n=-\infty}^{\infty} \delta(k - Tn) = \frac{1}{T} \sum_{n=-\infty}^{\infty} \mathrm{e}^{\frac{2\pi i k n}{T}}, \tag{5.14}$$

which is true for an infinite summation. The representation given in equation 5.13 is applicable to any monatomic lattice with Bessel type interactions. For simulating, it is more convenient to use the sinusoidal rather than the complex representation.

$$V_\infty(x,y) = \frac{2\pi\lambda^2}{a_x a_y} + \frac{4\pi}{a_x a_y}\sum_{n=1}^{\infty}\frac{\cos\frac{2\pi n x}{a_x}+\cos\frac{2\pi n y}{a_y}}{\frac{1}{\lambda^2}+(\frac{2\pi n}{a_x})^2} + \frac{8\pi}{a_x a_y}\sum_{n,m=1}^{\infty}\frac{\cos\frac{2\pi n x}{a_x}\cos\frac{2\pi m y}{a_y}}{\frac{1}{\lambda^2}+(\frac{2\pi n}{a_x})^2+(\frac{2\pi m}{a_y})^2}. \quad (5.15)$$

The infinite summation of Bessel functions has been replaced with a sum of more computationally accessible functions. Although we shall not use equation 5.15 again we comment on its convergence. Immediately, one can appreciate that we still have a double summation. Truncating each of the infinite sums in both expressions for $V_\infty(x,y)$ at N_{trunc}, we find the number of terms scales as $N_{\text{terms}} = (2N_{\text{trunc}}+1)^2$ for the Bessel sum and as $N_{\text{terms}} = N_{\text{trunc}}^2 + N_{\text{trunc}} + 1$ for the new representation.

We consider the value of the potential $(0.5, 0.5)$ for a square lattice ($a_x = a_y = 1$) with $\lambda = 1$. One finds that the Bessel form of the infinite lattice converges more readily than the new expression, converging to 6 significant figures for $N_{\text{trunc}} = 14$ for which $N_{\text{terms}} = 841$. Once it has undergone Poisson summation, the same potential only requires $N_{\text{trunc}} = 50$ for which $N_{\text{terms}} = 2551$ to achieve the same precision.

Whilst the new representation no longer requires one to call upon the Bessel library, it offers little to negligible improvement in convergence. Another impact of the new representation is that we can no longer identify the lattice sites from the sum, and so one cannot include disorder into the sum. Whilst it is true that the improvement in the convergence of the infinite lattice is negligible, the rate of convergence differs significantly for a partially-infinite lattice. We shall now consider a lattice infinite in one direction and semi infinite in the other.

5.3 The Semi-Infinite Lattice

We now consider the potential stemming from a semi-infinite lattice (SIL) comprised of pinned vortices. The vortex lattice is infinitely extended in the horizontal direction and only between $[0, -\infty]$ in the vertical direction, displayed in figure 5.3. In the original representation, the potential from the SIL at the point (x, y) where $y > 0$ is given by

$$V_{\mathrm{SIL}}(x,y) = \sum_{\substack{m=0,\\ n=-\infty}}^{\infty} \mathrm{K}_0\left(\frac{\sqrt{(x+a_x n)^2 + (y+a_y m)^2}}{\lambda}\right). \tag{5.16}$$

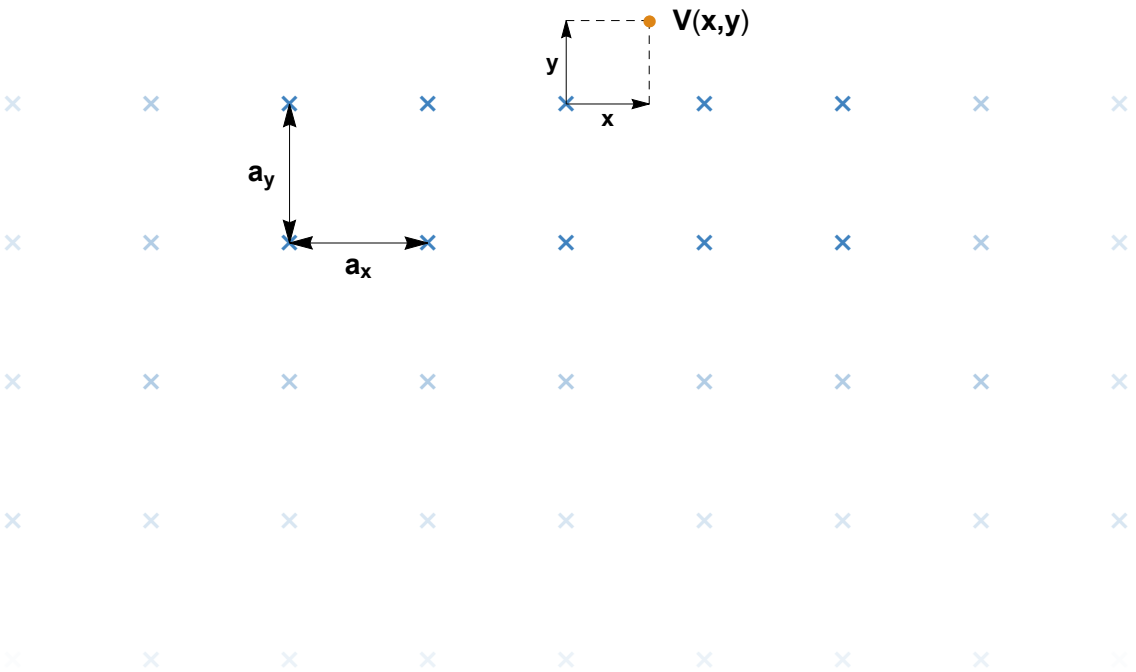

Figure 5.3: Plot of the semi-infinite rectangular lattice considered in this section. Lattice sites are located at $\mathbf{\Lambda} = na_x\hat{\mathbf{x}} + ma_y\hat{\mathbf{y}}$ where the integers $n \in (-\infty, \infty)$ and $m \in (0, \infty)$. To form a semi-infinite Abrikosov lattice one can set $a_x = 1,\ a_y = \sqrt{3}$ and then superimpose $V_{\mathrm{SIL}}(x, y)$ and $V_{\mathrm{SIL}}(x + a_x/2, y + a_y/2)$.

Employing the generalised technique in section 5.1.1, one arrives at

$$V_{\mathrm{SIL}}(x,y) = \frac{\pi}{a_x} \sum_{n=-\infty}^{\infty} \frac{\mathrm{e}^{-\frac{2\pi i n x}{a_x} - Q_n(a_y - y)}}{Q_n\left(\mathrm{e}^{Q_n a_y} - 1\right)}, \tag{5.17}$$

where $0 < y \leq a_y$ and

$$Q_n = \sqrt{\frac{1}{\lambda^2} + \left(\frac{2\pi n}{a_x}\right)^2}. \tag{5.18}$$

For $\lambda \geq 1$ we find that in the limit of large n, $Q_n \to n$. Whilst this expression is algebraically equivalent to the original Bessel summation, it is now exponentially convergent in y. The convergence shall be discussed in greater detail in section 5.4.

An expression for the semi-infinite hexagonal lattice can be found by superimposing the two semi-infinite rectangular potentials $V_{\mathrm{SIL}}(x,y)$ and $V_{\mathrm{SIL}}(x + a_x/2, y + a_y/2)$. This however leads to a cumbersome expression. We instead opt to derive an expression for the potential from an infinite line of superconducting vortices, which we then sum over to produce a semi-infinite hexagonal lattice. The potential at the point (x,y) from an infinite line of vortices is given by

$$V_{\mathrm{L}}(x,y) = \sum_{n=-\infty}^{\infty} \mathrm{K}_0\left(\frac{\sqrt{(x + a_x n)^2 + y^2}}{\lambda}\right). \tag{5.19}$$

The summation is now only in the horizontal direction. Fourier transforming and repeating the same method as outlined for the doubly infinite lattice, one arrives at

$$V_{\mathrm{L}}(x,y) = \sum_{n=-\infty}^{\infty} \int_{-\infty}^{\infty} \frac{dk_x}{\sqrt{2\pi}} \int_{-\infty}^{\infty} \frac{dk_y}{\sqrt{2\pi}} \frac{\mathrm{e}^{-\mathrm{i}k_x(n a_x + x) - \mathrm{i}k_y y}}{\lambda^{-2} + k_x^2 + k_y^2}. \tag{5.20}$$

As before, we can employ the identity given in equation 5.14 to complete the integration over k_x. The integral over k_y however, requires the use of the identity

$$I_2 = \int_{-\infty}^{\infty} dk \frac{\mathrm{e}^{-\mathrm{i}ak}}{Q^2 + k^2} = \pi \frac{\mathrm{e}^{-Q|a|}}{Q} \tag{5.21}$$

As such we find, for $y \geq 0$ that

$$V_{\mathrm{L}}(x, y) = \frac{\pi}{a_x} \sum_{n=-\infty}^{\infty} \frac{\mathrm{e}^{-\frac{2\pi i n x}{a_x} - Q_n y}}{Q_n} \tag{5.22}$$

Where Q_n is the defined in equation 5.18. One can now sum this in the vertical direction to retrieve the potential for a semi-infinite lattice. Summing over $V_{\mathrm{L}}(x, y+ma_y)$, we obtain the expression shown in equation 5.17. As we desire to simulate the Abrikosov lattice, we instead determine the summation $V_{\mathrm{L}}(x + ma_x/2, y + ma_y/2)$. The summation over m can be trivially shown to be a simple geometric series. The potential given in equation 5.23 can be set to that of the Abrikosov if one sets $a_x = 1$ and $a_y = \sqrt{3}$.

$$\begin{aligned} V_{\mathrm{SIL}}^{\mathrm{A}}(x, y) &= \sum_{m=0}^{\infty} V_{\mathrm{L}}(x + \frac{ma_x}{2}, y + \frac{ma_y}{2}) \\ &= \frac{\pi}{a_x} \sum_{n=-\infty}^{\infty} \frac{\mathrm{e}^{-\frac{2\pi i n x}{a_x} - Q_n y}}{Q_n} \sum_{m=0}^{\infty} \left(\mathrm{e}^{-in\pi - \frac{Q_n a_y}{2}} \right)^m \\ &= \frac{\pi}{a_x} \sum_{n=-\infty}^{\infty} \frac{\mathrm{e}^{-\frac{2\pi i n x}{a_x} - Q_n y}}{Q_n \left(1 - (-1)^n \mathrm{e}^{-\frac{Q_n a_y}{2}} \right)} \\ &= \frac{\pi}{a_x} \sum_{n=-\infty}^{\infty} \alpha_n \mathrm{e}^{-\frac{2\pi i n x}{a_x} - Q_n y} \end{aligned} \tag{5.23}$$

where

$$\alpha_n = \frac{1}{Q_n\left(1-(-1)^n \mathrm{e}^{-\frac{Q_n a_y}{2}}\right)} \tag{5.24}$$

Again, one can identify the exponential convergence of the expression in n. So far we have derived an expression for the fully infinite rectangular lattice potential $V_\infty(x,y)$, the potential stemming from an individual line of superconducting vortices, $V_\mathrm{L}(x,y)$, and the semi-infinite rectangular, $V_\mathrm{SIL}(x,y)$, and Abrikosov, $V_\mathrm{SIL}^\mathrm{A}(x,y)$, lattice structures. In this thesis, we investigate the dynamics of mobile superconducting vortices confined within a mobile channel etched into a pinned Abrikosov lattice. As such the final expression we require is that of the channel potential.

5.4 The Superconducting Channel

In this section, we take the potential for the semi-infinite Abrikosov lattice and use it to form a superconducting channel. This is, partially, motivated by finding a more efficient method of simulation the boundary potential. We numerically compare the alternative expression to the original Bessel summation for our channel, assessing the convergence at various points within the channel. We also evaluate the profile of the potential along the centre of the channel using the new representation and the original form for different values of the radial cut-off.

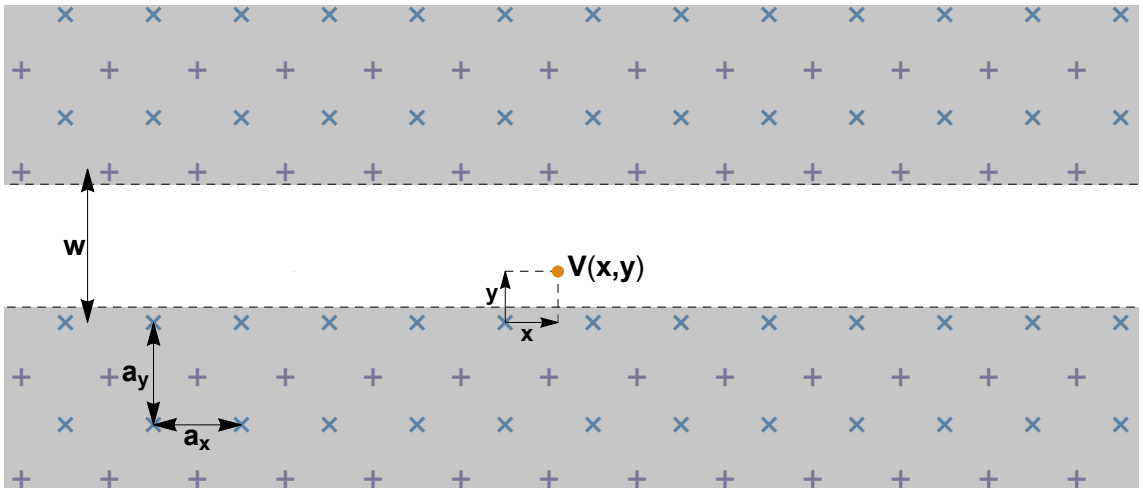

Figure 5.4: Schematic plot of the narrow superconducting channel. The grey region indicates sections of infinitely pinned vortex lattice separated by a width w. Two symbols are used to emphasise the two rectangular sub-lattices. Note: In forming the channel, one has to specify if the boundaries are symmetric or out of phase. This relates to an odd or even number of mobile lattice rows respectively. This figure depicts an even channel with a boundary translation of $\Delta x = \frac{a_x}{2}$.

Figure 5.4 is a schematic example of a narrow superconducting channel. Due to the different sub-lattices present (denoted by different symbols), one has to distinguish between odd and even channel widths

$$w = \begin{cases} (2n+1)b_0 & \text{for an odd channel,} \\ 2nb_0 & \text{for an even channel.} \end{cases} \tag{5.25}$$

Where $b_0 = \frac{a_x}{2}$. Odd and even channels are defined by the number of registered chains of vortices which fit within the mobile region, n. The narrow channel potential is therefore given by

$$V_{\mathrm{C}}(x,y) = V_{\mathrm{SIL}}^{\mathrm{A}}(x,y) + V_{\mathrm{SIL}}^{\mathrm{A}}(x+\Delta x, w-y) \tag{5.26}$$

where $\Delta x = 0$ for a channel containing an odd number of rows and $\Delta x = b_0 = \frac{a_x}{2}$ for a channel containing an even number of rows. One can trivially show that

$$V_{\mathrm{C}}(x,y) = \frac{\pi}{a_x} \sum_{n=-\infty}^{\infty} \alpha_n \mathrm{e}^{-\frac{2\pi i n x}{a_x}} \left(\mathrm{e}^{-Q_n y} + \tau_n \mathrm{e}^{-Q_n (w-y)} \right) \tag{5.27}$$

where

$$\tau_n = \begin{cases} 1 & \text{for an odd channel,} \\ (-1)^n & \text{for an even channel.} \end{cases} \tag{5.28}$$

Equation 5.27 provides an expression for the superconducting channel potential. It only uses computationally accessible functions, instead of relying on the summation of Bessel functions. One would anticipate that this new expression will be more computationally efficient. We shall now evaluate the convergence of this new form. Following on, we evaluate the profile of the potential along the channel as a function of cut-off radius, making a surprising finding about commonly used values.

From equation 5.27, one can see that the exponential convergence is position dependent. We therefore evaluate the convergence at various points within the channel. Unlike the Bessel summation, which is over discrete lattice sites, the sum in equation 5.27 has no real space association. When comparing the convergence of the potential we therefore treat the number of terms in each of the truncated sums as our variable. Converting the potential into sinusoidal form, one finds

$$V_{\mathrm{C}}^{F}(x,y) = V_{\mathrm{C}}^{0}(y) + \frac{2\pi}{a_x}\sum_{n=1}^{\infty}\alpha_n \cos\left(\frac{2\pi n x}{a_x}\right)\left(\mathrm{e}^{-Q_n y} + \tau_n \mathrm{e}^{-Q_n(w-y)}\right). \tag{5.29}$$

Where $V_{\mathrm{C}}^{0}(y)$ is the $n = 0$ contribution of the sum, which only depends on y. Truncating the sum in equation 5.29 at $n = N_{\mathrm{trunc}}$, the number of terms in the potential would be $N_{\mathrm{terms}}^{F} = N_{\mathrm{trunc}} + 1$. Whilst a channel constructed from semi-infinite Bessel summations, as shown in equation 5.30, would contain $N_{\mathrm{terms}}^{B} = 8N_{\mathrm{trunc}}^{2} + 4N_{\mathrm{trunc}}$. Not only does each term take longer to calculate, but the number of terms included grows much faster as function of N_{trunc}.

$$\begin{aligned} V_{\mathrm{C}}^{B}(x,y) =& V_{\mathrm{SIL}}(x,y) + V_{\mathrm{SIL}}(x - \frac{a_x}{2}, y + \frac{a_y}{2}) \\ &+ V_{\mathrm{SIL}}(x, w-y) + V_{\mathrm{SIL}}(x - \frac{a_x}{2}, w - y + \frac{a_y}{2}), \end{aligned} \tag{5.30}$$

where w is the channel width and $V_{\mathrm{SIL}}(x,y)$ is given in equation 5.16. Table 5.1 shows the convergence of the single chain ($n = 1,\ w = 2b_0 = a_x$) channel potential detailed above when evaluated at $(\frac{a_x}{2}, \frac{a_y}{2})$, at the minimum of the potential. One can see that truncating the summation of equation 5.29 at $N_{\mathrm{trunc}} = 6$ gives the correct potential to 15 significant figures. The Bessel summation given in equation 5.30 only achieves the correct potential to 7 significant figures for $N_{\mathrm{trunc}} = 16$, which means the Bessel function is evaluated 2112 times.

Table 5.1: Channel Potential Convergence. Table showing the convergence of the single chain potential at a central point of the channel $(\frac{a_x}{2}, \frac{a_y}{2})$, evaluated using both the original Bessel Summation, V_C^{B}, as well as the new representation, V_C^{F}.

N_{trunc}	$N_{\mathrm{terms}}^{\mathrm{B}}$	V_C^{B}	$N_{\mathrm{terms}}^{\mathrm{F}}$	V_C^{F}
1	12	3.16524499543214	2	4.55352552178547
2	40	4.03228932278470	3	4.55354360840724
3	84	4.36002683721161	4	4.55354355546269
4	144	4.48178944109878	5	4.55354355563586
5	220	4.52694272213426	6	4.55354355563526
6	312	4.54368613465819	7	4.55354355563526
7	420	4.54989304018604	8	4.55354355563526
8	544	4.55219261273093	9	4.55354355563526
9	684	4.55304395386813	10	4.55354355563526
10	840	4.55335890691338	11	4.55354355563526
11	1012	4.55347534690931	12	4.55354355563526
12	1200	4.55351837081431	13	4.55354355563526
13	1404	4.55353426013497	14	4.55354355563526
14	1624	4.55354012585283	15	4.55354355563526
15	1860	4.55354229048861	16	4.55354355563526
16	2112	4.55354308906979	17	4.55354355563526

As previously mentioned, the convergence of equation 5.29 is location dependent whilst the original Bessel form is not. Table 5.2 shows the same calculation but for a point closer to the boundary, $(\frac{a_x}{20}, \frac{a_y}{20})$ where both representations of the potential only achieve the correct potential to 6 significant figures for $N_{\mathrm{trunc}} = 16$. From tables 5.1 and 5.2, we have identified that whilst the convergence of the new representation can be significantly faster, it is positionally dependent. The convergence of the original form, without a cut-off radius, however is independent of location. We define the convergence to be

$$C_n(x, y) = 100 \frac{V_C^{\mathrm{B}}(x, y, 100) - V_C^{i}(x, y, n)}{V_C^{\mathrm{B}}(x, y, 100)}. \tag{5.31}$$

Where we treat the original Bessel summation evaluated to $N_{\mathrm{trunc}} = 100$ as the absolute value of the potential. The potential has converged to more than 15 significant figures for $N_{\mathrm{trunc}} = 100$ and is independent of location.

Table 5.2: Channel Potential Convergence. Table showing the convergence of the single chain potential near the channel edge at $(\frac{a_x}{20}, \frac{a_y}{20})$, evaluated using both the original Bessel Summation, V_C^{B}, as well as the new representation, V_C^{F}.

N_{trunc}	$N_{\mathrm{terms}}^{\mathrm{B}}$	V_C^{B}	$N_{\mathrm{terms}}^{\mathrm{F}}$	V_C^{F}
1	12	5.32467944413438	2	6.55781778806106
2	40	6.21472948604849	3	6.69316109970862
3	84	6.54252282276115	4	6.73131503922644
4	144	6.66289986979861	5	6.74005608213307
5	220	6.70728938130972	6	6.74005608213307
6	312	6.72370611597712	7	6.73809146405786
7	420	6.72978491458252	8	6.73623210830974
8	544	6.73203609883066	9	6.73493232094218
9	684	6.73286948350705	10	6.73414398533459
10	840	6.73317783066032	11	6.73371099663949
11	1012	6.73329185089524	12	6.73349372150392
12	1200	6.73333399029932	13	6.73339539155778
13	1404	6.73334955662202	14	6.73335711854484
14	1624	6.73335530443448	15	6.73334627489070
15	1860	6.73335742603385	16	6.73334627489070
16	2112	6.73335820890493	17	6.73334947071706

Figure 5.5 depicts the convergence of both the original representation (blue curve) and the Fourier representation as a function of location. From lowest to highest, each curve is obtained by incrementally moving closer to the channel edge from the centre of the channel. The results of which are summarised in the inset figure which denotes the point at which the original method has converged more than the new representation.

As one approaches a lattice point, the convergence of the new representation becomes considerably slower. Nearing the centre of the channel, however, the potential has almost converged after one term. In the majority of our numerical investigations, the motion in y is prohibited. Later we shall permit vertical motion, the extent to which a single vortex deviates from its expected position is $\mathcal{O}\left(\frac{a_y}{100}\right)$ and so the convergence of the new representation is still much faster.

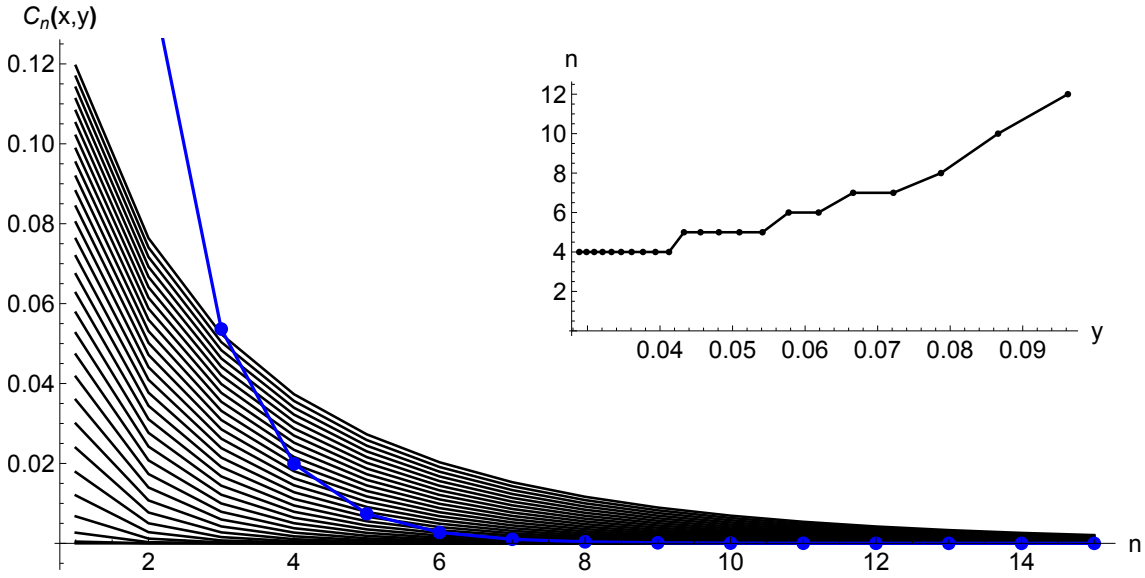

Figure 5.5: Plot of the convergence as function of the number of terms included in the summation, n for various locations within the channel ($x = 0,\ y = \frac{a_y}{2i}$ where i is iterated from 1 to 30). The blue curve details the convergence of the original Bessel summation. As the convergence is independent of location it is only evaluated at the point $(\frac{a_x}{2}, \frac{a_y}{2})$. The black curves represent the convergence of the Fourier transformed potential V_C^{F}. The convergence gets monotonically slower as one approaches the channel edge from the centre. The number of terms at which the original Bessel channel summation, V_C^{B} , has converged more than the Fourier representation is displayed within the inset figure.

As previously mentioned, one technique commonly employed to improve the efficiency of the simulation is to employ a radial cut-off distance to the interaction force, beyond which the contributions are considered negligible. We now compare the profile of the potential along the channel for various cut-off distances to that of the new representation for single chain channel of width $w = \sqrt{3}$, the results of which are displayed below.

From figure 5.6, we find that a cut-off radius of $R_c = 12.0$ is required to correctly match the profile from the channel potential $V_C(x, \sqrt{3}/2) = V(x)$. Despite the potential appearing to have converged sufficiently for $R_c = 6.0$, as observed from figure 5.2, the potential profile observed for this choice of cut-off does not provide an accurate representation. Therefore, to simulate the channel potential, using a

discrete set of lattice points, one has to evaluate the interaction with over 400 lattice points. One should note that studies which have employed a cut-off radius often rescale the potential such that $V(r_c) = F(r_c) = 0$.

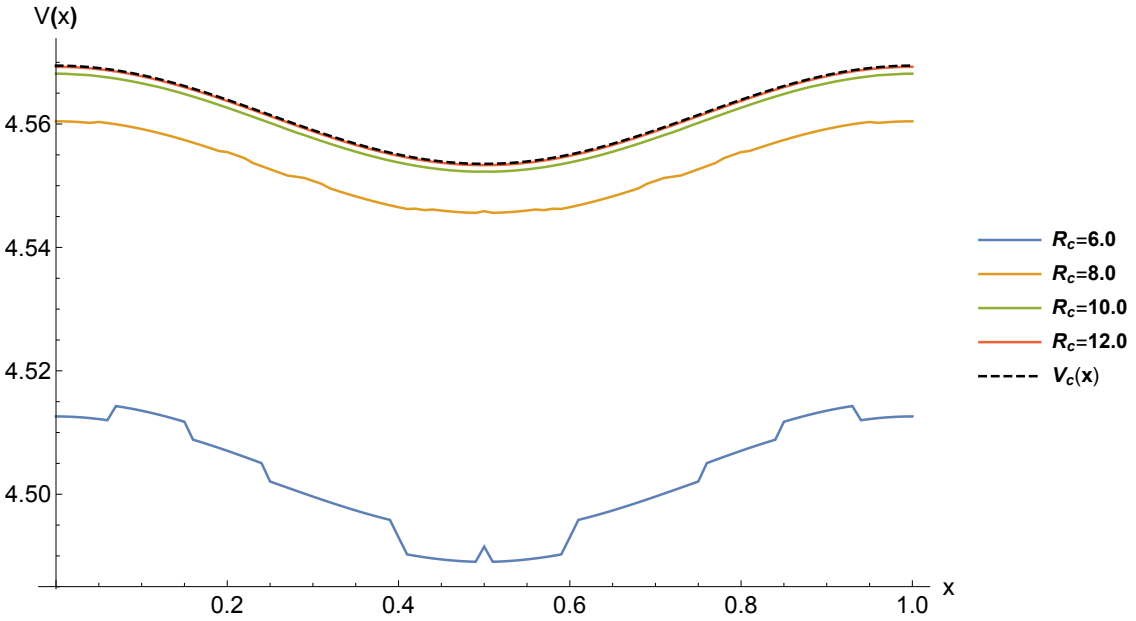

Figure 5.6: Plot of the potential experienced along the middle of the channel for $w = \sqrt{3}$, $a_x = 1$ and $b_0 = \sqrt{3}/2$ for a selection of cut-off distances as well as the Fourier representation of the potential.

5.5 Concluding Remarks

- It is common practice to iterate through a discrete set of lattice points when simulating a pinned superconducting lattice. As this technique is numerically intensive one often applies a variety of methods to improve the efficiency, as discussed in Chapter 4.
- These offer limited improvements in speed and a noticeable reduction in accuracy. We, however, use Poisson summation to find an alternative representation of the channel potential. One finds

$$V_{\mathrm{C}}^{F}(x,y) = V_{\mathrm{C}}^{0}(y) + \frac{2\pi}{a_x}\sum_{n=1}^{\infty}\alpha_n \cos\left(\frac{2\pi n x}{a_x}\right)\left(\mathrm{e}^{-Q_n y} + \tau_n \mathrm{e}^{-Q_n(w-y)}\right)$$

- This alternative representation offers faster convergence than the original representation, when compared to the original form for a point away from the lattice sites.
- We also observed that a commonly used cut-off length in bulk lattice systems ($R_c = 6.0\lambda$) is not appropriate for channel systems. Employing a cut-off radius of $R_c = 6.0\lambda$ both misrepresent the true critical shear and introduces noise which may lead to unnatural phenomena.
- Many simulated experiments have assumed a simple sinusoidal potential stemming from the channel edges, by analysing the convergence we have shown it to be appropriate.
- Unless otherwise stated, we shall now use this representation in all simulations.
- The work in this and some of the following chapter are summarised in our paper preprint [85].

Chapter 6

The Critical Drive of Registered Channels

This chapter comes in two halves, we first investigate the critical shear in wide registered channels analytically and then numerically. In section 6.2, we introduce the tilted washboard model, we derive the velocity profile for uniform drive and discuss the impact of an alternating current. Observational techniques are the subject of section 6.3, we review the observation of the dynamics of colloids by M. P. N. Juniper *et al.* [23] and discuss the feasibility of observation techniques of vortices in superconducting channels. In section 6.4, we use the Fourier form of the boundary, defined in equation 5.29, to show that even for two registered chains the phenomenological equation is not exact. In section 6.5, we derive the phenomenological equation for a reduced model by employing three assumptions. We simulate the registered channel in section 6.6, using the Fourier form as well as the discrete lattice sum with two different cut-off radii. Finally, in section 6.7 we investigate the impact of corrections to the reduced model have on the critical shear of registered chains.

6.1 Introduction

Up to this point, we have primarily discussed the properties of the ground state structure of the mobile vortex lattice in a channel of width $w = 2b_0 = a_y$. The ground state was discussed for a range of coverage parameters at zero temperature and no external force. The ground state has a rich set of phases as a function of the coverage parameter θ. To understand the system better, we work exclusively at $\theta = 1$ in this chapter, and make use of our Fourier representation of the boundary.

The registered channel is translationally invariant, which greatly simplifies the analysis. All findings in this chapter for a channel of width $w = 2b_0$ are technically valid for all coverage parameters $\theta = \frac{1}{p}$, where p is any integer between 1 for the registered system to L for a single particle at $T = 0$. Another advantage to only considering the registered dynamics is that the particles are all located at the potential minima at $F = 0$, the maximally locked state. By contrast, a vortex exists at every possible point within the periodic landscape in an incommensurate state, including the maxima and so motion can occur for any non-zero force.

6.2 The Tilted Washboard Model

In Chapter 2, we considered the ground state structure formed when interacting particles are placed on periodic potential, we now ask what happens when this effective substrate potential is tilted, see in figure 6.1. This model has a variety of applications including the RCSJ model for Josephson junctions [5]. One can consider the potential for a particle at a point within the narrow superconducting channel channel to be given by

$$V_{\text{Total}}(x,y,t) = V_{\text{Substrate}}(x,y,t) + V_{\text{Interaction}}(x,y,t) + V_{\text{External}}(x,y,t). \tag{6.1}$$

Where $V_{\text{Substrate}}$ is the periodic substrate potential which in our case is that of the pinned channel edge V_{C}. For the FK model to be applicable one requires $V_{\text{Substrate}}(x,y,t) = V_{\text{Substrate}}(x+a_x,y,t)$. In most experimental studies the substate potential considered is time independent with one clear exception, bulk lattice shearing [86]. In these experiments one boundary is sheared with respect to the other, either at a constant rate or in an oscillatory fashion.

The interaction potential $V_{\text{Interaction}}$ is the net potential a single vortex experiences from the surrounding mobile lattice. As we shall at first be dealing with a single registered chain of vortices this term can be neglected as it is constant. In this section, we shall see that once the channel is wide enough for $n > 2$ registered chains the interaction becomes important once again due to the relative displacement between neighbouring chains. Once decommensurations are introduced into the system the density gradient means we can no longer neglect the impact of this term even in single channels.

The final term in equation, V_{External}, is the potential stemming from the external forces, given by $\mathrm{F}_{\text{External}}(\mathbf{r},t) = \mathrm{F}_{\text{DC}}(\mathbf{r}) + \mathrm{F}_{\text{AC}}\sin(\omega t)$ where the subscripts denote direct and alternating forces respectively. Although we only consider a constant force $\mathrm{F}_{\text{External}} = \mathrm{F}_{\text{DC}}$ in our numerical study, a great deal of current interest lies in a position dependent force. D. V. Tkachenko *et al.* [19] applied a transverse force profile in wide channels and measured the associated velocity profile of each chain. M. P. N. Juniper *et al.* [23] apply both an AC and DC driving force to the colloids, their results are discussed below.

Let us first consider the simplest case in which we have one particle on a sinusoidal landscape with a constant force applied, such a model is applicable to a particle rolling down a washboard potential or a vortex driven by a Lorentz force, directed down the channel, through the periodic landscape stemming from the pinned channel edge. The equation of motion is given by

$$\dot{x} = \frac{1}{\eta}\left[\mathrm{F}_{\text{DC}} + \alpha\sin\left(\frac{2\pi x}{a_{\text{CE}}}\right)\right]. \tag{6.2}$$

Where η is the viscous drag, F_{DC} is the applied driving force which acts on the particle in a potential of amplitude α and period a_{CE}. As described in the section on the Langevin equation, we have opted to neglect the inertia of the particle as we are in the overdamped regime.

Considering the tilted washboard picture displayed in figure 6.1, one can identify that so long as a potential barrier exists the particle remains localised. At zero temperature, the particle will remain confined within its potential well at the point $x = \frac{2\pi}{a_{\text{CE}}}\sin^{-1}\left(\frac{\mathrm{F}_{\text{DC}}}{\alpha}\right)$ for $\mathrm{F}_{\text{DC}} < f_c$. Increasing the magnitude of the external force

causes the landscape to tilt further, eventually the potential barrier becomes a point of inflection and the particle is permitted to flow. This is often referred to as the locked to sliding transition or the saddle-node bifurcation [2].

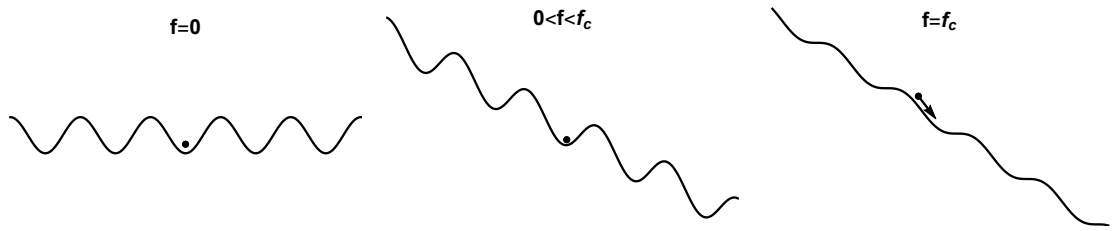

Figure 6.1: Schematic plot of the tilted washboard model at $f = 0$, $0 < f < f_c$ and at the critical shearing force $f = f_c$ for a registered chain of particles on a sinusoidal landscape.

A schematic plot of the average velocity as a function of driving force is displayed in figure 6.2, the dashed line shows how the average velocity profile in the limit of no substrate potential, $v = \mathrm{F}/\eta$. The solid line in figure 6.2 depicts the velocity profile for a single particle or registered chain for finite substrate potential. As already explained, there is a minimum force, F_{C}, required for motion to occur. This point marks the location of the locked to sliding transition, for a registered channel at zero temperature it is dependent only on the magnitude of the substrate potential. We now consider the profile of the average velocity immediately after the critical point by rearranging and integrating equation 6.2 over one lattice period.

$$\int_0^{a_{\mathrm{CE}}} \frac{dx}{\frac{\mathrm{F}_{\mathrm{DC}}}{\alpha} - \sin\left(\frac{2\pi x}{a_{\mathrm{CE}}}\right)} = \int_0^{T_p} \frac{\alpha}{\eta} dt. \tag{6.3}$$

At a fixed driving force the particles velocity oscillates about an average, $\bar{v}$, as it moves over the potential landscape, the time period for this motion is $T_p = a_{\mathrm{CE}}/\bar{v}$. The equation 6.3 can be readily solved to show that the average chain velocity is

$$\bar{v} = \frac{1}{\eta}\sqrt{\mathrm{F}_{\mathrm{DC}}^2 - \alpha^2}. \tag{6.4}$$

Let us now take a moment to examine this equation. When the driving force $\mathrm{F}_{\mathrm{DC}} < \alpha$ the average velocity of the chain is purely imaginary, this implies that in this simplified model the magnitude of the substrate potential gives the critical shear, $\mathrm{F}_{\mathrm{C}} = \alpha$. The critical exponent of this transition is $\nu = \frac{1}{2}$, which is the same as that found for the critical current in the RCSJ model for superconductors [5]. As the magnitude of the force increases the impact of the substrate diminishes, as such the average velocity eventually grows according to $v \propto \mathrm{F}/\eta$.

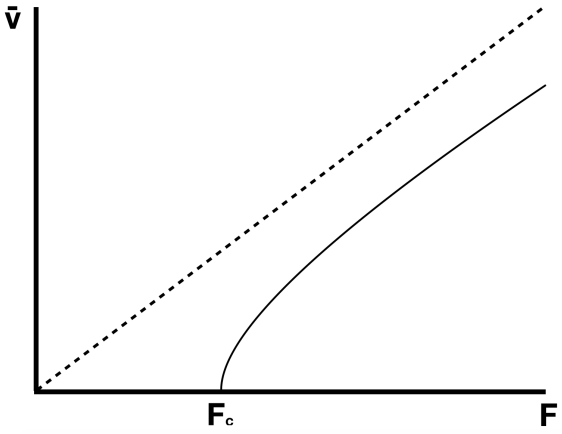

Figure 6.2: Schematic plot the average particle (or chain with coverage parameter $\theta = \frac{1}{p}$) velocity as a function of driving force when driven over a sinusoidal landscape by a homogeneous driving force. The solid (dashed) curve shows the velocity profile for a periodic potential with finite (zero) amplitude. F_{C} marks the location of the critical shearing force.

Above we considered the impact a constant driving force has on a particle in a sinusoidal trap, the particle is limited to motion down the potential only, applying an additional alternating force, $\mathrm{F}_{\mathrm{AC}}\sin(\omega t)$, dramatically changes the dynamics. The results of which are displayed in figure 6.3.

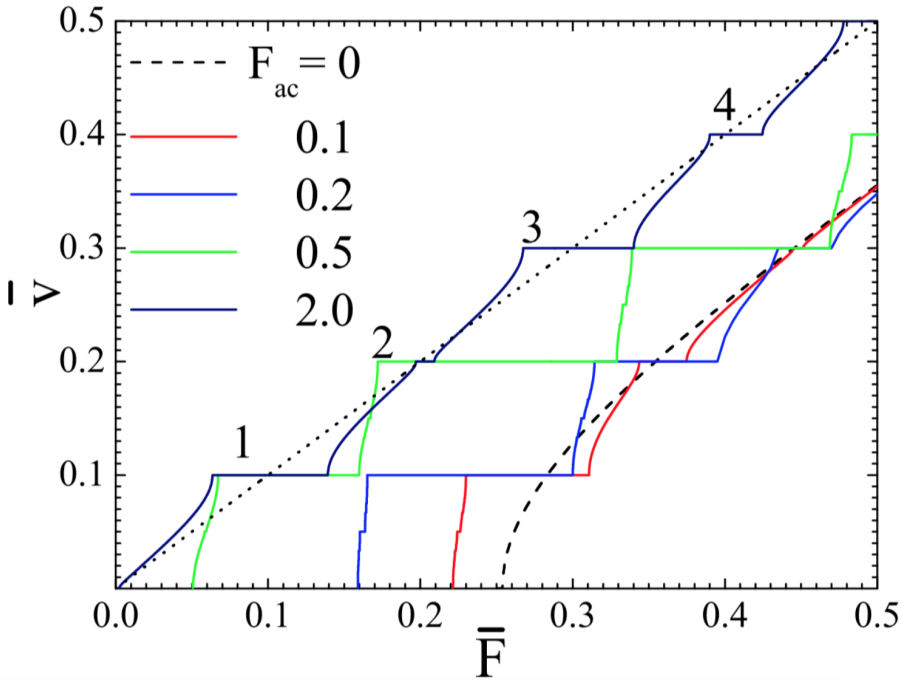

Figure 6.3: Plot the average particle velocity as a function of direct driving force when driven over a sinusoidal landscape by both a direct and alternating driving force. The dashed (dotted) curve shows the velocity profile for a periodic potential with finite (zero) amplitude. The coloured lines represent the response to direct driving force F_{DC} at different strength F_{AC} for fixed substrate potential. Figure taken directly from Fig. 1 in [7].

Figure 6.3 shows the velocity profiles for a chain of particles interacting on a substrate driven by a combination of alternating and direct forces. Compared to the previous profiles for $F_{AC} = 0$ in which the velocity increases monotonically beyond the critical shearing point, when $F_{AC} \neq 0$ a mode-locking behaviour is observed giving the appearance of Shapiro steps, named after their discovery in the AC Josephson effect [87]. The magnitude of the alternating force does not impact the velocity of these steps, only the relative width of each and their dependence on the constant force. These steps appear due to synchronisation, a phenomena first observed, in coupled pendula, by C. Huygens [88]. The interaction between multiple weakly coupled oscillators with similar frequencies causes the frequencies to become equal. In the washboard model the synchronisation would be between an applied AC driving force and the velocity oscillations from the substrate potential.

It has also been shown experimentally that introducing some anharmonicity into the substrate potential leads to a devils staircase of mode-locked velocities. To understand why these steps occur, one needs to observe the dynamics of the individual particles. Until recently, experiments have only had access to integrated properties. In the next section we discuss some experimental techniques, which allow insight into the particle dynamics, in greater detail.

6.3 Experimental Observations

In many of the experimental setups considered in this field of research, the dynamics of the system have to be inferred from indirect measurements. For example, for a Type-II superconductor in the mixed state the dynamics of the vortex lattice are inferred from the current-voltage characteristics. Whilst in the locked state, the vortex lattice remains motionless and the current flows with zero resistance. At a critical value of the current, the vortex lattice is no longer locked as it enters the flux flow regime which dissipates energy introducing a resistance.

These indirect measurements are useful when trying to understand the dynamics of a registered chain under the influence of a constant force. One can directly relate the measurements to the average chain velocity of the chain to the individual particle dynamics as every particle travels forward together. The relation between average properties and individual particle dynamics becomes less clear however when one introduces an alternating force or defects. Whilst the integrated properties do show distinctively different characteristics in each of these regimes, one cannot deduce the individual particles dynamics. Having access to the microscopic dynamics rather than just the average properties unleashes the potential for many new investigations. One is able to gain greater insight in to the behaviour of defects.

6.3.1 First Observation of Colloidal Dynamics

In the last section, we discussed how applying both an alternating and direct force Shapiro steps are observed in the average velocity-force profile. With access to only the average properties, one cannot identify the microscopic mechanisms which cause this mode-locking behaviour. This was rectified by M. P. N. Juniper *et al.* by experimentally observing the real time dynamics of colloidal particles in a periodic trap [23].

M. P. N. Juniper *et al.* created a sinusoidal trap in a water-ethanol mixture using optical tweezers. Within this trap the polystyrene particles, which can be magnetically charged, are driven using a piezo stage. The individual particle dynamics could then be recorded in real time using a 40Hz camera. The authors used this set up to study the motion of a chain of particles under the influence of an AC and DC force as a function of chain rigidity, as well as when the chain contains a defect, see chapter 7.

It was found that the mode-locking behaviour is due to the particles maintaining a periodic trajectory in which the velocity of the step is due to net result of both forwards and backwards motion of each particle. The authors could even differentiate between different periodic modes with the same velocity and could predict when each mode would become dominant. In this colloidal set up, one could study different substrate geometries and also varying interaction strengths.

6.3.2 Observation Techniques in Type-II Superconductors

As we are investigating the dynamics with a Type-II superconductor, it is natural to ask if it is feasible to experimentally observe the dynamics within these systems. Many techniques exist for visualising both the static and slowly varying mixed superconducting state. These include scanning tunnelling microscopy, magnetic force microscopy and scanning hall probes. Whilst all of these methods have been employed to view the static mixed phase as well as slowly varying dynamics such as flux creep and stochastic behaviour, the rate at which these methods can record limits their use in chain dynamics analysis. Two of the more promising methods include magneto-optical imaging and scanning superconducting quantum interference device (SQUID), both of which are discussed below.

In the mixed state, the magnetic field is expelled from the superconductor except in the normal cores of each vortex. One can therefore view the structure of the flux line lattice by displaying the magnetic field. In macroscopic systems one can visualise the magnetic field pattern using iron filings, one can achieve a similar visualisation in Type-II superconductors using a layer of ferrimagnetic crystal such as Bi:YIG. This layer, which is often evaporated onto the superconductor responds to its magnetic field pattern.

When a linearly polarised light is incident upon the Bi:YIG crystal, the light is rotated by an amount proportional to the local magnetic field. One can then infer the magnetic field structure by the reflected light intensity, this relation however is not linear so requires calibrating. This method is non destructive, capable of resolving the vortex lattice and the crystal can respond to local field changes on sub-nanoscale times. One of the main limitations of this method, image capture rate, has made

vast improvements in recent years with some experiments now claiming image rates of up to 30 000 fps [89]. The imagine quality can be enhanced by applying an additional reflective layer between the crystal and superconductor. To the best of our knowledge, this technology is yet to be used to experimentally study FK channels however. The rate of improvements in image resolution and rate suggest that even if it is not currently possible, it might be eventually.

Alternatively, one can use a SQUID as a magnetometer, such as that used by L. Embon *et al.* when imagining the dynamics of super-fast vortices [8]. By placing the SQUID on a sharp tip, L. Embon *et al.* increased the possible resolution enabling them to not only resolve the flux lattice but also identify subtle displacements, report they can identify vortices moving at velocities up to 20 km/s [8]. Using this set up they studied the dynamics of individual vortices under the influence of large current densities. Each image requires approximately four minutes to capture, the intensity profile of an image is related to time averaged magnetic field at each point. For a vortex moving with a small velocity, the small displacements could be stitched together to visualise the motion. For higher velocities however, one could only visualise time averaged trajectories.

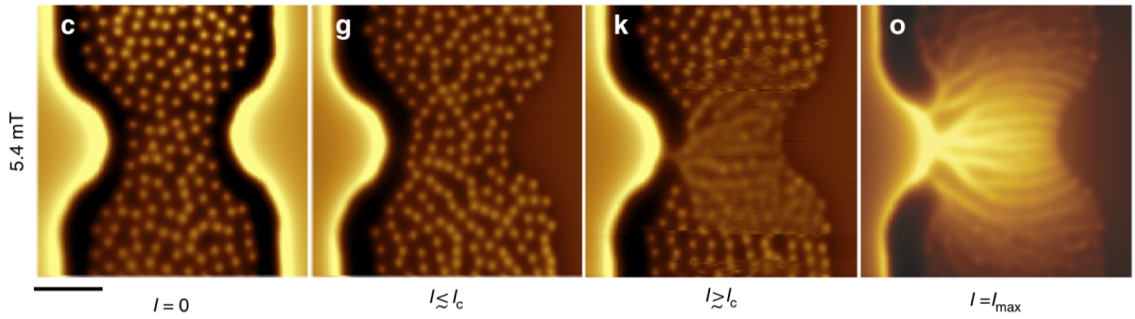

Figure 6.4: Plot of the magnetic imaging of vortices for an applied field of $B_a = 5.4$mT at driving currents both above and below I_c. The imaging process produces time-averaged locations for $I > I_c$ The scale bar is 3μm. Figure adapted from Fig. 2 in [8].

Information can be successfully gained by layering many trajectories, for example when simulating wide superconducting channels driven by an imposted density gradient, J. S. Watkins [27] visualised the localisation of the lattice defects by overlaying the trajectories of mobile vortices over long times. The trajectories of all particles in a channel with an imposed constriction allowed A. A. Tomlinson to identify long time, stable localised modes [28]. It is evident therefore that having experimental access to trajectories can be useful. Our investigation, however, requires the relative positions of particles within the same chain - as such the trajectories offer little insight into the dynamics.

6.4 Critical Shear of Narrow Channels

In this section, we determine the critical shear for a registered vortex lattice at zero temperature in a narrow superconducting channel. We define a channel to be narrow if it is only wide enough to only fit one registered chain of vortices, $w = 2b_0$, we define channels with $N \geq 2$ as wide channels. Due to the translational symmetry, the method used to derive the form of the shearing force required for a chain containing $N = 1$ registered chain is also applicable to a channel with $N = 2$ registered chains. We will then compare these values to that of the widely accepted phenomenological equation

$$\mathrm{F}_w^{\mathrm{C}} = \frac{2Ac_{66}}{w}, \tag{6.5}$$

where A encapsulates the microscopic details including the structure of both the pinned and mobile lattice, for a hexagonal pinned lattice the maximum value of this parameter is $A^0 = 1/(\pi\sqrt{3}) \approx 0.551329$ which occurs for a registered chain within a channel of width $w = Nb_0$. As the channel geometry is varied from this arrangement the parameter reduces in value, in the presence of a defect $A \to 0$.

The final parameter in equation 6.5 is the shear modulus of the vortex lattice c_{66} which Brandt found to be expressed by

$$c_{66} = \frac{\Phi_0 B_{c_2}}{16\pi\mu_0\lambda^2} b(1-b)^2(1-0.58b+0.29b^2). \tag{6.6}$$

Where Φ_0 is the flux quantum, B_{c_2} is the upper critical field strength, λ is the penetration depth and $b = B/B_{c_2}$ is the reduced field [21]. We have already discussed

how the magnetic flux enters the superconductor in discrete units of Φ_0, as such the parameter b can be treated as the channel density with $N_c \propto \frac{b}{\Phi_0}$. Equation 6.5 implies that a superconducting channel containing N registered chains has a critical shearing force $\mathrm{F}_N^{\mathrm{C}} \propto 1/N$. By determining the exact expressions for the critical shear of both the one and two chain channels, we shall see that although the force and channel width are approximately inversely related, there is a deviation.

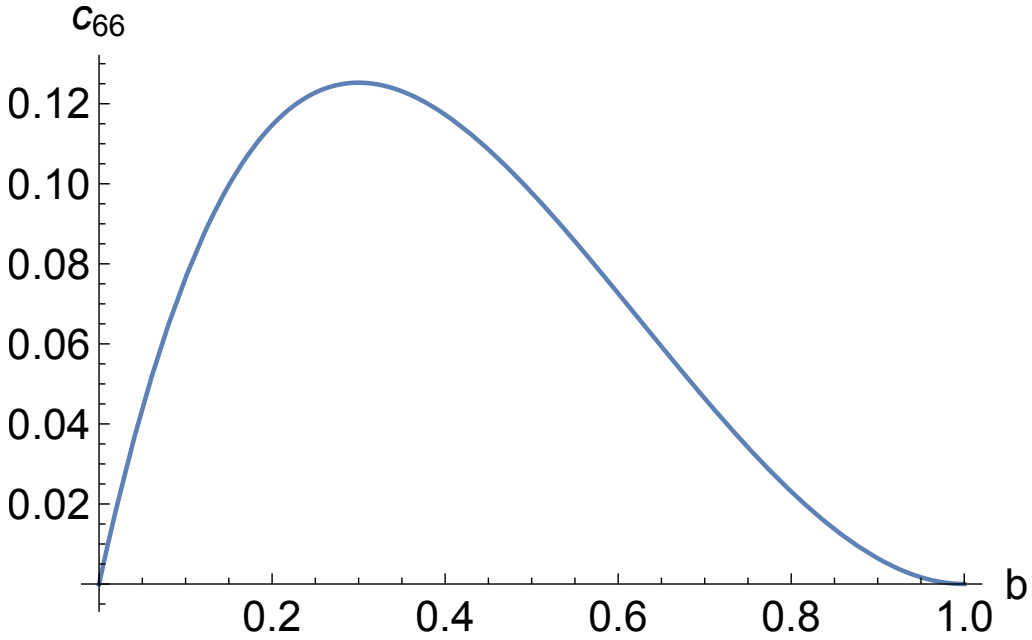

Figure 6.5: Plot the shear modulus c_{66} as a function of the reduced field $b = B/B_{c_2}$ determined by equation 6.6.

We compare our solution for the single and double channel to that of the phenomenological equation. In order to do so, we must first determine a suitable value for b. The appropriate choice of mobile vortex density is that of the pinned channel edge, at this density the shearing strength is maximal. Figure 6.5 shows how equation 6.6 varies as a function of b, the maximal value from the shear modulus is found to be $c_{66} = 0.1252587$ in units of $\frac{\Phi_0 B_{c_2}}{16\pi\mu_0\lambda^2}$ for which $b = 0.2999815$. Using the microscopic parameter A^0 one finds $\mathrm{F}_0^{\mathrm{C}} = 0.05316144$.

For a single registered vortex lattice line within the mobile region of an infinite superconducting channel of width $w = \sqrt{3}$ one can ignore the bulk interaction as each vortex is equally spaced and so the net interaction is zero, the only important consideration therefore is the force from the boundary which can be found by differentiating equation 5.29 for a single chain to find

$$\mathrm{F_C}\left(x, \frac{\sqrt{3}}{2}\right) = 8\pi^2 \sum_{n=1}^{\infty} \alpha_n n \sin(2\pi n x) \mathrm{e}^{-\frac{\sqrt{3}Q_n}{2}}. \tag{6.7}$$

We have set $y = \frac{\sqrt{3}}{2}$ which is the centre of the channel and restricted transverse motion. From equation 6.7 one can read off that the maximal force from the boundaries occurs at $x_c = 0.25$ for $n = 1$, at which point $\mathrm{F_C^{max}} \approx 0.0500164$. This value is of the same order of magnitude as that obtained from Brandt's expression. Some experiments have modelled the superconducting channel using a single cosine potential, whilst this does provide a simple approximation, we find that the $n \geq 2$ terms of the summation do contribute to the value of the critical shear despite the rapid convergence, the converged value of the critical force for a single chain 0.0500184.

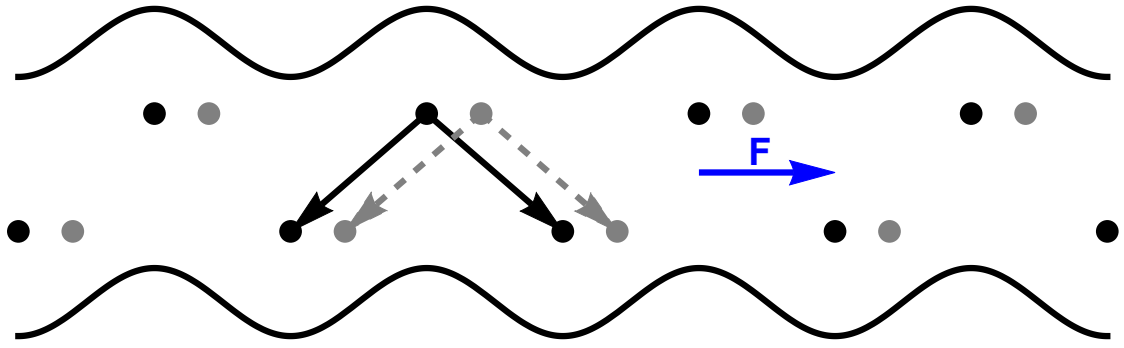

Figure 6.6: Schematic diagram of the ground state lattice sites in a registered channel of width $w = 3b_0$ before (black) and after (grey) a shear force $f < F_{\mathrm{crit}}$ is applied. We note how the relative shift of both chains is the same.

For the single channel system we can *rigorously* set transverse motion to zero due to the inversion symmetry around the centre of the channel. For a two row system, this is no longer the case, and this will be our first major approximation; we will restrict transverse motion. This is a somewhat severe approximation, the effect of which is discussed in section 6.7, but allows us to make analytical progress.

We now turn our attention to the two chain channel system. One might anticipate that we have to consider the bulk distortions, however the symmetry of the system means the bulk lattice always maintains hexagonal order once we have fixed y-motion, see figure 6.6. As the lattice shifts as one entity, there is no net interaction force meaning only one variable is required. Again we differentiate the channel potential to find

$$\mathrm{F_C}\left(x, \frac{\sqrt{3}}{2}\right) = 4\pi^2 \sum_{n=1}^{\infty} \alpha_n n \sin(2\pi n x) \mathrm{e}^{-\frac{\sqrt{3}Q_n}{2}} \left(1 + \underline{\underline{(-1)^n \mathrm{e}^{-\frac{\sqrt{3}Q_n}{2}}}}\right). \tag{6.8}$$

Without the presence of the underlined term in equation 6.8, the expression for the boundary force for the two chain channel is exactly one half of equation 6.7. The true critical shear however deviates from the phenomenologically predicted $\mathrm{F}^{\mathrm{C}}_{a_y}$ value (from equation 6.5) by

$$100\frac{\mathrm{F_C}(0.25, \sqrt{3}/2) - \mathrm{F}^{\mathrm{C}}_{a_y}}{\mathrm{F_C}(0.25, \sqrt{3}/2)} \approx 0.404440\%. \tag{6.9}$$

Even for two chains there is a finite deviation from the phenomenologically predicted value. Transverse motion does not remedy this, checked later. We now consider wider channels, as we no longer have such high symmetry, the interaction forces in the bulk must be included and new techniques for solving have to be employed.

6.5 Critical Shear of an N Chain Channel

When considering a superconducting channel containing N transversely constrained registered chains of vortices at zero temperature, one has $\frac{N+1}{2}$ free parameters when N is odd and $\frac{N}{2}$ when N is even. This is due to the symmetry about the centre of the channel. For $N \geq 3$ the hexagonal mobile lattice may deform under shear and so one has to consider the interaction of a particle with the neighbouring chains. As each chain maintains discrete translational invariance, only the relative separation of chains changes and one can employ equation 5.22 to determine the interaction between neighbouring chains. The force acting on a particle in the jth chain at (x_j, y_j) in a channel of width w containing N chains is

$$\mathrm{F}_{\mathrm{total}}(x_j, y_j) = \mathrm{F}_{\mathrm{C}}(x_j, y_j) + \sum_{\substack{i=1 \\ i \neq j}}^{N} \mathrm{F}_{\mathrm{L}}(x_i - x_j, y_i - y_j) + f, \tag{6.10}$$

where F_{C} is the force on the particle from the channel edge, F_{L} is the force on the particle from another chain and f is the driving force. And the associated energy of a particle is given by

$$\begin{aligned} E_{\mathrm{t}}(x_j, y_j) = {} & V^{\mathrm{A}}_{\mathrm{SIL}}(x_j, y_j) + V^{\mathrm{A}}_{\mathrm{SIL}}(x_j, w - y_j) + f x_j \\ & + \frac{1}{2} \sum_{\substack{i=1 \\ i \neq j}}^{N} V_{\mathrm{L}}(x_i - x_j, y_i - y_j) + \sum_{\substack{n=-\infty \\ n \neq 0}}^{\infty} \mathrm{K}_0 \left(n a_x \right). \end{aligned} \tag{6.11}$$

The total energy can then be obtained by summing over the chain index j. The first two terms in equation 6.11 are the energy associated with the interactions with the channel edge. Notice we have opted to use the semi-infinite lattice potential rather than the channel potential as was used in the determination of the single and double

channel critical shear, the reason for this is explained below. The third term is the driving force. The fourth term is the interaction energy of a particle with the other mobile chains. Finally we have the energy associated with inter chain interactions, as this is only a constant we shall now omit it.

As the number of chains increases, so too does number of terms that have to be considered. Accurate analytical solutions are therefore taxing to achieve using the original representation. Our Fourier representation has two appealing properties which we now make use of; it is exponentially convergent in *both* n (the number of Fourier modes) and y (the chain separation). We therefore approximate the inter-chain interaction using only one Fourier mode, and allowing each chain only to interact with its nearest neighbours. The outer chains interact with their respective boundary; we use the full semi-infinite lattice form (1^{st} harmonic), hence why we split the contribution in equation 6.11. This model is much simpler and allows one to determine the critical shear.

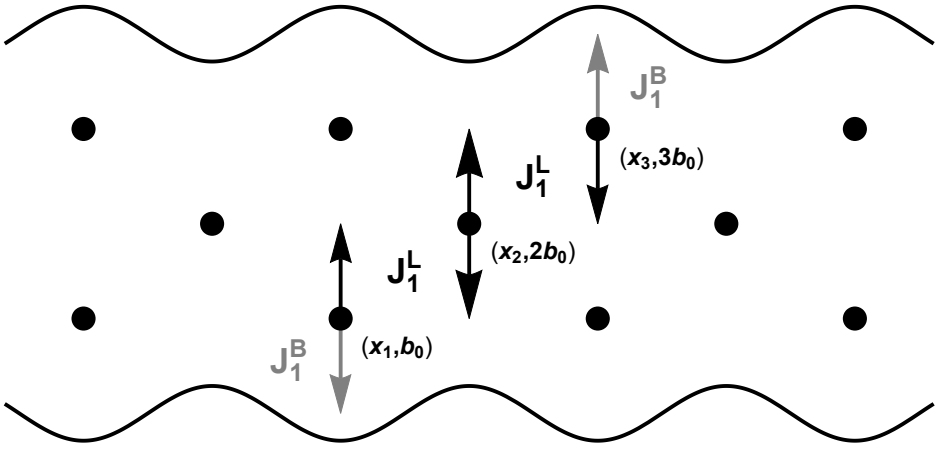

Figure 6.7: Schematic diagram of the reduced model considered in this section for a registered channel of width $w = 4b_0$. For a given particle, only the interaction with a neighbouring boundary, J_1^B, or mobile lattice line J_1^L are considered, all other interactions are neglected. As the transverse motion is restricted, the only free parameters are the longitudinal position of each chain x_i. We know from symmetry that $x_1 = x_3$.

Figure 6.7 displays the reduced model system for three mobile chains, we make the approximation that the central chain only interacts with the neighbouring mobile vortex lines and the outer chains interact with only the central vortex line and one boundary. We investigate the impact of these assumptions in section 6.7.

We now demonstrate the calculation for the simple case of one chain, comparing to the solution to the solutions above. We then use a three chain channel to discuss the new techniques required and then extend them to the N chain system. For the single chain with the assumptions described above, the energy of a particle is given by

$$E_{\mathrm{t}}(x_1) = 2J_1^B \cos(\omega x_1) + f x_1, \tag{6.12}$$

where $\omega = 2\pi/a_x$, and the factor of two is due to the interaction with each boundary. The coefficient J_1^B is the first Fourier term of the boundary potential, as depicted in figure 6.7, given by

$$J_1^B = 2\pi\alpha_1 \mathrm{e}^{-\frac{\sqrt{3}Q_1}{2}}. \tag{6.13}$$

Whilst in the locked state, the net force acting on the chain is zero. At the point of the critical shear, the net force is zero and there is a point of inflection in the tilted energy landscape. For a single chain, these can be expressed in terms of the total energy via:

$$\frac{dE_{\mathrm{t}}}{dx_1} = 0, \tag{6.14}$$

$$\frac{d^2E_{\mathrm{t}}}{dx_1^2} = 0. \tag{6.15}$$

Equation 6.14 describes no net force, and equation 6.15 describes the point of inflection. Applying these to equation 6.12 one finds:

$$f - 2\omega J_1^B \sin(\omega x_1) = 0, \tag{6.16}$$

$$\cos(\omega x_1) = 0. \tag{6.17}$$

One can immediately read off from equation 6.17 that at the moment of critical shearing, the particle is located at $x_c = .25$. Substituting this coordinate into equation 6.16 one finds the critical shearing force is

$$f_c = 2\omega J_1^B \approx 0.0500164. \tag{6.18}$$

Due to the convergence, this solution agrees with the exact value (of $f_c = 0.0500184$) up to 4 significant figures (deviation of 0.00399853%). We now consider N chains in this nearest neighbour model, for which we now have the additional approximation of nearest neighbouring interaction only, with interaction strength

$$J_1^L = \frac{2\pi}{Q_1} \mathrm{e}^{-\frac{\sqrt{3}Q_1}{2}}. \tag{6.19}$$

Note that $J_1^L = \left(1 - \mathrm{e}^{-\frac{\sqrt{3}Q_1}{2}}\right) J_1^B \approx J_1^B$. The energy for the N chain system up to a constant factor using these approximations is given by

$$\begin{aligned} E_{\mathrm{t}}(\mathbf{X}) &= J_1^B \left(\cos(\omega x_1) + \cos(\omega x_N)\right), \\ &+ J_1^L \sum_{n=1}^{N-1} \cos\left(\omega(x_n - x_{n+1})\right), \\ &+ f \sum_{n=1}^{N} x_n. \end{aligned} \tag{6.20}$$

Where $\mathbf{X} = (x_1, x_2, \ldots, x_N)$. We temporarily neglect any knowledge of the symmetry in this system and solve with N independent variables. As such the conditions defined by 6.14 and 6.15 are replaced by

$$\frac{\partial E_{\mathrm{t}}}{\partial x_n} = 0, \tag{6.21}$$

$$\left| \frac{\partial^2 E_{\mathrm{t}}}{\partial x_n \partial x_m} \right| = 0. \tag{6.22}$$

Equation 6.21 gives a set of N coupled equations of motion given by

$$\begin{aligned} f - J_1^B \omega \sin(\omega x_1) + J_1^L \omega \sin\left(\omega(x_1 - x_2)\right) &= 0, \\ f - J_1^L \omega \sin\left(\omega(x_1 - x_2)\right) + J_1^L \omega \sin\left(\omega(x_2 - x_3)\right) &= 0, \\ &\vdots \\ f - J_1^L \omega \sin\left(\omega(x_{N-2} - x_{N-1})\right) + J_1^L \omega \sin\left(\omega(x_{N-1} - x_N)\right) &= 0, \\ f - J_1^B \omega \sin(\omega x_N) + J_1^L \omega \sin\left(\omega(x_{N-1} - x_N)\right) &= 0. \end{aligned}$$

As each of these equations equal zero, one can add them up to find

$$Nf = J_1^B \left(\sin(\omega x_1) + \sin(\omega x_N)\right). \tag{6.23}$$

The equation 6.20 is symmetric under the inversion of the spatial parameters, i.e. $E(x_1, x_2, \ldots, x_N) = E(x_N, x_{N-1}, \ldots, x_1)$, therefore $x_n = x_{N-n+1}$ which reduces equation 6.23 to $Nf = 2J_1^B \sin(\omega x_1)$. In one dimension, the requirement given by equation 6.15 refers to a point of inflection in the energy profile. In systems with dimensions $d \geq 2$, the point of inflection might be a function of multiple variables. As such one solves for the Hessian, given in equation 6.22. The determinant of the Hessian matrix is given by the product of the eigenvalues. For it to be zero (equation 6.22) at least one of the eigenvalues must be zero, but the others matter for determining the *type* of criticality. If the eigenvalues of the Hessian are all positive (negative) at $\mathbf{X}$ then the energy $E_{\mathrm{t}}(\mathbf{X})$ is in a local minimum (maximum). If however the eigenvalues are both positive and negative at $\mathbf{X}$ then there is a point of inflection in E_{t}.

The Hessian matrix is given by

$$H = \begin{bmatrix} X_0 + X_1 & -X_1 & 0 & \ldots & 0 \\ -X_1 & X_1 + X_2 & -X_2 & \ldots & 0 \\ 0 & -X_2 & X_2 + X_3 & \ldots & \vdots \\ \vdots & \vdots & \vdots & \ddots & -X_M \\ 0 & 0 & \ldots & -X_M & X_M + X_{M+1} \end{bmatrix} \tag{6.24}$$

for the bulk energy given in equation 6.20. We employ the shorthand notation

$X_i \equiv \cos\left(\omega(x_i - x_{i+1})\right)$. For symmetry we introduce x_0 and X_{M+1}, both of which we set to zero after solving for the determinant as they are not true parts of the model. The full Hessian matrix is an $N \times N$ matrix, as we have invoked the natural symmetry we reduce the matrix to an $M \times M$ order matrix where

$$M = \begin{cases} \frac{N+1}{2} & \text{for an odd channel,} \\ \frac{N}{2} & \text{for an even channel} \end{cases} \tag{6.25}$$

due to the nearest neighbour interaction, the Hessian is tri-diagonal, and therefore the determinant may be found in terms of *continuants*, D_n, the first four of which are given by

$$\begin{aligned} D_0 &= 1, \\ D_1 &= X_0 + X_1, \\ D_2 &= (X_0 + X_1)(X_1 + X_2) - X_1^2, \\ &= (X_1 + X_2) D_1 - X_1^2 D_0, \\ D_3 &= (X_0 + X_1)\left[(X_1 + X_2)(X_2 + X_3) - X_2^2\right] - X_2^2 (X_2 + X_3), \\ &= (X_2 + X_3) D_2 - X_2^2 D_1. \end{aligned}$$

By evaluating each continuant, one can identify the emergence of a recursion relation. It is in fact well known that for a tri-diagonal matrix with the same symmetry as equation 6.24 obeys the following recursion relation

$$\begin{aligned} D_n &= (X_{n-1} + X_n)\, D_{n-1} - X_{n-1}^2 D_{n-2}, \\ &= X_{n-1}\left(D_{n-1} - X_{n-1} D_{n-2}\right) + X_n D_{n-1}, \\ &\rightarrow D_n - X_n D_{n-1} = X_{n-1}\left(D_{n-1} - X_{n-1} D_{n-2}\right), \\ \tilde{D}_n &= X_{n-1} \tilde{D}_{n-1}. \end{aligned} \tag{6.26}$$

Where $\tilde{D}_n = D_n - X_n D_{n-1}$. Evaluating this relation for $\tilde{D}_{M+1}$ one finds

$$\begin{aligned} \tilde{D}_{M+1} &= \prod_{i=0}^{M} X_i, \\ D_{M+1} - X_{M+1} D_M &= \prod_{i=0}^{M} \cos\left(\omega(x_i - x_{i+1})\right), \\ D_{M+1} &= \prod_{i=0}^{M} \cos\left(\omega(x_i - x_{i+1})\right) = 0. \end{aligned} \tag{6.27}$$

As such, the Hessian is the product of all neighbouring line interactions. For this equation to be satisfied only one of the terms is required to equal zero, as such there are many solutions. We therefore solve this set of equations numerically, figure 6.8 displays both the eigenvalues and the positions of the three chains.

Due to the symmetry of the chains, one has two independent variables x_1 and x_2 and three simultaneous equations. One initiates the system at $\mathbf{X}(f = 0) = (x_1, x_2, x_3) = (0, \frac{a_x}{2}, 0)$ at $f = 0$ and solves the equations 6.21 for the positions as a function of f. Using these coordinates, $X(f \neq 0)$, one can evaluate the value of the eigenvalues of the Hessian matrix as a function of f, the coordinates are only determinable up to the point of critical shearing. We therefore confirm the existence of criticality by observing one of the eigenvalues approaching zero.

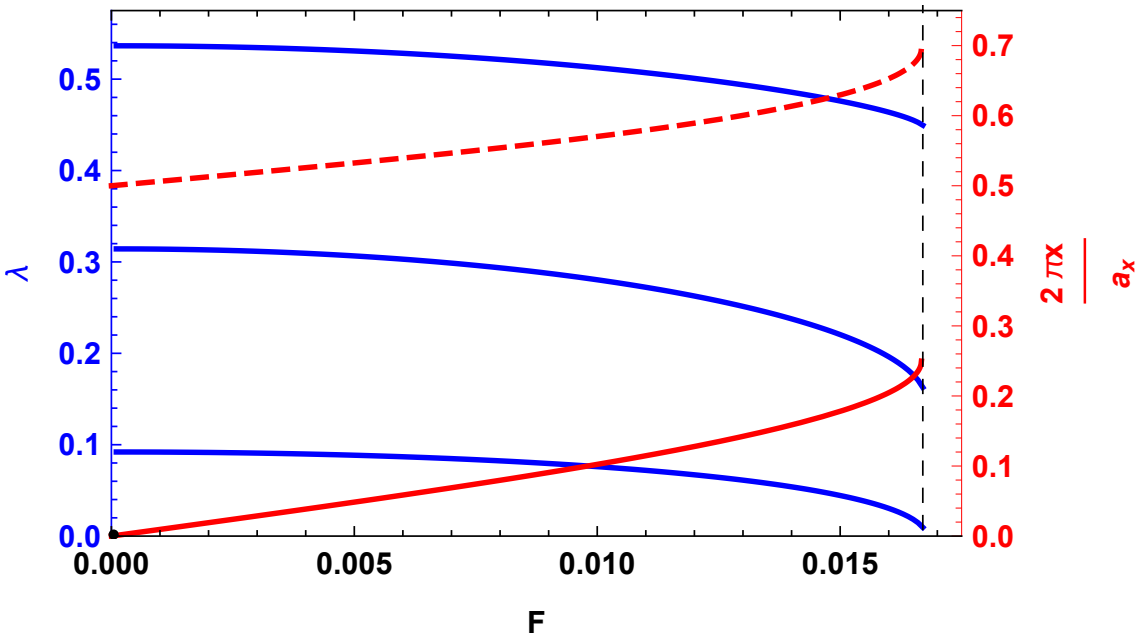

Figure 6.8: Plot of the eigenvalues (blue) and equilibrium positions (red) of the three chains as a function of applied driving force. The outer chains (solid red line) are degenerate and reach a point $x_1 = x_3 = 0.25$ at the moment of critical shear.

As one can see from figure 6.8, all three eigenvalues are all positive at $f = 0$ meaning a local minima exists. They reduce in magnitude as a function of driving force with one reaching zero at $f \approx 0.016701$ at which point the outer chain reaches $x_1 = x_3 = 0.25$. If the Hessian is negative a local minima exists, we cannot determine the value of the Hessian beyond f_c and so we infer the creation of a local minima from the trajectory of one of the eigenvalues as $f \to f_c$. In fact, one finds that the criticality occurs when the outer chains reach $x_1 = x_N = 0.25$ for any number of registered chains. Substituting this into equation 6.23 one finds that

$$f_{\text{crit}} = \frac{2J_1^B \omega}{N}, \tag{6.28}$$

as predicted phenomenologically. In deriving this expression, we had to omit higher order Fourier terms as well as treat next nearest neighbour interactions as negligi-

ble. Despite the convergence of the potential both radially and in Fourier terms, these two factors do contribute a small but finite amount to the critical shear of the system. We have already identified from equation 6.8 how even two chains causes a deviation from the phenomenologically predicted value.

6.6 Simulating of Driven Registered Channels

Although we are unable to analytically solve the full model due to the complexity, we can simulate a channel of N registered chains using the methods described in Chapter 4. All simulations were initiated at $f = 0$ with the mobile lattice in its ground state structure at $T = 0$ with transverse motion suppressed. The simulations were repeated using both the original Bessel summation and Fourier representation of the substrate potential.

Due to the smooth periodicity of the Fourier form one can simulate a fully registered system by just considering a single unit cell, this however would require sufficient wrapping of the bulk force. As seen in figure 5.6, the Bessel form has a discontinuous potential dependent on cut-off and so a large system must be simulated. We however consider of system of length $L = 20 > 2R_c^{\max}$ where $R_c^{\max} = 9$ here.

For each simulation, the applied driving force was incremented, from $f = 0$ to $f = 0.1$, by an amount $\Delta f = 0.0001$. After each increment the system was given 150000 time steps to equilibrate. The average velocity, displayed in figure 6.9, could then be determined by storing the particle positions as a function of time, the critical shear however required a slightly different approach.

Table 6.1: Critical shearing force of n registered chains within a channel of width $w = (n+1)b_0$ using both the Fourier representation of the channel edge potential as well as a discrete lattice with two different cut-off lengths for the interaction, $R_c = 6.0$ and $R_c = 9.0$. Each shearing force is given as an upper and lower bound. The lower bound is the last force for which the evolved particle position was localised to 6 significant figures and the upper bound is the force at which the particle has moved into the next potential well.

n	Fourier	Discrete $R_c = 6.0$	Discrete $R_c = 9.0$
1	0.050015 - 0.050019	0.051358 - 0.051359	0.050008 - 0.050009
2	0.024904 - 0.024909	0.026870 - 0.026869	0.024931 - 0.024932
3	0.016605 - 0.016611	0.018114 - 0.01815	0.016639 - 0.016640
4	0.012455 - 0.012581	0.014025 - 0.014026	0.012462 - 0.012463

Around the separatrix the net force is extremely small, as such the average velocity may appear to be zero from figure 6.9, as such the location of the transition was determined by a lack of long time convergence (to 6 s.f.) of the particle position. Once an approximate location of the shearing force was identified, the simulation was repeated for a longer simulation time in the vicinity of the transition using

$$\delta f = \frac{\Delta f}{100}. \tag{6.29}$$

Despite reducing the incremental step size, the precision with which f_{crit} can be determined is limited for finite time simulations due to the slow motion around the shearing point. From particle positions every 10000 iterations alone, it is difficult to determine if a particle is approaching convergence or has entered the sliding state. One could always simulate for longer, however this requires both more memory and time.

The values of the critical shear associated with each method are displayed in table 6.1. The lower bound is the last force for which the evolved particle position was

localised to 6 significant figures and the upper bound is the force at which the particle has moved into the next potential well. To the accuracy of the simulation, the phenomenologically accepted evolution of the shearing force is within the bounds of the shear for the Fourier representation of the boundary as well as the discrete lattice summation with a cut-off of $R_c = 9.0$. For a smaller cut-off there is a growing discrepancy in the simulated and expected shearing force.

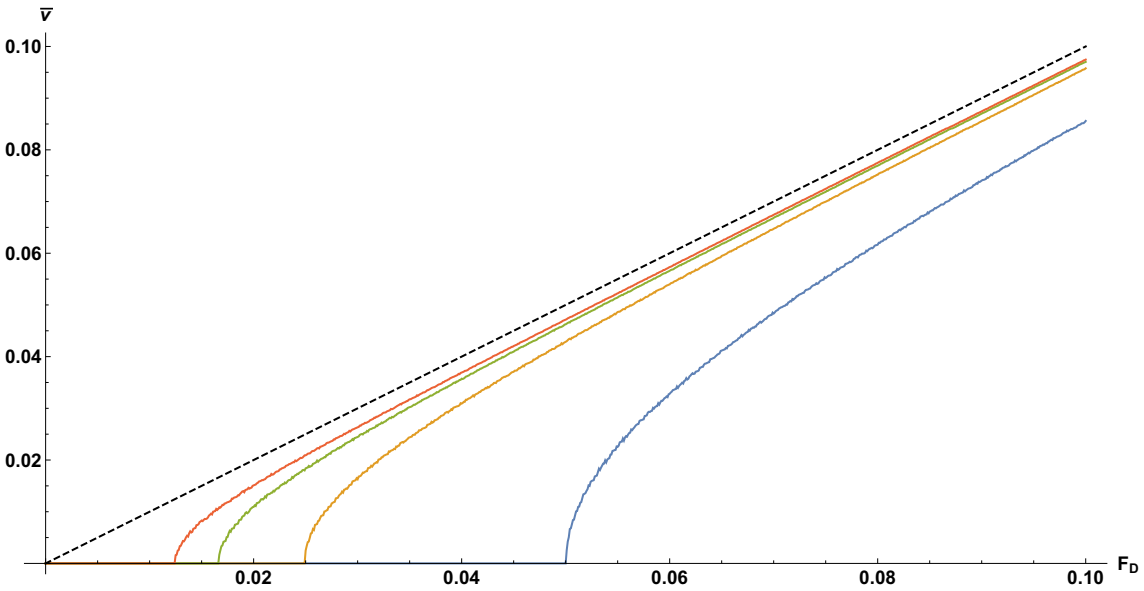

Figure 6.9: Plot the average chain velocity for $n = 1,\ 2,\ 3,\ 4$ chains shown via the blue, yellow, green and red lines respectively. In the large force limit all chains converge upon the velocity profile $\bar{v} = \mathrm{f}/\eta$ (dashed black line).

Figure 6.9 shows the average velocity of the mobile lattice as a function of applied driving force for $n = 1 - 4$ registered chains in a channel of length $L = 100a_{\mathrm{CE}}$ and using the Fourier representation of the boundary. The driving force was increased in small increments of Δf (defined above) initiating the particles from the final position at the previous driving force and allowed to equilibrate for 55000 time steps before any data was recorded. The average velocity was evaluated using

$$\bar{v} = \frac{1}{N}\sum_{i=1}^{N}\frac{1}{M}\sum_{i=1}^{M}\frac{x_i(t_j) - x_i(t_j + \Delta t)}{\Delta t}, \tag{6.30}$$

where N is the total number of mobile particles, $x_i(t_j)$ is the position of the ith particle at time $t_j = (j-1)\Delta t$. The final term, Δt, is the time interval used when determining the velocity, if Δt is too small, the impact of fluctuations in the velocity due to the potential landscape increases, see figure 6.10. If, however, Δt is too large then one is at risk of not detecting the particle loop through the periodic unit at large velocities. In the evaluation of the average velocity shown in figure 6.9, $\Delta t = 12.5$ which equates to measuring the change in position every 1000 time steps.

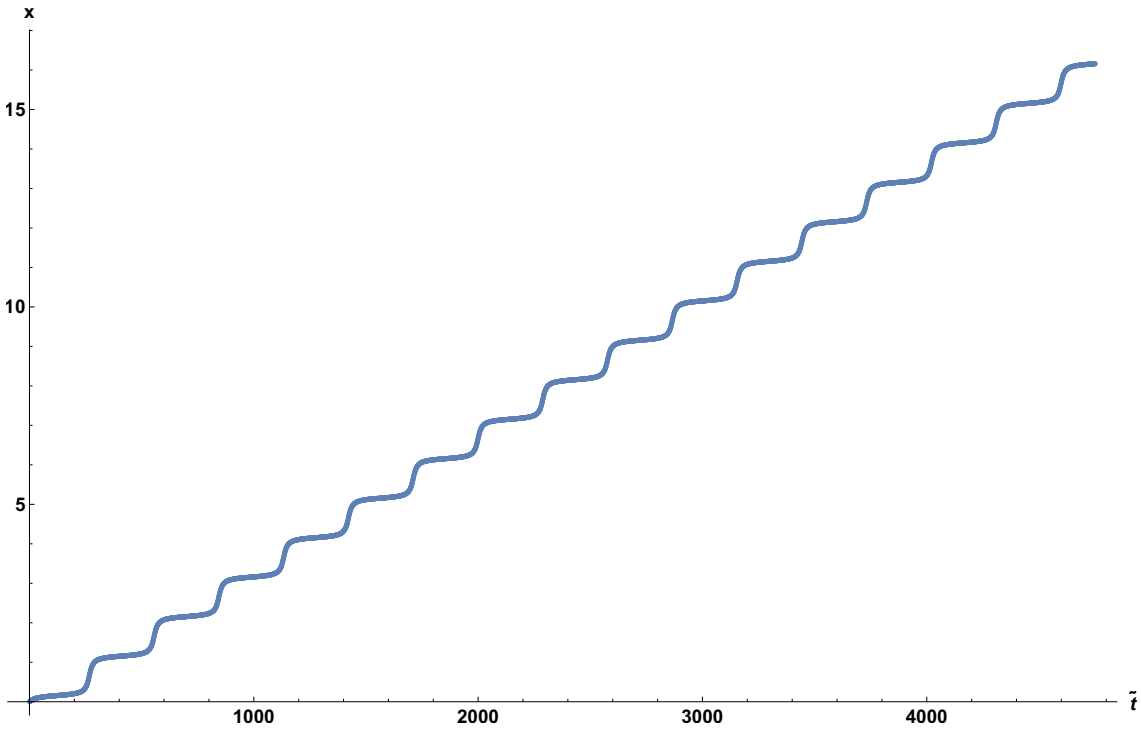

Figure 6.10: Plot of the position as a function of time for a vortex within a single chain channel for $f \gtrsim f_c$.

The average velocity profiles in figure 6.9 agree with the expected profile discussed in section 6.2. When deriving equation 6.4, we considered a single restricted chain

of vortices in a rigid sinusoidal potential. We now check how well this expression agrees not only with the single chain but its appropriateness it is to wider channels in which the substrate potential no longer has a simple sinusoidal profile.

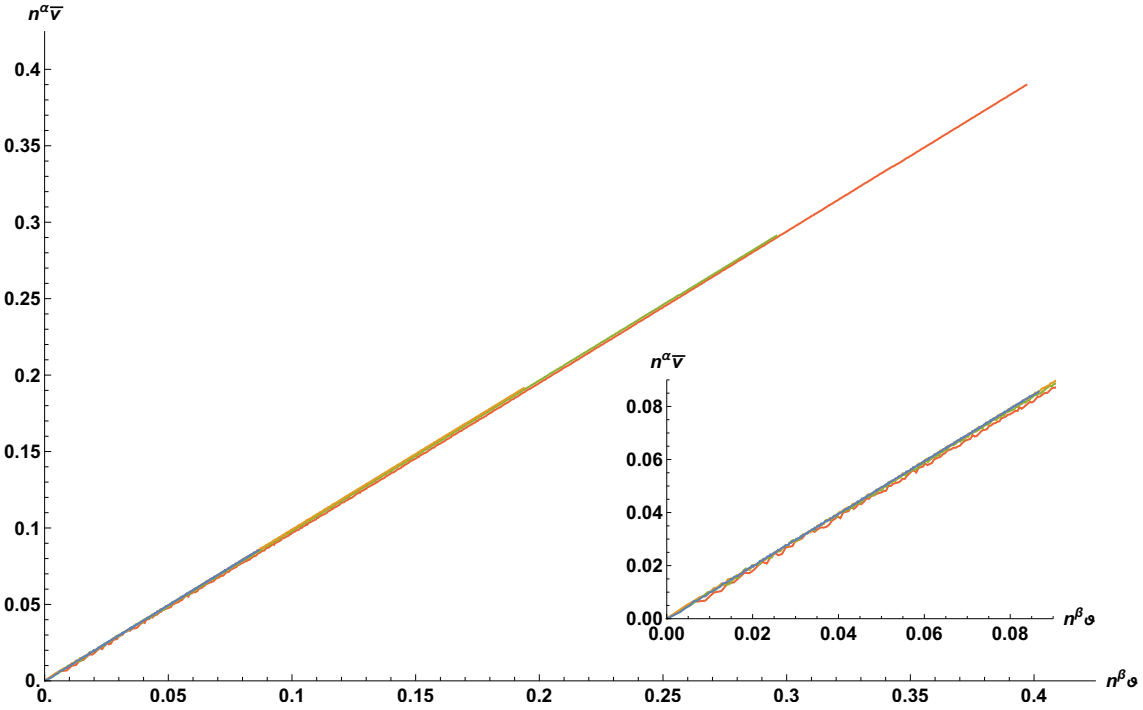

Figure 6.11: Plot of the scaled velocity relation for $n = 1,\ 2,\ 3,\ 4$ chains shown via the blue, yellow, green and red lines respectively. The scaling parameters used in this figure $\alpha = \beta = 1$. The inset provides an expanded view of the region in which all four chains profiles are visible.

We check the scaling of equation 6.4 by plotting $n^\alpha \bar{v}$ against $\vartheta^{\frac{1}{2}} n^\beta$ where $\vartheta = \left(f^2 - f_n^{c2}\right)$ where n is the number of registered chains with an associated critical shearing force f_n^c. We employ the quantity ϑ much like how the reduced temperature $\tau = (T - T_c)/T_c$ is used in conventional phase transition studies such as superconductivity. The critical exponent of this is $1/2$ for the locked to sliding transition. The parameters α and β are used to identify how the expression scales with dimension, in this system we consider the number of chains to be the dimension. The results, displayed in figure 6.11, show that the profiles are equivalent for $\alpha = \beta = 1$. Despite

only being derived for a single registered chain in a sinusoidal potential, the critical velocity relation stated in equation 6.4 is independent of dimension and appears to provide a good fit for $n = 1 - 4$ chains.

6.7 Corrections to the Reduced Model

In the above section, we found that the phenomenological expression for the critical shear of N registered chains is derivable once one disregards higher order Fourier modes and next nearest neighbouring chains. The inclusion of these factors allowed us to identify a, small, discrepancy with the theory for $n = 1,\ 2$ chains. For larger systems we required the use of simulations and identified that the velocity profile in the vicinity of the transition does not depend on the number of chains at zero temperature and for restricted transverse motion. In this section we now consider these two other factors which, when included into the model, can drastically impact the value of the critical shearing force.

Firstly, the chains thus far have been constrained to only move in x, we investigate the impact this has on the critical shearing force and describe any changes in the behaviour of the mobile lattice when its transverse motion is unrestricted. Finally, we briefly describe the impact thermal excitation has on the model, as this is a complex subject with an extensive field of research we only include it to justify why we refrain from annealing for the ground state as the driving force is varied.

6.7.1 Higher Order Terms

In our reduced model, we neglected the impact of higher order Fourier modes and beyond nearest neighbour interaction, we address these here. The interaction energy between a particle, in a channel of width $w = 6b_0$ (i.e. odd number of mobile rows), and the pinned channel edge (with $a_x = 1$) is given by the expression

$$F^B(x,y) = 2\pi^2 \sum_{n=1}^{\infty} \alpha_n n \sin(2\pi n x) \left(\mathrm{e}^{-Q_n y} + \mathrm{e}^{-Q_n(6b_0-y)}\right). \tag{6.31}$$

The force a particle at $(0.25, 2b_0)$ and $(0.25, 3b_0)$ from the channel edge expression above is 0.4% and 0.003% of that of a particle at $(0.25, b_0)$ respectively. For a particle at $(0.25, b_0)$, truncating the boundary interaction force after one Fourier component causes the force to vary by 0.002% from the true value. Similarly for the mobile chain interaction, including the interaction force from the chain a distance of $2b_0$ away reduces the force by 0.4% its value and truncating the force after one Fourier component deviates the force, from the true value, by 0.002%. It is therefore acceptable to approximate the interaction by nearest neighbour only with a truncated force.

6.7.2 Transverse Motion

For a single chain of N particles, we can solve when including transverse motion, due to the inversion symmetry. For wider systems however, the transverse motion affects the motion and the critical shear, and so we must assess its impact. Even for a single discrete chain of N particles, the model is extremely cumbersome to solve due to the number of coupled equations. This problem only increases in difficulty when one allows for transverse motion as well. For $T = 0$ our method for $n = 1$ is exact. When one restricts transverse motion it is possible to approximately determine the critical shearing force in wide channels. The inclusion of transverse motion permits the lattice to reduce its energy state through deformation.

Transverse deformations are commonly observed in superconducting channels with imposed variation, be it via motion through a restriction in the channel geometry or via a varying imposed density difference along the channel. In each of these studies the lattice reorientates to minimise its local energy state. In our registered channel however the system remains translationally invariant and so each chain deforms as one entity. We now determine the relative change in position of the chains and critical shearing force as a function of drive, f, and number of chains, n.

We simulate $n = 1 - 20$ chains both with and without transverse motion, for each simulation we increase the driving force by Δf every 150000 time steps from the perfect lattice at $f = 0$. At each new value of the force the system is allowed to equilibrate for 55000 time steps before the positional data was recorded. The system is kept at zero temperature and the Fourier representation of the channel potential is used as it has been shown to be a more accurate representation when simulated. The critical shear of each system size is displayed in figure 6.12.

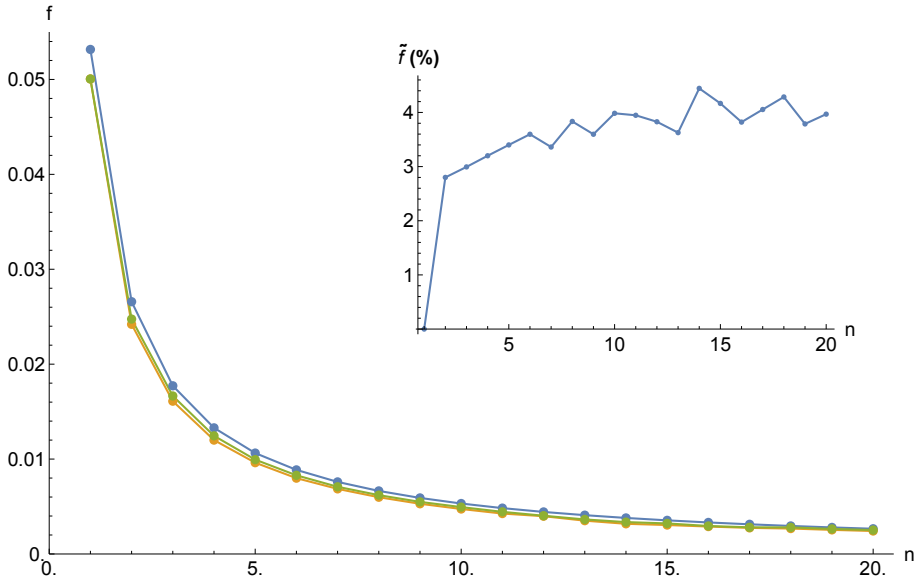

Figure 6.12: Plot of the critical shearing force as a function of number of chains for transverse motion permitted (yellow) and forbidden (green), for comparison we also plot the predicted shearing value using the phenomenological expression discussed above. The inset shows the relative difference in the shearing force with and without transverse motion as a function of number of rows. Inset contains numerical errors and we do not believe these to be physically relevant.

Figure 6.12 shows how the critical shear of each size system compares with the predicted value by Brandt with transverse motion both on and off. One can identify that the general form of the variation as a function of width agrees with the $f_c \propto n^{-1}$ derived earlier and that the critical shear is lower when transverse motion is permitted. The inset in figure displays the relative difference in the critical shear between transverse motion on and off, defined as

$$\tilde{f} = 100 \frac{f^c_{\text{off}} - f^c_{\text{on}}}{f^c_{\text{off}}} \tag{6.32}$$

From the inset, one can see that there is zero difference in having transverse motion permitted for a single channel, this discrepancy in shearing force then appears to level off at $\tilde{f} \approx 3 - 4\%$, subject to significant numerical error. The transverse motion, therefore, has a much larger impact on the critical shear than truncating the Fourier expansion or considering only nearest neighbours.

We now evaluate how the lattice structure changes to permit this reduction in critical force, figure 6.13 shows the transverse deviation, Δy, for each chain as a function of relative driving force. Due to the symmetry of the channel we only evaluate the positional change of chains originally located at $y < y_m$, the curves displayed in figure 6.13 are labeled by their chain number n_c and the total number of chains in the channel n with $n_c = 1$ being the outermost chain, see index subscripts of the chains in figure 6.7.

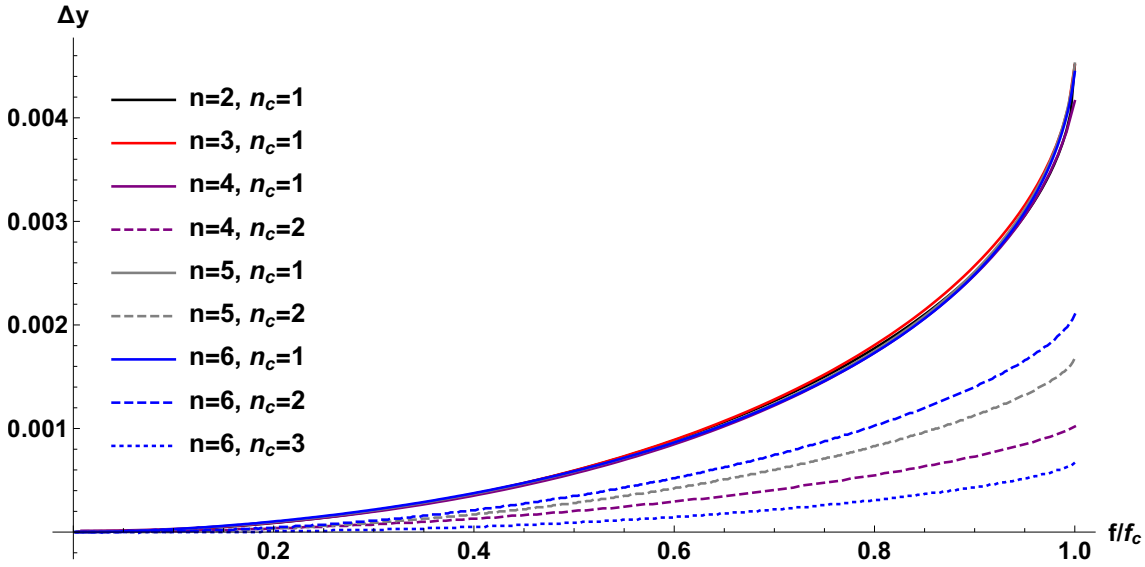

Figure 6.13: Plot of the transverse deviation from the expected position of the n_c th chain as a function of drive in a channel containing n registered chains $\Delta y = y_k - kb_0$. Each curve has been scaled by the systems relative shearing force. Chains from the same system are displayed in the same colour.

For odd channels, the central chain of vortices is situated along the midpoint of the channel, the symmetry ensures the chain does not deviate in position. Interestingly, from figure 6.13 we can see that in all channel sizes displayed, for both odd and even widths, the outermost chain of vortices follows the same profile $\Delta y(f)$. The interior chains also move further from the channel edge but by a smaller extent which depends on the total number of chains within the channel.

Overall, it is evident that as one approaches the critical shear, the mobile lattice compresses to reduce the friction from the boundary. To appreciate why the mobile lattice compresses, we qualitatively consider the transverse force acting on a particle in the $n_c = 1$ chain of the $n = 2$ channel, for simplicity we consider a single unit cell of width a_0. When a driving force is applied, both chains of the mobile lattice are shifted forward with respect to the pinned channel edge.

As the mobile lattice maintains its order, the separation between neighbouring vortices from opposite chains is $r_m = \sqrt{(a_{\text{bulk}}/2)^2 + (\Delta y_m)^2}$ whilst the separation of a mobile particle with the nearest pinned vortex $r_p = \sqrt{(\Delta x_p)^2 + (\Delta y_p)^2}$. The associated transverse force on the particle from the mobile, $F_T^m(r_m)$, and pinned, $F_T^b(r_b)$, must balance in equilibrium.

It was shown in section 6.5 that the interaction strength from a neighbouring line and boundary are approximately equal, as such the transverse forces acting on the particle are balanced when radial separation from are similar. We have identified that $\Delta x_p < a_{\text{bulk}}/2$ and so to compensate for this the transverse separation $\Delta y_p > \Delta y_m$. This qualitatively justifies why the outside chains move in, it does not however answer why the outside chains follow the same profile $\Delta y(f)$ independent on channel width.

For channels with $n > 2$ chains, the horizontal separation of neighbouring mobile chains $\Delta x_p \neq a_{\text{bulk}}/2$, as such the separating in neighbouring chains is reduced. The profile of the outermost chain is maintained because, whilst the separation of the outermost chain with its neighbour is reduced, the relative position of the neighbouring chain has also shifted. These two effects might cancel each other out.

6.7.3 Temperature

Whilst increasing the temperature of a two dimensional Abrikosov lattice of vortices, the system may undergo a phase transition in which the structural order is abruptly lost. This transition is due to the thermostat inducing stochastic motion. Far below the melting temperature, $T_m \approx 0.0143$ for our system the structural order remains intact and the thermostat only induces temporary displacements. In a channel system, however, a thermostat can drastically modify the critical shear profile.

In the washboard model, the potential barrier U reduces in magnitude as the force approaches the critical shear. Introducing a stochastic term gives a particle getting an energetic kick, ΔE, with a probability $\mathrm{e}^{-\Delta E/k_B T}$. If this energy gain is larger than the potential barrier, the particle may escape its well creating a kink/anti-kink pair. As we shall explain in Chapter 7, this pair causes the whole chain to shear. After the shear the particles remain locked one well further on than they were initially located. This process occurs each time a particle in the chain is kicked by a sufficient amount, the average chain velocity is due to instantaneous kicks.

As the temperature of the channel increases, or the driving force approaches the critical shearing force. The probability of a particle receiving a sufficient amount of energy, $\Delta E > U$, becomes more likely and the average chain velocity increases. Within the context of overdamped Josephson junctions, this effect is referred to as thermally activated phase slip and was first found by Ambegaokar and Halperin in 1969. A plot of the average velocity as a function of drive obtained from simulations at a range of temperatures using our set up is displayed in figure 6.14. For a truly random thermostat, one requires transverse motion too.

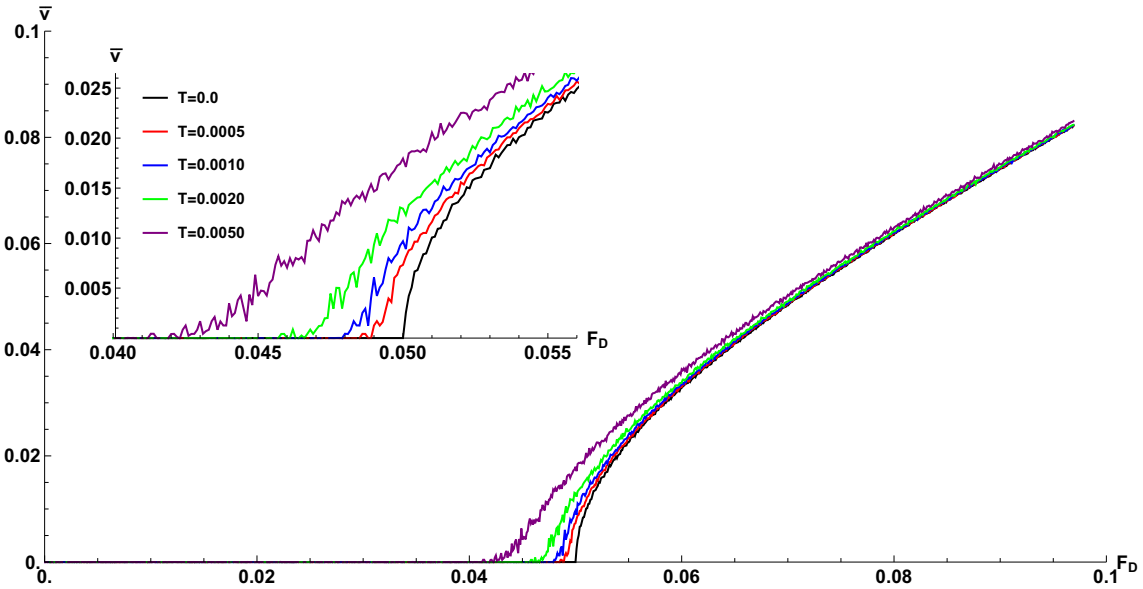

Figure 6.14: Plot of the average velocity of a registered chain in a channel of width $w = \sqrt{3}$ as a function of applied driving force at a selection of temperatures. The inset plot shows an enhanced view of the average velocity in the vicinity of the critical point.

One must be careful when deciding if annealing is appropriate. In section 4.2, it was explained that bulk systems may occasionally be trapped in an excited state and annealing the system is a useful technique in aiding the system in relaxing to its true ground state. The energy imparted to the particles can allow them to free themselves from unnatural states. When seeding a wide ($w > 2b_0$) registered channel from a random arrangement, it may take an exponentially long time for the system to arrive at its natural ground state without the aid of annealing.

For the tilted washboard model, however, this additional energy may change the natural state of the system. As discussed above as one approaches the critical driving force, the presence of a thermostat may permit motion before reaching the critical point. In the following investigations, annealing is only employed at zero driving force as an additional verification of the ground states obtained at $T = 0$ only.

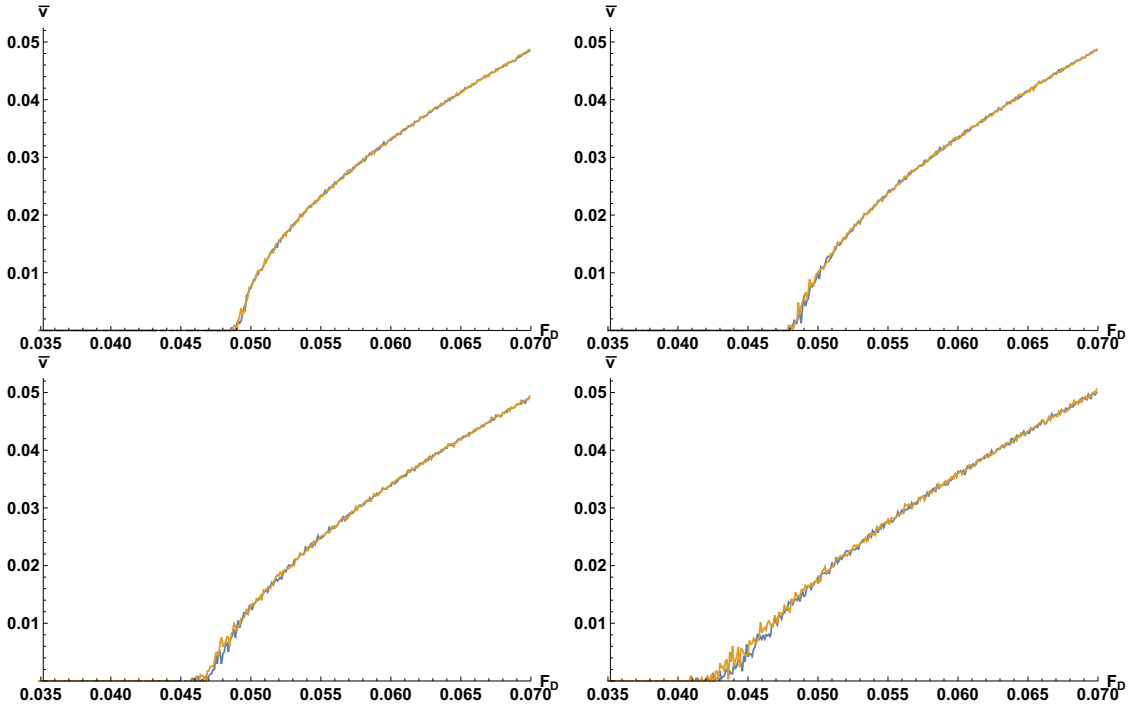

Figure 6.15: Plot of the average velocity of a registered chain in a channel of width $w = \sqrt{3}$ as a function of applied driving force at a selection of temperatures. Displayed from top left to bottom right are the simulated data for $T = 0.0005,\ 0.001,\ 0.002$ and 0.005, each temperature profile was simulated in a channel of length $L = 100a_{\mathrm{CE}}$ (blue curve) as well as $L = 200a_{\mathrm{CE}}$ (yellow curve).

6.8 Concluding Remarks

- An exact form of the critical shearing force in both one and two registered chain systems was derived for one dimensional chains, these values were compared with the phenomenologically accepted expression.
- A derivation for the phenomenologically accepted expression was provided, along with a justification of all assumptions made.
- Simulated data with the Fourier form of the boundary potential identified an issue with the commonly accepted cut-off length of $r_c = 6\lambda$.
- We investigated the scaling of the critical exponent of the velocity profile and found that the relation holds for $n = 1 - 4$ registered chains.
- Finally, we discussed three alternative approximations commonly made in simulations and presented the impact of each of them.

Chapter 7

Defects in Narrow Channels

In this chapter, we investigate the static and dynamical properties of interstitials and vacancies within a "free" vortex chain in a 1D narrow channel. Whilst the content in this chapter is, mostly, well understood in the context of kinks in the discrete FK model, a global summary of the physics in the context of SCNCs does not exist. In this chapter, we provide this summary with accompanying numerics. This chapter provides the background for the novel dynamics observed in wider channels, which we discuss in chapter 8. In section 7.2 we describe the simulation and compare the simulated ground state to that of the continuum limit solution. Further, in section 7.2, we verify the 1D approximation by simulating the zig-zag transition for the modulated SCNC. The averaged dynamics of the driven channel are discussed in section 7.3. We show how one can infer the defect velocity from the average velocity, up to the critical shear, and introduce the anharmonicity of the system. Motivated by N. Kokubo *et al.* [70], the individual particle dynamics are discussed in section 7.4, explaining both the discrete and anharmonic effects. Also in section 7.4, we analyse the kink's motion both above and below the critical shear. The dynamics of the kink above the critical shear are novel results.

7.1 Introduction

The critical shear of a crystalline lattice was found to be many orders of magnitude lower than the value predicted from uniformly sliding one lattice place with respect to another [11]. As discussed in Chapter 2, this drastic reduction is due to the emergence of defects known as dislocations [11]. These defects, which form within the crystal, permit the motion of locked particles. Since their discovery, a vast amount of research has been conducted on the static and dynamic properties of defects in crystal structures [90]. In the wider context of the FK model, these dislocations are referred to as kinks and have been observed in a wide range of systems including coupled pendula [13] and arrays of Josephson junctions [16].

One of the main reasons we, and many others, have chosen to simulate a narrow superconducting channel system is its versatility. In section 6 we focused on a commensurate channel as this offers the strongest confinement. As the application of superconductors depends on the pinning of these mobile chains, a great deal of work has gone into considering the impact of perturbations to the channel geometry [18, 73] or pinned edge [45]. Here we choose to investigate the impact decommensurations have on the average velocity of the channel particles or vortices and so we consider the channel edges to be the pinned hexagonal lattice, for this chapter.

Historically, experiments have only had access to integrated properties, such as the resistance profile in type II superconductors [22]. The experimental accessibility motivated theoretical investigations of integrated properties such as the average chain velocity [19]. We, however, use real time dynamics to explain these integrated observations in terms of the individual particle motion. Such observations were shown to be possible experimentally by P. H. Kes *et al.* [17], see section 6.3. By

analysing the neighbouring separations in the chain (inter-particle distance within the mobile chain) the dependence of the kinks dynamics on the driving force are determined.

7.2 Kink Ground State

The topic of defects was first introduced in section 2.3 as an exact solution to the sine-Gordon equation. Defects were then reintroduced in section 2.4.3 where it was explained how they may become the natural ground state in discrete channels with $a_{\mathrm{CE}} \approx a_{\mathrm{bulk}}$. The concept of minimising the energy in such systems by localising the discrepancy was discussed as well as a brief introduction to how the shape of this defect depends on the properties of the model. In this section, we discuss their static properties in a tightly confined superconducting channels.

It has been noted, in section 2.4.3, that kinks (and anti-kinks) have extended tails which leads to long distance interaction. When considering a defect within a periodic unit, one must ensure that the simulated region is sufficiently long that the kink does not self interact. Simulating long systems is more accessible with the Fourier form of the channel edge potential than with a discrete set of pinned lattice points. In this chapter we consider a superconducting channel with length $L_c = 200a_{\mathrm{CE}}$ and width $w_c = \sqrt{3}a_{\mathrm{CE}} = \sqrt{3}$. The width is chosen to be exactly wide enough to fit one registered chain, the channel has periodic boundary conditions.

A decommensuration occurs in these systems when vortices are added or removed from the registered chain. To achieve the correct ground state, we seed each simulation with both a random arrangement as well as a line of equally spaced vortices with spacing $a_{\mathrm{bulk}} = (N + \sigma)/L_c$ where σ is the topological charge. Each vortex

was located along the centre of the channel with transverse motion prohibited. The ground state was then found by allowing the mobile vortices to relax over an extended period of time. All simulations were conducted at $T = 0$, the annealed ground state is discussed in section 7.2.1.

Each of the methods described above resulted in the same ground state vortex arrangement, only differing in the location of the excitation. The location of the kink in the randomly seeded channel was, unsurprisingly, random. When initiating with a uniformly spaced line of vortices, the location at which the kink would localise was more predictable. For simplicity, consider the pinned lattice sites being $x_i^p = x_0^p + ia_{\mathrm{CE}}$ and the initial mobile sites being $x_i^m = x_0^m + ia_{\mathrm{bulk}}$. As the spacings are not equal, the two chains will have regions of being maximally in and out of phase. The defects will naturally localise at either the minima or maxima of the alignment with the channel edge depending on the topological charge of the defect.

Figure 7.1 displays the deviation from expected position (when compared to a registered chain) for a typical ground state obtained from a uniformly spaced mobile lattice containing one vacancy with respect to the channel edge. The uniform lattice was seeded in such a way that the pinned and mobile lattice was maximally out of phase at the mid point of the periodic unit for easy visualisation. Instead of plotting actual positions, we plot the deviation from the expected position $u_i = x_i - ia_{\mathrm{CE}}$ as it enhances the defect.

Overlaid onto the figure a fit of both the sG profile for a stationary anti-kink (black) as well as an approximate profile (red). An appropriate expression for the deviated profile of an isolated anti-kink confined in a quasi-one-dimensional superconducting channel was derived, in the sG limit, by R. Besseling *et al.* [45] for zero drive. Using

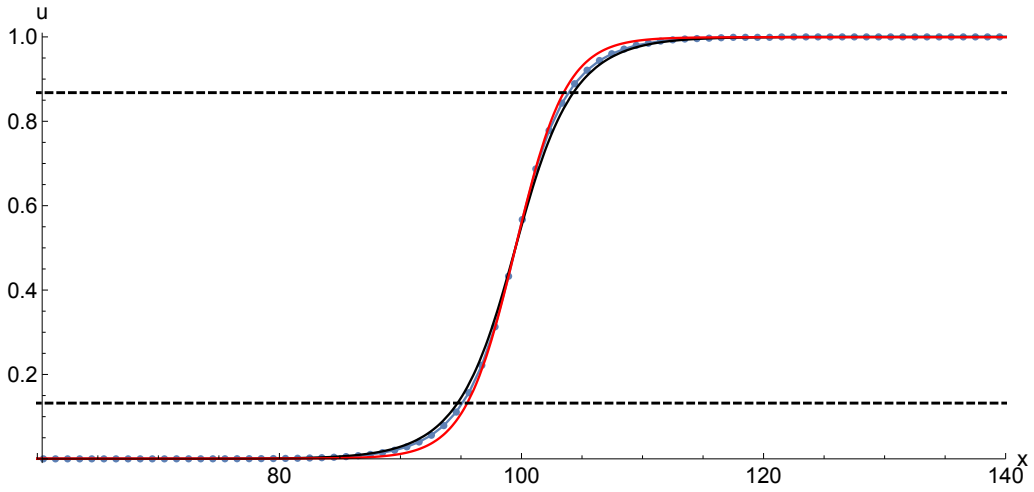

Figure 7.1: Plot of the deviation (blue) from the expected particle position (when compared to a registered chain) along the chain of length $L = 200a_{\mathrm{CE}}$ containing one vacancy $\sigma = -1$. Overlaid onto the plot is a fit of both the continuum limit function (black) and an approximate function (red) to the data as well as the kink's length positions, defined to be where $u(x_{\pm}) = 0.5 \pm 1/\mathrm{e}$.

the first order term of the Fourier form of the boundary potential, derived in Chapter 5, the authors employed linear elasticity theory (l.e.t) to derive

$$u_{\mathrm{l.e.t}}(x) = \frac{2a_{\mathrm{CE}}}{\pi} \tan^{-1}\left[\exp\left(\frac{+2\pi(x - x_c)}{l_d}\right)\right], \tag{7.1}$$

where x_c denotes the position of anti-kinks centre, $u(x_c) = 0.5$ and the anti-kink's length (core-size) is defined in [45] as

$$l_d = 2\pi\sqrt{3\pi\lambda a_{\mathrm{CE}}}. \tag{7.2}$$

In our model $\lambda = a_{\mathrm{CE}} = 1$ and so $l_d = 19.29$, comparing this value with our simulated data we find $u_{\mathrm{sim}}(x_c - l_d) \approx 0.001$.

Interestingly, we can alternatively approximate the deviation profile for the isolated anti-kink at zero drive using the function

$$u_{\text{approx}}(x) = \alpha \tanh\left[\beta\left(x - \gamma\right)\right] + \delta. \tag{7.3}$$

The fitting parameters were determined to be $\alpha = \delta = 0.49927$, $\beta = 0.236889$ and $\gamma = 99.5$ using the *Mathematica* function `FindFit[]`. Both the profile derived by R. Besseling *et al.* in equation 7.1 and the approximate profile in equation 7.3 appear to model the simulated data well, deviating only around the extended tails, as seen in figure 7.2.

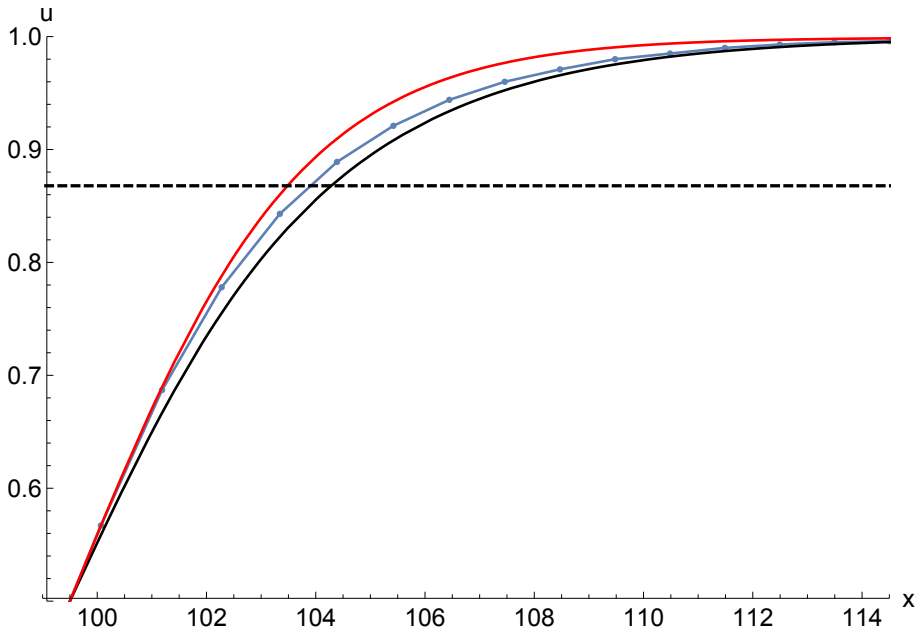

Figure 7.2: Plot of the deviation from the expected particle position (blue) along the chain of length $L = 200a_{\text{CE}}$ containing one vacancy $\sigma = -1$ in the vicinity of the tail. Overlaid onto the plot is a fit of both the sG limit function (black) and an approximate function (red) to the data as well as the length positions, defined as $u(x_{\pm}) = 0.5 \pm 1/\text{e}$.

We define the kinks length as $\tilde{l}_d = x_+ - x_-$, where $u(x_{\pm}) = 0.5 \pm 1/\text{e}$ as shown by the dashed lines in figure 7.1. We determine an approximate value for the kinks length by finding the intersects of the functions given in equations 7.1 and 7.3 with the dashed lines. The widths for each method are listed in Table 7.1. Outside of

Table 7.1: Table of the kinks length $\tilde{l}_d$, determined using equations 7.1 and 7.3 as well as using a linear extrapolation of the simulated data.

$u(x)$	$\tilde{l}_d$
$u_{\text{l.e.t}}$	104.3 - 94.7 = 9.6
u_{sim}	103.9 - 95.1 = 8.8
u_{approx}	103.5 - 95.5 = 8.0

this region the function slowly decays, after which $u(x)$ returns to a constant value. As there is a vacancy, the particles to the right of the defect is one well further on than expected.

An alternative way to represent the positional data of the anti-kink is displayed in figure 7.3 which depicts the nearest neighbour separations

$$\Delta u(i) = x_{i+1} - x_i. \tag{7.4}$$

A positive value of $\Delta u(i) - a_{\text{CE}}$ implies a local dilation, whilst $\Delta u(i) - a_{\text{CE}} < 0$ implies a contraction of the chain. We can relate the nearest neighbour separation to the derivative of the anti-kink profile given in equation 7.3.

$$\frac{\partial u_{\text{approx}}(x)}{\partial x} = \alpha\beta \operatorname{sech}^2\left[\beta\left(x-\gamma\right)\right]. \tag{7.5}$$

Similarly, differentiating equation 7.1 gives

$$\frac{\partial u_{\text{l.e.t}}(x)}{\partial x} = \frac{4a_{\text{CE}} e^{\frac{2\pi(x-x_c)}{l_d}}}{l_d\left(e^{\frac{4\pi(x-x_c)}{l_d}}+1\right)} \tag{7.6}$$

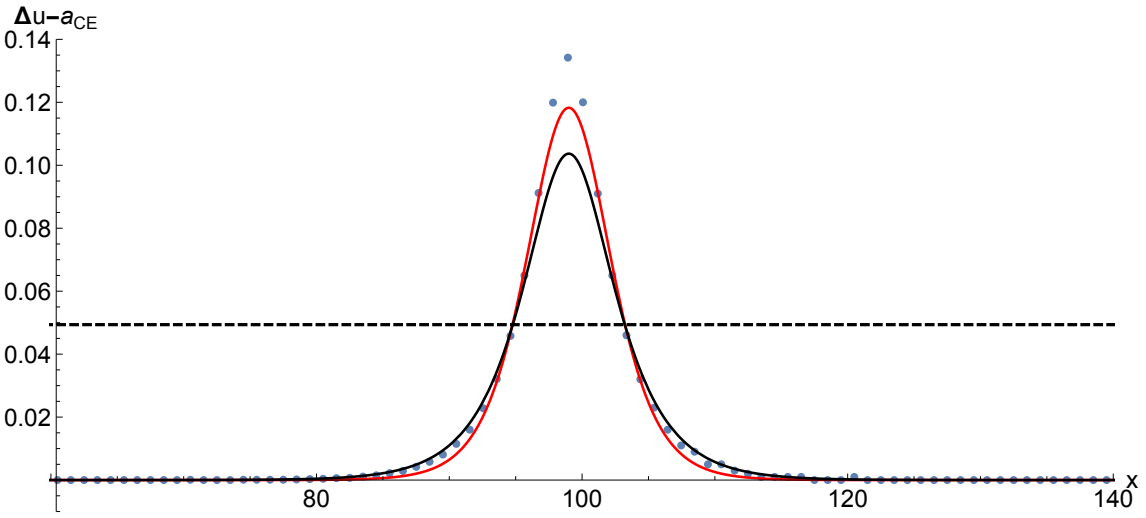

Figure 7.3: Plot of the deviation in the nearest neighbour separation (blue) along the chain of length $L = 200a_{\mathrm{CE}}$ containing one vacancy $\sigma = -1$. The derivatives of both the sG limit function (black) and an approximate function (red) to the data are also overlaid as well as the length positions, defined to be 1/e of the amplitude of the simulated data.

The profile of the differential of equation 7.1 (see figure 7.3) shows that the function does not match the simulated nearest neighbour separation of an anti-kink well in the core of the defect, this suggests a limitation to the use of linear elastic theory for our defect in the region where the separation of vortices are maximal. The profile of equation 7.5 is displayed in figure 7.3, using the parameters found for the fit of equation 7.3. Neither $u'_{\mathrm{l.e.t}}$ or u'_{approx} match the simulated data in the core, both match well in the vicinity of the core boundaries, predicting a kink $\tilde{l}_d \approx 8.4$, as seen in figure 7.3, it correctly predicts the kinks length. The benefit of using $\Delta u(x)$ to depict the defect is one can integrate it to determine the topological charge. For a single chain, the topological charge can be readily determined from

$$u(+\infty) - u(-\infty) = \sigma. \tag{7.7}$$

Using the integral of $\Delta u(x)$ however allows one to isolate different regions of the defect, which shall be crucial when considering wider channels.

In section 4.4, we introduced the hexatic order parameter and discussed how it is commonly used to identify defects in a bulk lattice. In our investigation into static and dynamical properties of defects in narrow channels, however, we opt not to use it in our analysis. Figure 7.4 shows the hexatic order of each mobile vortex in the channel, the hexatic order was obtained by performing a Delaunay triangulation on the mobile and pinned lattice combined and then selecting only the mobile vortices.

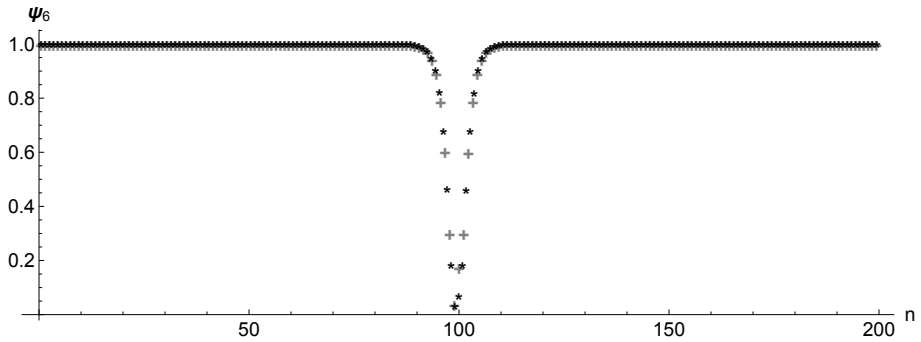

Figure 7.4: Plot of the hexatic order ψ_6 of each mobile vortex in a channel ($L = 200a_{\text{bulk}}$). The hexatic order of the channel containing $n = 199$ (201) is denoted by the $+(*)$ symbol.

Whilst figure 7.4 does show a drastic loss of order in the vicinity of the defect, we are unable to determine its topological nature. The hexatic order is more commonly used to determine the order of a bulk rather than individual vortices. Relaxing from the uniform uniformly spaced chain, the hexatic order of the bulk increases from $\psi_6 = 0.23$ to $\psi_6 = 0.95$.

We have identified that the ground state of an anti-kink may be achieved from a uniform or random arrangement of vortices, both with and without annealing. The deviation from the expected position for an anti-kink can be approximately modelled using both the continuum limit equation 7.1 as well as the approximation equation 7.3, as seen in figure 7.1. Using the approximate form, we can seed defects at desired locations within the channel with much greater precision when compared to the uniform or random seeding previously used.

7.2.1 The Zig-Zag Transition

Above, we determined the ground state of a 1D chain containing a vacancy. We found that the defect is localised to a region a width $7a_{\mathrm{CE}}$, with slowly decaying tails extending beyond. Here we include transverse motion and determine the density range for which the one-dimensional assumption is valid. Each randomly seeded arrangement was annealed, as described in section 4.2.

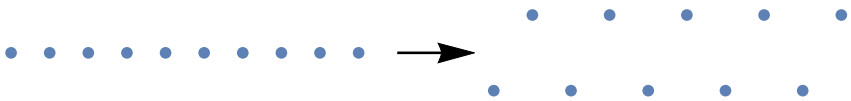

Figure 7.5: Schematic plot of the conventional zig-zag transition, in which one chain bifurcates into to chains with each particle joining alternating chains.

The term zig-zag comes from the way in which one chain bifurcates into two chains, each particle alternating in which new chain it joins, see figure 7.5. It is commonly studied in parabolic confining potentials where there is a trade off between potential energy and maximal separation. G. Piacente *et al.* [91] performed ground state energy calculations on charged particles interacting with a screened Coulomb (Yukawa) potential whilst confined to a parabolic potential. The authors determine a structural phase diagram as a function of density and parabolic confinement which extends far beyond the conventional zig-zag transition.

O. M. Braun and Y. S. Kivshar [41] have studied the zig-zag transition in the FK model. They consider a chain of repulsive atoms confined to a potential which is modulated along the chain and parabolic in the transverse direction. They investigate the transition in a registered chain as a function of repulsion. In addition they repeat this for a one dimensional chain containing a kink as well as an anti-kink, then they compare the dynamics of the zigzag kink with the zigzag anti-kink. Not-

ing that the additional degree of freedom induces an effective anharmonicity.

Here we determine the location of the "zig-zag" transition for the narrow superconducting channel, where the confining potential is described by equation 5.29. Unlike O. M. Braun and Y. S. Kivshar [41], our transverse confinement is exponential. We do not address the nature of the transition, we only identify the density at which it occurs. To identify the number of defects a single chain can support before it becomes energetically favourable to spread in the transverse direction, one can evaluate the "zig-zag" transition. This transition marks the location a 1D chain, partially, bifurcates. We use the term "zig-zag" loosely here because the chain does not experience the conventional zig-zag observed in uniform confinement such as in [91]. The ground state, at densities just above the bifurcation, are not translationally invariant due to the modulated potential, see inset in figure 7.6.

Figure 7.6 displays the average horizontal, vertical and radial spacings of nearest neighbours in a channel of length $L = 100a_{\mathrm{CE}}$ as a function of number of vortices n. As the number of particles increases from zero, the average horizontal and radial separation decrease whilst the vertical separation is zero until there are 125 vortices in the channel beyond which there is a sudden increase in the average vertical separation. Beyond this critical point the decrease in horizontal separation is almost perfectly balanced by the increase in average vertical separation.

We therefore find that a chain of length $L = 100a_{\mathrm{bulk}}$ and width $w = \sqrt{3}a_{\mathrm{bulk}}$ can host a maximum of $n_{\mathrm{k}} = 25$ interstitials with associated coverage parameter $\theta_{\mathrm{crit}} = \frac{5}{4}$ before it becomes energetically preferential for the chain to bifurcate. In this chapter, we are only consider $\theta \ll \theta_{\mathrm{crit}}$ and so we are justified in neglecting transverse motion.

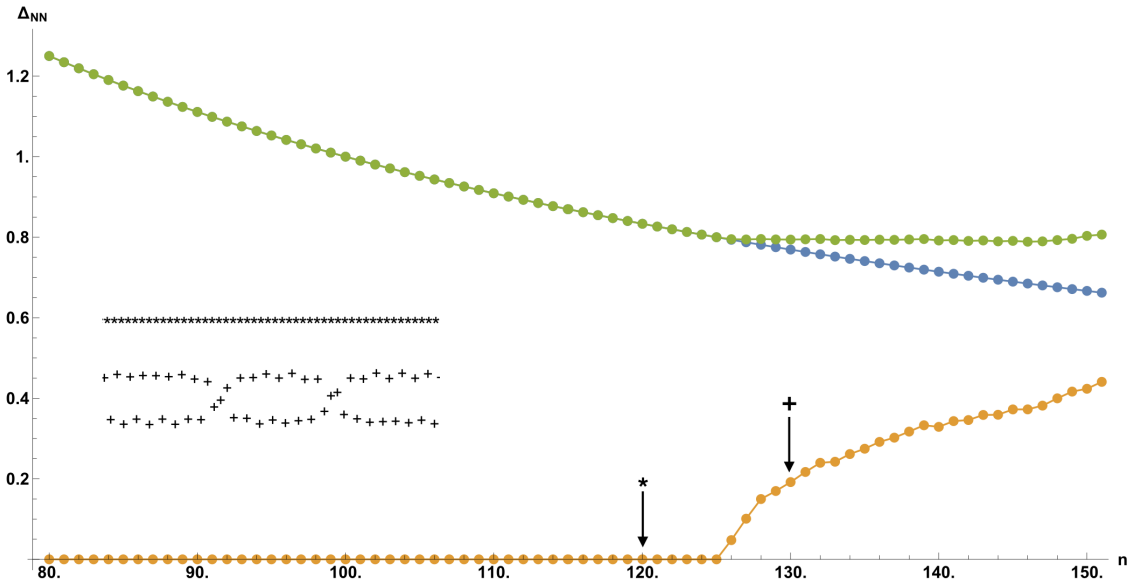

Figure 7.6: Plot of the horizontal (blue), vertical (yellow) and radial (green) separation of neighbouring vortices within a channel of width $w = \frac{\sqrt{3}}{2}$ and length $L = 100a_{\mathrm{CE}}$. The inset shows the arrangement for $n = 120$ $(*)$ and $n = 130$ $(+)$.

7.3 Integrated Chain Dynamics

In the previous section, we found that when an interstitial or vacancy is placed into a long channel the effect of the defect is localised to only a few particles. The defect was comprised of a local expansion or contraction, symmetric about its centre. Away from the defect the chain is found to be the registered state. In a channel of length $L = 200a_{\mathrm{CE}}$ the deformation induced by the defect only covered a region of approximate length $40a_0$, with $\sigma \approx 0.7$ within $\tilde{l}_d$. We now determine what impact defects have on the average velocity of the chain.

Repeating the method of section 6.6, we measure the average velocity of the single chain of length $L = 200a_{\mathrm{CE}}$ containing $n = 200 + \sigma$ vortices. The resulting average

velocity profiles are displayed in figure 7.7 along with the profile registered chain found earlier. Again, we identify two distinct regions with the the profile for $f > f_c$ being similar to the registered chain. In the region $0 < f < f_c$, however, the profile is significantly different to the registered chain.

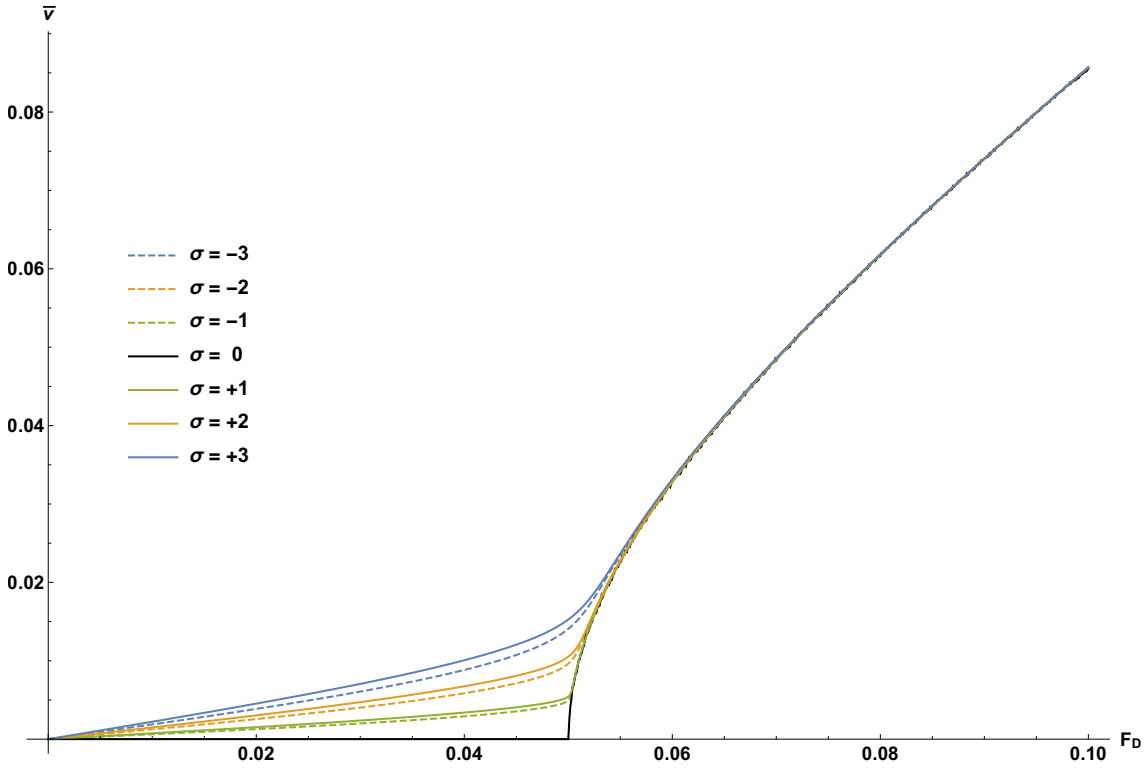

Figure 7.7: Plot of the average velocity of a chain as a function of applied driving force in a channel of width $w = \sqrt{3}$ and length $L = 200a_{\mathrm{CE}}$. The chain contains σ defects within an otherwise registered chain. The chain contains kinks if $\sigma > 0$ and anti-kinks if $\sigma < 0$. The PN barrier for a defect is four orders of magnitude smaller than the amplitude of the potential landscape, as such the critical shear of a defect is extremely close to the origin.

Below the critical shearing force of a single registered channel at zero temperature, each particle in the chain is bound. As such, the average velocity of the chain is zero. From figure 7.7 it is clear that when the channel contains a defect the chain has a finite average velocity, even as one approaches zero drive. The gradient of the linear velocity profile appears to be dependent on the magnitude of the topological charge $|\sigma|$, however there is a difference in the velocity profile depending on the

sign of the topological charge. A chain containing $|\sigma|$ anti-kinks (dashed) appears to have a slightly lower velocity than a chain containing $|\sigma|$ kinks (solid) for a given drive, the discrepancy increases with the number of defects.

Two notable figures in this field of research are O. M. Braun and Y. S. Kivshar. They contributed to the understanding of the finite velocity below the critical shearing force as well as the velocity profile dependence on the sign of topological charge [39]. As the dynamics of the vortices are the subject of the next section, we only outline the reasons for each of these features of figure 7.7 in this section.

The vortices comprising the kink are in an excited state when compared to their registered configuration. These vortices, therefore, face a reduced potential energy barrier. The extent to which the potential barrier has been reduced depends on a number of variables including the width of the kink. As the vortex-vortex interactions are anharmonic, a contraction of particles has a higher energetic cost than a dilation does. A kink therefore has a higher energy than an anti-kink and should therefore flow faster. Likewise the more kinks present in the channel the more compressed the whole chain causing it to flow faster. According to O. M. Braun and Y. S. Kivshar, the net impact of these factors on the average velocity is described by

$$\bar{v} = c_D v_D = \left| 1 - \left(\frac{a_{\mathrm{CE}}}{a_{\mathrm{bulk}}} \right) \right| v_D, \tag{7.8}$$

where v_D is the speed of a kink (or anti-kink) [39]. This formula is valid when the chain is locked and only the kink can flow (i.e. $f < f_c$). Rearranging equation 7.8, we evaluate the decommensuration speed in each of the channels considered in figure 7.7. As shown in figure 7.8 the channels with topological charge of the same

sign have collapsed onto each other for $f < f_c$, after which the profiles diverge. As expected the kink and anti-kink have different speeds, which we have already attributed to the difference in width due to the anharmonic interactions.

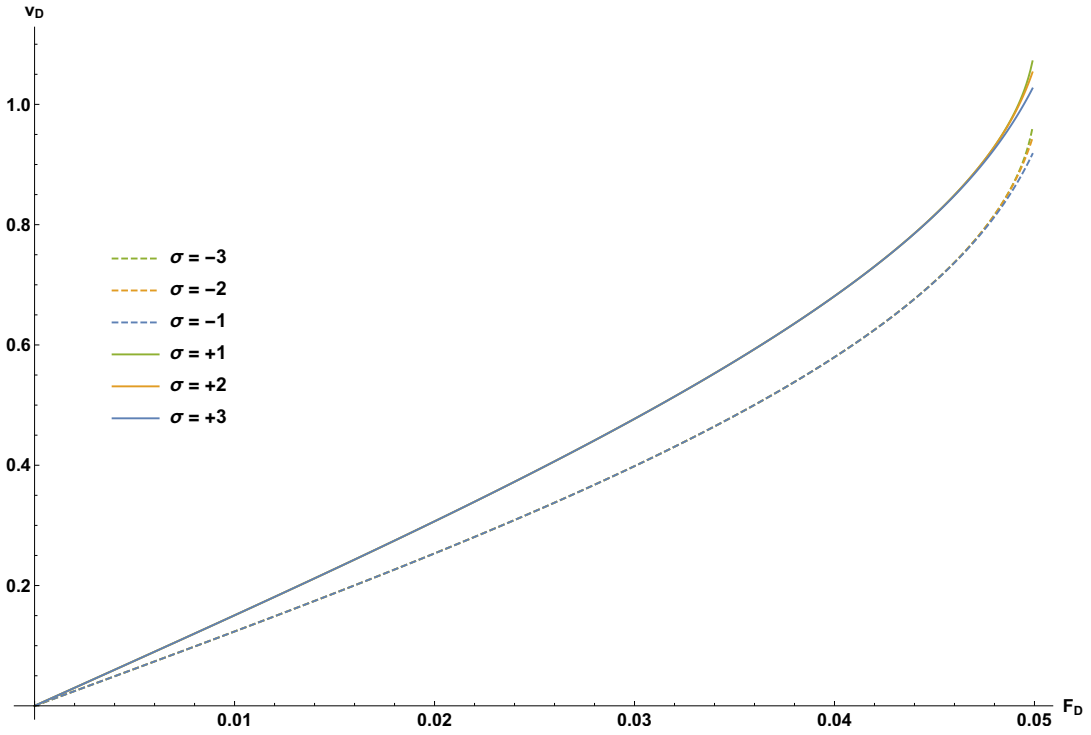

Figure 7.8: Plot of the defects speed of a registered chain in a channel of width $w = \sqrt{3}$ containing σ defects as a function of applied driving force according to equation 7.8. The chain contains kinks if $\sigma > 0$ and anti-kinks if $\sigma < 0$. The formula is only value for $f < f_c$.

The defects in each of the channels travels through at a significantly faster rate than the average registered chain, moving two orders of magnitude faster. It is, therefore, not surprising that observing the defect motion experimentally has proven difficult. As the magnitude of the topological charge increases, the once abrupt locked to sliding transition evolves into a gradual variation in the velocity profile. In the large force limit, each of the profiles in 7.7 collapse onto each other. This implies that the impact of the defects diminishes once the whole chain is in motion. Having discussed the average properties of the chain as a whole, we not delve further and explain these integrated properties in terms of the individual particle motion.

7.4 Kink Dynamics

In this section, we look at the dynamics of each particle in the channel to understand the motion of the kink through the rigid channel. We shall describe how the individual particles permit the kink and anti-kink to flow through the channel, why a defect in the superconducting channel is static at zero drive and how the structure of the defect evolves as a function of drive.

From figure 7.7 it was evident that both the kink and anti-kink increased the average channels velocity below the critical shear. What was not clear, however, was the kinks dynamics and how they increase the channels average velocity.

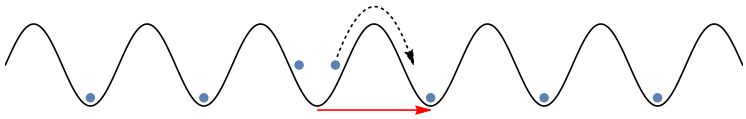

(a) Kink motion.

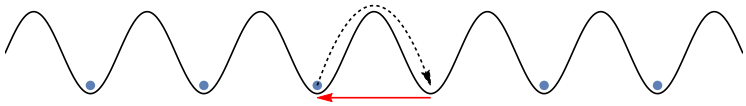

(b) Anti-kink motion.

Figure 7.9: Schematic diagrams of the particle and hole defects motion through the chain. The motion of the particle is given via the black - dashed arrow and the motion of the defect is given by the solid red arrow. The periodic potential is shown in black. Note: both the shape of the well and the position of all particles have been simplified.

Figure 7.9 outlines how the (a) kink and (b) anti-kink evolves through the channel. As the particles move to the right the interstitial (vacancy) moves to the right (left) meaning the kink (anti-kink) travels forward (backwards). Each time the defect evolves through the periodic unit, each particle will be displaced into the next well. The average chain velocity is determined by the rate at which the defect can pass through the channel section. For $|\sigma|$ defects in a region of length L, each particle in the channel will be displaced $|\sigma|$ wells per cycle of the defect.

7.4.1 Peierls Nabarro Barrier

We have addressed the direction in which a kink/anti-kink moves and how its motion results in an average channel velocity. We have not yet explained why the kink can move in the first place, for $f < f_c$. When a defect is present in the channel, the driving force is not acting on the quasiparticle but the particles that form it. For a chain to be in motion each particle must shift wells, which means overcoming the potential barrier. The translation of a particle from one minima to the next requires a gain in energy of $\Delta V = V_{\min} - V_{\max} = 0.0159569866 = \epsilon_s$ in registered systems. The particles comprising the kink however are not initially situated in their respective minima, instead they are located higher up the potential well. Meaning the associated energy cost to shift wells $\Delta V < \epsilon_s$ for a particle comprising the kink.

The kink profile given in equation 7.1 was found by modelling the sine-Gordon equation [39]. This equation is valid in the continuum limit. With the exception of some adiabatic dressing, it was shown in figure 7.1 that the ground state structure of a kink within a discrete channel can be closely approximated using the equation 7.1. In the continuum limit, the complete translational invariance means, however, that the kink can be in motion even at zero drive. This is not the case here, for zero drive the defect is static.

We have identified that whilst the discreteness only has a small impact on the static structure of the kink, it does impact dynamics. Instead of continuous translational invariance the system now has discrete translational invariance. The associated energy barrier which the chain is required to overcome when translating the system by $\Delta x = a_{\mathrm{CE}}$ is known as the Peierls Nabarro potential, E_{PN} [47, 48].

The Peierls Nabarro potential is defined as the difference in the channels energy between the stable and unstable stationary ground states. Due to the numerical fluctuations in the simulations, it proved difficult to simulate the unstable configuration. In order to simulate the unstable ground state, a mobile vortex was pinned at the maxima of the potential landscape and the remaining vortices were evolved about it. Figure 7.10 depicts where each particle, from the evolved ground state for both the stable (blue) and unstable (yellow) configurations, reside on the potential energy landscape defined in equation 5.29.

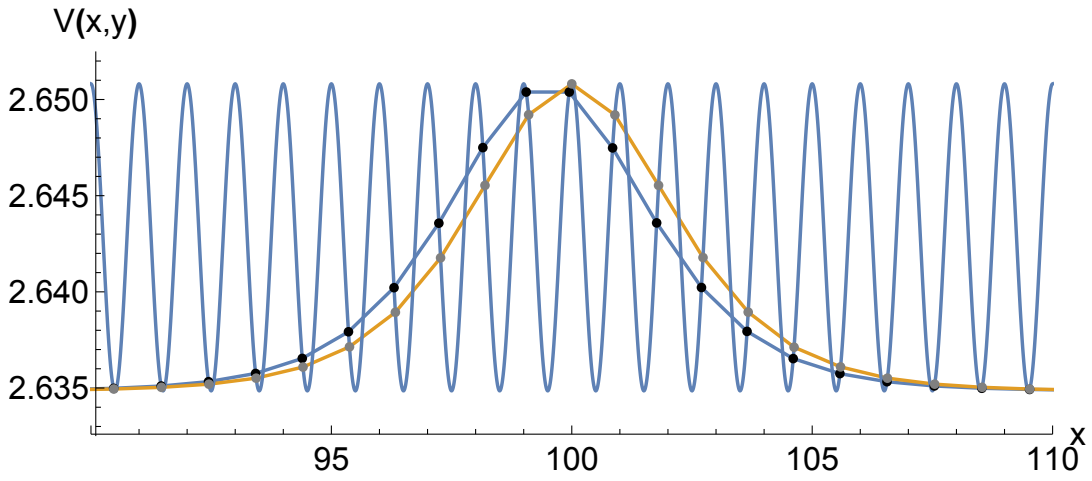

Figure 7.10: Plot of the potential energy each particle experiences from the channel edge in the vicinity of the defect, the simulated stable ground state is shown in blue whilst the unstable ground state is shown in yellow. The horizontal positions are the true positions of the particles, the vertical position is found using $V_{\mathrm{C}}^{F}(x, \frac{\sqrt{3}}{2})$ from equation 5.29.

The first thing to note from figure 7.10 is how high up the substate potential the maximum particles are situated. One also notes the symmetry of both the stable and unstable configuration about their respective centres. The full ground state energy of each configuration is determined via

$$V(\mathbf{X}) = \sum_{i=1}^{N} V_{\mathrm{C}}^{F}\left(x_i, \frac{\sqrt{3}}{2}\right) + \sum_{\substack{j=1,\\ j\neq i}}^{N} \mathrm{K}_0\left(\frac{|x_i - x_j|}{\lambda}\right), \tag{7.9}$$

where $\mathbf{X}$ denotes the ground state configuration of the channel. The relative difference in energy between the stable and unstable state is given by

$$100\frac{E_{\mathrm{PN}}^{\mathrm{Sim}}}{\epsilon_s} = 100\frac{V(\mathbf{X}_{\mathrm{Stable}}) - V(\mathbf{X}_{\mathrm{Unstable}})}{\epsilon_s} = 0.06769279\%. \tag{7.10}$$

For the chain to slide it no longer requires each particle to overcome the full potential well ϵ_s, one only requires $E_{\mathrm{PN}} \ll \epsilon_s$. The drastic reduction in the potential barrier can be attributed to the structure of the kink. Consider the stable (blue) and unstable (yellow) configurations are displayed in figure 7.10 to be the initial and final position of a translation. From our simulated data we find $E_{\mathrm{PN}}^{\mathrm{Sim}} = 0.000010801729$.

The constituents of the kink to the right (left) of the centre all slide up (down) their respective wells. The net energy required to move the particles up their wells is approximately balanced by the gain in energy from the other particles moving down their wells, the discrepancy in loss and gain reduces as a function of kink length. In the limit of strong coupling, $g \gg 1$, V. L. Pokrovsky obtained

$$E_{\mathrm{PN}}^{\mathrm{Pok}} \approx 32\pi^2 g \mathrm{e}^{-\pi^2\sqrt{g}}, \tag{7.11}$$

by employing a Poisson summation technique similar to the one used to derive the channel potential in section 5 [92]. In section 2.4, it was stated that the kinks size is $\propto \sqrt{g}$, as such it is clear from equation 7.11 that an increase in the kinks length results in a reduction in the Peierls Nabarro barrier. From Chapter 2, the dimensionless coupling constant is

$$g = \left(\frac{a_{\mathrm{CE}}}{2\pi}\right)^2 V''_{int}(a_{\mathrm{bulk}}) \left(\frac{\epsilon_s}{2}\right)^{-1} = 3.2830547. \tag{7.12}$$

Substituting this into equation 7.11 one finds that the expected potential barrier $E_{\mathrm{PN}}^{\mathrm{Pok}} = 0.000017752835$, this is approximately 1.64 times larger than the simulated value of $E_{\mathrm{PN}}^{\mathrm{Sim}} = 0.000010801729$, it is unclear what causes the discrepancy in values. The magnitude of the PN barrier, E_{PN}, is three orders of magnitude less than the substrate potential, ϵ_s, as such it only becomes important when $f \to 0$ where it prohibits free flowing kinks in discrete channels at zero drive.

In section 6.7, we found that an applied temperature smeared the locked-to-sliding transition. Temperature increases the probability of a vortex being kicked into the next well, this creates a kink/anti-kink pair. If the driving force is great enough to over come the attraction of this pair (see equation 2.18), then the pair will travel in opposite directions through the channel translating one particle at a time. In a periodic system these two defects meet up and annihilate after each period.

7.4.2 Anharmonic Interactions

In this chapter so far, we have explained how defects move in terms of the particles comprising them, how this motion causes a channel flow, why these defects are permitted to flow for $f \ll f_c$ and how the barrier each particle has to overcome is related to the width of the defect. We now address the discrepancy in the speed of the kink and anti-kink identified in figure 7.8. As suggested earlier this is due to the anharmonicity of the particle interactions.

In section 2.2, we derived the FK model by considering the energy of a chain of particles coupled by perfect springs. The nearest neighbour interaction potential for

spring coupling is $V_{\text{int}} \propto (\delta x)^2$ where δx is the deviation from the expected separation, a_{bulk}. Unlike the vortex-vortex interaction, the interaction force for expansion and contraction is identical. The ideal vortex separation is enforced by the density of the periodic unit of length L, extending the length of the channel for a fixed number of vortices would result in a larger value of a_{bulk}.

It is not the lack of a natural length scale which makes the interaction anharmonic. Many anharmonic interaction potentials with a natural length scale exist in nature, such as the Lennard-Jones potential which models the interaction between atoms [93]. The degree of anharmonicity simply refers to how much the potential deviates from a harmonic oscillator, for weak anharmonicity and $\delta x \ll 1$ one can approximate the potential as harmonic.

In the vicinity of a kink (anti-kink) there is a local contraction (expansion) of the mobile channel. Due to the anharmonicity, the energy of a static kink is therefore larger than that of a static anti-kink and therefore the PN barrier of a kink is also lower. The rest energy of a defect is defined as

$$E_{k,\tilde{k}} = V\left(\mathbf{X}^N_{k,\tilde{k}}\right) - V\left(\mathbf{X}^N_{\text{reg}}\right), \tag{7.13}$$

where $\mathbf{X}^N_{k,\tilde{k}}$ is the ground state configuration of all N containing a kink (k) or anti-kink ($\tilde{k}$) and $\mathbf{X}^N_{\text{reg}}$ is the ground state configuration of N registered particles. The rest energy of the kink is $E_k = 2.45478$ which is the due to an increase in interaction energy of $E_k^{\text{int}} = 2.35697$ and an increase in the substrate energy of $E_k^{\text{sub}} = 0.09781$. One can see that the increase in interaction energy due to the contraction is far greater than the increase in potential energy, as we are in the strongly interacting

limit. The energy of the anti-kink is $E_{\tilde{k}} = -1.90443$ with an increase in substrate potential energy of $E_{\tilde{k}}^{\text{sub}} = 0.08056$ and a decrease in the interaction energy of the channel by $E_{\tilde{k}}^{\text{int}} = -1.98499$. For reference, each vortex in the registered channel has a rest energy of $E = 3.8076$. We identify the presence of anharmonicity through the difference in magnitudes of the interaction energy in the addition and removal or a particle.

7.4.3 Kink Motion

We now take a closer look at the kink dynamics, investigating the structural and dynamical changes as a function of driving force. By measuring the nearest neighbour separation at each time frame, we deduce a behaviour of a decommensuration either side of the critical driving force. We first discuss how the structure of the kink evolves with increasing drive and then move on to discuss its motion.

The Deformable Particle

The kink (anti-kink) is a deformable quasi-particle comprised of many mobile vortices. Its malleable structure can deform to maintain a minimum energy. An example of this is how a kink breathes as it is adiabatically translated from one well to the next, as seen from the two ground states in figure 7.10. We first consider the height of the defect as a function of drive, shown in figure 7.11 below. In order to track the defect one must first define its location, X. Bergman *et al.* [94] define the coordinate of the kink via

$$X = -\frac{\sigma}{a_{\text{CE}}} \int x \; y'(x - X) \; dx, \tag{7.14}$$

where $y(x)$ describes the profile of the defect. We, however, define the kink (anti-kink) coordinate as the maximum (minimum) of the $\Delta u(x)$ profile shown in figure 7.3 as it provides a quick and reliable method for locating the kink to within one a_{CE}. Unless in the unstable configuration, there is always a single maxima in the nearest neighbour separation. The height of the defect is defined as the magnitude of the maximum (minimum).

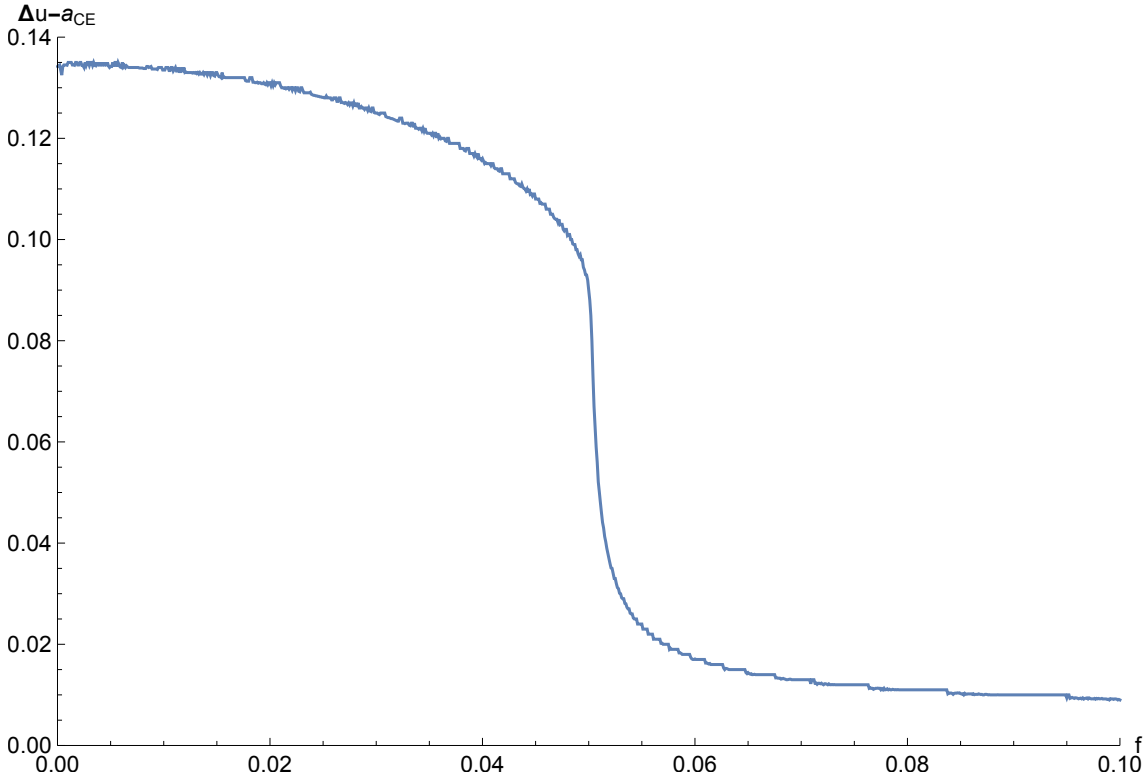

Figure 7.11: Plot of the maximum nearest neighbour separation of the anti-kink as a function of drive, for a channel of length $L = 200a_{\mathrm{CE}}$ containing $n = 199$ vortices.

Figure 7.11 shows the measured height of an anti-kink as a function of drive. As the driving force increases from zero there is a gradual reduction in the height, meaning there is a slow increase in the local vortex density. In the vicinity of the critical shearing force of a single chain there is an abrupt drop in the height of the kink,

reducing almost to zero. The amplitude of the anti-kink separation at large drive is less than 10% of the ground state amplitude. We now take a closer look at the separation profile at different drives to determine how the system is compensating for this reduction in height.

Figure 7.12 shows the nearest neighbour separation of the mobile channel of length $L = 200a_{\mathrm{CE}}$ containing $n = 199$ vortices at a selection of drives, shown in blue. Also displayed in figure 7.12 is the inter-particle separation profile which has been reflected about the centre of the defect, yellow curves. This allows one to identify any asymmetry in the profile. Whilst the data is only displayed for a single time frame, it was found the structures displayed are stable in the long time limit with only small perturbations as it passes over the potential landscape.

We have already discussed the profile of the anti-kink at zero drive in great detail, displayed in the top figure of figure 7.12. From figure 7.11, it was evident that for low drive the height of the anti-kink remains mostly constant. This is observed in the first 3 graphs in which the height and width are approximately constant. As well as consistent shape, its clear that the deformation is localised as away from the peak the deviation in neighbouring spacing being equal to zero. With the deformation only reducing in height and broadening as f approaches f_c.

The prominent difference in each profile in figure 7.12 is the increasing asymmetry observed. As the driving force increases from $f = 0$ to $f < f_c$, the anti-kinks tails alter their shape. The trailing tail, located to the right of each (blue) peak, becomes elongated. Whilst the leading tail becomes sharper. This compression and dilation is due to the mobility of the particles either side of the kink. To conserve area, the amplitude reduces as the kinks tail grows.

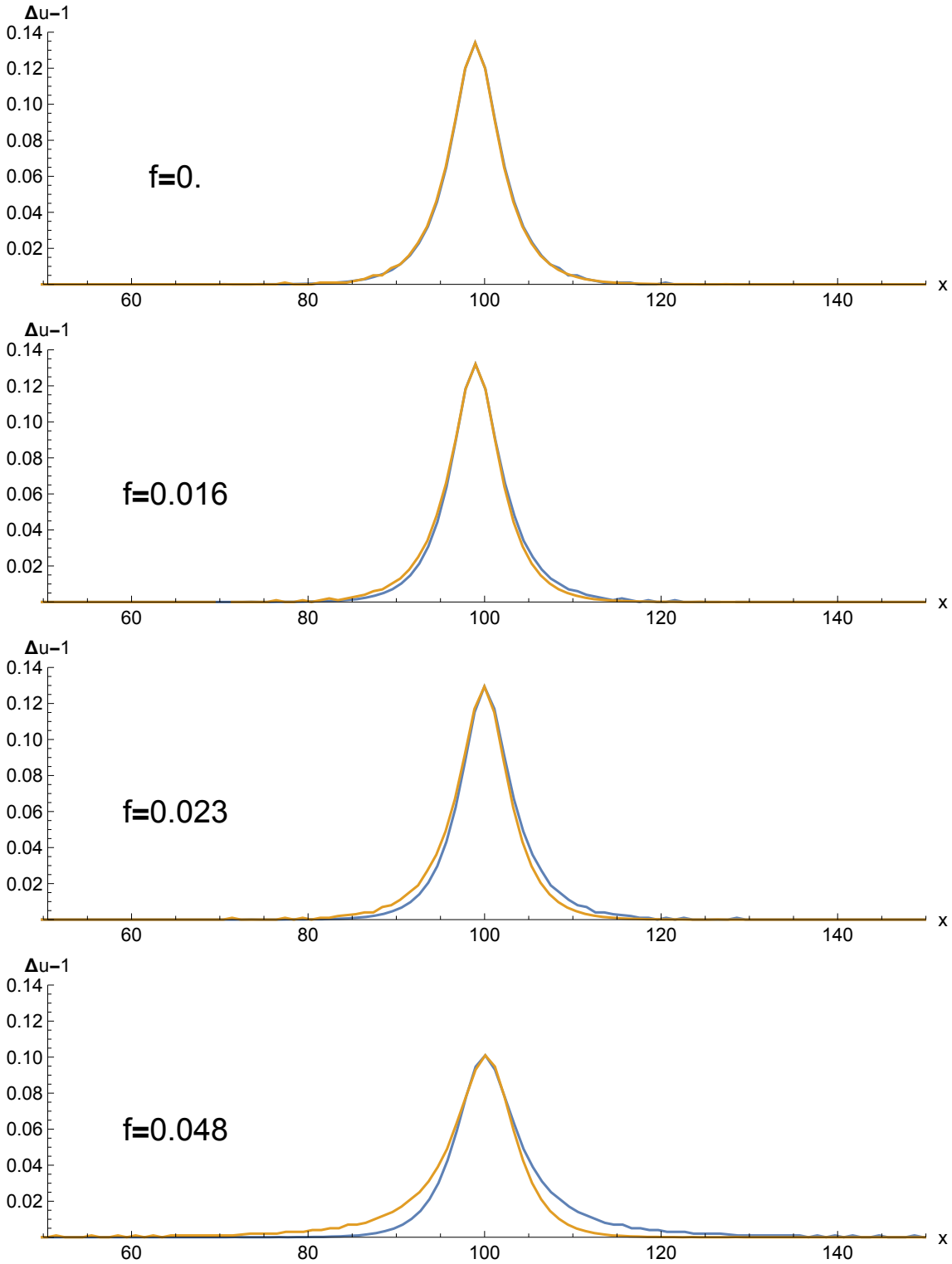

Figure 7.12: Plot of the nearest neighbour separation (blue) for a channel of length $L = 200a_{\mathrm{CE}}$ containing $n = 199$ vortices at a selection of driving forces below the critical shear. The inverted data is shown in yellow.

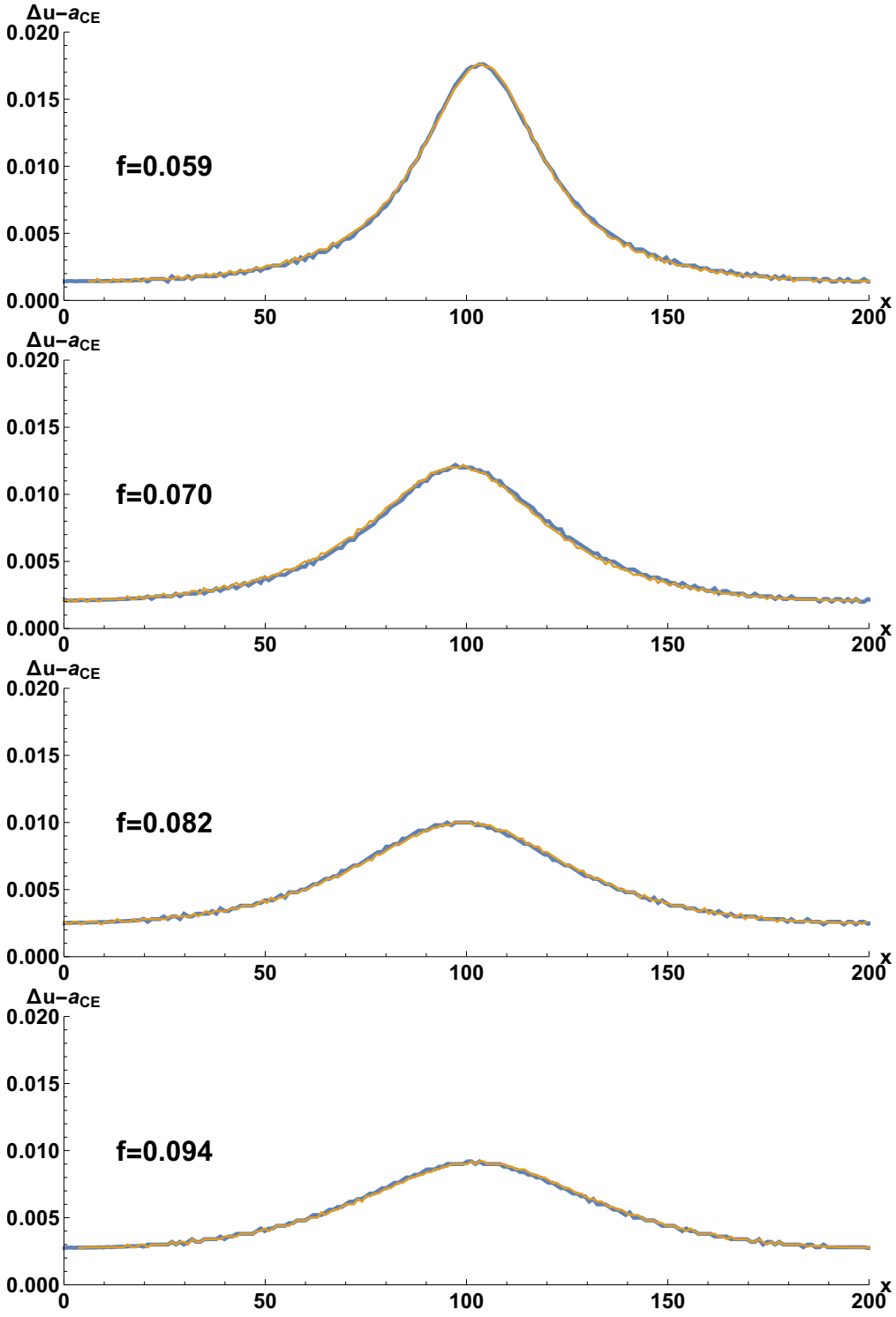

Figure 7.13: Plot of the nearest neighbour separation (blue) for a channel of length $L = 200a_{\mathrm{CE}}$ containing $n = 199$ vortices at a selection of driving forces above the critical shear. The inverted data is shown in yellow.

Figure 7.13 shows the nearest neighbour separation of the mobile channel containing an anti-kink for the high drive regime $f > f_c$. The defect is no longer localised, with each set of neighbouring particles being dilated with respect to the registered spacing. As the driving force increases, the peak is broadened further until it ceases to exist at large driving force. The topological charge of the chain is constant, this is equivalent to preserving the area under each curve in figure 7.13. As the height of the deformation peak reduces the overall shape must broaden to maintain area. We also note that the effect of noise is more prominent in figure 7.13 compared to figure 7.12 as the scale of the figure has changed. The asymmetry in the profile, as observed in figure 7.12, is gone. This implies that the kink is moving at a low velocity in the rest frame of the mobile chain.

Kink Motion

Figure 7.14 shows the displacement a kink (blue) and anti-kink (black) in a channel containing one of the defects at different driving forces drive. Data associated with transient states has been discarded. Independent of driving force, the defect always travels at constant velocity. With the kink travelling forwards and anti-kink travelling backwards, justified above. The trajectories displayed are at equal spacing of driving force, with each line further from the centre having a driving force $\Delta f = 0.005$ larger than the previous. For both types of defects we identify two different regimes, the collection of trajectories with small gradients and then a number of faster moving chains. The two different regimes of motion for each defect are emphasised by the schematic red lines shown in figure 7.14.

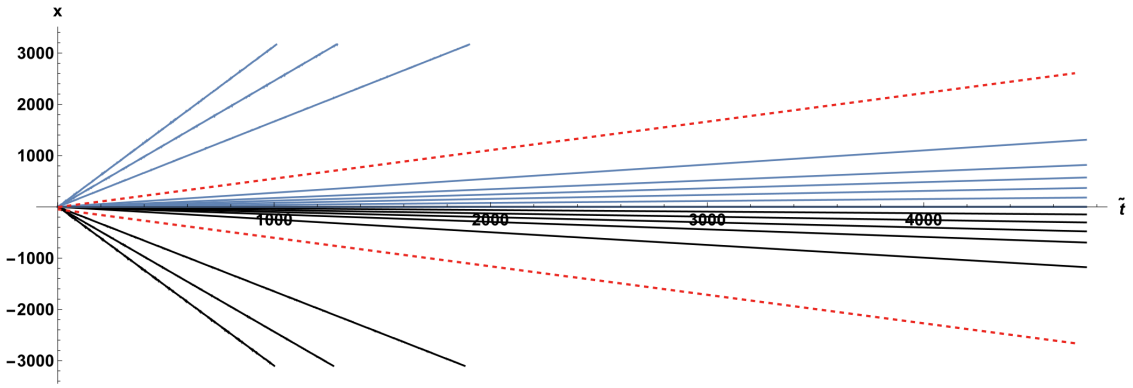

Figure 7.14: Plot of the kink (blue) and anti-kink (black) displacements as a range of different driving forces, the trajectories fan out for increasing driving force. Dashed red lines mark approximate transition.

As each of the defects has a linear trajectory, one can readily determine its velocity. It was shown in figure 7.8 that the kink (and anti-kink) move 2 orders of magnitude faster than the average channel velocity. One can, however, employ equation 7.8 to scale them accordingly. For both a single kink or an anti-kink in a channel of length $L = 200a_{\mathrm{CE}}$, the scaling parameter was shown to be $c_D = \frac{1}{200}$. Applying the scaling equation 7.8 we compare the kink and anti-kink velocity to that of a single registered chain, see figures 7.15 and 7.16 respectively. The scaled kink velocity, shown in figure 7.15 (dashed yellow), matches the profile of the registered channel (blue) well straight after the critical shear. As the driving force grows, however, the two curves diverge.

We determine the scale factor defined equation 7.8 for $f > f_c$ for the kink and anti-kink, see insets of figures 7.15 and 7.16. For the kink one finds $\tilde{c}_D^{-1}(k) = \langle \bar{v}/v_D \rangle = 203.137$, whilst for the anti-kink one finds $\tilde{c}_D^{-1}(\tilde{k}) = 201.136$ where $\langle \ldots \rangle$ the average. For both the kink and anti-kink, the scalar is just greater than that of the locked phase $c_D^{-1} = 200$. Implying the defect does contribute a finite amount to the average velocity for $f > f_c$.

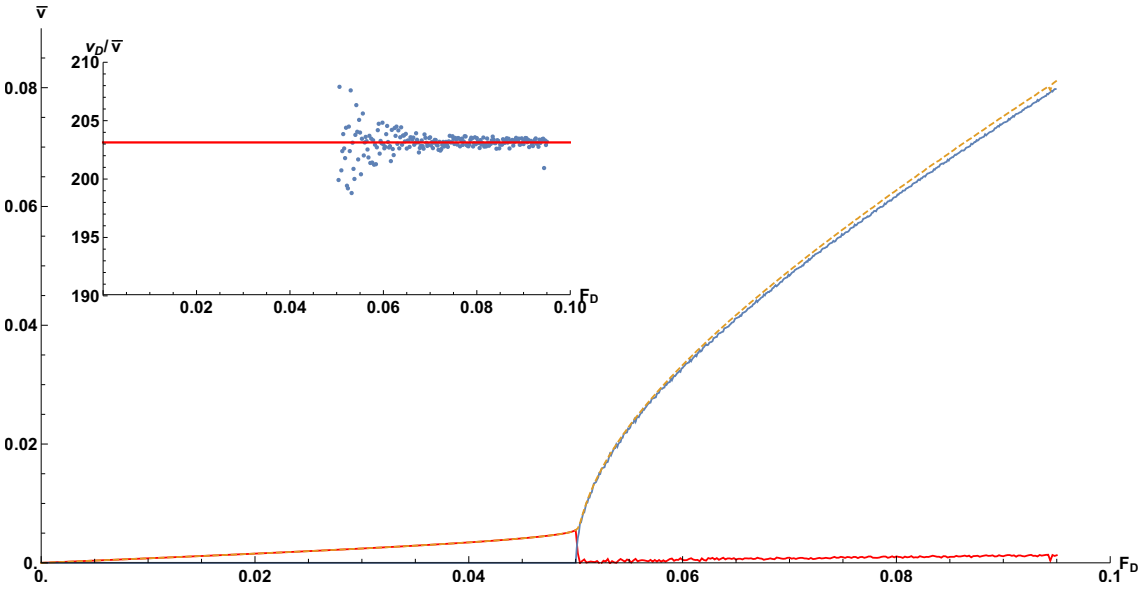

Figure 7.15: Plot of the average channel velocity for a registered chain (blue), scaled kink velocity (dashed yellow) and scaled kink velocity in the rest frame of the channel (red). The inset shows the ratio, $\tilde{c}_D = \bar{v}/v_D$ of the kink for $f > f_c$.

To isolate the kink motion, we subtract the registered chain velocity from the scaled kink/anti-kink velocity, this is displayed on both figure 7.15 and 7.16 and more clearly in figure 7.17. As the drive increases from zero to f_c, each vortex resides higher up in its respective well the Peierls Nabarro barrier reduces and so both the kink and anti-kink can travel at increasing speeds. As the kink is wider than the anti-kink its velocity remains greater. As seen in figure 7.17, the velocity of the kink and anti-kink diverges at $f = f_c$.

Beyond the locked to sliding transition, the registered sections of the chain are mobile. Removing the registered channel motion (moving to the resting frame of the chain) we find that there is a significant reduction in the mobility of the kink and anti-kink. The defect's velocity appears to linearly increase from zero. Once the chain is in motion, there is no longer a preference for the defect to transport mass through the channel. The defect therefore is almost at rest beyond f_c in the moving frame.

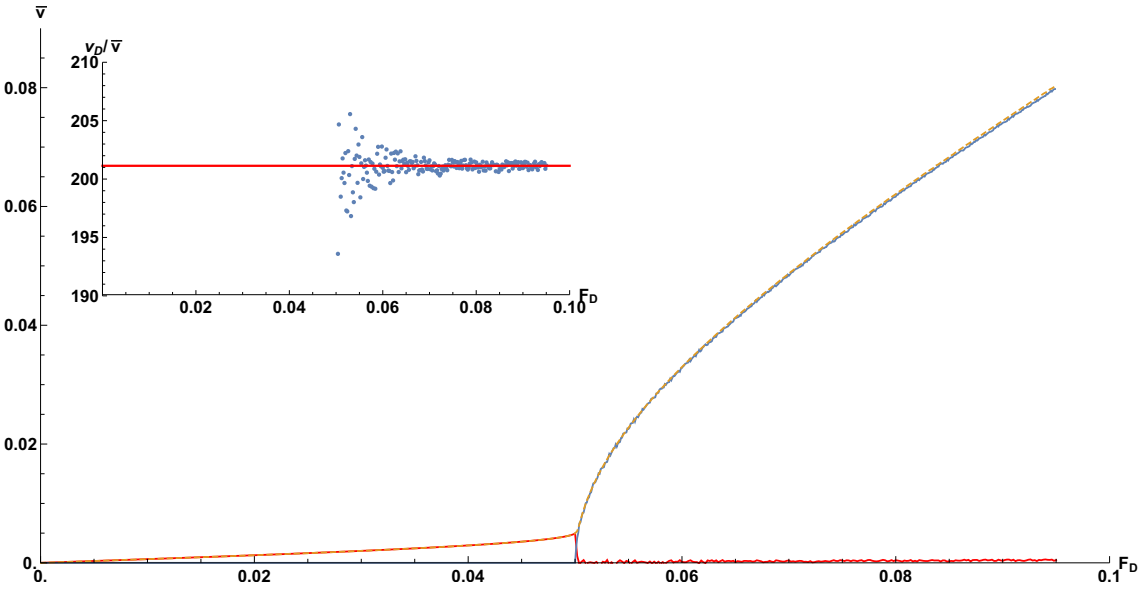

Figure 7.16: Plot of the average channel velocity for a registered chain (blue), scaled anti-kink velocity (dashed yellow) and scaled anti-kink velocity in the rest frame of the channel (red). The inset shows the ratio, $\tilde{c}_D = \bar{v}/v_D$ of the kink for $f > f_c$. As the anti-kink travels backwards we plot $-v_{\tilde{k}}$ instead.

The simulation for each driving force both above and below the critical shear was produced by incrementally increasing the drive by Δf from the previous value, using the final state as the initial conditions for the new drive. Each simulation was repeated, now with an abrupt increase in the force from $f = 0$ to the desired value, initiating the simulation with the ground state configuration. In agreement with the findings of Middleton, the resulting steady state dynamics were independent of initial configuration [82]. The minimisation process, used to find the ground state structure, was independent of the method of seeding for the single chain. The choice becomes important in wider systems as we shall see in the next chapter.

In this section, we have identified how the particles motion leads to the quasiparticle dynamics and established why the defect is permitted to flow below the critical shearing force of a single chain. We then proceeded to investigate why there is an

asymmetry in the velocity of a kink and anti-kink, this led us to determine the rest energy of a kink and anti-kink as well as determine how this energy varies when its width is varied. Considering the particle dynamics in even greater detail, we concluded the section with looking at the stable state motion of these quasi-particles and their deformation as a function of drive. We identified the drastically different profiles of the kink both above and below the critical shear force. Using what we have learnt we now address some applications of defects.

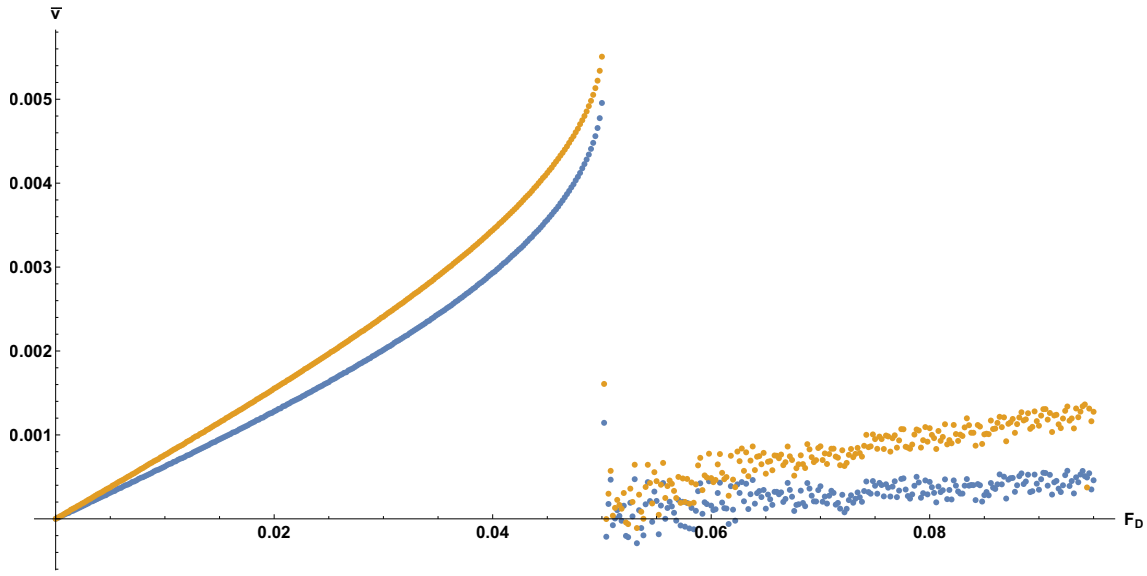

Figure 7.17: Plot of kink (yellow) and anti-kink (blue) velocity in the rest frame of the $L = 200a_{\mathrm{CE}}$ long mobile section of the channel.

The defects studied in this chapter move under the influence of a direct force only in a fixed-density chain. As such the velocity, for a given direct force, is constant. R. Besseling *et al.* [45] visualised the motion of a kink in a finite length chain under the influence of both an AC and DC driving force.

R. Besseling *et al.* found that defects, much like the individual particles, experiences mode locking with visible steps. They were able to directly observe the oscillating motion of a defect in a chain of particles. When a sufficiently large force is applied

to the free chain, a kink forms at the tail end of the chain. This kink then evolves along the chain until it reaches the front, where it is reflected and transformed into an anti-kink which flows backwards through the chain. The overall effect is an oscillating transformation between kink and anti-kink, with each particle moving two wells along with every period. For this reason it is often referred to as caterpillar-like motion [2].

7.5 Concluding Remarks

- The deviation from expected position for an anti-kink in an otherwise registered channel can be approximately modelled using equation 7.1 from R. Besseling *et al.* [45] . Similarly, we can approximate the profile equation 7.3.
- We estimate the anti-kink core to have a width of approximately $7a_{\mathrm{CE}}$, including the extended tails the width is approximately $40a_{\mathrm{CE}}$.
- The inter-particle spacing is an appropriate quantity to quantify defects as it preserves topological charge and differentiates kinks and anti-kinks, unlike the hexatic order.
- From studying the "zig-zag" transition, we determine the assumption of a one dimensional chain is valid up to a coverage parameter of $\theta_c = \frac{5}{4}$.
- Introducing defects into the chain alters the integrated properties, seen in the average velocity as a function of drive.
- The average velocity profile depends on the topological charge, σ, of the chain. Using the scaling relation, presented by O. M. Braun and Y. S. Kivshar [39], one can deduce the defects velocity from the chains average velocity using equation 7.8. This relation is true below the critical shear.

- The kink and anti-kink travel in opposite directions when acted upon by a driving force. The particles comprising the quasi-particles travel in the direction of the force.

- Chains containing defects are permitted to flow for drives below the critical shear (of the associated registered system) because the potential barrier each particle must overcome is lower in the vicinity of the defect. This reduced potential is called the Peierls-Nabarro Barrier [47, 48].

- The anharmonicity of the Bessel interaction force means contractions are a higher energy state compared to dilations. This property explains the discrepancy in the properties of the kink and anti-kink.

- For finite drive, below the critical shear force, the inter-particle spacing profile of the anti-kink is tall, narrow and asymmetric. Above the critical drive, it is broad, shallow and symmetric.

- The reduction in localisation causes the abrupt reduction in the defect velocity, in the rest frame of the chain.

Chapter 8

Defects in Wide Channels

In this chapter, we investigate the static and dynamical properties of defects in wide channels. In section 8.2, we consider the dynamics of a driven channel when a vortex from one registered chain is placed in the neighbouring chain, creating a kink and anti-kink in neighbouring chains. Comparing this dynamics with conventional single chain defect interaction we identify an interesting phenomena. To explain the dynamics of interaction we consider a channel of two chains with just one defect present, this is the subject of section 8.3 onwards. We investigate both the ground state and dynamics of both chains; the chain containing the defect as well as the neighbouring registered chain. Finally, we deduce the underlying mechanism of this phenomena and use it to explain the kink/anti-kink interactions introduced in section 8.2.

8.1 Introduction

In Chapter 6, we employed analytical and numerical techniques to investigate the locked-to-sliding transition of registered chains within wide channels. We found that at zero temperature, the critical shear of interacting chains constrained to move in one-dimension could be approximately modelled using the phenomenological equation 6.5. Approaching the critical shearing force from the ground state, each chain is elastically sheared with respect to both its neighbouring chains and the rigid channel edge potential. Central chains were displaced further than the outer chains with respect to the ground state position. At driving forces above the critical shear, the state moved as a rigid-body. Rigid-body motion was observed for all registered channel widths and the critical behaviour of the average chain velocity was found to be scale invariant.

In Chapter 7, we presented the static and dynamical behaviour of an isolated defect in a one-dimensional chain in a rigid channel potential. We reviewed the ground state structure of the isolated defect, its profile was well approximated by equation 7.1. At zero drive, the symmetric kinks length, defined as 1/e of the amplitude, was approximately $7a_{\mathrm{CE}}$. The velocity and asymmetry of the isolated kink increased with drive, for drives below the critical shear. In the long time limit, the defect's velocity was constant at a given drive. Above the critical shear there is a significant reduction in the amplitude and velocity of the kink.

We now combine these systems to investigate the static and dynamical behaviour of defects in wide channels. This novel system, displayed in figure 8.1, allows us to investigate the properties of kinks in a channel with both a rigid potential stemming from the channel edge and a deformable potential from the neighbouring chain. We

will investigate the dynamics in both the low and high driving regimes, with respect to the critical shear of the defected channel. Whilst the properties of defects in wide channels is a natural extension to chapters 6 and 7, the coupling of rigid and deformable potentials may seem esoteric to the wider physics community. We now give an overview of some of the areas in which similar studies arise.

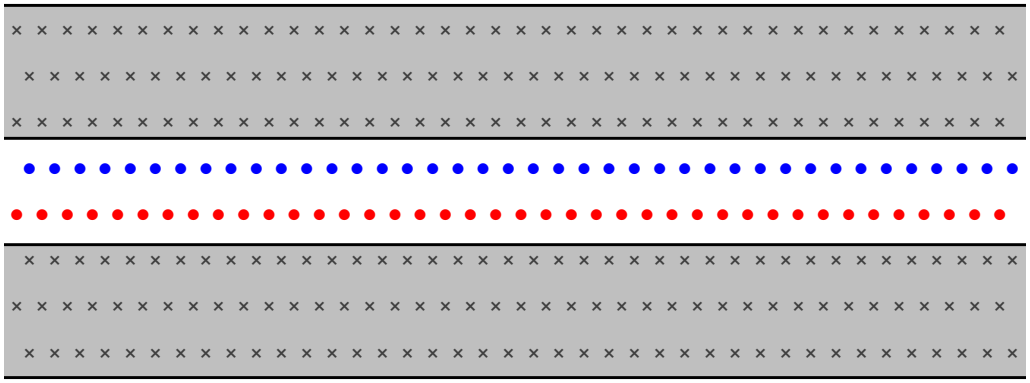

Figure 8.1: Schematic plot of the channel studied in this chapter. The grey region represents the pinned channel edge, modelled using the Fourier form given in equation 5.29. The white region is the homogeneous channel of width $w = \frac{3\sqrt{3}}{2}a_{\mathrm{CE}}$ and length $L = 200a_{\mathrm{CE}}$ unless otherwise stated. Each mobile chain is displayed in a different colour to signify that they are treated separately.

Original motivation for this investigation was to understand the underlying mechanism of the relative slip of chains in wide channels (typically 8 chains wide) when half of chains experience a different response to shearing than the others. This difference in response is achieved through varying the viscosity across the width of the channel, this leads to the natural question; how does the critical shear of this system change when each individual chain has a unique critical shear? Moreover is it true that each chain goes one at once or does it slip as a whole, and are there localised defects which mediate such a motion?

There are many systems in which the slip mechanism in wide inhomogeneous channels has been studied. The average velocity of individual chains, rather than the

mechanism, of such a system was considered by D. V. Tkachenko *et al.* [19]. The colloids with interparticle interaction $V(r) \propto r^{-3}$ were subject to a nonuniform driving force $F_{dr}(y)$. A similar study was conducted by C. Reichhardt *et al.* [20] for particles interacting with Yukawa potential confined to a channel geometry. Instead of the nonuniform driving force used in [19], C. Reichhardt *et al.* drive only one chain. Both groups use the average velocity of each chain to investigate the transition from rigid-body motion to plastic motion.

Initially we considered a wide channel in which the chains experienced different driving forces, like D. V. Tkachenko *et al.* [19]. We found a pronounced effect in the relative slip when one of the neighbouring chains contained a different number of vortices, for a given driving difference. A similar increase in shearing effects in the presence of mismatched densities was shown by R. Besseling *et al.* who evaluated the critical shear as a function of boundary misalignment of each channel edge [18]. Defects were created by translating one edge diagonally with respect to the other at constant density. R. Besseling *et al.* only consider the average motion of all the vortices, rather than of each chain individually.

The investigations mentioned above were concerned with the integrated properties, neglecting the behaviour of individual particles. We will now discuss some of the background physics, which looks at particle motion, that is relevant to this particular work. Our literature search has led us to four main areas: Josephson junctions, colloids, crowdions, and other research within the field of vortices. While these areas have some similarities to the work here, we have found very little in the way of directly related work, though the crowdion literature comes closest with an equivalent system in the static limit. We now discuss each field and the most relevant studies therein.

A crowdion is created by inserting an extra atom into a row of atoms located within the bulk of a lattice, meaning it can be treated in a one dimensional chain in a background potential. A.S. Kovalev *et al.* considered the impact of perturbations in the background potential due to the presence of defects (crowdions) [14]. A.S. Kovalev *et al.* determined that the perturbation to the potential landscapes changes the form of defect-defect interaction from the exponential form predicted by the FK model and given in equation 2.18 to the inverse power law R^{-3}. In the static case that A.S. Kovalev *et al.* consider, the surrounding three dimensional potential was only elastically perturbed. Additionally, A.S. Kovalev *et al.* found that the Peierls-Nabarro barrier experienced by the defect is greater in the case of the elastic potential compared to the rigid potential, the ratio of the difference in the barrier is shown to be greater for broader defects.

In the continuum limit, the fluxon (kink) mobility has been studied in stacked Josephson junctions, as this field is extensive and beyond the scope of this thesis we only introduce it briefly. An intrinsic Josephson effect can be studied in high temperature superconductors, such as in BSCCO where the copper-oxide/bismuth-oxide/copper-oxide layers form a superconductor-insulator-superconductor junction [95]. V. M. Krasnov and D. Winkler showed that fluxons in adjacent layers of this thin geometry are attractive [96]. Alternatively one can study the effects of fluxons in stacked junctions comprised of thicker, low temperature superconducting layers in which a similar phase-locking effect has been observed [97].

Whilst we are unable to find any reference, in the colloidal literature, to the dynamics of defects in channels with imposed order from the channel edge we believe it to be a feasible system to study the effects in. P. Henseler *et al.* [98] and M.

Köppl *et al.* [99] have studied the properties of defects in constricted microchannels with constant channel edges. The motion of a single colloidal particle confined to a periodic potential generated by charged particles was studied by S. Bleil *et al.* [100]. By oscillating the charged particles in the channel edge, S. Bleil *et al.* were able to direct the brownian motion of the single particle.

Previously, our group has investigated defect mediated density changes in long channels (typically $6-10$ chains wide) through an ordered channel edge [27]. Imposing different vortex densities at either end of the channel induced a density driven flux flow. J.S. Watkins and N.K. Wilkin found that for suitable density difference the two different lattice structures would form in the channel, aligned with the channel edges. These lattice structures contain a different number of chains (rows). To mediate this row drop between the different flowing lattice structures, a dislocation travels transversely to the flowing lattice. Upon reaching the channel edge the dislocation is reflected through an interaction with geometrically necessary defects (GNDs). These GNDs occur because of a mismatch in the density of the bulk and channel edges. In the density driven wide channel system considered by J.S. Watkins and N.K. Wilkin, the properties of these defects flowing along the channel edges in the presence of both a rigid and elastic potential are difficult to decipher. The system we have chosen to consider, depicted in figure 8.1, allows greater access to these properties.

Having discussed the relevant literature from a results and experimental perspective, we now look at modelling. One can model the physical systems described above in a number of ways. In the continuum limit case of stacked Josephson junctions V. M. Krasnov and D. Winkler employed a coupled sG model [96]. In the discrete limit, A. S. Kovalev *et al.* employ a generalised FK model in which they can solve the

coupled equations describing the channel and potential landscape for the ground state structure [14]. We employ numerical techniques as we are interested in the dynamical properties of a discrete chain in the presence of a deformable potential which experiences both elastic and plastic shearing. In these limits both the coupled sG and generalised FK are no longer valid.

In this chapter we investigate the dynamics of defects in wide channels which experience both a rigid and deformable potential at driving forces both above and below the critical shear. The closest things we have found in the literature are the study of crowdions in the generalised FK model, one dimensional defects in the high-drive and high-mobility regime as well as previous work of our group conducted by J.S. Watkins and N.K. Wilkin. A. S. Kovalev found that the presence of a deformable potential landscape altered the interaction between of static defects (crowdions) and increased the Peierls-Nabarro barrier [14].

We conduct a similar study of a kinks response to drive to that of O. M. Braun *et al.* [101] in a one-dimensional underdamped FK model. O. M. Braun *et al.* found that at high drive and low damping, the enhanced oscillation of atoms situated in the kinks tail grew leading to the creation of a kink/anti-kink pair in the tail. This leads to a cascading effect where each newly formed defect decay or collide leading to a sliding state. They do not observe such effects in an overdamped system. The defects which exist between the rigid and mobile potentials (GNDs) have been shown by J.S. Watkins and N.K. Wilkin to be of vital importance in mediating density reductions in confined channels [27]. It is the dynamics of defects situated in a similar fashion to the GNDs that we are interested in.

8.2 Channel Flow with Kink/Anti-Kink Pair

Using the cantilever tip of a magnetic force microscope it is possible to manipulate the position of an individual vortex, as shown by E. W. J. Straver *et al.* in a Nb film [102]. By moving one vortex from one registered chain to the other, one can create a kink in one chain and an anti-kink in the other. Whilst in a large bulk lattice a misplaced vortex might be energetically trapped, often requiring a thermostatic kick to minimise the energy state, the excited states in highly confined systems tend to have short lifetimes. Therefore, within the context of simulations, initial conditions for these excited states is crucial, and we discuss them now.

8.2.1 Seeding a Kink/Anti-Kink Pair

Stabilising a kink and an anti-kink in neighbouring chains at zero drive, with transverse motion included, presents difficulties. Simply moving one vortex, transversely, to the neighbouring chain results in an immediate annihilation of the interstitial and vacancy. Instead one could seed each chain using a uniform lattice with a different parameter $a_{\pm} = \frac{L}{N_C \pm 1}$ where N_C is the number of vortices in a registered chain of length L. This stability of the uniform arrangement however is dependent on where the uniform chains are seeded with respect the channel edge.

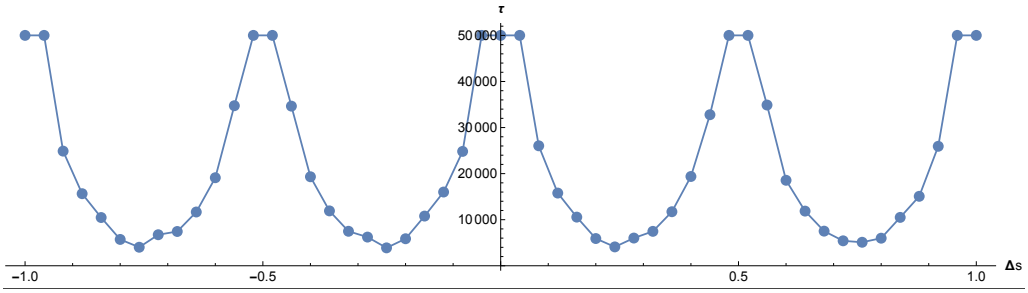

Figure 8.2: Plot of the life time of a kink and anti-kink when initiated from two uniform chains of different spacing, seeded from the starting point $x_0 = x_0^{\min} + \Delta s$. Produced for a channel of length $L = 60a_{\mathrm{CE}}$, similar effects were observed in longer systems.

Figure 8.2 shows the lifetime of the kink and anti-kink in a channel of length $L = 60a_{\mathrm{CE}}$ at zero drive with lattice parameters $a_{\pm}$. The first particle of each chain was located at $x_0 = x_0^{\min} + \Delta s$ where $x_0^{\min}$ is the position of the minima of the first well and Δs is the relative shift. It is clear from figure 8.2 that as the seeding location is translated across one lattice site the lifetime of the state drastically changes.

If the natural locations for the kink/anti-kink to form, discussed in section 7.2, are too close then they move towards each other as they form and annihilate. Seeding with a uniform chains was repeated for $L = 80a_{\mathrm{CE}},\ 100a_{\mathrm{CE}},\ 200a_{\mathrm{CE}}$. Increasing the length of the channel does increase the lifetime however this method is prone to instability. Initiating each chain using equation 7.1 proved to be a more stable method. As the kink and anti-kink move in opposite direction when under the influence of a driving force, we set the kink to the left of the anti-kink.

The inter-particle separation Δu for the ground state structure of the chain containing an anti-kink ($N = N_c - 1$) is depicted in figure 8.3. We observe the large profile of the anti-kink at $x \approx 75$ and a small perturbation at $x \approx 25$ which is the response of the chain to the neighbouring kink, this perturbation is similar to that observed by A.S. Kovalev *et al.* [14].

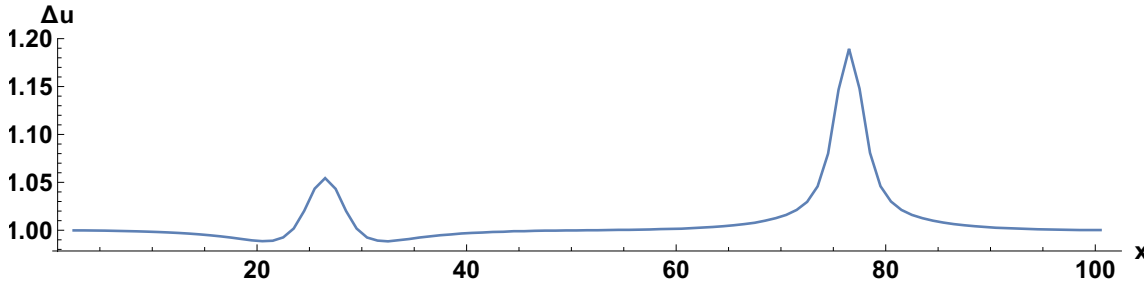

Figure 8.3: Plot of the interparticle spacing of the chain containing an anti-kink, the peak at $x \approx 75$ is the anti-kink and the peak at $x \approx 25$ is the perturbation due to the neighbouring kink.

8.2.2 Driven Channel Dynamics

For a single chain seeded with a kink and anti-kink well separated, the pair annihilated for all drives in our simulations. With a kink and anti-kink stabilised within the two chain channel, a driving force was then applied abruptly at time $t_1 = 50000$ (time steps). We can visualise the dynamics from the contour plot shown in figure 8.4, this shows position plotted against time with the colour associated with the nearest neighbour separation Δu for one of the chains, as depicted in figure 8.3. The broad region at $x \approx 75$ shows the location of the anti-kink within that chain, and the narrow region at $x \approx 25$ is the response of the registered chain to the kink in the neighbouring chain. At low drive ($F_D = 0.0050$) the two travel towards each other and eventually annihilate (at t_2) as one might expect.

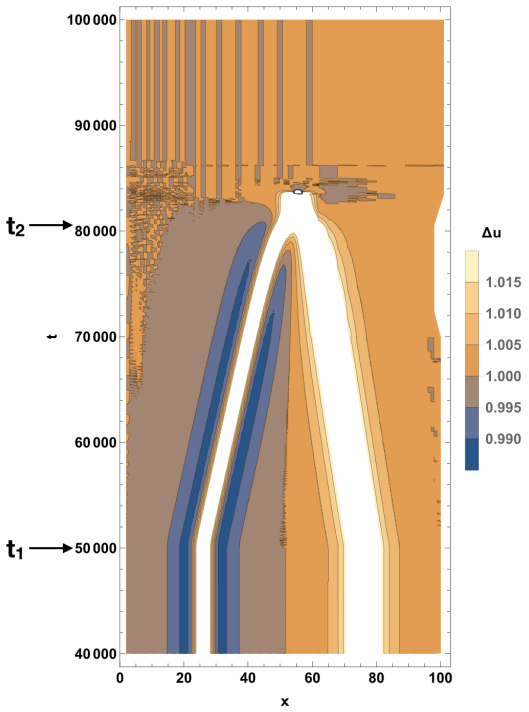

Figure 8.4: Contour plot of nearest neighbour separation Δu as a function of time for the chain containing an anti-kink in a channel of length $L = 100a_{a_{CE}}$ with a neighbouring chain containing a kink. A driving force, $F_D = 0.0050$, is abruptly applied at t_1.

At increased driving force, whilst still in the low drive regime, the kink and anti-kink pass over each other, imprinting only a phase shift, as depicted in figures 8.5. This phase shift in the trajectory of the defects is due to the attraction between them, the kink and anti-kink accelerate towards each other and decelerate as they separate. A similar phase shift is observed in kink-anti-kink interaction in the continuum limit [2].

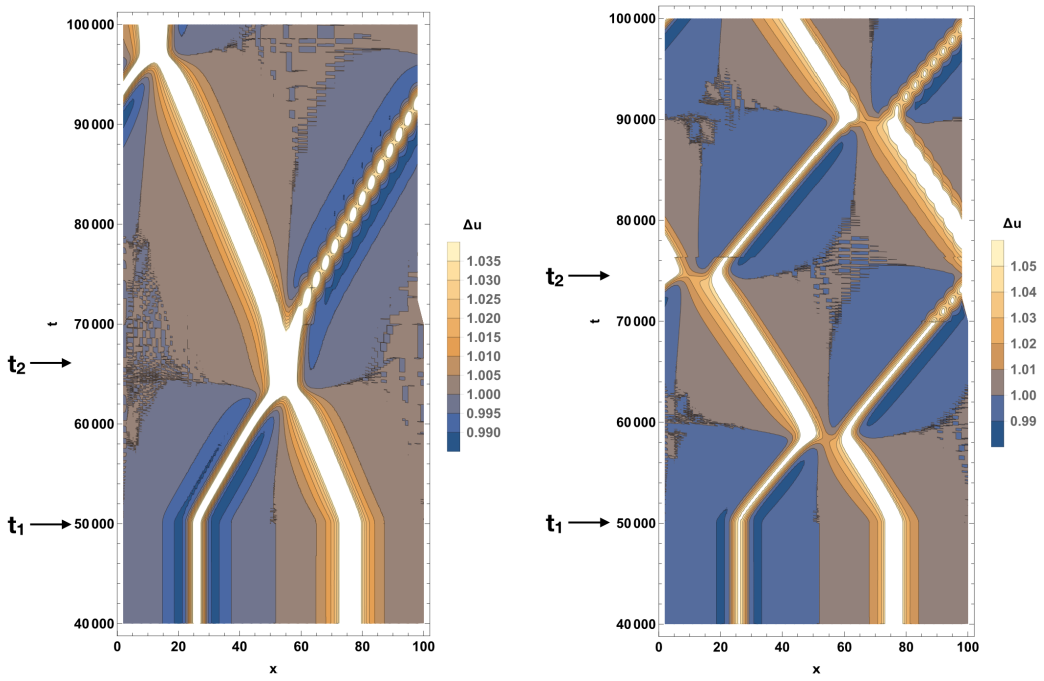

Figure 8.5: Contour plot of nearest neighbour separation Δu as a function of time for the chain containing one vacancy in a channel of length $L = 100a_{a_{\mathrm{CE}}}$ with a neighbouring chain containing an interstitial vortex,for driving force $\mathrm{F_D} = 0.0125$ and $\mathrm{F_D} = 0.0175$ respectively.

For higher drives, however, the dynamics completely changes. Figure 8.6 depicts the dynamics for the driving forces $F_D = 0.0225$ and $F_D = 0.0275$ respectively. Once the drive is applied, the anti-kink appears to undergo a continuous transition reversing its direction of motion and reducing its shape to that of the perturbation. The opposite effect happens to the original perturbation. As the driving force increases, the rate of these oscillations and the horizontal separation between the defects increases. This behaviour is very different to anything observed in single chain channels discussed thus far.

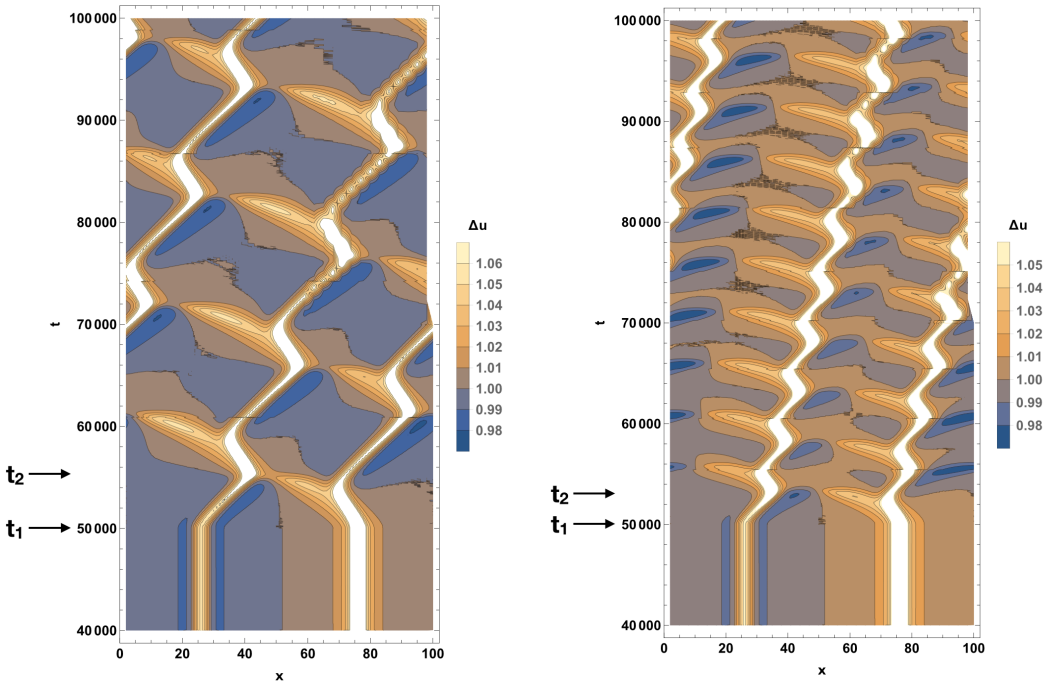

Figure 8.6: Contour plot of nearest neighbour separation Δu as a function of time for the chain containing one vacancy in a channel of length $L = 100a_{a_{\mathrm{CE}}}$ with a neighbouring chain containing an interstitial vortex,for driving force $F_D = 0.0225$ and $F_D = 0.0275$ respectively.

To explain this oscillating action at a distance, we now consider a single defect within a channel with two otherwise registered chains. The effects at high drive (above F_{crit}) presented in this section also occur when y-motion is restricted and channels of length $L = 80a_{\mathrm{CE}},\ 100a_{\mathrm{CE}},\ 200a_{\mathrm{CE}}$.

8.3 Single Defect in a Wide Channel

8.3.1 Introduction

Here we consider two registered chains with either a kink or anti-kink placed within one of the chains. We first describe the ground state, both how the defects structure relaxes within the less rigid potential as well as the resulting deformation of the registered neighbouring chain in the presence of the defect. We refer to the local deformation in the registered chain as a breather as it has zero topological charge, however both its profile and dynamics are different to the continuum limit solution, see equation 2.11.

We then investigate the dynamics, comparing the defect motion for both the low ($f < f_2^c$) and high ($f > f_2^c$) velocity regime as well as analysing the breathers dynamics and how this influences the behaviour of the system. Using what we learn from the single defect, we explain the behaviour of the kink/anti-kink interaction described previously. Finally we describe how this behaviour adapts to even wider channels in which the influence of the substrate potential is even weaker.

8.3.2 Ground State Structure

As with the single chain we evaluate the nearest neighbour deviation. Despite transverse motion being included, no vortices are exchanged between the chains and so the topological charge of each chain remains constant at zero for the registered chain and $\sigma = \pm 1$ for the defect chain. The results of which are displayed in figure 8.7 for a channel of length $L = 200a_{\mathrm{CE}}$ containing $N = 399$ vortices. For comparison the data displayed is for no transverse motion, the impact of transverse motion will be shown later in figure 8.11.

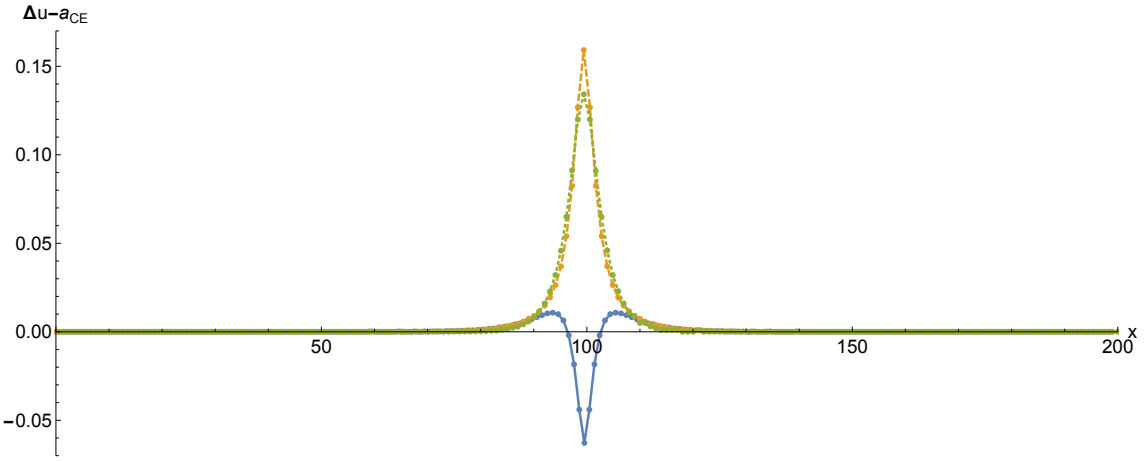

Figure 8.7: Plot of the deviation in the nearest neighbour separation along the chain of length $L = 200a_{\mathrm{CE}}$ and width $w = \frac{3\sqrt{3}}{2}$ in a channel with two chains with no transverse motion. The registered chain is displayed via the solid blue line whilst the chain containing one vacancy ($\sigma = -1$) is shown via the dashed yellow line, for comparison the single chain for zero transverse motion is also displayed via the dotted green line.

We first consider the nearest neighbour deviation for the anti-kink. The overall shape is still symmetric about its centre with a clear maxima in separation, suggesting the structure is in the stable ground state, see section 7.4.1. The ratio of amplitudes, of the nearest neighbour deviation, for the anti-kink in a two chain system compared to a one chain system is approximately 5 to 4. To maintain topological charge, the resulting defect in the two chain channel has a narrower length.

In section 7.2 we defined the defects length as 1/e the nearest neighbour separation amplitude. For the anti-kink in a channel of width $w = \frac{3\sqrt{3}}{2}$, the defects length is $\tilde{l}_{d2} \approx x_2 - x_1 = 102.7 - 96.3 = 6.4 < \tilde{l}_{d1} \approx 8.4$.

We now consider the deformation of the registered chain. The overall shape of the deformation is a compressed core surrounded by two expansive tails. Interestingly, the anti-kinks length $\tilde{l}_{d2}$ is exactly the same as the length of the compression region of the breather, defined as region two in figure 8.8.

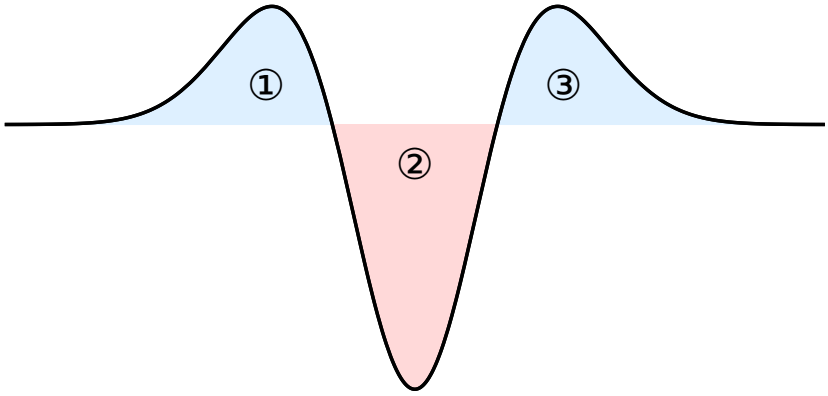

Figure 8.8: Schematic plot of nearest neighbour profile for a breather in the vicinity of an anti-kink at zero drive. The region highlighted red is the contracted core whilst the identical blue regions are the breathers expansive tails.

The topological charge of the registered chain is zero, as such the net effect of the expansive tails must cancel out with the compressive core. To determine the topological charge of each of the three regions depicted in figure 8.8, we must first determine the boundary points of each region. Region one extends between $(0, x_{1\to2})$, region two is between $(x_{1\to2}, x_{2\to3})$ and region three is between between $(x_{2\to3}, L)$. The points between each region $x_{1\to2}$ and $x_{2\to3}$ were determined by locating the points either side of $\Delta x_{NN} - a_{\mathrm{CE}} = 0$ and linearly fitting between the two points. Although approximate, this linear fit proved to be most effective method of locating the zeros at all drives and only results in a maximal positional error of less than $\frac{a_{\mathrm{CE}}}{10}$.

With the boundaries between regions established one could then determine the topological charge of each region, defined as the area between the curve and the axis. Although more sophisticated techniques for numerical integration exist [103], the method which proved most resilient was to employ.

$$\tilde{\sigma} = \sum_{i=1}^{M} \left[\Delta x_{NN} - a_{\mathrm{CE}}\right]_i + \triangle, \tag{8.1}$$

where $\tilde{\sigma}$ is the regional topological charge which despite not being itself conserved must combine with the other regions to give the actual topological charge and $\triangle$ refers to the contribution to the regional topological charge around the axial intersect, its magnitude at least two orders of magnitude smaller than $\tilde{\sigma}$. Applying this to the ground state, one finds the area of each region to be $A_1 = 0.0943074$, $A_2 = -0.188542$ and $A_3 = 0.0942792$ respectively. Giving a net charge for the registered chain of $\sigma = 0.00004496 \neq 0$, this error is due to the handling of the charge at the boundary of each region. This error is three orders of magnitude smaller than the area of each region and so the trapezium rule used in equation 8.1 is suitable for our purpose.

Figures 8.9 - 8.11 show the difference in the ground state profile of the anti-kink and breather, both with and without transverse motion. It is evident that the anti-kink and breather have larger structures when transverse motion is permitted, this is due to the interaction with the neighbouring chain inducing transverse deviations. For simplicity, however, we prevent transverse motion in all further simulations. Whilst there is a slight impact on the ground state structure, the dynamical phenomena observed at high drive in section 8.2 does not rely on transverse motion.

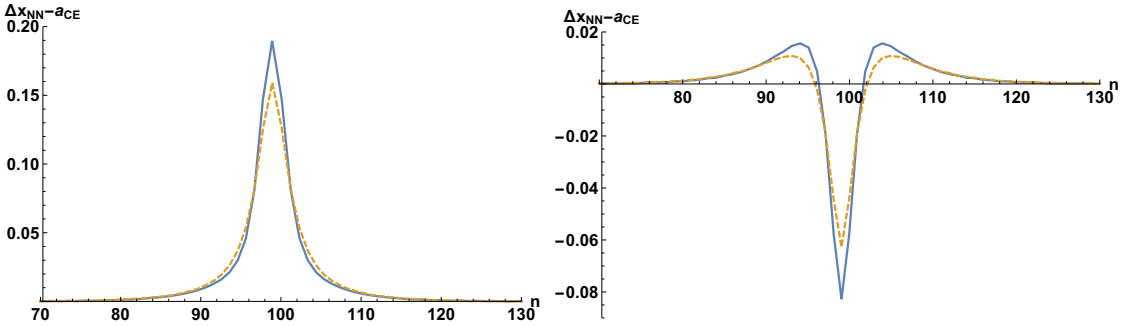

Figure 8.9: Plot of the horizontal component of the nearest neighbour in the chain of length $L = 200a_{\mathrm{CE}}$ with (left) and without (right) a defect in. The blue (yellow) curve is with (without) transverse motion.

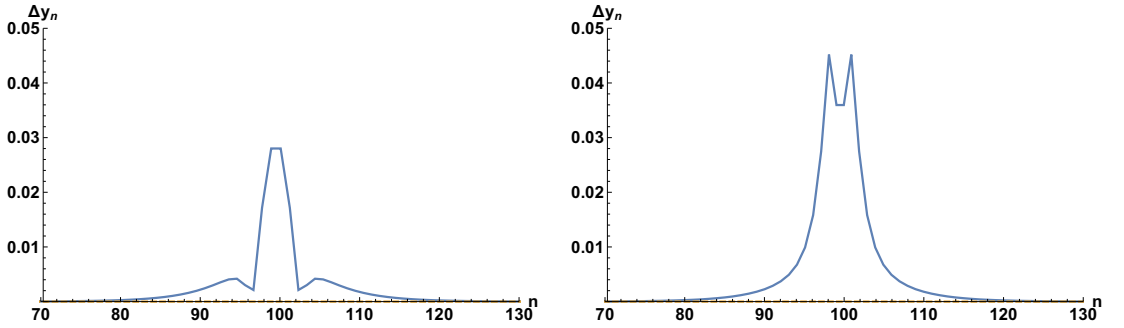

Figure 8.10: Plot of the transverse deviation from expected position of each vortex in the chain of length $L = 200a_{\mathrm{CE}}$ with (left) and without (right) a defect in. The blue (yellow) curve is with (without) transverse motion.

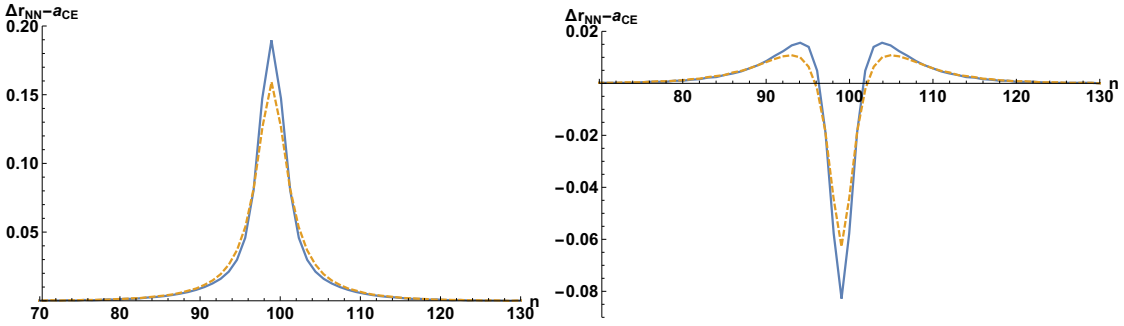

Figure 8.11: Plot of nearest neighbour radial separation in the chain of length $L = 200a_{\mathrm{CE}}$ with (left) and without (right) a defect in. The blue (yellow) curve is with (without) transverse motion.

8.4 Driven Dynamics

Before we can investigate the low drive dynamics, we must first define what is meant by low drive. Using equation 6.8, we can determine the critical driving force of a registered channel of width $w = \frac{3\sqrt{3}}{2}$ exactly. Whilst the low drive dynamics were different when a defects were included in a single chain, the location of the low to high drive transition remained fixed. This, however, is not obvious for wider channels with defects.

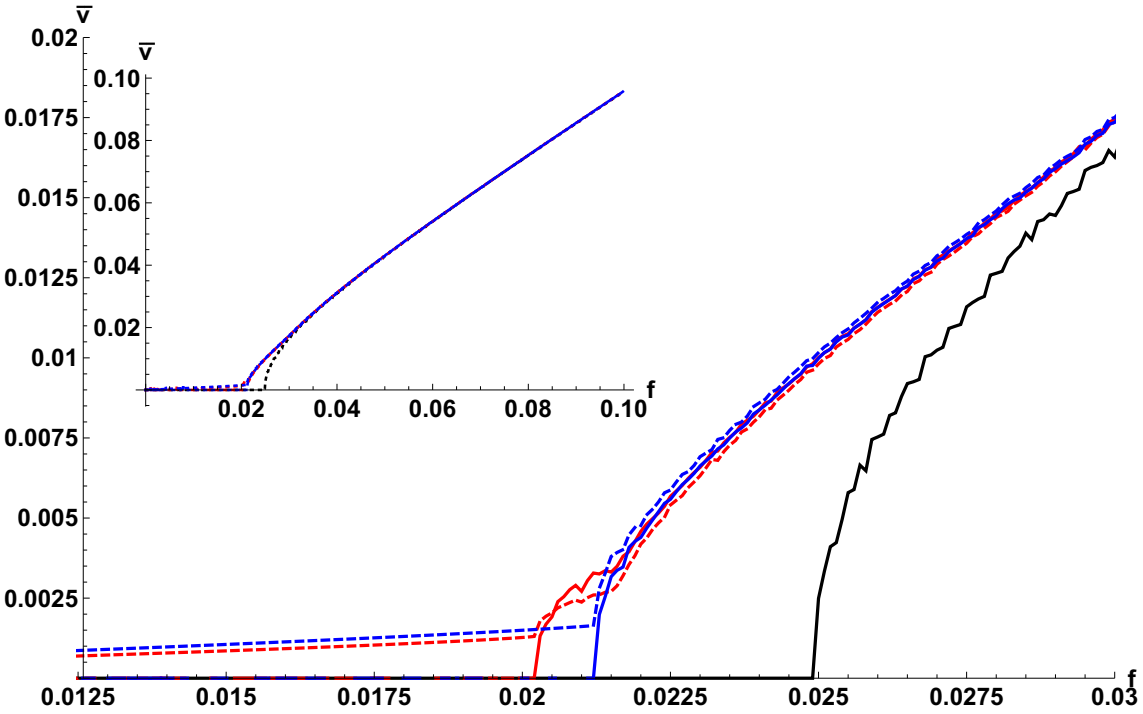

Figure 8.12: Plot of the average velocity as a function of driving force for each chain in a two chain channel of width $w = \frac{3\sqrt{3}}{2}$ and length $L = 200a_{\text{bulk}}$ containing $n = 399$ (red), $n = 400$ (black) and $n = 401$ (blue) particles. The dashed lines depict the average velocity for the chain containing the defect and the solid line is that of the neighbouring registered chain. The inset shows the same profile but over a wider range of driving forces.

Figure 8.12 shows the average chain velocity as a function of drive for a channel of width $w = \frac{3\sqrt{3}}{2}$ and length $L = 200a_{\text{CE}}$ containing either one kink or one anti-kink. As the chain with the defect responds differently to its neighbouring registered

chain, the velocity profile of each chain is shown rather than just a channel profile. As with the single channel, the kink flows faster through the channel than the anti-kink. Unlike the single chain system, however, the presence of a defect lowers the critical drive of the locked to sliding transition. With the extent to which it is lowered depending on the polarity of the topological charge. As the sharpness of the transition is lost when defects are present, we define the low (high) drive regime to be below (above) the transition region. We define the transition region to be $0.020 \lesssim f_c \lesssim 0.023$.

8.4.1 Low Drive

In section 7.4, we identified the growing asymmetry in the anti-kink's profile as a function of drive. The same is not observed here, as the drive varies between $0 \leq f < f_c$ the height, width and symmetry are unperturbed. The increasing driving force however does impact the structure of the breather.

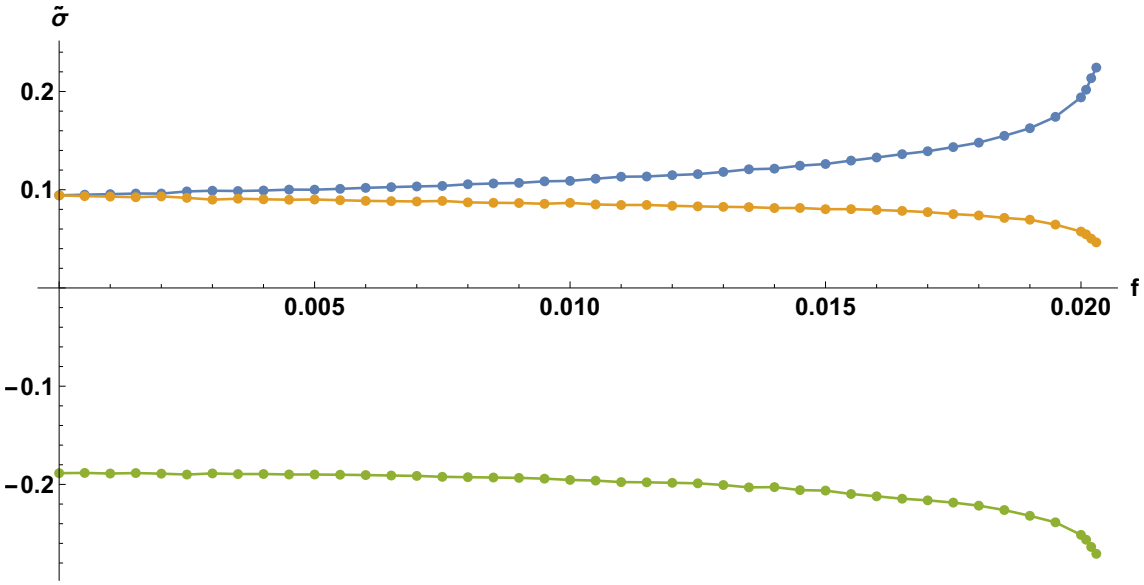

Figure 8.13: Plot of the integrations of each of the breathers three regions as depicted in figure 8.8. Region 1-3 are shown via the blue, green and yellow curves respectively.

So far we have established that the breather remains localised to the neighbouring defect and has zero topological charge with the combined effect of each of the three regions depicted in figure 8.8 cancelling out. As the driving force increases however, the relative size of each of these regions varies with the leading edge increasing in size whilst the trailing edge reduces to compensate. The structure of both the anti-kink and its associated breather at increasing driving force are depicted in figure 8.14 The topological charge of each region as a function of drive is depicted in figure 8.13. As the driving force increases the trailing edge decreases in size until it ceases to exist, at which point only regions one and two exist.

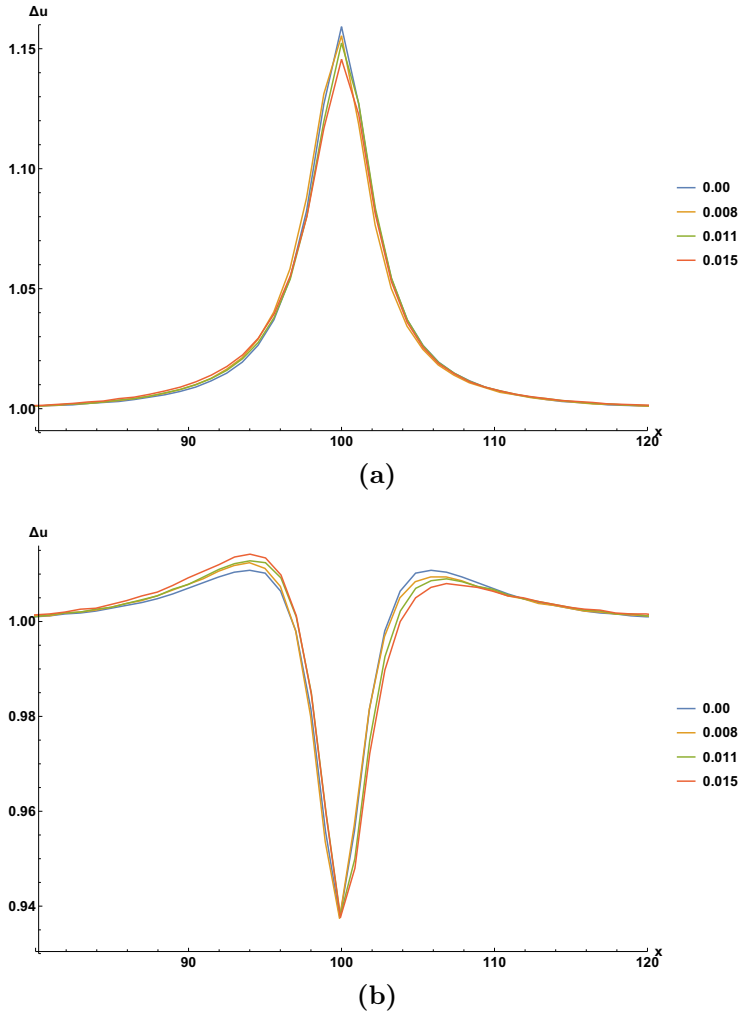

Figure 8.14: Nearest neighbour separation in the (a) anti-kink and its associated (b) breather for a selection of driving forces, below the critical shear.

8.4.2 Novel Dynamics at High Drive

One can see from figure 8.13 that as one approaches the critical driving force of the two chains containing one anti-kink, see figure 8.12, the magnitude of the charge of regions one and two increases. They increase to integer charge of opposite polarity at the critical shear of the channel. Meaning they have accumulated enough charge to become a *kink/anti-kink pair*. The driving force acting on the chain forces these two entities in opposing directions causing them to split apart. As the kink and anti-kink have equal and opposite charge, the topological charge of the chain remains equal to zero.

The original anti-kink locks to the newly formed anti-kink from the breather decay. The bound propagating pair of anti-kinks is stable in the long-time limit. As it propagates it permits each vortex to translate, as seen in the single chain at low drive. The newly formed kink propagates in the opposite direction, its existence causes a breather to form in the neighbouring registered chain.

From this point one of two things occurs, depending on system length, L, and driving force. Firstly, for either short periodic units or driving forces just above critical the by-products of the decay come together and annihilate at which point the cycle starts again. In longer systems or at higher drive a more interesting effect occurs.

When a low driving force ($f < f_c$) is abruptly applied to the static ground state, the time required for the deformed breather to stabilise from the ground state arrangement to its stable structure decreases with drive. Similarly, at high drive ($f > f_c$), the time taken for the trailing edge to disappear decreases with increasing driving force. Consider then an infinitely long system, immediately after the initial decay

the anti-kink pair travels to $x = -\infty$ whilst the kink/breather travel to $x = \infty$. As the kink travels, its associated breather deforms and eventually decays.

As the kink's breather has a reversed polarity to the anti-kink's breather, its decay causes a kink in each chain to combine and travel to $x = \infty$ leaving behind an anti-kink and breather. The anti-kink travels slower than the kink, and its decay time is shorter. The combined impact of this means in an infinitely long two chain channel, a driven defect serves as a quasi-localised source of stable pairs of kinks and anti-kinks, with the production rate dependent on the driving force. In fact, as the original defects profile remains largely unchanged up to the moment of decay, one can pin a defect in the channel edge and have a fixed source of kinks and anti-kinks. The contour plot of simulated date depicting this behaviour is given in figure 8.15 where the colour scale is similar to that of 8.6. A schematic of the mechanism observed in figure 8.15 is given in figure 8.16.

Using the mechanism outlined above, we now explain the kink/anti-kink interaction observed in section 8.2. As the original kink and anti-kink approach, the relatively high driving force causes the associated breathers to decay, resulting in the reflection at a distance observed in figures 8.6. Due to their close proximity, the stable pair of kinks and anti-kinks annihilate. Then another decay occurs reflected in the defects again. One can see from figures 8.6 that the trajectory of the centre of the kink and anti-kink, this is due to the subtle difference in velocity.

8.5 Concluding Remarks

- The dynamics observed in a channel containing a kink and an anti-kink in neighbouring chains is drive dependent.
- At very low drive, the kink and anti-kink annihilate. Remaining below the critical shearing force of the defected channel, an increases in drive causes the kink and anti-kink to pass over each other, only imprinting a phase shift in the process.
- Above the critical shearing force of the defected channel, a novel interaction is observed. This was originally identified as "action at a distance".
- By studying an isolated defect in a two chain channel, a breather was identified in the neighbouring chain. This excitation has zero topological charge, does not oscillate like the sG breather and is caused by the interaction with the neighbouring defect.
- The anti-kink's breather consists of a contracted core surrounded by expansive tails. As drive is applied an asymmetry is identified in the profile of the breather, this asymmetry was drive dependent. The magnitude of the topological charge in the leading (trailing) tail increases (decreases) with increasing drive.
- At the critical driving force of the channel, the trailing tail ceases to exist. The remaining two regions, which have equal and opposite topological charge, each grow in magnitude forming a kink/anti-kink pair which separate .
- The original anti-kink and the anti-kink formed in the breather decay propagate along the chain as a pair. The nearly formed kink propagates in the opposite direction until its associated breather can decay, repeating the cycle.

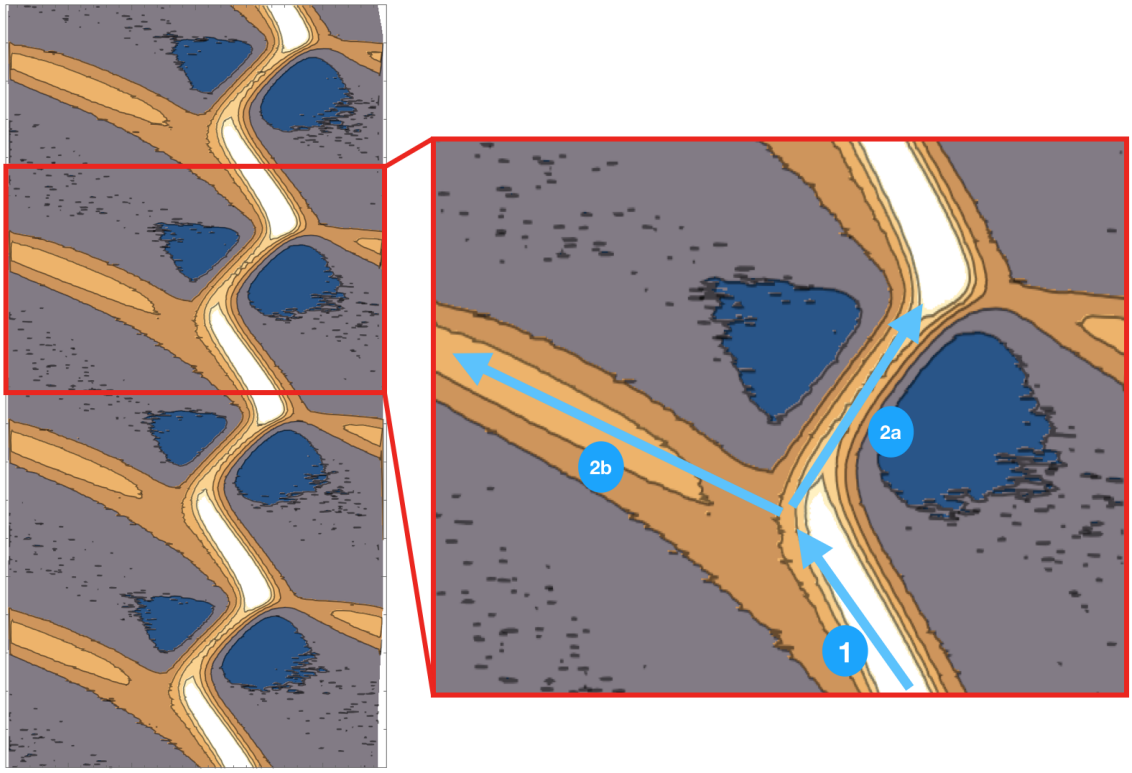

Figure 8.15: Contour plot of the many time frame data of a single anti-kink evolving in the high drive regime.

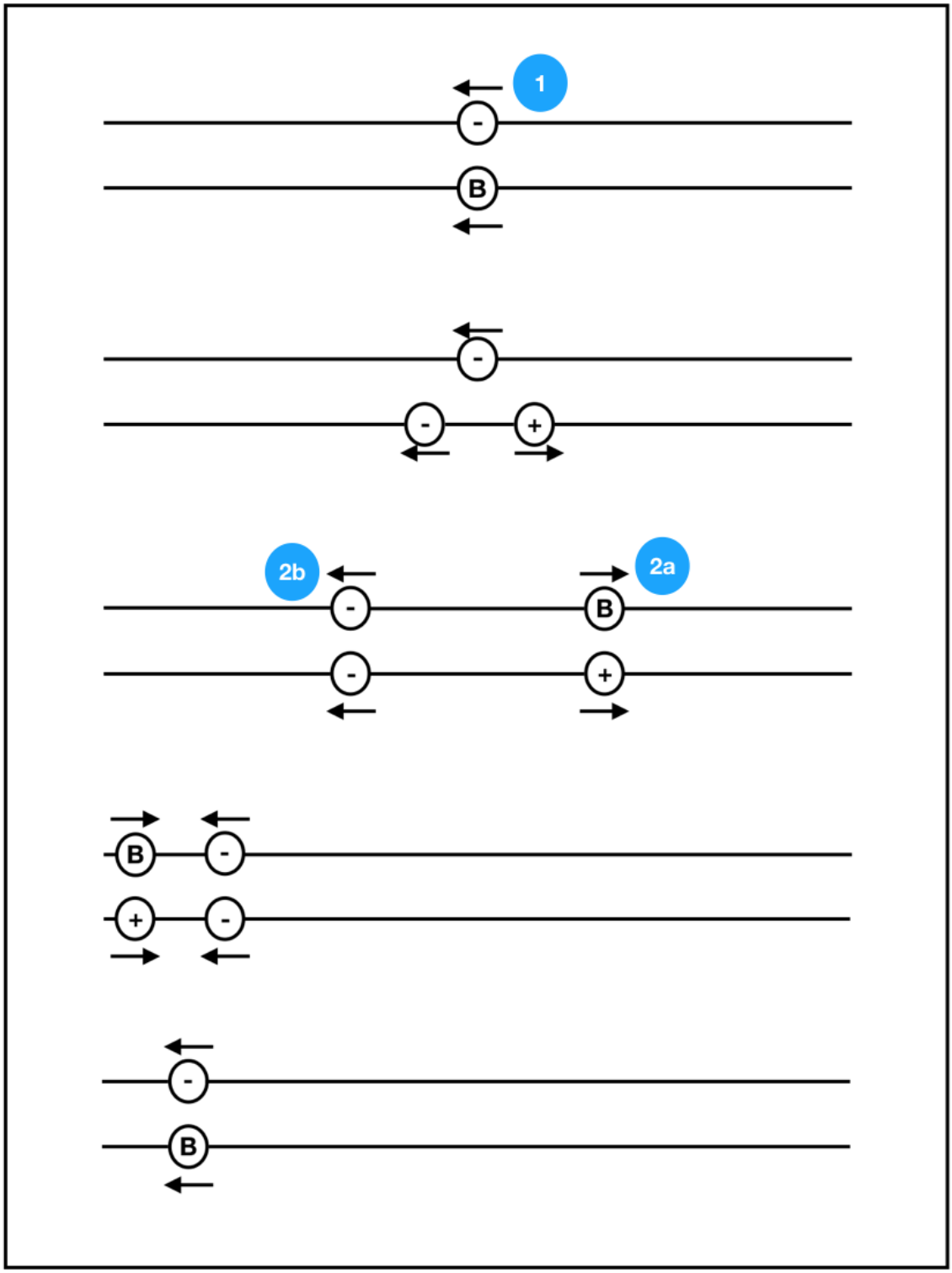

Figure 8.16: Schematic plot outlining the mechanism of defect motion in figure 8.15.

Chapter 9

Conclusion

In Part I of this thesis we have investigated the shear response of free vortices confined to a superconducting channel. We presented the methods used to simulate superconducting narrow channels such as the NbN/Nb_3Ge channel created by A. Pruymboom *et al.* [1]. We have studied three main areas: deriving an expression for the boundary potential and analytically solving registered systems for a reduced model; reviewing and summarising defects in narrow channels; and examining defects in wider channels (amounting to defects in deformable potentials).

We, independently, derive an alternative representation for the potential which stems from the channel edge. Using this new representation we investigate the exactness of the phenomenologically accepted equation for the critical shear of registered channels. This formula is widely accepted by a number of experiments [17, 18, 45] which simulate longitudinal motion only. In this limit we employ translational invariance to explicitly show that the phenomenological equation is not exact for two chains. We then show how this expression can be derived for a reduced model. The reduced model makes three assumptions:

1. Vortices are only permitted to move in one-dimension;

2. The interaction potential is truncated to the lowest order Fourier mode;

3. Interaction is calculated from neighbouring chains only.

We address the impact of these assumptions and note that the most significant is prohibiting transverse (y-) motion. We finally show, for $n = 1 - 4$ chains, that the response of the channel, for driving forces above the critical shear, is scale invariant.

We present a detailed account for the dynamics of an isolated defect confined to a one-dimensional channel, identifying the differences in the shape and velocity of a defect for low- and high- driving force. In both driving regimes the long time limit behaviour of the defects is shown to be stable, with amplitude and velocity fluctuating a small amount as the defects evolve over the underlying potential. We calculate the Peierls-Nabarro barrier for a registered channel containing an isolated defect and asymmetry observed in the integrated dynamics of sheared one-dimensional chains.

We finally move onto studying defects in deformable potentials. Using the Fourier representation of the channel potential we observe dynamics which are only visible for long channels. Our original motivation was to look at two chains with different topological charge. We identified novel interactions in this system which we originally classified as "action at a distance". Investigating each defect in isolation we determined the mechanisms which underpin the novel motion. We find that the drive-induced asymmetry in the perturbed registered channel decays at high drive. This decay process causes a reflection in the topological charge and trajectory of the defect. The quasi-localised oscillating defect acts as a source of stable bound kink/kink and anti-kink/anti-kink pairs.

9.1 Further Work

In figure 8.12, we plot the average velocity of each chain of a two chain channel in which one chain contains a defect. This contains two interesting features which are worthy of further investigation.

Firstly, the critical shear of each chain is lowered in the presence of a defect, the extent to which it is lowered is dependent on the topological charge of the defect. This effect is also observed by C. Reichhardt *et al.* [20], however, they only show this effect $N = 16$ particles in the "registered" chain which we have shown to be too few to form a kink in our system. An explanation for this may lie in the *effective* potential the registered chain experiences in the vicinity of the neighbouring defect. We propose that one approach for studying this effect would be to pin a defect into one of the channel edges and study a registered chain. As mentioned in section 8.4.2, pinning a defect in the channel edge is an effect source of kink/anti-kink pairs.

Secondly, in figure 8.12 we observe an additional feature, between the critical shear of the anti-kink system and the critical shear of the kink system. This feature appears to be a scaled down version of the critical shear profile.

Shapiro steps have been commonly observed in the velocity profile of single chains, both in the average velocity of the whole chain [7] as well as the defect velocity [23]. As discussed in section 6.2, these steps are due to the synchronisation between the applied AC driving force and the frequency of motion over the periodic landscape from the DC driving force. M.P. N. Juniper *et al.* [23] determined the cause of the steps, in a colloidal chain with free-ends, were due to an defect propagating through the chain and reflecting at each end, this reflection also changed the topological

charge of the defect. Here we present an alternative oscillating defect which experiences AC-like behaviour under a DC driving force. The impact of including an AC driving force is, therefore, of great interest.

Lastly, the novel oscillations observed for a single defect in a wide channel, were found to quasi-localise the defect, a slow drift occurs due to the asymmetry in the kink and anti-kinks velocity. M. Danckwerts *et al.* [76] have proposed a mechanism to enhance the viscous force a vortex experiences, discussed in section 3.6. Applying a different drag to each chain, one could both improve the localisation of the defect, and study the stability of the defect/defect pairs which are produced as a product of the oscillations.

Part II

Photonic Crystal Fibres

Chapter 10

Introduction to Part II

Motivation

Since the first experimental realisation in 1995 by Cornell and Wieman [104], both the size and lifetime of Bose-Einstein condensates (BECs) have significantly increased. Cornell and Wieman produced a BEC of 2000 condensed ^{87}Rb atoms, their BEC had a lifetime of 15-20 seconds. Modern experiments, such as E. W. Streed *et al.* [105], can now stabilise BECs for several minutes. Extending the lifetime of a condensate is crucial, it allows one to investigate the broad range of nonlinear phenomena observed within the condensate such as vortices [106], solitons [107, 108] and shock waves [109, 110]. In this part of the thesis, we investigate the feasibility of transporting BECs within the confines of a photonic crystal fibre (PCF).

Typically a condensate undergoes thermal depletion when it interacts with the environment, be it via a poor confining vacuum [111] or interaction with a resonant flash from a CCD camera [104]. By confining a BEC to the hollow-core of a PCF, one can isolate it from stray gas particles and/or selectively transport it to a higher vacuum.

Pioneered by Philip St. J. Russell *et al.* [112], the PCF has found a range of uses beyond its original motivation of high power optical transport, such as micron-sized particle transport [113].

Collimating and guiding in hollow-core photonic crystal fibres has already been achieved for both atoms [114–116] and larger molecules [117, 118]. Beyond guiding, there are other benefits to storing matter within a PCF core such as investigating low-intensity highly-nonlinear phenomena [119]. D. S. Bykov *et al.* have also shown how atoms within the PCF core can be used as a strain, temperature and electric field sensor [120]. M. Bajcsy *et al.* have constructed an all-optical switch from atoms in the PCF core [121]. Attempts to guide BECs through a PCF have resulted in significant depletion [122, 123]. N. K. Wilkin and J. M. F. Gunn found that the light-matter coupling between a uniform Bose gas and a standing wave within the PCF core lead to modulational instabilities [124].

We investigate a different regime to [124] in which a dilute, low temperature condensate of $N \gg 1$ bosons interact with the gapped fibre mode. By treating the radiation as a dynamic participant, rather than just a background potential, we find that the slowly varying envelope of the field is described by the nonlinear Schrödinger equation. Taking advantage of the PCFs properties, we identify a stable light-matter solitonic solution to the nonlinear Schrödinger equation with variable amplitude and velocity.

Overview

In Chapter 11 of this thesis we present an overview of the broad physics of optical guides. We begin by reviewing two conventional guides; solid core dielectric fibres and metallic waveguides. By discussing the beneficial properties as well as the loss mechanisms, we motivate the photonic crystal fibre design. Following the methods presented in [10, 125], we explain the key properties of a Bragg fibre [126] by considering both a 1D photonic crystal as well as the hollow metallic waveguide discussed in section 11.2.3. We conclude this section by presenting an overview of confined matter guidance. In this section, we introduce the prominent guiding method, we then discuss key historical moments in the evolution of this field. From the proposal of atomic transport [127] through to modern attempts at BEC loading [128].

As we are considering a novel way of transporting a Bose-Einstein condensate within the hollow core of a PCF, we introduce the key features of condensates and derive a model commonly used to study the dynamical behaviour of a low temperature, dilute vapour of interacting bosons. This model is referred to as the Gross-Pitaevskii equation (GPE) after its namesakes E. P. Gross [129] and L. P. Pitaevskii [130]. As we are interested in the mobility of the BEC, we express the GPE in its hydrodynamic form. We also outline the limits we investigation within section 12.2.

Finally, in Chapter 13 we combine our expression for the dynamics of both the light and matter to formulate an equation for the effective 1D dynamics along the fibre core, the nonlinear Schrödinger equation. This equation supports a light-matter soliton. Taking advantage of the properties of the PCF, we identify a regime in which the soliton is stable and can evolve down the fibre core with variable amplitude and velocity.

Chapter 11

Photonic Crystal Fibres

In this chapter, we introduce the key concepts of the manipulation of light. Two conventional methods of guiding radiation; the solid core dielectric fibre and the hollow metallic fibre are discussed in section 11.2. We qualitatively describe the different methods of confinement, the construction and composition as well as the benefits and limitations of each method. As the mode structure of the hollow-core PCF and the hollow metallic waveguide have been shown to be similar [125], we also derive the profile of the transverse magnetic and transverse electric modes of a cylindrical metallic waveguide in section 11.2.

This chapter will go on to introduce the photonic crystal fibres, in section 11.3. We use the limitations discussed in section 11.2 to justify the PCF design. In our research, we consider the Bragg fibre rather than the holey fibre, as such we develop the theory of the Bragg fibre from a simple one dimensional photonic crystal. We conclude this chapter with a historical review of atomic transport. The content of this chapter is a culmination of a number of source; two prominent sources of information are [10] and [131].

11.1 Introduction

The interaction of electromagnetic fields with matter has a vast range of applications. One of the most ubiquitous is the role of radiation pressure in astrophysics, a concept first put forward by Kepler in 1619. The pressure created stabilises large stars preventing them from collapsing under their own weight. Additionally, it contributes to the Poynting-Robertson effect where dust is sent spiralling into the Sun and removed from the Solar System [132]. Currently, researchers are utilising radiation pressure for the propulsion of Solar Sails in Space [133].

Through advances in our understanding of the interaction between light and matter, electromagnetic fields are now capable of cooling matter [134] and localised electromagnetic radiation can even be used to confine and transport atoms and molecules [118,135]. However, one flaw is that the radiation is prone to dispersing if left unconfined. This can be caused by scattering from air molecules and can therefore limit transportation. Fortunately, techniques exist to control the guiding light which helps to maintain a strong electromagnetic field. The focus of this chapter is to gain an understanding of such devices, such that we can utilise them to guide a coupled light-matter wave.

For centuries, simple plane mirrors have been used to produce reflections. Next, mirrors and lenses were redesigned to further manipulate the trajectory of light. In 1609, Galileo employed this technique to visualise celestial bodies. Going beyond its visual applications, light can also be used to send information in the form of optical signals. We can now transmit optical signals along a curved trajectories using optical fibres. Combining the ability to manipulate both light and atoms introduces many more possibilities which we shall discuss in this chapter.

11.2 Guiding Light

11.2.1 Manipulating the Trajectory of Light

Most natural sources produce radiation with a spectrum of frequencies, for centuries we have been able to reflect and diffract as well as disperse this light into its components. Advances allowed us to develop lasers which produce collimated radiation at a desired frequency, combinations of these lasers can be used to then create standing waves and other optical traps. We now have devices capable of prohibiting certain frequencies and localising light along a certain trajectory [10].

Light can be guided along a confined path using optical waveguides. Such devices are of paramount importance to the telecommunications industry. Two early examples are hollow metallic waveguides and dielectric fibres. Both of these are capable of guiding electromagnetic radiation and can be designed using many different materials and/or geometries to tailor to the specific needs. However, the inherent nonlinearities of solid core dielectric fibres limits the maximum signal intensity and hollow metallic waveguides only have a finite window of permitted frequencies.

11.2.2 Solid-Core Dielectric Fibres

Since the Ancient Greeks, information has been encoded in optical signals. One benefit of this is the almost instantaneous speed at which information can be transmitted. Despite a significant amount of research dedicated to improvements, free-space optical communication is limited to a maximum signal range of a few kilometres within earths atmosphere [136]. This is, in large part, due to atmospheric attenuation and beam dispersion. By propagating the signal through a dielectric fibre, one can transmit over distances which are two orders of magnitude larger than that of free-space signals along any trajectory [137].

The electromagnetic field is primarily localised within the high refractive index core. The extent to which the light is confined depends on the geometry of the fibre and the refractive indices of the core and cladding. The optical fibre localises light via total internal reflection, a process first demonstrated in a "light fountain" by J. Babinet and D. Colladon. Light incident upon this boundary obeys Snells law $n_{\text{core}} \sin(\theta_{\text{core}}) = n_{\text{clad}} \sin(\theta_{\text{clad}})$ where n_i is the refractive index of the material and θ_i is the angle the light is incident/emergent from the boundary. As θ_i is defined from normal incidence, for light to remain localised in the core $\theta_{\text{clad}} = 90°$, from this we find that the critical angle for light incident upon the interface from the core is given by

$$\theta_{\text{core}}^{\text{crit}} = \arcsin\left(\frac{n_{\text{clad}}}{n_{\text{core}}}\right). \tag{11.1}$$

It is evident from equation 11.1 that the core must have a higher refractive index than the cladding in order for light to remain localised. Increasing the difference in refractive index causes an increase in the range of acceptable incident angles, re-

ferred to as the acceptance cone. Naïvely, then, one may assume that a larger index contrast between the core and cladding is always beneficial. One can appreciate why this may not be desirable by considering dispersion using geometric optics. As the acceptance cone increases, so too does the range of time of flight. Those that enter at a larger angle, with respect to the fibre axis, take a longer time to traverse a section of the fibre when compared to those travelling straight down causing an increase in dispersion. As such, small differences in refractive index, achieved by varying the silica doping, are often preferential.

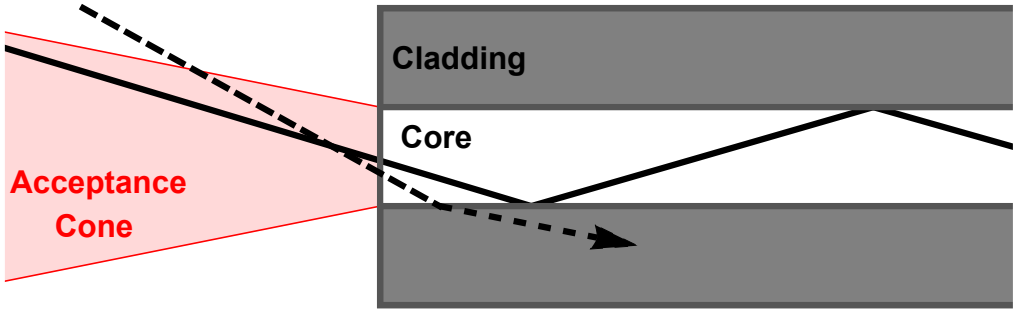

Figure 11.1: Schematic of the acceptance cone for a multimode dielectric step-index fibre. Light incident from within the acceptance cone, with an angle $\theta \leq \theta_{\text{core}}^{\text{crit}}$ will propagate down the fibre core (solid line). If the incident angle is $\theta > \theta_{\text{core}}^{\text{crit}}$ then the light will escape into the cladding (dashed line). The cladding is often wrapped in additional layers.

In the previous paragraph we considered an optical fibre which has an abrupt change in the refractive index at the core - cladding interface. More sophisticated designs have also been created where a gradual change in the refractive index allows the light to follow a curved trajectory within the core. Most step index dielectric fibres, like the one displayed in figure 11.1, are constructed with the same transverse structure. This comprises of a solid dielectric core that is in direct contact with a dielectric cladding, enclosed in a buffer/jacket which provides strength. The relative diameter of each of these layers can drastically change the properties of the fibre.

If the core radius is small, around $5 - 10\mu$m, the modes are only permitted to travel straight down the fibre rather than repeatedly bounce off the boundary. These single mode fibres are less prone to dispersion and are commonly used within the telecommunications sector as signals can be sent over very long distances. As previously mentioned, increasing the core diameter means more modes can evolve down the fibre simultaneously, where the number of supported modes is proportional to the square of the radius [138]. These multimode fibres have a core radius an order of magnitude larger than that of the single mode fibre and are commonly used in short devices which require multiple modes. One example is the endoscope, its low-cost wide aperture design allows doctors to easily visualise internal organs.

Fibres are constructed from a large cylinders of dielectric material, known as a preform, which is heated up and drawn out. The drawing process reduces the size of the preforms diameter by a factor of order $\mathcal{O}(10^4)$ and so many metres of optical fiber can be produced from one preform. One has to be careful not to introduce any defects in the drawing out process as these can diffract the light reducing the signal strength. Most commonly these preforms are made of doped silica but other materials include fluoride, phosphate and chalcogenide glasses.

Producing fibres from only dielectric materials means they are resistant to electrical interference, unlike the copper wire. They are however still prone to attenuation, the main causes of which are light scattering and absorption. Through improvements in composition and manufacturing the fibres are now achieving losses as low as 0.17 dB/km at 1550 nm [139]. Meaning optical signals can be sent over much longer distances without any significant loss. The fibre attenuation coefficient, α, is defined as

$$\alpha = -\frac{10}{z}\log_{10}\left(\frac{P(z)}{P(0)}\right), \tag{11.2}$$

where $P(z)$ is the power of the optical signal at the distance z in kilometres [138]. A fibre with an attenuation coefficient $\alpha = 0.17$dB/km retains 1/e of the original signal intensity at a distance of approximately 25km. In order to maintain a strong signal over long distances, repeaters are required. Repeaters convert the optical signal into an electrical one, amplify it and then transform it back into an optical signal.

Optical fibres also display nonlinearity. In some cases these nonlinear effects are beneficial as they allow one to study the properties of optical solitons [140]. The Kerr effect is an example of one such nonlinear effect observed in solid core fibres [141], a phenomenon in which the local refractive index of a material depends on the field intensity, I, via

$$n \approx n_0 + n_2 I. \tag{11.3}$$

For $n_2 > 0$ ($n_2 < 0$) the mode self-focuses (self-defocuses). As $n_0 \gg n_2$ (for fused silica: $n_0 \approx 1.453$, $n_2 \approx 3.2 \times 10^{-16}\text{cm}^2/\text{W}$ [142]) this effect can often be ignored in many optical devices. The nonlinear effects cannot be ignored in optical fibres as their effect can grow as a signal evolves [140]. Consider a Gaussian beam evolving down a fibre core; in accordance with equation 11.3 the radial intensity profile causes a small but finite change to the refractive index profile. In turn, this causes the beam to self-(de)focus. Above a critical power this can lead to a run away effect as the beam evolves down the fibre. The critical power is defined by

$$P_{\text{crit}} = \alpha_b \frac{\lambda^2}{4\pi n_0 n_2}, \tag{11.4}$$

where λ is the wavelength and α_b is a constant which is dependent on the input beam profile [143]. The Kerr effect, therefore, puts a limitation on both the maximum intensity of a signal and the distance it can be transmitted. Silica, for example, has a critical power of $P_{\text{crit}} \approx 2.8\text{MW}$. More sophisticated repeaters, then described above, exist which can both reshape and enhance a signal. Another optical application which can occur as a result of the Kerr effect is optical biastability, this is the ability to switch between two different optical states. This property is exploited in nonlinear Fabry-Perot interferometry [140].

11.2.3 Metallic Waveguides

The nonlinear effects discussed above occur due to the transmission of electromagnetic radiation through a dielectric medium. One could circumvent these effects by transmitting light through the vacuous core of a hollow metallic waveguide. For simplicity, we determine the transverse mode structure and associated dispersion relations of a cylindrical metallic waveguide where the walls of the guide to be comprised of a perfect conductor, following the methods of [131]. If these walls are not perfect, the field penetrates the conductor and causes resistive losses. This skin effect has an associated length scale which is dependent on the conductivity and frequency [131]. In order for there to be zero penetration, a node must exist in the radial profile of the field at the conductor surface and the field must also be perpendicular to the surface at the boundary.

Maxwells equations for a plane, monochromatic wave with frequency ω evolving down the empty core of a cylindrical metallic waveguide are

$$\nabla \times \mathbf{E} = \frac{\mathrm{i}\omega}{c}\mathbf{B}, \tag{11.5}$$

$$\nabla \times \mathbf{H} = -\frac{\mathrm{i}\omega}{c}\mathbf{D}, \tag{11.6}$$

$$\nabla \cdot \mathbf{D} = 0, \tag{11.7}$$

$$\nabla \cdot \mathbf{B} = 0. \tag{11.8}$$

The displacement field $\mathbf{D}$ is related to the electric field through the expression $\mathbf{D} = \epsilon\mathbf{E} = \epsilon_0(1+\chi)\mathbf{E} = \mathbf{E}$. As we are dealing with a vacuum containing zero charge and current density ($\rho = \mathbf{J} = 0$), the dielectric constant is just the free space value $\epsilon = \epsilon_0 = 1$, as the electric susceptibility $\chi = 0$. The magnetic field $\mathbf{H}$ is related to the magnetic induction via $\mathbf{H} = \mu\mathbf{B} = \mathbf{B}$ where $\mu = 1$ is the permeability. Taking the curl of the first of Maxwell's equations and applying equation 11.6 gives

$$\nabla \times (\nabla \times \mathbf{E}) = \frac{\mathrm{i}\omega}{c}\nabla \times \mathbf{B},$$

$$\nabla(\nabla \cdot \mathbf{E}) - \nabla^2\mathbf{E} = \frac{\omega^2}{c^2}\mathbf{E}. \tag{11.9}$$

Since $\epsilon = \mu = 1$ in our units, the speed of light $c = (\mu\epsilon)^{-\frac{1}{2}} = 1$. To simplify the analysis of the mode structure we assume the cross sectional area of the waveguide remains constant. Bends and rotations play an important role in the application of waveguides, we however omit them from consideration allowing us to assume a plane wave in the axial direction and $\mathbf{E}(r,\theta,z,t) = \mathbf{E}(r,\theta)\mathrm{e}^{\pm\mathrm{i}kz-\mathrm{i}\omega t}$. Utilising the

transversality constraint given in equation 11.7, one produces the two-dimensional wave equation

$$\left[\nabla_{\mathrm{t}}^2 + \left(\frac{\omega^2}{c^2} - k^2\right)\right] \begin{Bmatrix} \mathbf{E} \\ \mathbf{B} \end{Bmatrix} = 0, \tag{11.10}$$

where

$$\nabla_{\mathrm{t}}^2 = \frac{1}{\rho}\frac{\partial}{\partial\rho}\left(\rho\frac{\partial}{\partial\rho}\right) + \frac{1}{\rho^2}\frac{\partial^2}{\partial\theta^2}, \tag{11.11}$$

denotes the transverse components of the cylindrical Laplacian. An identical wave equation to equation 11.10 can be derived for the magnetic field [131]. We shall solve the wave equation, subject to the boundary conditions

$$\hat{\mathbf{n}} \times \mathbf{E} = 0 \qquad \hat{\mathbf{n}} \cdot \mathbf{B} = 0, \tag{11.12}$$

where $\hat{\mathbf{n}}$ is the unit normal, these are imposed by assuming a perfectly conducting metallic boundary. Solving the wave equation with these constraints allows us to not only find the mode structure but also the associated dispersion relation for the mode.

The modes of a metallic waveguide come in two distinct forms, depending on which component of the electromagnetic wave is transverse to the propagation axis. The mode can either have its magnetic field entirely in the transverse direction ($\mathrm{B}_z = 0$) with $\mathrm{E}_z(R) = 0$ at the cylinder's boundary, $\rho = R$. These modes are referred to as transverse Magnetic (TM). Alternatively, one could have a transverse electric (TE) mode with $\mathrm{E}_z = 0$ everywhere and $\partial_n \mathrm{B}_z = 0$ at $\rho = R$.

The boundary conditions mentioned above can be identified by writing the electric field in terms of the components parallel and transverse to the axis as $\mathbf{E} = \mathbf{E}_z + \mathbf{E}_t$. Similarly for the magnetic field and operator $\boldsymbol{\nabla} = \boldsymbol{\nabla}_\mathbf{t} + \hat{\mathbf{z}}\frac{\partial}{\partial z}$. From this, one can express the boundary conditions in the direction parallel to unit normal, $\hat{\mathbf{n}}$. Both the transverse electric and magnetic can be solved by considering the scalar potential ψ defined by

$$\mathbf{X}_t = \pm\frac{\mathrm{i}k}{\gamma^2}\nabla_t\psi, \tag{11.13}$$

where $\mathbf{X}$ denotes either $\mathbf{E}$ or $\mathbf{B}$ for transverse magnetic or electric fields respectively and $\gamma^2 = \frac{\omega^2}{c^2} - k^2$. One arrives at equation 11.13 by substituting the separated components of the field and the operator, discussed above, into Maxwell's equations and simultaneously solving for $\mathbf{B}_t$ ($\mathbf{E}_t$). Finally, by setting E_z (B_z) to zero one arrives at equation 11.13 where $\psi = \mathrm{B}_z$ (E_z) is the transverse electric (magnetic) mode. As such, the associated boundary condition is now $\partial_n\psi = 0$ ($\psi = 0$) at $\rho = R$.

Note there is no solution to the wave equation for both a transverse electric and magnetic field (TEM) as the boundary conditions would imply zero field everywhere. A TEM mode is, however, possible when considering a coaxial cable [131]. We shall now consider a transverse electric mode ($\mathrm{E}_z = 0$) and as we are dealing with a cylindrical waveguide, we change to a more natural coordinate system. Applying the separation of variables $\mathrm{B}_z(\rho, \phi) = \xi(\rho)\Phi(\phi)$ to the cylindrical wave equation 11.10 gives

$$\frac{\rho^2}{\xi}\frac{\partial^2\xi}{\partial\rho^2} + \frac{\rho}{\xi}\frac{\partial\xi}{\partial\rho} + \rho^2\gamma^2 = -\frac{1}{\Phi}\frac{\partial^2\Phi}{\partial\phi^2}. \tag{11.14}$$

As each side of equation 11.14 depends only on one variable, both must equal the same constant, which we define to be P^2. This allows us to solve for both the radial $\xi(\rho)$ and azimuthal $\Phi(\phi)$ solutions independently. One can read off that the angular dependence of the mode is given by

$$\Phi(\phi) = A\cos(P\phi) + B\sin(P\phi). \tag{11.15}$$

As the mode cannot be multivalued upon complete rotations about the axis, the constant $P = m$ where m be an integer. The remaining expression for the radial profile is given by

$$\rho^2\frac{\partial^2\xi}{\partial\rho^2} + \rho\frac{\partial\xi}{\partial\rho} + \left(\rho^2\gamma^2 - P^2\right)\xi = 0. \tag{11.16}$$

This is the Bessel equation, an equation which arises in many different fields of physics including the interaction of superconducting vortices [5] and patterns in acoustical radiation [144]. Equation 11.16 is satisfied by the Bessel function of the first kind $\xi(\rho) = \mathrm{J}_P(\gamma\rho)$. The boundary condition for the transverse electric mode is $\partial_n\psi = 0$, i.e. the first derivative of the mode in the direction normal to the surface must be zero at $\rho = R$. For a perfect cylinder the surface normal is in the radial direction, $\hat{\mathbf{n}} = -\hat{\boldsymbol{\rho}}$ as such the boundary condition is satisfied by

$$-\partial_\rho\xi(\rho) = \frac{\gamma}{2}\left[\mathrm{J}_{P+1}(\gamma\rho) - \mathrm{J}_{P-1}(\gamma\rho)\right] = 0. \tag{11.17}$$

The values of ρ which satisfy equation 11.17 are well documented in [84]. We denote the radial locations at which the nth derivative of the P^{th} order Bessel function is

equal to zero by

$$\rho'_{P,n} = \gamma R = \sqrt{\frac{\omega^2}{c^2} - k^2} R. \tag{11.18}$$

We include a prime in the symbol to emphasise that it is the zero of the first derivative. If instead we were solving for the TM modes, we would determine the locations the function itself equaled zero, denoted by $\rho_{P,n}$. Rearranging equation 11.18 for k gives

$$\begin{aligned} k^2 &= \left(\frac{\omega}{c}\right)^2 - \left(\frac{\rho'_{P,n}}{R}\right)^2, \\ \rightarrow k &= \frac{1}{c}\sqrt{\omega^2 - \omega_c^2}. \end{aligned} \tag{11.19}$$

Here we can see the frequency of the incident radiation, ω, has a minimum value for propagation, below which the wavevector, k, is purely imaginary and the field is evanescent. Alternatively, we can express this in terms of wavelengths

$$\frac{1}{\lambda^2} = \frac{1}{\lambda_0^2} - \frac{1}{\lambda_c^2}. \tag{11.20}$$

Where λ is the guided wavelength, λ_0 is the free space wavelength of the incident radiation. The maximum wavelength, λ_c, which can be guided down a hollow metallic waveguide is directly dependent on the dimensions of the guide as

$$\lambda_c = \frac{2\pi R}{\rho'_{P,n}}. \tag{11.21}$$

One can also rearrange equation 11.19 to consider $\omega(k)$, a schematic plot of equation 11.19 for the $P = 0$ modes is given in figure 11.2, whilst other modes are possible they are not considered in this thesis. We have established that there is a minimum frequency for a given mode which depends on both the cylinders radius R, as well as the choice of P and n. As the frequency increases more modes become available and the spacing between modes decreases. The mode with the lowest cut-off frequency is called the dominant mode, this is commonly the $\mathrm{TE}_{0,1}$ mode.

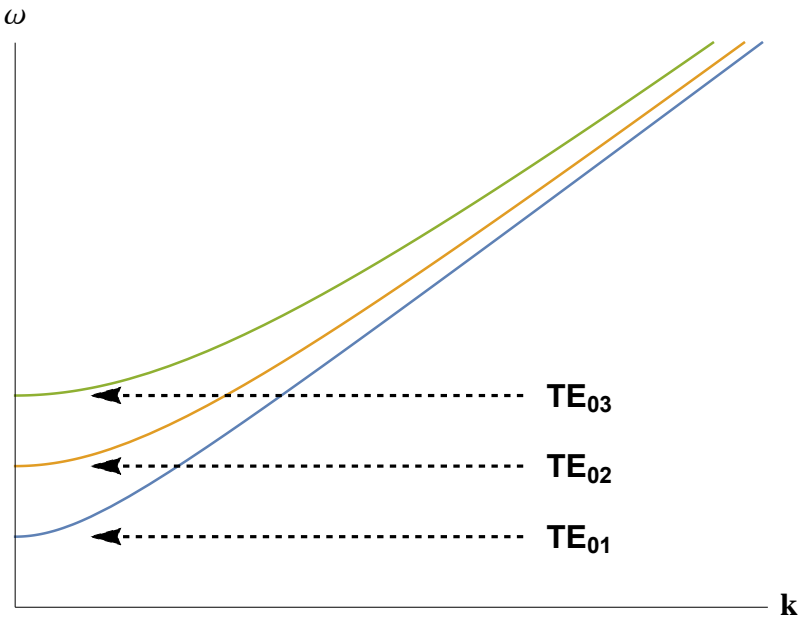

Figure 11.2: Dispersion relations for the three lowest TE_{0n} mode. As the frequency increase the distance between modes decreases.

The transverse electric modes of the cylindrical metallic waveguide are denoted by $\mathrm{TE}_{P,n}$ and have an axial magnetic field given by

$$\mathrm{B}_z = \left[A\cos\left(P\phi\right) + B\sin\left(P\phi\right)\right]\mathrm{J}_P\left(\gamma\rho\right). \tag{11.22}$$

In order to find the transverse profile of the electric field we define

$$\mathbf{E}(\rho,\phi) = \mathrm{E}_\rho(\rho,\phi)\hat{\boldsymbol{\rho}} + \mathrm{E}_\phi(\rho,\phi)\hat{\boldsymbol{\phi}} + \mathrm{E}_z(\rho,\phi)\hat{\boldsymbol{z}}, \tag{11.23}$$

and similarly for the magnetic field. We substitute the decomposed form of the electric and magnetic field back into equations 11.5 and 11.6. As both of these are vector equations, we obtain six equations by comparing components. These can then be solved simultaneously to express each component in terms of E_z and B_z as listed below.

$$\mathrm{E}_\rho = \frac{\mathrm{i}}{\gamma^2}\left(\frac{\omega}{\rho}\partial_\phi \mathrm{B}_z - k\partial_\rho \mathrm{E}_z\right), \tag{11.24}$$

$$\mathrm{E}_\phi = \frac{\mathrm{i}}{\gamma^2}\left(\frac{k}{\rho}\partial_\phi \mathrm{E}_z - \omega\partial_\rho \mathrm{B}_z\right), \tag{11.25}$$

$$\mathrm{B}_\rho = \frac{\mathrm{i}}{\gamma^2}\left(\frac{\omega}{c^2}\frac{1}{\rho}\partial_\phi \mathrm{E}_z - k\partial_\rho \mathrm{B}_z\right), \tag{11.26}$$

$$\mathrm{B}_\phi = \frac{\mathrm{i}}{\gamma^2}\left(\frac{k}{\rho}\partial_\phi \mathrm{B}_z + \frac{\omega}{c^2}\partial_\rho \mathrm{E}_z\right). \tag{11.27}$$

These equations can be applied to both transverse electric and magnetic modes. For the TE modes, $\mathrm{E}_z = 0$ and B_z as defined in equation 13.15 thus

$$\mathrm{E}_\rho = \frac{\mathrm{i}\omega P}{\gamma^2\rho}\left[-A\sin(P\phi) + B\cos(P\phi)\right]\mathrm{J}_P(\gamma\rho), \tag{11.28}$$

$$\mathrm{E}_\phi = -\frac{\mathrm{i}\omega}{2\gamma}\left[A\sin(P\phi) + B\cos(P\phi)\right]\left[\mathrm{J}_{P-1}(\gamma\rho) + \mathrm{J}_{P+1}(\gamma\rho)\right], \tag{11.29}$$

$$\mathrm{B}_\rho = -\frac{\mathrm{i}k}{2\gamma}\left[A\sin(P\phi) + B\cos(P\phi)\right]\left[\mathrm{J}_{P-1}(\gamma\rho) + \mathrm{J}_{P+1}(\gamma\rho)\right], \tag{11.30}$$

$$\mathrm{B}_\phi = \frac{\mathrm{i}\omega P}{\gamma^2\rho}\left[-A\sin(P\phi) + B\cos(P\phi)\right]\mathrm{J}_P(\gamma\rho). \tag{11.31}$$

Thus far, we have maintained a general form of the TE mode. We now consider the lowest order modes $\mathrm{TE}_{0,n}$ which have no azimuthal dependence and are given by

$$\mathrm{E}_\rho = 0 \qquad \mathrm{E}_\phi = -\frac{\mathrm{i}\omega}{2\gamma}\mathrm{J}_1(\gamma\rho)\,. \tag{11.32}$$

The factor of i is associated with a $\frac{\pi}{2}$ phase difference between E_ϕ and B_ϕ. A plot of the radial dependence the transverse electric modes is given below, see figure 11.3. The $\mathrm{TE}_{0,n}$ modes have a ring like structure with a node at the boundary. While other, more complex modes exist, we shall not discuss such modes in this thesis as we only require the $\mathrm{TE}_{0,n}$ mode.

As previously mentioned, the field does penetrate the metallic walls of the guide for finite conductivity, especially at high frequencies. The field exponentially decays into the metal over the length known as the skin depth δ_s, typically of the order of a few micrometers within a good conductor like copper. The wavelength of high frequency microwave radiation, however, is of the order of millimetres. As $\lambda_{\mathrm{Cu}} \gg \delta_s$, the assumption of perfect conductivity is appropriate.

Figure 11.3 shows the radial intensity of the first three $\mathrm{TE}_{0,n}$ modes as a function of ρ. The boundary conditions, discussed earlier, imply the function must have a node at $\rho = R$. With each higher order mode, another node is present between $0 < \rho < R$. The maximum amplitude of each mode appears closer to $\rho = 0$ for higher order modes. The cross-sectional profile of each of these modes is produced by revolving this function by 2π about the z-axis, as seen in figure 11.4.

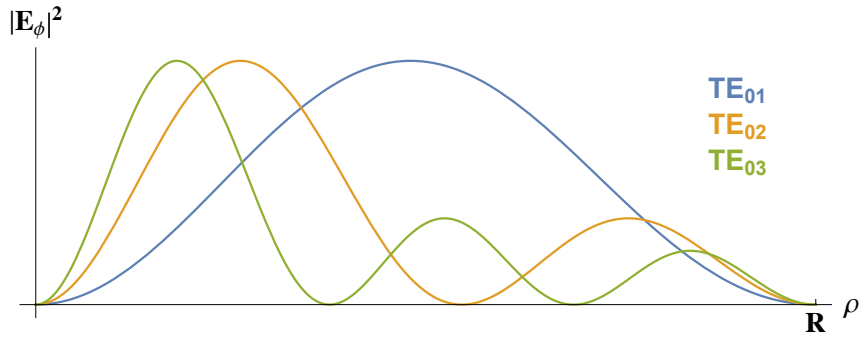

Figure 11.3: Radial intensity profile, $|E_\phi|^2$, for the first three TE_{0n} modes as a function of radii for a perfect metallic waveguide. Each higher order mode has one more node, the associated cross-sectional area is displayed in figure 11.4.

In this section on hollow metallic waveguides, we discussed the benefits of guiding light, derived the modal profile for a perfect cylindrical conductor and introduced the cut-off frequency below which the mode is evanescent. We also mentioned the resistive losses which arise when the conductivity is finite, it is this skin effect which limits the use of metallic waveguides in telecommunications.

As the amount of data being transmitted increases, shorter length pulses are required to increase the density of transmitted information. The losses due to field penetration into the conductor increases with frequency and, as such, the guiding of radiation is limited to the microwave range. For high frequency transmission an alternative guide is required, one such example is the photonic crystal fibre.

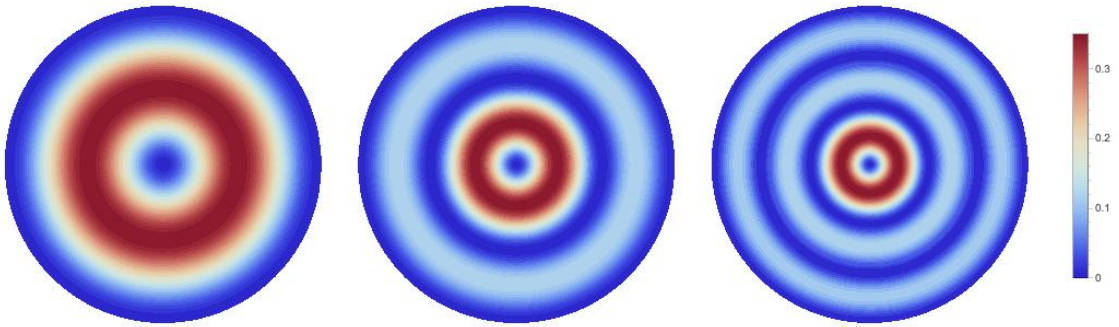

Figure 11.4: Cross sectional profile of the first three TE_{0n} modes of a perfect metallic waveguide respectively. Each higher order mode has one more node, as seen in figure 11.3.

11.3 Photonic Crystal Fibres

11.3.1 Overview

In section 11.2 we discussed two different methods of guiding light. We considered a straight cylindrical guide both for the solid core dielectric fibre and the hollow metallic waveguide and discussed the mechanisms by which they localise light. The dielectric fibre can transport a wide range of frequencies down its solid core but due to the inherent nonlinearities there is a limit on the light intensity. Guiding light down the vacuous core of a metallic guide alleviates these concerns. There is, however, a limit on the frequency which can be efficiently guided due to the skin effect.

Combining the useful features of each guiding method, we now consider a hollow core dielectric fibre and discuss how such a device could guide light. In section 11.2.2, we explained why $n_{\text{core}} > n_{\text{clad}}$ is required for dielectric guiding. As $n_{\text{core}} < n_{\text{clad}}$ for hollow-core PCFs, the light must be confined by a new mechanism. In this section we give a brief overview of photonic crystal fibres, discussing their proposal, design and production. We then consider a simple one dimensional photonic crystal which can be used to explain how the two dimensional fibre works.

Unlike solid core fibres which confine light via total internal reflection, photonic crystal fibres employ a periodic dielectric function to confine light via a band gap. This concept was first proposed by Yeh and Yariv in 1976 [9]. They originally considered a one dimensional slab of stratified dielectric medium, see figure 11.5. By considering both a semi and fully infinite periodic dielectric, they analysed both surface and bulk modes respectively. Although Yeh and Yariv were not the first to

propose a stratified dielectric medium [145], they were the first to realise the possibility of confining light within a region of lower refractive index.

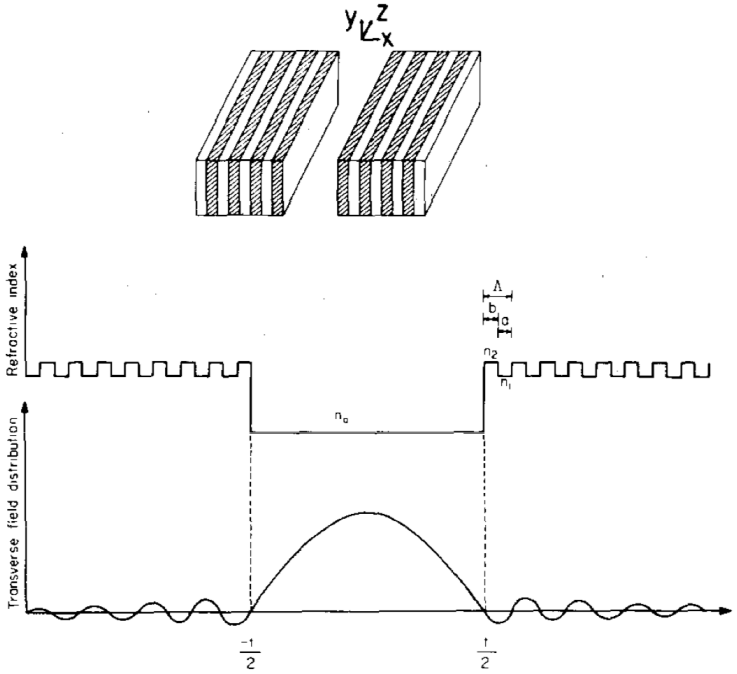

Figure 11.5: Starting from the top, the figure includes the waveguide design, dielectric profile and transverse field distribution of the fundamental mode of a typical Bragg reflection waveguide with $n_a, = 1.0,\ n_z = 3.38,\ n_l = 2.89$. Figure taken from [9].

As we shall later discuss, the mode is evanescent within the stratified dielectric medium and so remains primarily localised within the air region. Shortly after publishing their analysis of the 1D slab guide, Yeh, Yariv and Marom realised a 2D trap could be created by forming a cylinder from periodic layers of dielectric material [126]. They coined this design the Bragg cylinder/fibre due to its similarities with the Bragg reflector, a schematic example is given in figure 11.6a.

Yeh et al. also discussed how the Bragg fibre, much like the metallic waveguide, can be designed to support only a single mode within its core. This reduces the broadening of a light signal from modal dispersion, an effect brought on by the phase

velocity dispersion of modes within the fibre. Using the transfer matrix method at each interface, Yeh *et al.* were able to deduce the electric field amplitude for the TE_{01} mode. They found that the amplitude decayed by an amount proportional to the refractive index ratio through each cladding pair.

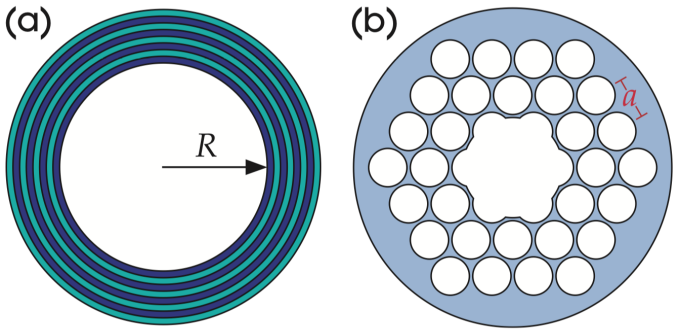

Figure 11.6: a) Schematic diagram of the Bragg fibre, similar to the one used by Yeh, Yariv and Marom. The hollow core is surrounded by concentric rings of high and low dielectric material. b) An alternative form of photonic crystal fibre which is made of one dielectric material with a two dimensional periodic array of holes, known as holey fibres. This figure is taken directly from [10]

The one dimensional periodic Bragg fibre is not the only possibility, as seen in figure 11.6b one can also confine light using a two dimensional array of holes within a dielectric medium. A wide range of fabricated lattice structures allows one to tailor the functionality of the fibre to the specific requirements [146]. Varying the radius and separation of the surrounding holes alters the confined frequency range.

Both the Bragg and holey fibre rely on band gaps opening within the dispersion relation, the mechanisms is discussed in section 11.3.2. The Bragg fibre offers stronger confinement of light than the holey fibre, requiring only roughly 10 layers of cladding pairs [10]. It is also less prone to surface modes at the core-cladding interface. The holey fibre, however, is more commonly used as it is simpler to construct.

PCFs are constructed in a similar way to solid core fibres. A preform is heated up and drawn out into a long thin strand. The two dimension fibre shown in figure 11.6b is formed by first fusing a collection of individual hollow core preforms. This collection is then drawn out producing the fibre. The Bragg fibre requires a preform with concentric layers, the difficulty is in finding materials with both a large contrast in their refractive index and compatible thermal properties.

A Bragg fibre was first produced by Temelkuran et al in 2002 [147] using layers of a low index polymer (PES, $n \approx 1.55$) and a high index chalcogenide glass (As_2Se_3, $n \approx 2.8$). The fibre was produced by rolling a flat periodic slab into a hollow cylinder and drawing it to the desired layer thickness, which was roughly 900nm of PES and 270nm of As_2Se_3 with two half layers of glass either side to reduce surface modes. Fink *et al.* [148] found that the attenuation of the Bragg fibre was roughly 1.0dB/m which is significantly lower than the materials comprising it (7-10dB/m for As_2Se_3 and 100000dB/m for PES). The large difference justifies how well the light is confined to the core. Fink *et al.* also displayed omni-directionality, reflecting light from all incident angles, as well as transmitting through curved PCFs.

Due to the strong confinement and low attenuation, one could fill the core with a medium and study nonlinear effects. Which we shall discuss this, in the context of transporting matter, presently. In our investigation, we consider a Bragg fibre as it is most convenient for calculations due to the symmetry and tight confinement. We have identified that the intense confinement is due to the periodic design of the fibre, to understand how this works in greater detail we shall now consider a one dimensional photonic crystal. We develop this one dimensional crystal into the slab considered by Yeh and Yariv, introducing all new concepts along the way. This will introduce all the key concepts and ideas needed to describe the Bragg fibre.

11.3.2 One Dimensional Crystal

As previously mentioned, the photonic crystal fibre uses an underlying periodicity to confine light. To understand this concept more, we consider an infinite one dimensional photonic crystal - constructed by layering infinite sheets of alternating dielectric media.

First we present the physics of on-axis propagation, where light travels at normal incidence to the dielectric interface. We introduce the concept of band gaps, how they can be manipulated and the existence of evanescent modes within the gaps. We then discuss how the band gaps change when the wavevector has a component parallel to the interface, for both a finite and infinite photonic crystal.

For the purpose of our study, we require light to be confined to the air core of a Bragg fibre. As such we discuss how modes are localised within either the crystal or the air. We then go onto briefly discuss loss mechanisms and the structure of the Bragg fibre modes, for an in-depth account of the loss mechanisms see [10].

On-Axis Propagation

Taking advantage of the periodic geometry, we write the mode in Bloch form. For now we assume that the crystal has discrete periodicity along the z-axis, with period a, and homogeneous in the xy plane. The wavevectors describe how the field transforms under translation, as the crystal is homogeneous in the horizontal plane the associated wavevector, $\mathbf{k}_{\|}$, can take any value. The periodicity in z means there is a discrete translation symmetry, we can therefore restrict the range of the wave vector in this direction: $-\frac{\pi}{a} < k_z \leq \frac{\pi}{a}$. This region is defined as the Brillouin zone.

The mode is, therefore, given by

$$\mathbf{B}_{n,\mathbf{k}_\parallel,k_z}(\mathbf{r}) = \mathrm{e}^{\mathrm{i}\mathbf{k}_\parallel\cdot\boldsymbol{\rho}}\mathrm{e}^{\mathrm{i}k_z z}\mathbf{u}_{n,\mathbf{k}_\parallel,k_z}(z), \tag{11.33}$$

where $\boldsymbol{\rho}$ is the transverse component of $\mathbf{r}$ and the spatial profile is defined by $\mathbf{u}_{n,\mathbf{k}_\parallel,k_z}(z) = \mathbf{u}_{n,\mathbf{k}_\parallel,k_z}(z+a)$. For on-axis propagation $\mathbf{k}_\parallel = 0$, as such, the magnitude of the total wavevector $|\mathbf{k}| = \sqrt{k_\parallel^2 + k_z^2} = k_z$.

The discrete translational symmetry imposes restrictions on the structure of the modes. A translation by an integer number of dielectric periods must return the same field intensity. The nodes of the field must, therefore, be located in either the high or low dielectric region, not both. As such gaps open in the dispersion, within these gaps exists a range of forbidden frequencies. The band upon which mode is situated, shown by the blue lines in figure 11.7, is referred to as the band number n as seen in equation 11.33

A photonic band gap opens as soon as there is a periodic variation in the dielectric, $\Delta\epsilon$. As the frequencies scale with crystal size, the size of the band gap, $\Delta\omega$, is more commonly defined with respect the midgap frequency, ω_m, found to be

$$\frac{\Delta\omega}{\omega_m} \approx \frac{\Delta\epsilon}{\epsilon}\cdot\frac{\sin(\pi d/a)}{\pi}, \tag{11.34}$$

where d is the thickness of the higher dielectric material, the gap-midgap ratio is given as a percentage [10]. One consequence for the band gap is the difference in where the field is most concentrated. If we consider just the first band gap in figure 11.7, the lower (upper) band is concentrated in the high (low) dielectric region.

Modes with frequencies within the gap may exist but they are evanescent and decay spatially at an exponential rate depending on how far into the gap the frequency is. The decay rate is maximal in the middle of the gap and reduces as one approaches a band. One can also vary the decay rate by optimising the relative thickness of each layer, the optimum design is very close to quarter wave thickness [10].

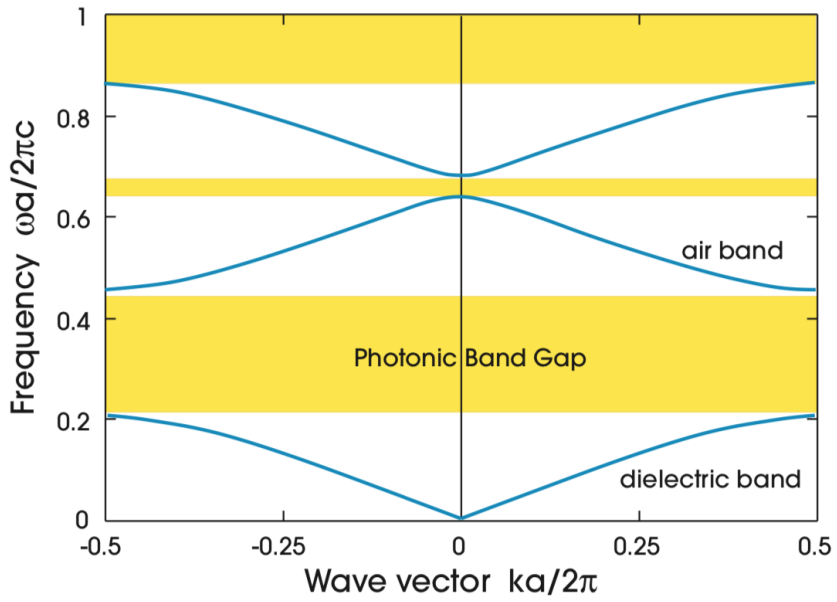

Figure 11.7: Dispersion relations for "on axis" propagation. The dispersion bands are shown in blue and the regions with no allowed modes (band gaps) are highlighted in yellow. This figure is taken directly from [10].

A typical plot of the dispersion relation for on-axis propagation in a dielectric crystal is displayed in figure 11.7, the width of the gap is always minimal/maximal at either at $k = 0$ or at the zone boundary $k = \frac{\pi}{a}$ with the first band gap often being the largest. At both of these points, each dispersion curve has zero gradient.

Off-Axis Propagation

We now consider off-axis propagation, in which the field has a component parallel to the dielectric interface, $\mathbf{k}_{\parallel} \neq 0$. One consequence of off-axis propagation is the removal of mode degeneracy, now either the electric (TE) or magnetic (TM) field is transverse to the direction of propagation, but not both. As stated above, the crystal is homogeneous in the xy plane, as such all wavevectors are permitted and there is no longer a band gap.

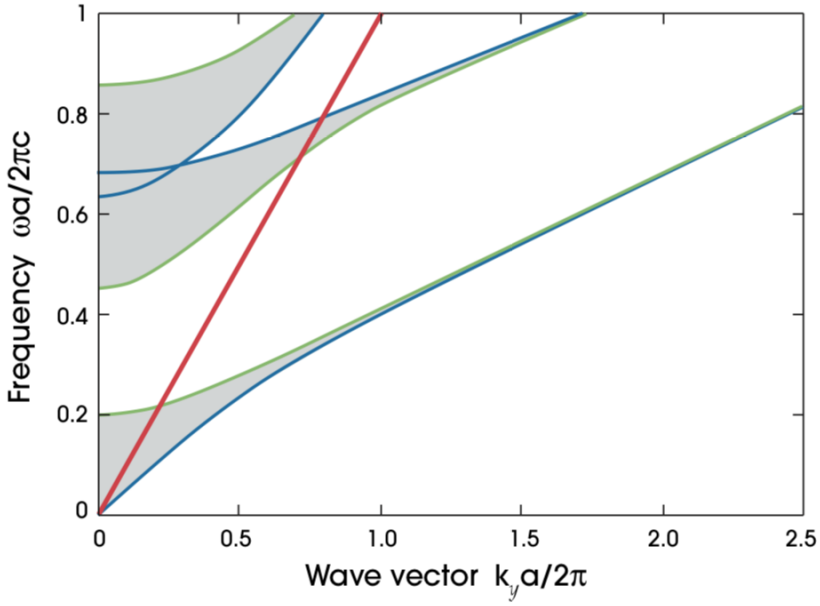

Figure 11.8: Projected dispersion relation for "off axis" propagation for a TE field. The blue (green) line refer to propagation with $k_z = 0$ ($k_z = \frac{\pi}{a}$). The grey regions in between the blue/green lines indicate where "on axis" modes exist. The red line is the light line $\omega = ck_y$ above which light may propagate in free space. This figure is taken directly from [10]

We have seen above that for on-axis propagation $(k_x, k_y, k_z) = (0, 0, k_z)$, band gaps open in the dispersion for any periodic dielectric. The dispersion relation for on-axis propagation is reduced to $0 \leq k_z \leq \frac{\pi}{a}$ due to the periodicity. Propagating in the direction perpendicular to the periodicity $(k_x, k_y, k_z) = (0, k_y, 0)$, the homogeneity implies no band gaps in the dispersion. It is, therefore, natural to enquire how the system transitions between these two limits.

Figure 11.8 is referred to as the projected band structure. In short, this depicts a condensed version of the on-axis dispersion relation as a function of off-axis wavevector, here $|\mathbf{k}_{\parallel}| = k_y$. To understand the projected band structure, compare the locations of the band gaps and modes in figure 11.7 to the regions at $k_y = 0$ in figure 11.8. The green and blue lines in figure 11.8 mark the locations of the points $(0, k_y, 0)$ and $(0, k_y, \frac{\pi}{a})$ in the on-axis profile respectively, the end points of each band.

The grey regions in figure 11.8 mark the regions where on-axis propagation is permitted for a given k_y. As the off-axis component k_y grows, the size of the photonic band gap in the perpendicular propagation reduces until it ceases to exist. The band gap, therefore, completely disappears as one introduces an off-axis term as a propagating k_y can be found at any frequency.

If, however, the one dimensional crystal is instead finite in the xy plane and semi-infinite in z, then the propagation is dependent on the modes position with respect to the light line $\omega = ck_y$, shown in red in figure 11.8. In free space, far away from the crystal the plane waves must obey $\omega = c\sqrt{k_y^2 + k_z^2}$. At a given k_y, a free space mode exists for any frequency above or on the light line. Below the light line requires an evanescent mode with an imaginary k_z component.

Frequencies above the light line within the grey regions are permitted to propagate in the both the crystal and free space, whilst those frequencies found within the gap are forbidden to propagate through the crystal. Below the light line, light may propagate within the crystal for modes within the grey regions but cannot extend into free space. Modes in a band gap below the light line are evanescent everywhere. Utilising the band gap above the light line, Yeh and Yariv confined light between two semi-infinite 1D crystals, as displayed in figure 11.5.

Defect Modes

Defects can come in many forms, any region in which the translational symmetry is broken is a defect. For example, slabs of different thickness or refractive index can be defects in a one dimensional crystal. These defects can exist either within the bulk of the crystal or at the surface. Modes within a band gap are evanescent in the periodic crystal, the only way a mode within the gap can propagate is if localised to a defect. To reduce the impact of surface modes, the interior layer of Bragg fibres is often half the thickness [126]. Optimising the structure of a holey fibre is much more difficult as many defected surface modes may exist [149].

The thickness and index of the defected layer determines the modes which can be localised by it. We have previously mentioned that the decay rate of an evanescent mode is maximal at the midpoint of a band gap, designing a defect which supports a mid-gap mode ensures a tight confinement. Increasing the thickness of the defect can also increase the number of supported modes, much like how a wider metallic waveguide could be used as a single or multimode guide. The hollow-core in Yeh and Yariv's waveguide could be considered as a defect within an infinite crystal.

Omnidirectional Mirror

Yeh, Yariv and Marom realised that forming cylinder of concentric layers would create defect modes and confine light to the core. The first experimental realisation of the Bragg fibre was by Temelkuran *et al.* in 2002, they constructed it by rolling a flat one dimensional Bragg mirror into shape. The defect mode is localised to the fibre core if it exists above the light line and within the one dimensional band gap, green region in figure 11.9. Within the blue region, the fibre acts as an omni-directional mirror [148].

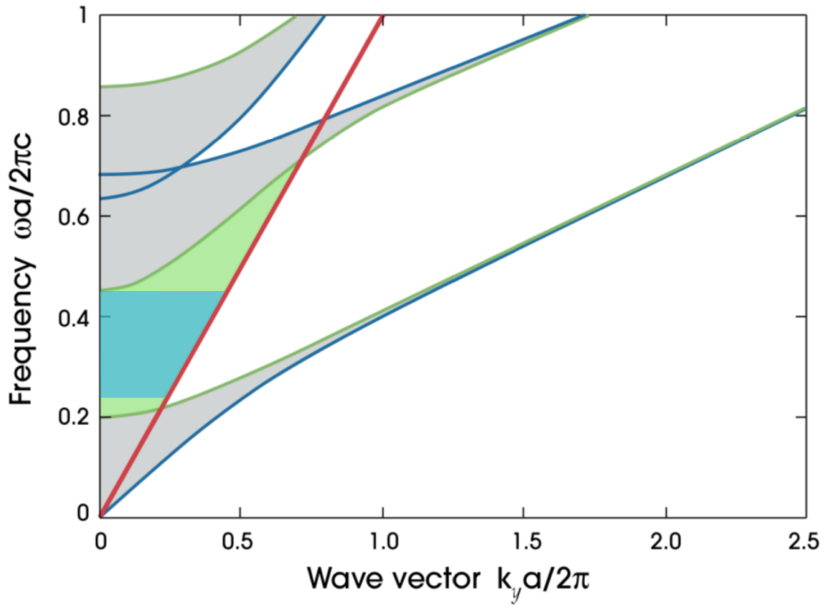

Figure 11.9: Schematic representation of the projected band structure for both the Bragg fibre. The green region highlights where defect modes can be localised within the core. For modes within the blue region, the fibre acts as an omni-directional mirror. Figure adapted from [10].

In the discussion of the 1D crystal above, we assumed that the perfectly flat and homogeneous in the xy plane. For the Bragg fibre this assumption is no longer true. To justify the confinement, the light must not escape to infinity. As the radii increases, the curvature decreases and the fibre walls tend to the one dimensional limit. We are justified in approximating the band diagram using the 1D solution.

Ibanescu *et al.* recognised the similarities between the omnidirectional Bragg fibre and the hollow core metallic waveguide [125]. They found that both guides, which localise light in the hollow core, have similar modes and dispersion relations. The magnetic (electric) field in the TE (TM) modes of a metallic waveguide must remain in the axial direction. The equivalent modes of a Bragg fibre, however, the non transverse field can point in any direction. For this reason Bragg fibre modes are commonly denoted by the lower case letters te and tm.

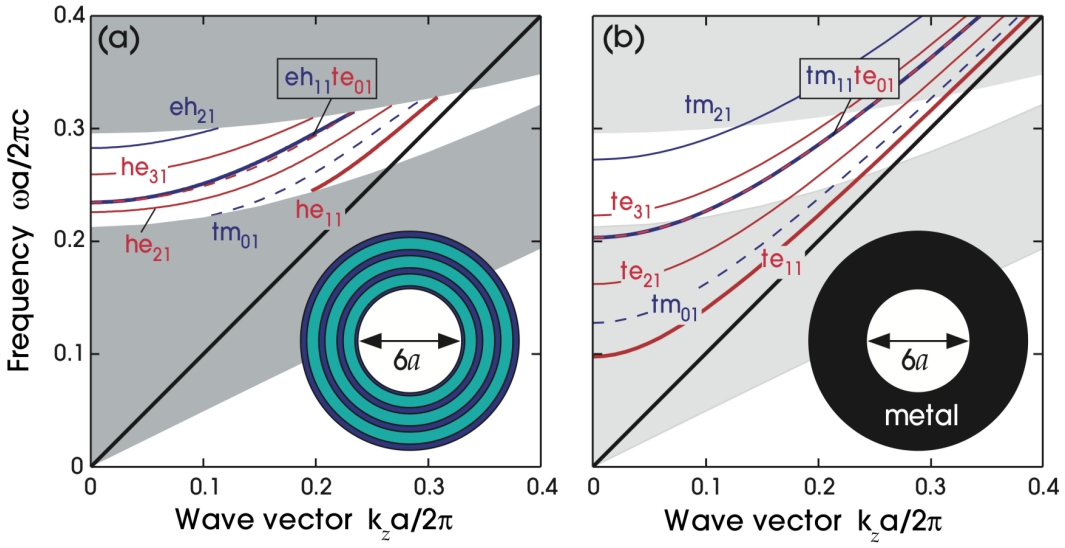

Figure 11.10: Band diagram for both the Bragg fibre and hollow core metallic waveguide. Figure taken directly from [10]. The modes are labeled as *te* for transverse electric, *tm* for transverse magnetic or *he*/*eh* for a hybrid mode. The grey region in figure (b) are the allowed modes of the Bragg fibre included for comparison.

The core radius of a Bragg fibre governs both the cut-off position of each mode and the dominant cause of losses in the fibre. We have already mentioned that the combination of a hollow core and all dielectric materials may reduce the loss rates when compared to the metallic waveguide and solid core optical fibre, but that does not mean losses are completely removed. For small core radius, the primary cause of signal loss is due to field penetrating the fibre walls. As the core radius increases, the impact of the fibre walls is reduced and more modes exist within the band gap. The dominant loss mechanism within large core fibres then becomes inter-modal coupling. Optimising the core radius to reduce losses is therefore imperative.

The hollow core enclosed by a dielectric material should permit higher intensities that the solid-core dielectric fibre as well as higher frequencies that hollow metallic waveguides. These, however, are not the only benefits of the hollow core photonic crystal fibre. One can also guide atoms and molecules down the hollow core as we shall now discuss.

11.4 Transport in Fibres

Electromagnetic radiation is a very versatile tool when it comes to manipulating matter. For example, one can use the Doppler effect to heat a sample up or cool it down [134]. Most importantly for our purposes, electromagnetic radiation can be used to trap and guide atoms. These traps can be designed in a whole host of ways, one can tightly confine atoms within a small region to increase the atomic density. This can be achieved via an all optical trap such as in optical molasses or an MOT which uses a combination of optical and magnetic fields. Alternatively the interference pattern from a collection lasers can create a tuneable optical lattice to provide a periodic potential landscape [111].

In this section we provide a historical overview of light-matter guidance within waveguides, we first motivate this work by mentioning some of the advantages over free space guiding. Despite some experimental groups opting to use a combination of guiding techniques, the primary method of localising matter remains unchanged. Therefore, before we discuss the evolution of transportation we describe the mechanism by which light can trap and guide matter.

Advances in understanding and technology have lead to a vast improvement in the efficiency of atomic transport, one is now able to transport higher yields over longer distances. When these same techniques are applied to transporting cold atoms, the same success is not repeated. We conclude this section by reviewing the experimental literature on cold atom transport in hollow optical fibres, motivating an alternative approach to be discovered.

Advantages of Waveguide Transport

Free space traps have proven to be an invaluable tool [150], it does however have its limitations. The dispersion and attenuation of light in free space significantly limits its use in atomic transport. The trapped state may also be short lived due to interaction with the environment, this can be particularly troubling when creating an extremely cold state such as a BEC.

The above limitations can be overcome by transporting atoms within the confines of a waveguide, PCFs can significantly reduce a signals attenuation and isolate from the environment. Selectivity in the loading process also allows one to transport a sample from a poor vacuum to a better one. One can transport along a variable trajectory, a task which is cumbersome in free space, and monitor by exposing a section of the guide permitting certain frequencies to propagate through the walls.

Alternatively, instead of transporting to a new environment one can perform experiments within the guide itself. V. Venkataraman *et al.* used the hollow core of a holey fibre to investigate low intensity nonlinear phenomena. D. S. Bykov *et al.* have constructed a multi-purpose sensor from light-matter interactions within a PCF. It is possible to use the narrow core to investigate strongly 1D systems [151–155].

Detuned Guiding

Lasers are an essential tool for trapping atoms, especially when other methods, such as magnetic fields, cannot be used. When studying BEC, one may need to alter the scattering length of the atoms. This can be achieved using Feshbach resonances, for this one needs to be able to vary the magnetic field. A common, all-optical, method employed to localise atoms is the dipole gradient force. This technique utilises the

variety of spacings in the energy levels of the atom, the frequency can be chosen to excite a transition between two specific levels. These levels are labelled to be the ground state $|g\rangle$ and the excited state $|e\rangle$ with associated energies E_g and E_e respectively. The electric dipole interaction potential is given by

$$V(\boldsymbol{r},t) = -\boldsymbol{d}\cdot\mathbf{E}(\boldsymbol{r},t), \tag{11.35}$$

where $\boldsymbol{d}$ is the electric dipole moment and $\mathbf{E}(\boldsymbol{r},t)$ is the electric field at $\boldsymbol{r}$. Using second order perturbation theory, it was shown that the change in the ground state energy ΔE_g

$$V(\boldsymbol{r}) = -\frac{1}{2}\alpha(\omega)\langle E(\boldsymbol{r},t)^2\rangle_t, \tag{11.36}$$

where $\langle E(\boldsymbol{r},t)^2\rangle_t$ denotes the time average of the field intensity and $\alpha(\omega)$ is the atomic polarisability given by

$$\alpha(\omega) \approx \frac{|\langle e|\boldsymbol{d}\cdot\hat{\boldsymbol{\varepsilon}}|g\rangle|^2}{\hbar(\omega_{eg}-\omega)}, \tag{11.37}$$

where $\hat{\boldsymbol{\varepsilon}}$ is the unit vector in the direction of the electric field and $\omega_{eg} = (E_e - E_g)/\hbar$ [156]. The difference in the incident and natural frequencies is known as the detuning $\delta = \omega - \omega_{eg}$. Also in equation 11.37 is the Rabi frequency $\Omega_{\mathrm{R}} = |\langle e|\boldsymbol{d}\cdot\mathbf{E}|g\rangle|/\hbar$ which quantifies the frequency in population changes in the ground and excited state. The force experienced on the atom by the potential $V(\boldsymbol{r})$ is given by the dipole force

$$\mathbf{F}_{\mathrm{dipole}} = -\boldsymbol{\nabla}V(\boldsymbol{r}) = \frac{1}{2}\alpha(\omega)\boldsymbol{\nabla}\langle E(\boldsymbol{r},t)^2\rangle_t. \tag{11.38}$$

From equation 11.38, one can identify that the force an atom will experience with respect to the potential landscape depends on the exact nature of the detuning parameter δ. If δ is positive (negative) then the atom will be repelled (attracted) to regions of high field intensity, this is referred to as blue (red) detuned guiding.

We now provide a historical timeline of the experimental literature. Starting with the initial proposal and experiments, then reviewing how the guiding capabilities improved with advancements in technology. We conclude with an overview of the limited success in guiding cold atoms.

11.4.1 Transport in Fibres

Using inhomogeneous radiation to collimate and guide beams of atoms dates back to the early 1970s, A. Ashkin was the first to use radiation pressure from focused visible light to accelerate freely suspended particles [157]. Early experiments used either an array of mirrors [158] or an axicon [159] to produce a focused beam of light. These beams, however, have a limited axial focal length. M. Florjanczyk and R. Tremblay used a axicon to produce a donut shaped beam with an axial focal length of the order $\mathcal{O}(10^2)$cm [160], an order of magnitude larger than the beam length produced by J. E. Bjorkholm *et al.* [158]. In each of the experiments referenced, the donut beam profile provided transverse confinement.

The concept of using an optical guide to transport atoms was first proposed by M. A. Ol'Shanii *et al.* in 1993 [127]. M. A. Ol'Shanii *et al.* considered a glass capillary in which the light, confined by total internal reflection, was capable of transporting

atoms tens of metres. Although the Bragg fibre offers stronger confinement and therefore permits higher optical transmission, it had not been fabricated at the time of writing. Those thermal atoms which emerged from the atomic source with a small transverse velocity could then be guided down the fibre. Additionally, M. A. Ol'Shanii *et al.* determined the maximal fibre curvature for a given atomic velocity.

Shortly after M. A. Ol'Shanii *et al.* , S. Marksteiner *et al.* proposed a similar guide which supported a single optical mode [113]. The difference in S. Marksteiner's *et al.* approach is the light was blue detuned with respect to the atomic transition. This meant that rather than guiding the atoms along the fibre core, the light provided a repulsive enclosure from the evanescent fields at the boundary surface. The benefit of this design is a reduction in spontaneous emissions from thermal excitations. However, one has to consider a very narrow core in order to produce a collimated beam.

In the years immediately following M. A. Ol'Shanii *et al.* and S. Marksteiner *et al.* publications, M. J. Renn experimentally verified both red- [114] and blue [115]-detuned guiding. Whilst the blue detuned guiding was capable of producing three times the flux of red detuned guiding, an additional red detuned laser was required for loading and the set up offered limited axial confinement. Following the work of M. J. Renn *et al.* , V. I. Balykin *et al.* reported an increase in the atomic density guided in a hollow laser waveguide with blue detuned light [116]. Using a convergent design, V. I. Balykin *et al.* reported a density increase by a factor of 10^5 whilst reducing the temperature by a similar factor.

Atoms are not the only thing to be successfully transported through hollow cores, with the advent of the photonic crystal fibre, micron-sized particles were successfully

transported over 5m by O. A. Schmidt *et al.* [117, 118]. Shortly after T. Takekoshi *et al.* displayed atomic transportation with a photonic crystal fibre [135]. Hollow optical fibres offer much lower loss rates compared to glass capillaries, the current lowest loss rate recored is 1.2dB/km, achieved by P. J. Roberts *et al.* [161]. The increased confinement offered by photonic crystal fibres means greater transportation distances [118] and deeper optical depths achievable. In 2011, M. Bajcsy successfully loaded 30,000 rubidium atoms, which they report as a sixfold increase compared to maximum depths previously achieved [162].

Loading of energetic particles commonly involves the fibre being located close to a vapour source [114] - [115], less energetic particles are loaded either using gravity [162] to lower the particles in or more commonly, via an optical gradient trap [118]. The optical gradient trap is created by injecting the radiation from the opposite end of the fibre to the atomic source, as the light emerges from the fibre it diffuses creating a dipole gradient funnel.

Alternatively one can inject radiation from each end of the fibre, by varying the frequency of one with respect to the other a standing wave is created. The standing wave allows particles to be selectively launched and with tuneable mobility, this was first shown by S. Okaba *et al.* [137] who referred to it as an optical conveyor belt. S. Ghosh *et al.* take a very different approach to the conventional loading discussed above. The fibre in their experiment is coated with an atomic layer, when irradiated the atoms in this layer occupy the core [163].

There has also been significant interest in light-matter interactions within the hollow core of tapered optical fibres [151–155]. Tapering the fibre involves smooth reduction in the core diameter. As the number of supported modes is related to the

core diameter, tapering can filter out higher order modes whilst leaving fundamental modes largely unaffected. The tapering in [151–155], however, is drastic with the core diameter reduced to a few hundred nanometer. It is commonly used to investigate enhanced light-matter coupling.

Whilst thermal [135] and laser-cooled [164] atoms have been successfully stored and manipulated in the hollow core of photonic crystal fibres, ultra-colds samples have reported limited success. The loading efficiency of an ultra-cold sample from an MOT trap has significantly improved. By optimising the optical conveyor belt M. Langbecker *et al.* reported a loading efficiency of 40% [128], much higher than previous loading efficiencies of 2.56% and 3.0% achieved by F Blatt *et al.* [165] and A. P. Hilton *et al.* [166] respectively.

Guiding ultra-cold atoms once inside the core has proven difficult, despite the improved loading efficiency. C. A. Christensen *et al.* retrieved approximately 5% of the initial population for a red detuned guiding potential in a 2cm long hollow-core fibre [122]. A similar depletion rate was found by S Vorrath *et al.* two years later, when they loaded a 8.8cm long fibre with ultracold ^{85}Rb atoms [123].

To explain the atomic attenuation observed in ultracold guiding, N. K. Wilkin and J. M. F. Gunn examined the light-matter interaction of a Bose gas and a standing wave within the confines of a hollow core [124]. They found the light-matter coupling leads to modulational instabilities. In this thesis, we utilise the properties of the hollow optical fibre and propose an alternative method by which ultra-cold atoms, or a Bose-Einstein condensate, can be guided through the hollow core.

11.5 Concluding Remarks

- Solid-core dielectric fibres are commonly used in a range of applications from endoscopy to telecommunications. Their low loss design provides an excellent medium for guiding light over long distances. The maximum power which can be transmitted is limited due to the onset of nonlinear effects.
- Hollow metallic waveguides can circumvent these nonlinear issues, the frequency range is limited to microwaves however because of the significant attenuation from the skin effect. In the limit of perfect conductivity one can derive the profiles of the transverse electric and transverse magnetic fields.
- Photonic crystal fibres combine the useful features of both dielectric fibres and metallic waveguides to create an optical guide capable of transmitting high intensities with a relatively low loss.
- An extensive range of PCF designs exist, we consider the Bragg fibre because of its simple design and high confinement.
- The band gaps, impurity modes and losses of the Bragg fibre are dependent on the design. It is possible to create a single-mode omniguide fibre.
- Whilst the collimating and guiding of atoms in photonic crystal fibres has proven successful, similar experiments with ultra-cold gases have experienced significant depletion.

Chapter 12

Bose Einstein Condensates

In this chapter, we outline the important features of the Bose Einstein condensate. In section 12.1, we describe how and why the condensate forms. In section 12.2, we introduce the Gross-Pitaevskii equation (GPE), a model which is commonly used to study the condensates dynamics. Whilst formulating the GPE, an account of the assumptions made are stated. The content of this chapter is a synthesis of a number of sources, namely [111] and [150].

12.1 Introduction

In section 11.4, we discussed the techniques commonly employed to transport atoms and molecules through the core of photonic crystal fibres. We also highlighted the limited success when these same techniques were applied to ultracold atoms. Each experiment reported with a significant reduction in the number of atoms when retrieved from the fibre core. In this section we introduce the BEC.

12.1.1 Bose-Einstein Statistics

The statistics of indistinguishable particles falls into one of two categories, depending on the particles spin. Bosons (fermions) have integer (half-integer) spin, in units of $\hbar$, and obey Bose-Einstein (Fermi-Dirac) statistics. The crucial difference between bosons and fermions is the symmetry of their many body wavefunction. The wavefunction of identical bosons (fermions) is symmetric (anti-symmetric) under the exchange of any two particles, meaning N identical bosons (fermions) can (can not) occupy the same state.

Fermions therefore obey Pauli's exclusion principle. Not only can bosons occupy the same state, but the probability of finding all N identical bosons in the same state is $N!$ times more likely than it is for non-identical bosons [150]. In fact, for an ideal non interacting gas of N bosons at temperature T in a volume V, the average occupation of the i^{th} state is determined by the Bose-Einstein distribution function

$$\langle n(\epsilon_i, T)\rangle = \left(\mathrm{e}^{(\epsilon_i-\mu)/k_{\mathrm{B}}T} - 1\right)^{-1} \tag{12.1}$$

where ϵ_i is the energy of the i^{th} state, μ is the chemical potential and k_{B} is the

Boltzmann constant. Compared to the Fermi-Dirac distribution, the occupation is unbounded as the argument of the exponent tends to zero. The statistics of photons was proposed by Bose [167] and extended by Einstein to include integer spin particles [168]. Einstein's study of a non-interacting bosonic gas also discovered that a macroscopic portion of an ideal Bose gas would occupy the lowest energy level, below a critical temperature.

By considering an ideal, non-interacting Bose gas one can show that the transition temperature for BEC is given by

$$k_{\mathrm{B}}T_0 = 3.3125\frac{\hbar^2}{M}\left(\frac{N}{V}\right)^{\frac{3}{2}} \tag{12.2}$$

where M is the mass of the boson [111]. One can also arrive at equation 12.2 by equating the de Broglie wavelength with the average inter-particle spacing. The critical temperature of BEC is of the order of $\mathcal{O}(10^2)$nK. Below this critical temperature, the fraction of the bosons in the condensate is given by

$$N_0 = N\left[1 - \left(\frac{T}{T_0}\right)^{\frac{3}{2}}\right] \tag{12.3}$$

Equations 12.2 and 12.3 are only applicable for a three dimensional ideal Bose gas. Table 3.1 in [111] outlines how these expressions alter in lower dimensions as well as when trapped in a harmonic potential, following the work of Mullin [169]. The dimensionality plays a crucial role in the properties of BEC. For a spatially uniform infinite system, BEC can only occur at $T = 0$ for a two dimensional system [170] and not at all for one dimension [171].

Elementary examples of bosons include exchange particles such as photons. One can also have composite bosons which obey Bose-Einstein statistics even if the particles comprising them do not, two examples are He^4 and Rb^{87}. For atoms to obey Bose-Einstein statistics, it must contain an even number of neutrons. The fermionic components of a neutral atom all have half-integer spin. As the number of protons matches the number of electrons, the combined spin of these two components is integer. The net spin of the atom is therefore determined by the neutrons.

12.1.2 BEC Production

Producing a BEC proved to be a difficult task, one had to reduce the temperature of a large Bose gas without letting it solidify. This was first achieved by Cornell and Wieman [104]. Seventy years after Einsteins prediction, the pair managed to stabilise a BEC comprised of around 2000 ^{87}Rb atoms for $15-20$s. For their efforts, the pair shared the Nobel Prize with Ketterle who produced a BEC containing around 10^5 ^{23}Na atoms shortly after [172]. Since then, there has been a significant increase in both the size and lifetime of the BEC [110]. The cooling methods employed, however, remain largely unchanged.

In section 11.4, we introduced the dipole gradient force which can manipulate matter. We now describe how electromagnetic fields can be employed to cool a vapour down. The first stage of cooling is to trap the atoms, this is most commonly achieved using a potential trap as shown via equation 11.36. One then employs doppler cooling [105], counter propagating lasers with frequencies detuned just below an atomic transition are incident upon the sample. Due to the Doppler effect, atoms absorb more radiation from the opposing beam, to the direction of travel, which causes a momentum kick slowing the atom down. Applying counter propagating beams along

each axis can fully localise a boson gas.

Doppler cooling reduces the temperature of the vapour to hundreds of micro-Kelvin. To reach the temperatures needed for BEC, one must then apply evaporative cooling. Essentially, this process involves reducing the depth of the trap allowing the more energetic particles to escape and removing a significant portion of the vapours average energy in the processes. Whilst this method has proven to be effective, it does cause a reduction in the atom number by approximately 99%. Alternative cooling methods have more recently been proposed which can cool a sample much faster and maintaining a greater portion of the original sample [173].

Once created, they are visualised by processing the shadow from a CCD camera image, this gives the spatial distribution of the BEC. For the velocity distribution one can release the BEC and visualise after a delay. Both methods are destructive.

12.1.3 Interaction Bosons

Much like a finite temperature, the presence of interactions implies that the ground state is no longer fully condensed, with collisions causing scattering to higher energy states. We now review the interaction force in a BEC, this will prove important when deducing an appropriate model in the next section. The collisions of interacting atoms in a Bose gas can be cumbersome to accurately model. Fortunately for a dilute BEC at low temperatures, one can employ a pseudo-potential which accurately models the low energy behaviour.

Not only does the diluteness condition ($|a|n^{\frac{1}{3}} \ll 1$) ensure that the average par-

ticle spacing, is much greater than the interaction range r_0, but it also suppresses three body collisions which are necessary for solidification. In this limit, one can show that the pseudo-potential for two body interaction between particles at **r** and **r'** is given by

$$U_{\text{eff}} = U_0\delta(\mathbf{r} - \mathbf{r'}) = \frac{4\pi\hbar^2 a_{\text{Born}}}{M}\delta(\mathbf{r} - \mathbf{r'}) \tag{12.4}$$

where M is the atoms mass, δ is the Dirac delta function and a_{Born} is the s-wave scattering length, as determined from the Born approximation [174].

The most commonly used composite bosons used to create a BEC are alkali metals, such as ^{7}Li, ^{23}Na and ^{87}Rb. Not only do each of these isotopes have an even number of neutrons, but the interaction force can be tuned using Feshbach resonance [175, 176]. This process involves altering the energy shift of a collision by coupling to a bound state. As such, by tuning the magnetic field to vary the Zeeman effect, one can alter the scattering length, a_{Born}, to be strong or weak, attractive or repulsive [177, 178].

In this section, we have provided an overview of Bose-Einstein condensates, discussing the transition temperature and the associated condensate fraction. We then introduced examples of composite Bosons, from which a BEC with tuneable interactions can be produced. The form of the effective interactions was discussed as well as a brief account of how one can vary the interaction strength using Feshbach resonance. In our investigation we consider the effective one dimensional form of the three dimensional BEC, comprised of weakly interacting atoms, by averaging over the transverse components.

12.2 The Gross-Pitaevskii Equation

As previously mentioned, a BEC forms when a dilute vapour of indistinguishable bosons in the thermodynamic limit condense together to form one single entity. We now derive the Gross-Pitaevskii equation (GPE) from the Hamiltonian for an interacting Bose gas. The GPE is a useful tool for describing the zero temperature behaviour of a non uniform Bose gas with an effective pseudo-potential interaction [111].

For the GPE to be appropriate, certain conditions must be satisfied. As the GPE describes zero temperature behaviour, one must ensure that the temperature is sufficiently low. As this is a mean field approach which neglects the effects of short range interaction it is only useful for studying phenomena which occurs over length scales $l \gg a$. Meaning the inter-particle spacing is much larger than the interaction range, the diluteness condition must, therefore, be satisfied. Fortunately, the density of a typical BEC is approximately five orders of magnitude lower than the number density at atmospheric pressure.

If we consider a system of N identical bosons each of mass M confined to a one body potential $\mathrm{V}(\mathbf{r}_i)$, interacting via a delta function potential (i.e. contact interactions) then the Hamiltonian is

$$\mathcal{H} = \sum_{i=1}^{N} \frac{\mathbf{p}_i^2}{2M} + \sum_{i=1}^{N} \mathrm{V}(\mathbf{r}_i) + \frac{U_0}{2} \sum_{i \neq j}^{N} \delta(\mathbf{r}_i - \mathbf{r}_j), \tag{12.5}$$

where $\mathbf{p} = -\mathrm{i}\hbar\nabla$ is the momentum operator, U_0 is the s-wave scattering amplitude defined in equation 12.4 and $\mathbf{r}_i$ is the position of the i^{th} boson. Let Ψ be a normalised eigenstate of the Hamiltonian, $\mathcal{H}$, that satisfies the Schrödinger equation,

$\mathcal{H}\Psi = \mathrm{E}\Psi$. Multiplying the Schrödinger equation by Ψ^* and integrating over all coordinates gives the energy

$$\mathrm{E} = \int \Psi^* \mathcal{H} \Psi \mathrm{d}\mathbf{r}_1 ... \mathrm{d}\mathbf{r}_\mathrm{N}. \tag{12.6}$$

We make the assumption that all N particles are condensed. Whilst the actual number of condensed atoms is in fact less than N for interacting bosons at finite temperature, the condensate interaction (quantum) and thermal depletion is sufficiently low in the limit we consider [179]. As such, we employ the Hartree - Fock ansatz for the condensate wavefunction

$$\Psi(\mathbf{r}_1, ..., \mathbf{r}_N) = \prod_{\mathrm{i}=1}^{N} \psi_1(\mathbf{r}_\mathrm{i}), \tag{12.7}$$

The wavefunction of an N boson system is the product of each individual single particle state, the Hartree - Fock ansatz assumes that all bosons are in the same single particle state $\psi_1(\mathbf{r})$. Substituting the approximated wavefunction back in to the integral given in equation 12.6 gives

$$\mathrm{E} = \mathrm{N} \int \psi_1^*(\mathbf{r}) \left[-\frac{\hbar^2}{2M} \nabla^2 + \mathrm{V}(\mathbf{r}) + U_0 \frac{N-1}{2} \left| \psi_1(\mathbf{r}) \right|^2 \right] \psi_1(\mathbf{r}) \mathrm{d}\mathbf{r}. \tag{12.8}$$

Where the coefficient $(N-1)/2$ is the total number of possible pairs of bosons. Note that only two body interaction is included. With $\psi(\mathbf{r}) = \sqrt{N}\psi_1(\mathbf{r})$ and treating $N - 1 \approx N$ in equation 12.8 for sufficiently large N, yeilding

$$\mathrm{E}\left[\psi\right] = \int \psi^*(\mathbf{r}) \left[-\frac{\hbar^2}{2M} \nabla^2 + \mathrm{V}(\mathbf{r}) + \frac{U_0}{2} \left| \psi(\mathbf{r}) \right|^2 \right] \psi(\mathbf{r}) \mathrm{d}\mathbf{r}. \tag{12.9}$$

The first term in the integrand is the kinetic energy of the BEC. In the Thomas-Fermi limit of a large condensate, which we operate in, the contribution from the kinetic energy is negligible. The second term defines the interaction with the external potential, the final term is the Hartree Energy which describes the mean field interactions between bosons. By requiring the Gross-Pitaevskii energy functional to be extremal subject to the normalisation condition: $\int |\psi|^2 \, \mathrm{d}\mathbf{r} = N$, it is possible to determine ψ. Using the Langrange multiplier associated with this condition

$$\frac{\delta}{\delta\psi^*(\mathbf{r})}\left[\mathrm{E} - \mu \int |\psi|^2 \, \mathrm{d}\mathbf{r}'\right] = \left[-\frac{\hbar^2}{2M}\nabla^2 + \mathrm{V}(\mathbf{r}) + \frac{U_0}{2}|\psi(\mathbf{r})|^2 - \mu\right]\psi(\mathbf{r}) = 0, \tag{12.10}$$

where μ is the chemical potential and $\psi,\ \psi^*$ are be considered independent in functional differentiation [30]. Solving this we find the condensate wavefunction must satisfy the nonlinear Schrödinger (NLS) equation

$$\mu\psi(\mathbf{r}) = \left[-\frac{\hbar^2}{2M}\nabla^2 + \mathrm{V}(\mathbf{r}) + U_0|\psi(\mathbf{r})|^2\right]\psi(\mathbf{r}). \tag{12.11}$$

This is equivalent to the NLS equation with the chemical potential in place of the energy eigenvalue. For the dynamics of the condensate, however, we use the time dependent Gross-Pitaevskii (GP) equation

$$\mathrm{i}\hbar\frac{\partial}{\partial t}\psi(\mathbf{r},t) = \left[-\frac{\hbar^2}{2M}\nabla^2 + \mathrm{V}(\mathbf{r}) + U_0|\psi(\mathbf{r},t)|^2\right]\psi(\mathbf{r},t). \tag{12.12}$$

To describes the dynamics of a BEC in an a detuned guiding potential, one lets $\mathrm{V}(\mathbf{r}) = -\frac{1}{2}\alpha_0\langle \mathrm{E}^2\rangle$ where $\langle ...\rangle$ is the time average of the electric field, as stated in

equation 11.38. This is the dipole gradient potential from *red*-detuned light (i.e $\alpha_0 < 0$), the condensate energy is minimised with respect to the external potential by localising at the regions of high intensity.

12.2.1 Hydrodynamic Representation

Multiplying equation 12.12 by the wavefunction $\psi^*(\mathbf{r}, t)$ and subtracting the complex conjugate equation, one finds

$$\frac{\partial|\psi|^2}{\partial t} + \nabla \cdot \left[\frac{\hbar^2}{2\mathrm{i}M}\left(\psi^*\nabla\psi - \psi\nabla\psi^*\right)\right] = 0. \tag{12.13}$$

This has the form of the continuity equation, implying the condensate velocity is

$$\mathbf{v} = \frac{\hbar^2}{2\mathrm{i}M}\frac{\left(\psi^*\nabla\psi - \psi\nabla\psi^*\right)}{|\psi|^2}. \tag{12.14}$$

As we are studying the transport properties of the condensate, it is useful to reconstruct the Gross-Pitaevskii equation into a more useable form. To do so we employ the Madelung transformation

$$\psi(\mathbf{r}, t) = \sqrt{\rho(\mathbf{r}, t)}e^{\mathrm{i}S(\mathbf{r},t)}, \tag{12.15}$$

where ρ is the density and S contains information about the velocity via

$$\mathbf{v} = \frac{\hbar}{M}\nabla S, \tag{12.16}$$

as shown in equation 12.14. To leading order (for systems in their ground state) the phase S gives the chemical potential via

$$\mu = -\frac{S}{t}. \tag{12.17}$$

This is a consequence of particle conservation in the NLSE and is incorporated as part of the phase. Substituting the Madelung representation of the wavefunction into equation 12.12, factorising and separating the real and imaginary parts gives the following two equations and recasting the variables, the dimensionless equations are

$$\rho_t + \partial_z(\rho S_z) = 0, \tag{12.18}$$

$$\frac{1}{2}S_z^2 - \mu + \rho - \frac{1}{4}\left(\frac{\rho_{zz}}{\rho} + \frac{1}{2}\frac{\rho_z^2}{\rho^2}\right) - \frac{1}{2}\alpha\langle \mathrm{E}^2\rangle = 0, \tag{12.19}$$

where A_z denotes the partial differential of A with respect to the fibre axial direction, z. Up to now we have considered a fully three dimensional BEC. Here we present the effective one dimensional form of the hydrodynamic equations. We make the assumption that the light-matter dynamics are separable and that the transverse profile of the light and matter remain constant. The variables z, t and ρ have been replaced by

$$z' = \frac{\hbar}{\sqrt{M\rho_0 U_0}}z, \quad t' = \frac{\hbar}{\rho_0 U_0}t, \quad \rho' = \frac{\rho}{\rho_0} \quad \text{and} \quad \alpha = \frac{\alpha_0}{U_0\rho_0}. \tag{12.20}$$

Equation 12.18 is a continuity equation, equivalent to equation 12.13. Equation 12.19 is a Bernoulli-like equation, the terms from left to right are: the kinetic energy, the chemical potential, the Hartree potential, $U_0\rho$ and the quantum pressure.

The final term in equation 12.19 is the dipole force. This term describes the forces due to spatial variations in the density, and is a direct consequence of the Heisenberg uncertainty principle. For variations on length scales greater than the coherence length this term is negligible. The simplest solution to the GPE is the free particle soliton $\psi(\mathbf{r}) = \sqrt{N/V}e^{i\mathbf{k}\cdot\mathbf{r}}$, known as the Hartree solution. One can recover the Bogoliubov-de Gennes equations by linearising the GPE by considering $\psi(\mathbf{r},t) = \psi_0(\mathbf{r},t) + \delta\psi(\mathbf{r},t)$ where $\delta\psi(\mathbf{r},t)$ accounts for small deviations [150].

12.3 Concluding Remarks

- Bose-Einstein condensates are coherent states of matter in which a large number of bosonic atoms occupy the same state. The occur when the temperature of an ideal Bose gas is reduced below a critical value.
- In our investigation we consider a large, dilute BEC at zero temperature which is comprised of weak repulsive composite Bosons. We model the dynamics of this condensate using the Gross-Pitaevskii equation.
- In this limit the Hartree-Fock ansatz for the ground state wavefunction is appropriate. The interactions can be modelled by only considering the s-wave scattering in this limit.
- For a sufficiently large BEC, one can employ the Thomas-Fermi approximation and neglect the contribution from the kinetic energy term in the GPE.
- We employ the Madelung transformation to express the GPE in its effective one dimensional hydrodynamic form.

Chapter 13

BEC Transport in Crystal Fibres

13.1 Hollow Optical Fibre Modes

Often, when studying the dynamics of matter, one treats the electromagnetic field as fixed, only there to provide a background potential. Allowing the light to instead be a dynamical participant leads to a host of nonlinear effects. Much like the derivation of the hollow metallic waveguide modes we begin with Maxwell's equations, except now we no longer make the assumption that the medium is homogeneous or that the mode can be treated simply as plane wave. We do however maintain the assumption of no currents ($\mathbf{J} = 0$) and that $\mu = 1$. Maxwell's equations are

$$\nabla \times \mathbf{E} = -\frac{1}{c}\frac{\partial \mathbf{B}}{\partial t}, \tag{13.1}$$

$$\nabla \cdot \mathbf{D} = 0, \tag{13.2}$$

$$\nabla \times \mathbf{H} = \frac{1}{c}\frac{\partial \mathbf{D}}{\partial t}, \tag{13.3}$$

$$\nabla \cdot \mathbf{B} = 0. \tag{13.4}$$

Now with

$$\mathbf{D}(\mathbf{r},t) = \epsilon(\mathbf{r})\mathbf{E}(\mathbf{r},t) = (1 + 4\pi\alpha_0\rho(\mathbf{r}))\mathbf{E}(\mathbf{r},t), \tag{13.5}$$

where the susceptibility depends on the atomic density $\rho(r)$. We work under the assumption that BEC is tightly confined within the electric field and as such remains localised with respect to the field profile. This allows us to neglect the time dependence of the BEC, treating it to be constant with respect to the electromagnetic field. We employ the transversality constraint to derive the wave equation. As we no longer have a homogeneous medium, we have to select a mode which obeys the transversality constraint.

$$\begin{aligned}\nabla \cdot \mathbf{D} &= \nabla \cdot [(1 + 4\pi\alpha_0\rho(\mathbf{r}))\mathbf{E},] \\ &= (1 + 4\pi\alpha_0\rho(\mathbf{r}))(\nabla \cdot \mathbf{E}) + \mathbf{E} \cdot \nabla(4\pi\alpha_0\rho(\mathbf{r})).\end{aligned} \tag{13.6}$$

We now let $\rho(\mathbf{r}) = \bar{\rho}\nu(\mathbf{r})$ where the average density obeys $4\pi\alpha_0\bar{\rho} \ll 1$. The electric field can be expanded in powers of $\bar{\rho}$ to give

$$\mathbf{E} = \mathbf{E}_0 + 4\pi\alpha_0\bar{\rho}\mathbf{E}_1 + \mathcal{O}(\mathbf{E}_2). \tag{13.7}$$

Substituting this form into equation 13.6 gives

$$\begin{aligned}\nabla \cdot \mathbf{D} &= \nabla \cdot \mathbf{E}_0 + 4\pi\alpha_0\bar{\rho}(\nabla \cdot \mathbf{E}_1 + \mathbf{E}_0 \cdot \nabla\nu) + 4\pi\alpha_0\bar{\rho}\nu(\nabla \cdot \mathbf{E}_0) + \ldots \\ &\simeq 0.\end{aligned} \tag{13.8}$$

To lowest order we find: $\nabla\cdot\mathbf{E}_0 = 0$ and to first order: $\nabla\cdot\mathbf{E}_1+\mathbf{E}_0\cdot\nabla\nu = 0$. In order to take advantage of the transversality constraint, we must select a mode which obeys these requirements. Due to the geometry of the fibre, it is most intuitive to consider cylindrical polars, $\mathbf{E} = \mathrm{E}^r\hat{\mathbf{r}} + \mathrm{E}^\phi\hat{\boldsymbol{\phi}} + \mathrm{E}^z\hat{\mathbf{z}}$. The first order requirement, $\nabla\cdot\mathbf{E}_0 = 0$, implies that the lowest order component of the mode remains transverse, as such we require $\mathrm{E}^z_0 = 0$, likewise we see $\mathrm{E}^z_1 = 0$.

We also require $\mathbf{E}_0\cdot\nabla\nu = 0$. As stated above the BEC is dilute and confined within the core of the fibre. As the fibre is considered to be long and thin, its intuitive that the leading order component of $\nabla\nu \propto \hat{\mathbf{r}}$. Thus $\mathrm{E}^\rho_0 = 0$ as well, the mode is therefore entirely in the $\hat{\boldsymbol{\phi}}$ direction. Excitations in the BEC density occur along the $\hat{\mathbf{z}}$ direction, therefore $\nabla\nu^{\mathrm{ex}}$ always remains perpendicular to the field $\mathbf{E} = \mathrm{E}^\phi\hat{\boldsymbol{\phi}}$. The density is assumed to have no azimuthal dependence, such excitations in transverse azimuthal traps have been considered by others, such effects have been studied in pancake BECs by G. Theocharis *et al.* [180]. With the transversality constraint obeyed, the wave equation is given by

$$\nabla^2\mathbf{E} = c^{-2}\partial_{tt}[(1+4\pi\alpha_0\rho)\mathbf{E}]. \tag{13.9}$$

Above, we have justified the leading order components of both the electric field and the density. Despite the density having its greatest variation in the radial direction, the tenuous density has little impact on the robust transverse structure of the mode, $f(r)$, over the diameter of the core. Small axial variations in the atomic density, however, can have a noticeable effect on the dielectric properties in the direction of propagation.

The axial variation of the electric field occurs over length scales much longer than the wavelength of the light $\lambda \propto \Omega_0^{-1}$, where Ω_0 is the frequency of the dominant Fourier component. We, therefore, consider a plane wave $\mathrm{e}^{-\mathrm{i}\Omega_0 t}$ within a slowly varying envelope $\epsilon(z,t)$. As we have have assumed no azimuthal density variations, we anticipate the field to also have no ϕ dependence.

$$\mathbf{E}(\mathbf{r},t) = \epsilon(z,t) f(r) \mathrm{e}^{-\mathrm{i}\Omega_0 t} \hat{\boldsymbol{\phi}}. \tag{13.10}$$

The left hand side of the wave equation 13.9 is the vector Laplacian, which for the mode defined by equation 13.10 gives

$$\begin{aligned}\nabla^2 \mathbf{E} = {} & 0\hat{\mathbf{r}} + 0\hat{\boldsymbol{z}} \\ & + \left[\left(\frac{1}{r} \frac{\partial}{\partial r} \left(r \frac{\partial f(r)}{\partial r} \right) - \frac{f(r)}{r^2} \right) \epsilon(z,t) + \epsilon_{zz}(z,t) f(r) \right] \mathrm{e}^{-\mathrm{i}\Omega_0 t} \hat{\boldsymbol{\phi}}.\end{aligned} \tag{13.11}$$

Had we introduced azimuthal field dependence, the vector Laplacian would have contained a term in the radial direction. The right hand side of the wave equation gives

$$\begin{aligned}& \frac{1}{c^2} \partial_{tt} [(1 + 4\pi\alpha_0 \rho) \mathbf{E}] \\ & \qquad = \frac{1}{c^2} (1 + 4\pi\alpha_0 \rho) \left[\epsilon_{tt}(z,t) - 2\mathrm{i}\Omega_0 \epsilon_t(z,t) - \Omega_0^2 \epsilon(z,t) \right] f(r) \mathrm{e}^{-\mathrm{i}\Omega_0 t} \hat{\boldsymbol{\phi}}.\end{aligned} \tag{13.12}$$

Equating each side of the wave equation, we can partially separate the equation to

isolate the radial dependence.

$$-\gamma^2 = \frac{1}{f}\left[\frac{1}{r}\frac{\partial}{\partial r}\left(r\frac{\partial f}{\partial r}\right) - \frac{f}{r^2}\right] = -\frac{\epsilon_{zz}}{\epsilon} + \frac{1}{c^2}(1 + 4\pi\alpha_0\rho)\frac{1}{\epsilon}\left[\epsilon_{tt} - 2\mathrm{i}\Omega_0\epsilon_t - \Omega_0^2\epsilon\right]. \tag{13.13}$$

As each side of equation 13.13 depends on different variables each side must be equal to the same constant, which we define as $-\gamma^2$. Thus the radial dependence of the mode is governed by

$$r^2\frac{\partial^2 f(r)}{\partial r^2} + r\frac{\partial f(r)}{\partial r} + (\gamma^2 r^2 - 1)f(r) = 0. \tag{13.14}$$

This is the Bessel equation as seen in section 11.2 for the radial profile of the hollow metallic waveguide. As discussed in the previous chapter, M. Ibanescu *et al.* showed that despite the hollow Bragg fibre being an all dielectric device, it has similar dispersion properties to the hollow metallic waveguide [125]. Including cut-off frequencies and mode profiles. The radial profile is therefore given by

$$f(\rho) = \mathrm{J}_1(\gamma r). \tag{13.15}$$

We have assumed azimuthal symmetry, as such the only mode available is the TE_{01} mode. This is not a requirement, it merely simplifies the calculation. Other benefits of the TE_{01} mode is the lowest loss, so if many modes are incident upon the fibre, after a finite length/time only the TE_{01} mode will be present. It also offers the lowest cut-off frequency [125], and has a node within the hollow core near the boundary layer - this reduces the likelihood of atoms escaping and sticking to the fibre walls. Higher order TE_{0n} modes may, however, offer tighter confinement.

With the transverse profile fixed, we now turn our attention to the axial behaviour of the electric field. Both the magnitude and slope of $\epsilon(z,t)$ are assumed to be small, we are therefore justified in omitting terms such as $\mathcal{O}(\epsilon_{tt}\epsilon,\ \epsilon_t^2\epsilon,\ \epsilon_t\epsilon^2)$ as they are considerably smaller. Rearranging equation 13.13 gives

$$\epsilon_{zz} - \frac{2\mathrm{i}\Omega_0}{c^2}\epsilon_t + \left[\frac{1}{c^2}(1+4\pi\alpha_0\rho) - \gamma^2\right]\epsilon = 0. \tag{13.16}$$

In order to get this differential equation entirely in terms of the slowly varying component of the field $\epsilon(z,t)$, we utilise the Bernoulli-like equation 12.19. We first convert equation 13.16 into its dimensionless form by employing the variable change defined earlier. This gives

$$\epsilon_{zz} + 2\mathrm{i}\Omega\epsilon_t + \frac{Mc^2}{g\rho_0}\left[\Omega^2\left(1+4\pi\alpha\rho_0^2 g\rho\right) - \Lambda^2\right]\epsilon \approx 0, \tag{13.17}$$

where we have defined

$$\Omega = \frac{\hbar}{Mc^2}\Omega_0 \quad \text{and} \quad \Lambda = \frac{\hbar}{Mg\rho_0}\gamma. \tag{13.18}$$

In the previous section, we showed how the BEC can be described using a Bernoulli-like equation

$$\rho = \mu + \frac{1}{4}\alpha|\epsilon|^2 f^2(r). \tag{13.19}$$

Utilising the relation between the differential of the phase and the velocity. We remove all of the r dependence from equation 13.19 by averaging over it by multiplying each term by $f^2(r)$ and then integrate overall r, setting

$$\int_0^\infty f^2(r) r dr = 1 \quad \text{and} \quad \int_0^\infty f^4(r) r dr = \eta, \tag{13.20}$$

where η is a constant resulting from the integration of the radial profile with the weight function r identified by rearranging equation 13.14 into Sturm-Liouville form. One can now replace the density in equation 13.16 with

$$\rho = \mu + \frac{1}{4}\alpha\eta|\epsilon|^2. \tag{13.21}$$

We are now faced with two possible mechanisms by which the density can go to zero depending on the chemical potential, both mechanisms are depicted in the figure 13.1. Firstly, if one considers zero chemical potential, both the density ρ and electric field ϵ, can tend to zero smoothly as $z \to \pm\infty$, figure 13.1a. Alternatively for negative chemical potential, the density could be localised to a finite width, smoothly going to zero at $z = \pm z_0$, figure 13.1b. In the latter regime, the electric field is evanescent beyond $z = \pm z_0$ and so one has to match the solutions.

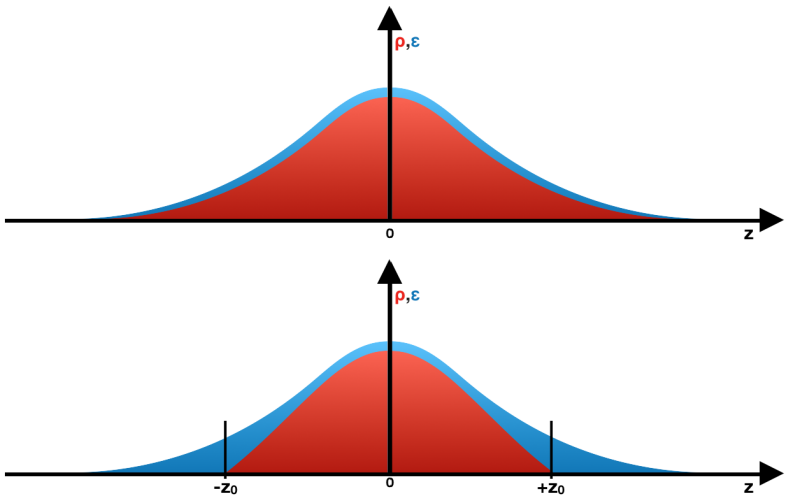

Figure 13.1: a) Schematic diagram of the two localised light-matter solutions to equation 13.21. The blue (red) region shows the radiation (BEC) density profile.

Zero Chemical Potential

We first consider zero chemical potential, for which the BEC gains/loses no energy from entering the fibre core. One can show

$$\frac{1}{2}\epsilon_{zz} + \mathrm{i}\Omega\epsilon_t + 2T\Omega^2|\epsilon|^2\epsilon = 0, \tag{13.22}$$

Where we have set $\Omega = \Lambda$ and

$$T = \frac{Mc^2\alpha^2\pi\eta\rho_0}{4}. \tag{13.23}$$

Applying a final variable change, for convenience, of $\tau = 2\Omega Tt$ and $\bar{z} = 2\sqrt{T}\Omega z$ one arrives at the one-dimensional nonlinear Schrödinger equation

$$\epsilon_{zz} + \mathrm{i}\epsilon_t + |\epsilon|^2\epsilon = 0. \tag{13.24}$$

We now follow the methods presented in [181] to determine an appropriate solution to equation 13.24. As we desire a solution localised in space/time, we consider a travelling wave solution of the form

$$\tilde{\epsilon}(\bar{z}, \tau) = A(\xi)\mathrm{e}^{\mathrm{i}(r\bar{z} - s\tau)}, \tag{13.25}$$

where $\xi = \bar{z} - \bar{U}\tau$ and both $r,\ s$ are real constants. Substituting the travelling wave solution into the NLS equation gives $r = \bar{U}\Omega$ from the imaginary components and

$$A_{\xi\xi} = \Delta A - A^3, \tag{13.26}$$

from the real components where $\Delta = r^2 - s$. One can replace the second differential of A with respect to ξ in equation 13.26 by employing

$$A_{\xi\xi} = \frac{1}{2A_\xi}\frac{\mathrm{d}}{\mathrm{d}A}(A_\xi^2). \tag{13.27}$$

Rearranging and integrating both sides of the equation with respect to A one arrives at

$$A_\xi^2 = \Delta A^2 - \frac{1}{2}A^4. \tag{13.28}$$

The solution of which can be more readily seen by letting $A = B^{-1}$, one can show

$$B_\xi^2 = \Delta B^2 - \frac{1}{2}. \tag{13.29}$$

From which it is evident that $B(\xi) = \frac{1}{\sqrt{2\Delta}}\cosh\left(\sqrt{\Delta}\xi\right)$. Here, Δ is a free parameter which we set to be $\Delta = \frac{A_0^2}{2}$ to simplify the solution. The complete expression for the slowly varying component of the electric field is therefore

$$\epsilon(z,t) = A_0\,\mathrm{sech}\left[\sqrt{2T}A_0\Omega(z-Ut)\right]\mathrm{e}^{\mathrm{i}\Omega\left(Uz+\left[TA_0^2-\frac{1}{2}U^2\right]t\right)}. \tag{13.30}$$

A few interesting things can be noted from this solution (which is for $\mu = 0$). Firstly, the presence of the BEC lowers the cut-off frequency. If light is launched down a

fibre with frequency below the empty fibre cut-off but above the new cut-off the light is forbidden to flow down the fibre without the presence of the BEC. The extent to which the cut-off frequency is reduced is given by

$$\omega = \frac{\hbar^2}{M\rho_0^2 g^2}\left[TA_0^2 - \frac{1}{2}U^2\right]\Omega_0 \tag{13.31}$$

The extent to which the mode frequency is lowered is therefore controlled by the two independent parameters A_0 and U. Due to the dipole force, the BEC desires to remain in the regions with high light intensity and the light cannot escape from the BEC. The full expression for the mode is given by

$$\mathbf{E}(\mathbf{r},t) = A(z-Ut)f(r)\mathrm{e}^{-\mathrm{i}(\Omega_0-\omega)t}\hat{\boldsymbol{\phi}}, \tag{13.32}$$

and is displayed schematically in figure 13.2. Once can see the light-matter soliton evolves down the fibre core with velocity U in a ring-like structure with no obvious decay modes. N. S. Ginsberg *et al.* demonstrated the retrieval of ultraslow light propagated in BEC [182], the light was retrieved after travelling 160μm. One could envisage that our light-matter soliton could propagate ultra slow light over much longer distances along variable trajectories within the isolated enclosure.

Solitons were first observed, using absorption imaging, in a repulsive ^{23}Na, it was created by imprinting a phase step in the BEC. Bright solitons, such as ours, have also been observed within an attractive ^{7}Li BECs.

Víctor M. Pérez-García *et al.* identify soliton propagation through a BEC trapped in a cigar shape potential [183]. This highly asymmetric limit allows them to analyse

the effective one dimensional dynamics of the BEC, they find that the width of the soliton is inversely proportional to number of atoms in the BEC. Therefore, too large of a number would cause it to become unstable and collapse. We also observe an amplitude dependent width in equation 13.30, implying that there may be a limit to the size permitted.

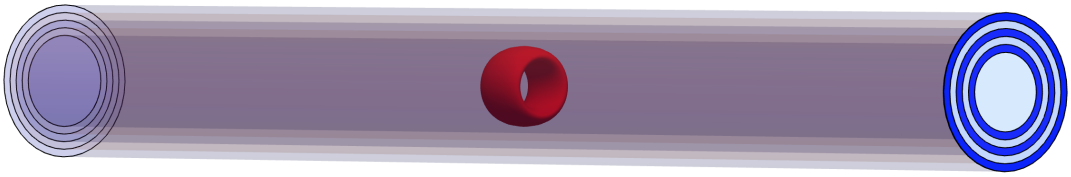

Figure 13.2: Schematic diagram of light-matter soliton propagating through the hollow-core of the Bragg fibre.

Negative Chemical Potential

The solution derived above is obtained for zero chemical potential, in which the BEC has no energetic preference on entering the fibre or not. As such the mode was localised by both the density and field going to zero at the infinity. We now consider the case a fibre with negative potential, energy is therefore required for the BEC is exist within the fibre core. Referring back to the Bernoulli-like equation governing the dynamics of the BEC

$$\rho = -|\mu| + \frac{1}{4}\alpha\eta|\epsilon|^2. \tag{13.33}$$

Where we consider a BEC at rest with respect to the confining potential ($u = 0$). The density is a positive quantity, as such it goes to zero at the point

$$|\mu| = \frac{1}{4}\alpha\eta|\epsilon|^2. \tag{13.34}$$

From this we can define the location at which the density goes to zero, $\rho(z_0) = 0$. First we determine the field profile within the region $|z| \leq z_0$, substituting in the new form of the density and setting

$$\epsilon(z,t) = \tilde{\epsilon}(z,t)\mathrm{e}^{-2\mathrm{i}\Omega Mc^2\pi\alpha\rho_0|\mu|t}, \tag{13.35}$$

we arrive at the same NLS equation observed earlier

$$\frac{1}{2}\tilde{\epsilon}_{zz} + \mathrm{i}\Omega\tilde{\epsilon}_t + 2T\Omega^2|\tilde{\epsilon}|^2\tilde{\epsilon} = 0. \tag{13.36}$$

The profile of the electric field within the region of finite density is therefore the same as before that of zero chemical potential, up to a phase factor. As before we see this causes a reduction in the allowed modes in the fibre, however the reduction is less than before due to the negative chemical potential, utilising this mechanism puts a constraint on the allowed value of μ, from equation 13.34 we can see

$$|\mu| = \frac{\alpha\eta\mathrm{A}^2}{4}\,\mathrm{sech}^2\left[\sqrt{2\mathrm{T}}\Omega\mathrm{A}(z_0)\right] \leq \frac{\alpha\eta\mathrm{A}^2}{4} \tag{13.37}$$

Beyond z_0, the atomic density, which permits the existence of the mode, is no longer present. Setting $\rho = 0$ in equation 13.17 gives

$$\epsilon_{zz} + 2\mathrm{i}\Omega\epsilon_t = 0 \tag{13.38}$$

The time dependence of both solutions much match up at the boundary therefore

$$\epsilon_t = \mathrm{i}\Omega \left[TA_0^2 - \frac{1}{2}U^2 - 2Mc^2\pi\alpha\rho_0|\mu| \right] \epsilon \tag{13.39}$$

The spatial dependence of the linear solution must be exponential decay, $\epsilon \propto \mathrm{e}^{-\mathrm{K}z}$. Substituting this form back into equation 13.38 we find

$$\mathrm{K} = \sqrt{2}\Omega \left[TA_0^2 - \frac{1}{2}U^2 - 2Mc^2\pi\alpha\rho_0|\mu| \right]^{1/2} \tag{13.40}$$

Firstly, we can see that for a solution to exist we require TA_0^2 to be larger than the sum of the remaining terms, otherwise the mode will be oscillatory. This is because the frequency shift $\omega < 0$ and so the cut-off is raised. Alternatively, one can find an appropriate value for K by matching both the magnitude and the gradient of $\epsilon(z_0^-)$ and $\epsilon(z_0^+)$ for $u = 0$.

$$\mathrm{A}_1 e^{-\mathrm{K}z_0} = \mathrm{A}\,\mathrm{sech}\left(\mathrm{A}\sqrt{2\mathrm{T}}\Omega z_0\right) \tag{13.41}$$

$$-\mathrm{K}\mathrm{A}_1 e^{-\mathrm{K}z_0} = -\mathrm{A}^2\sqrt{2\mathrm{T}}\Omega\,\mathrm{sech}\left(\mathrm{A}\sqrt{2\mathrm{T}}\Omega z_0\right)\tanh\left(\mathrm{A}\sqrt{2\mathrm{T}}\Omega z_0\right) \tag{13.42}$$

Hence

$$\mathrm{K} = \mathrm{A}\sqrt{2\mathrm{T}}\Omega\tanh\left(\mathrm{A}\sqrt{2\mathrm{T}}\Omega z_0\right) \tag{13.43}$$

We have obtained two different forms of the decay constant K, we now equate the two forms to find

$$\tanh^2\left(\mathrm{A}\sqrt{2\mathrm{T}}\Omega z_0\right) = 1 - \frac{1}{\mathrm{TA}^2}\left(\rho_0 Mc^2 2\pi\alpha\mu\right) \tag{13.44}$$

For a solution to exist, $0 \leq \tanh^2(...) < 1$ therefore for zero velocity

$$|\mu| < \frac{\alpha\eta}{8}\mathrm{A}^2. \tag{13.45}$$

This constraint, which is tighter than the requirement from equation 13.37 implies that the chemical potential has to be big enough to overcome the dipole energy ($\propto \mathrm{A}^2$) to populate the solution. Assuming this constraint can be achieved, we have shown that it is possible to evolve a light-matter soliton down the core of a hollow optical fibre. Uncoupled, neither component are permitted to exist within the core, but together they can evolve.

Whilst the coupled light-matter soliton is stable within the core, individually both are forbidden from entering the core. It is, therefore, natural to ask how one could launch such a state into the fibre. Whilst this is beyond the scope of our analytical calculation, we briefly mention some experimental methods which may offer a solution. Firstly, similar optical-gap-solitons have been identified in solid core fibres by E. Lidorikis *et al.* [184]. The solitons, in their investigation, are launched using the phenomena of bistability, where their is an abrupt change in transmission as the input flux is increased. Alternatively, tapering the fibre limits how far a mode can propagate, as seen the the dimensional dependence of the cut-off frequency in 11.21. A tapered fibre could, therefore house the reduced cut-off for a finite length.

Chapter 14

Conclusion

We have studied the interaction between light and matter within the confines of a hollow photonic crystal fibre. Approaches conventionally used to collimate and guide atoms through the fibre core had limited success when applied to ultracold gases. Motivating the search for an alternative mechanism for guiding Bose-Einstein condensate which utilise the rich physics of photonic crystal fibres.

We demonstrated that combining the useful design features of both solid-core dielectric fibre and hollow metallic fibre, one can create an optical guide capable of delivery high intensity radiation over a wide range of frequencies. We reviewed the mode profile and dispersion relation of the all-dielectric Bragg fibre. We recognised that the TE_{01} mode commonly has the lowest cut-off frequency as well as the lowest attenuation. These factors combined with its rotational symmetry and intensity peak far from the fibre walls make it an ideal candidate for guiding.

We consider a large, dilute BEC at zero temperature which is comprised of weak repulsive composite Bosons which we model using the Gross-Pitaevskii equation. In

this limit, we employ the Hartree-Fock ansatz as well as the Born approximation for the interaction. The GPE was expressed in its hydrodynamic form and the kinetic energy was neglected as we operate in the Thomas-Fermi limit.

N. K. Wilkin and J. M. F. Gunn have shown that any perturbations to a uniform condensate density within the fibre core lead to modulational instabilities when coupled to a standing wave. We instead consider the dynamics of the slowly varying envelope of the field in an effectively one dimensional system. We report on a coupled light-matter soliton with variable amplitude and speed. As a result of the variation in the susceptibility due to the BEC, the cut-off frequency of the radiation is reduced when coupled.

We identify that radiating the core with the reduced cut-off frequency permits the formation of a light-matter soliton with no evident decay modes. This opens up a host of applications such as the possibility of both a BEC and ultraslow light source. Further work is required to determine how to launch the light-matter soliton into the fibre core.

Bibliography

[1] A Pruymboom, PH Kes, E Van der Drift, and S Radelaar. Flux-line shear through narrow constraints in superconducting films. *Physical Review Letters*, 60(14):1430, 1988.

[2] Oleg M Braun and Yuri S Kivshar. *The Frenkel-Kontorova model: concepts, methods, and applications*. Springer Science & Business Media, 2013.

[3] W Chou and RB Griffiths. Effective potentials, a new approach and new results for one-dimensional systems with competing length scales. *Phys. Rev. Lett*, 56(18):1929–31, 1986.

[4] Mario Marchand, Kevin Hood, and Alain Caillé. Nonconvex interactions and the occurrence of modulated phases. *Physical Review Letters*, 58(16):1660, 1987.

[5] Michael Tinkham. *Introduction to superconductivity*. Courier Corporation, 2004.

[6] David R Tilley. *Superfluidity and superconductivity*. Routledge, 2019.

[7] I Sokolović, Petar Mali, J Odavić, S Radošević, S Yu Medvedeva, Andre E Botha, Yu M Shukrinov, and Jasmina Tekić. Devil's staircase and the absence of chaos in the dc-and ac-driven overdamped frenkel-kontorova model. *Physical Review E*, 96(2):022210, 2017.

[8] Lior Embon, Yonathan Anahory, Željko L Jelić, Ella O Lachman, Yuri Myasoedov, Martin E Huber, Grigori P Mikitik, Alejandro V Silhanek, Milorad V Milošević, Alexander Gurevich, et al. Imaging of super-fast dynamics and flow instabilities of superconducting vortices. *Nature Communications*, 8(1):85, 2017.

[9] Pochi Yeh and Amnon Yariv. Bragg reflection waveguides. *Optics Communications*, 19(3):427–430, 1976.

[10] Jhon D Joannopoulos, R Meade, and J Winn. Photonic crystals princeton university press. *Princeton New Jersey*, 1995.

[11] Geoffrey Ingram Taylor. The mechanism of plastic deformation of crystals. part i. theoretical. *Proceedings of the Royal Society of London. Series A, Containing Papers of a Mathematical and Physical Character*, 145(855):362–387, 1934.

[12] FC Frank and Jan H van der Merwe. One-dimensional dislocations. i. static theory. *Proceedings of the Royal Society of London. Series A. Mathematical and Physical Sciences*, 198(1053):205–216, 1949.

[13] Alwyn C Scott. A nonlinear klein-gordon equation. *American Journal of Physics*, 37(1):52–61, 1969.

[14] AS Kovalev, AD Kondratyuk, AM Kosevich, and AI Landau. Generalized frenkel-kontorova model for point lattice defects. *Physical Review B*, 48(6):4122, 1993.

[15] David W McLaughlin and Alwyn C Scott. Perturbation analysis of fluxon dynamics. *Physical Review A*, 18(4):1652, 1978.

[16] AV Ustinov, M Cirillo, and BA Malomed. Fluxon dynamics in one-dimensional josephson-junction arrays. *Physical Review B*, 47(13):8357, 1993.

[17] PH Kes, N Kokubo, and R Besseling. Vortex matter driven through mesoscopic channels. *Physica C: Superconductivity*, 408:478–481, 2004.

[18] R Besseling, R Niggebrugge, and PH Kes. Transport properties of vortices in easy flow channels: a frenkel-kontorova study. *Physical Review Letters*, 82(15):3144, 1999.

[19] DV Tkachenko, VR Misko, and FM Peeters. Dynamics of colloids in a narrow channel driven by a nonuniform force. *Physical Review E*, 80(5):051401, 2009.

[20] C Reichhardt, C Bairnsfather, and CJ Olson Reichhardt. Positive and negative drag, dynamic phases, and commensurability in coupled one-dimensional channels of particles with yukawa interactions. *Physical Review E*, 83(6):061404, 2011.

[21] Ernst Helmut Brandt. The flux-line lattice in superconductors. *Reports on Progress in Physics*, 58(11):1465, 1995.

[22] CF Hempstead and YB Kim. Resistive transitions and surface effects in type-ii superconductors. *Physical Review Letters*, 12(6):145, 1964.

[23] Michael PN Juniper, Arthur V Straube, Rut Besseling, Dirk GAL Aarts, and Roel PA Dullens. Microscopic dynamics of synchronization in driven colloids. *Nature communications*, 6:7187, 2015.

[24] Philip Rosenau. Dynamics of nonlinear mass-spring chains near the continuum limit. *Physics Letters A*, 118(5):222–227, 1986.

[25] Yong-Lei Wang, ML Latimer, Zhi-Li Xiao, R Divan, LE Ocola, GW Crabtree, and Wai-Kwong Kwok. Enhancing the critical current of a superconducting

film in a wide range of magnetic fields with a conformal array of nanoscale holes. *Physical Review B*, 87(22):220501, 2013.

[26] Ch Reichhardt, CJ Olson, RT Scalettar, and GT Zimányi. Commensurate and incommensurate vortex lattice melting in periodic pinning arrays. *Physical Review B*, 64(14):144509, 2001.

[27] Jonathan Stewart Watkins. *Density Driven Vortex Motion in Narrow Channel Superconductors*. PhD thesis, University of Birmingham, 2016.

[28] Austin Alexander Tomlinson. *On the Effect of Boundaries on Confined Vortex Matter Systems*. PhD thesis, University of Birmingham, 2018.

[29] T Dröse, R Besseling, P Kes, and C Morais Smith. Plastic depinning in artificial vortex channels: Competition between bulk and boundary nucleation. *Physical Review B*, 67(6):064508, 2003.

[30] Thierry Dauxois and Michel Peyrard. *Physics of Solitons*. Cambridge University Press, 2006.

[31] Constance F Elam. Tensile tests for large gold, silver and copper crystals. *Proceedings of the Royal Society of London. Series A, Containing Papers of a Mathematical and Physical Character*, 112(760):289–296, 1926.

[32] Abram Fedorovich Joffe, Leonard Benedict Loeb, et al. *Physics of Crystals*. McGraw-Hill book company, inc., 1928.

[33] Ulrich Dehlinger. Zur theorie der rekristallisation reiner metalle. *Annalen der Physik*, 394(7):749–793, 1929.

[34] Ya I Frenkel and TA Kontorova. see phys. z. sowietunion 13 1. *Zh. Eksp. Teor. Fiz*, 8:89, 1938.

[35] J Frenkel and T Kontorova. On the theory of plastic deformation and twinning. *Izv. Akad. Nauk, Ser. Fiz.*, 1:137–149, 1939.

[36] Oleg M Braun and Yuri S Kivshar. Nonlinear dynamics of the frenkel–kontorova model. *Physics Reports*, 306(1-2):1–108, 1998.

[37] JF Currie, SE Trullinger, AR Bishop, and JA Krumhansl. Numerical simulation of sine-gordon soliton dynamics in the presence of perturbations. *Physical Review B*, 15(12):5567, 1977.

[38] Oleg M Braun and Yuri S Kivshar. Nonlinear dynamics of the frenkel-kontorova model with impurities. *Physical Review B*, 43(1):1060, 1991.

[39] Oleg M Braun and Yuri S Kivshar. Concentration dependence of the conductivity and diffusivity in one-dimensional anharmonic lattices. *Physical Review B*, 50(18):13388, 1994.

[40] OM Braun, Yu S Kivshar, and II Zelenskaya. Kinks in the frenkel-kontorova model with long-range interparticle interactions. *Physical Review B*, 41(10):7118, 1990.

[41] Oleg M Braun and Yuri S Kivshar. Zigzag kinks in the frenkel-kontorova model with a transversal degree of freedom. *Physical Review B*, 44(14):7694, 1991.

[42] OM Braun, Yu S Kivshar, and AM Kosevich. Interaction between kinks in coupled chains of adatoms. *Journal of Physics C: Solid State Physics*, 21(21):3881, 1988.

[43] R Kleiner and P Müller. Intrinsic josephson effects in high-t c superconductors. *Physical Review B*, 49(2):1327, 1994.

[44] P Woafo. Kink dynamics in the highly discrete and coupled sine-gordon system. *Physical Review B*, 52(9):6170, 1995.

[45] R Besseling, PH Kes, T Dröse, and VM Vinokur. Depinning and dynamics of vortices confined in mesoscopic flow channels. *New Journal of Physics*, 7(1):71, 2005.

[46] SW Englander, NR Kallenbach, AJ Heeger, JA Krumhansl, and S Litwin. Nature of the open state in long polynucleotide double helices: possibility of soliton excitations. *Proceedings of the National Academy of Sciences*, 77(12):7222–7226, 1980.

[47] Rudolf Peierls. The size of a dislocation. *Proceedings of the Physical Society*, 52(1):34, 1940.

[48] FRN Nabarro. Dislocations in a simple cubic lattice. *Proceedings of the Physical Society*, 59(2):256, 1947.

[49] OM Braunand VK Medvedev. Interaction between particles adsorbed on metal surfaces. *Usp. Fiz. Nauk*, 157:631–666, 1989.

[50] Luis M Floría and Fernando Falo. Shapiro steps in the steady-state dynamics of incommensurate structures. *Physical Review Letters*, 68(18):2713, 1992.

[51] Serge Aubry. The twist map, the extended frenkel-kontorova model and the devil's staircase. *Physica D: Nonlinear Phenomena*, 7(1-3):240–258, 1983.

[52] Ronald M Scanlan, Alexis P Malozemoff, and David C Larbalestier. Superconducting materials for large scale applications. *Proceedings of the IEEE*, 92(10):1639–1654, 2004.

[53] H Kamerlingh Onnes. Further experiments with liquid helium. In *Through Measurement to Knowledge*, pages 261–263. Springer, 1991.

[54] A Schilling, M Cantoni, JD Guo, and HR Ott. Superconductivity above 130 k in the hg–ba–ca–cu–o system. *Nature*, 363(6424):56, 1993.

[55] AP Drozdov, PP Kong, VS Minkov, SP Besedin, MA Kuzovnikov, S Mozaffari, L Balicas, FF Balakirev, DE Graf, VB Prakapenka, et al. Superconductivity at 250 k in lanthanum hydride under high pressures. *Nature*, 569(7757):528, 2019.

[56] SR Foltyn, L Civale, JL MacManus-Driscoll, QX Jia, B Maiorov, H Wang, and M Maley. Materials science challenges for high-temperature superconducting wire. *Nature materials*, 6(9):631, 2007.

[57] BI Halperin, TC Lubensky, and Shang-keng Ma. First-order phase transitions in superconductors and smectic-a liquid crystals. *Physical Review Letters*, 32(6):292, 1974.

[58] Charles K Poole, Horacio A Farach, and Richard J Creswick. *Handbook of superconductivity*. Elsevier, 1999.

[59] U Gottlieb, JC Lasjaunias, JL Tholence, O Laborde, O Thomas, and R Madar. Superconductivity in tasi 2 single crystals. *Physical Review B*, 45(9):4803, 1992.

[60] MK Wu, JR Ashburn, and CJ Torng. Superconductivity at 93k in a new mixed-phase y-ba-cu-o compound system at ambient pressure. *Phys. Rev. Lett*, 58(9):908–910, 1987.

[61] Th Schweizer, R Müller, and LJ Gauckler. A wet-chemistry method to determine the bi and cu valencies in bi-sr-ca-cu-o (2212) high-temperature superconductors. *Physica C: Superconductivity*, 225(1-2):143–148, 1994.

[62] Hiroki Takahashi, Kazumi Igawa, Kazunobu Arii, Yoichi Kamihara, Masahiro

Hirano, and Hideo Hosono. Superconductivity at 43 k in an iron-based layered compound lao 1-x f x feas. *Nature*, 453(7193):376, 2008.

[63] Fritz London and Heinz London. The electromagnetic equations of the supraconductor. *Proceedings of the Royal Society of London. Series A-Mathematical and Physical Sciences*, 149(866):71–88, 1935.

[64] Walther Meissner and Robert Ochsenfeld. Ein neuer effekt bei eintritt der supraleitfähigkeit. *Naturwissenschaften*, 21(44):787–788, 1933.

[65] Lev Petrovich Gor'kov. Microscopic derivation of the ginzburg-landau equations in the theory of superconductivity. *Sov. Phys. JETP*, 9(6):1364–1367, 1959.

[66] John Bardeen, Leon N Cooper, and J Robert Schrieffer. Microscopic theory of superconductivity. *Physical Review*, 106(1):162, 1957.

[67] Alexei A Abrikosov. On the magnetic properties of superconductors of the second group. *Sov. Phys. JETP*, 5:1174–1182, 1957.

[68] WA Little and RD Parks. Observation of quantum periodicity in the transition temperature of a superconducting cylinder. *Physical Review Letters*, 9(1):9, 1962.

[69] U Essmann and H Träuble. The direct observation of individual flux lines in type ii superconductors. *Physics Letters A*, 24(10):526–527, 1967.

[70] N Kokubo, R Besseling, VM Vinokur, and PH Kes. Mode locking of vortex matter driven through mesoscopic channels. *Physical Review Letters*, 88(24):247004, 2002.

[71] N Kokubo, TG Sorop, R Besseling, and PH Kes. Vortex-slip transitions in superconducting a- nbge mesoscopic channels. *Physical Review B*, 73(22):224514,

2006.

[72] Petrucio Barrozo, André A. Moreira, J. Albino Aguiar, and José S. Andrade. Model of overdamped motion of interacting magnetic vortices through narrow superconducting channels. *Phys. Rev. B*, 80:104513, Sep 2009.

[73] K. Yu, M. B. S. Hesselberth, P. H. Kes, and B. L. T. Plourde. Vortex dynamics in superconducting channels with periodic constrictions. *Phys. Rev. B*, 81:184503, May 2010.

[74] Gianni Blatter, Mikhail V Feigel'man, Vadim B Geshkenbein, Anatoly I Larkin, and Valerii M Vinokur. Vortices in high-temperature superconductors. *Reviews of Modern Physics*, 66(4):1125, 1994.

[75] Philip W Anderson. Theory of flux creep in hard superconductors. *Physical Review Letters*, 9(7):309, 1962.

[76] M Danckwerts, AR Goni, C Thomsen, K Eberl, and AG Rojo. Enhanced vortex damping by eddy currents in superconductor-semiconductor hybrids. *Physical Review Letters*, 84(16):3702, 2000.

[77] Dennis C Rapaport and Dennis C Rapaport Rapaport. *The Art of Molecular Dynamics Simulation*. Cambridge university press, 2004.

[78] Hans Fangohr, Simon J Cox, and Peter AJ de Groot. Vortex dynamics in two-dimensional systems at high driving forces. *Physical Review B*, 64(6):064505, 2001.

[79] HJ Jensen, A Brass, Y Brechet, and AJ Berlinsky. Current-voltage characteristics in a two-dimensional model for flux flow in type-ii superconductors. *Physical Review B*, 38(13):9235, 1988.

[80] Hans C Andersen. Molecular dynamics simulations at constant pressure and/or temperature. *The Journal of chemical physics*, 72(4):2384–2393, 1980.

[81] AE Koshelev and VM Vinokur. Dynamic melting of the vortex lattice. *Physical Review Letters*, 73(26):3580, 1994.

[82] A Alan Middleton and Daniel S Fisher. Critical behavior of pinned charge-density waves below the threshold for sliding. *Physical Review Letters*, 66(1):92, 1991.

[83] Paul P Ewald. Die berechnung optischer und elektrostatischer gitterpotentiale. *Annalen der physik*, 369(3):253–287, 1921.

[84] Milton Abramowitz and Irene A Stegun. *Handbook of Mathematical Functions: with Formulas, Graphs, and Mathematical Tables*, volume 55. Courier Corporation, 1965.

[85] R.J. Mason, J. Gartlan, J.S. Watkins, A.A. Tomlinson, N.K. Wilkin, and J.M.F Gunn. Critical shear in superconducting vortex lattice channel systems. *Unpublished*, 2019.

[86] J Röder, JE Hammerberg, BL Holian, and AR Bishop. Multichain frenkel-kontorova model for interfacial slip. *Physical Review B*, 57(5):2759, 1998.

[87] Sidney Shapiro. Josephson currents in superconducting tunneling: The effect of microwaves and other observations. *Physical Review Letters*, 11(2):80, 1963.

[88] Christiaan Huygens. *Horologium Oscillatorium: sive de motu pendulorum ad horologia aptato demonstrationes geometricae*. F. Muguet, 1966.

[89] M Baziljevich, D Barness, M Sinvani, E Perel, A Shaulov, and Y Yeshurun. Magneto-optical system for high speed real time imaging. *Review of Scientific Instruments*, 83(8):083707, 2012.

[90] Wei Cai and William D Nix. *Imperfections in Crystalline Solids*. Cambridge University Press, 2016.

[91] G Piacente, IV Schweigert, Joseph J Betouras, and FM Peeters. Generic properties of a quasi-one-dimensional classical wigner crystal. *Physical Review B*, 69(4):045324, 2004.

[92] VL Pokrovsky. Splitting of commensurate-incommensurate phase transition. *Journal de Physique*, 42(6):761–766, 1981.

[93] JE Byrne and MD Miller. Ground-state phase diagrams for one-dimensional chains with nonlinear interactions. *Physical Review B*, 39(1):374, 1989.

[94] DJ Bergman, E Ben-Jacob, Y Imry, and K Maki. Sine-gordon solitons: Particles obeying relativistic dynamics. *Physical Review A*, 27(6):3345, 1983.

[95] R. Kleiner, F. Steinmeyer, G. Kunkel, and P. Müller. Intrinsic josephson effects in $bi_2sr_2cacu_2o_8$ single crystals. *Phys. Rev. Lett.*, 68:2394–2397, Apr 1992.

[96] V. M. Krasnov and D. Winkler. Static and dynamic properties of stacked josephson junctions: Analytic solution. *Phys. Rev. B*, 56:9106–9115, Oct 1997.

[97] M. G. Blamire, E. C. G. Kirk, J. E. Evetts, and T. M. Klapwijk. Extreme critical-temperature enhancement of al by tunneling in nb/alo_x/al/alo_x/nb tunnel junctions. *Phys. Rev. Lett.*, 66:220–223, Jan 1991.

[98] P. Henseler, A. Erbe, M. Köppl, P. Leiderer, and P. Nielaba. Density reduction and diffusion in driven two-dimensional colloidal systems through microchannels. *Phys. Rev. E*, 81:041402, Apr 2010.

[99] M. Köppl, P. Henseler, A. Erbe, P. Nielaba, and P. Leiderer. Layer reduction in driven 2d-colloidal systems through microchannels. *Phys. Rev. Lett.*, 97:208302, Nov 2006.

[100] S. Bleil, P. Reimann, and C. Bechinger. Directing brownian motion by oscillating barriers. *Phys. Rev. E*, 75:031117, Mar 2007.

[101] O. M. Braun, Bambi Hu, and A. Zeltser. Driven kink in the frenkel-kontorova model. *Phys. Rev. E*, 62:4235–4245, Sep 2000.

[102] Eric WJ Straver, Jennifer E Hoffman, Ophir M Auslaender, Daniel Rugar, and Kathryn A Moler. Controlled manipulation of individual vortices in a superconductor. *Applied Physics Letters*, 93(17):172514, 2008.

[103] Kenneth Franklin Riley, Michael Paul Hobson, and Stephen John Bence. *Mathematical Methods for Physics and Engineering: A Comprehensive Guide*. Cambridge university press, 2006.

[104] Mike H Anderson, Jason R Ensher, Michael R Matthews, Carl E Wieman, and Eric A Cornell. Observation of bose-einstein condensation in a dilute atomic vapor. *Science*, pages 198–201, 1995.

[105] Erik W Streed, Ananth P Chikkatur, Todd L Gustavson, Micah Boyd, Yoshio Torii, Dominik Schneble, Gretchen K Campbell, David E Pritchard, and Wolfgang Ketterle. Large atom number bose-einstein condensate machines. *Review of Scientific Instruments*, 77(2):023106, 2006.

[106] Chad N Weiler, Tyler W Neely, David R Scherer, Ashton S Bradley, Matthew J Davis, and Brian P Anderson. Spontaneous vortices in the formation of bose–einstein condensates. *Nature*, 455(7215):948, 2008.

[107] J Denschlag, Je E Simsarian, Dl L Feder, Charles W Clark, La A Collins, J Cubizolles, Lu Deng, Edward W Hagley, Kristian Helmerson, William P Reinhardt, et al. Generating solitons by phase engineering of a bose-einstein condensate. *Science*, 287(5450):97–101, 2000.

[108] Andrea Trombettoni and Augusto Smerzi. Discrete solitons and breathers with dilute bose-einstein condensates. *Physical Review Letters*, 86(11):2353, 2001.

[109] Jia J Chang, Peter Engels, and MA Hoefer. Formation of dispersive shock waves by merging and splitting bose-einstein condensates. *Physical Review Letters*, 101(17):170404, 2008.

[110] R Meppelink, SB Koller, JM Vogels, P Van Der Straten, ED van Ooijen, NR Heckenberg, H Rubinsztein-Dunlop, SA Haine, and MJ Davis. Observation of shock waves in a large bose-einstein condensate. *Physical Review A*, 80(4):043606, 2009.

[111] Masahito Ueda. *Fundamentals and New Frontiers of Bose-Einstein Condensation*. World Scientific, 2010.

[112] RF Cregan, BJ Mangan, JC Knight, TA Birks, P St J Russell, PJ Roberts, and DC Allan. Single-mode photonic band gap guidance of light in air. *Science*, 285(5433):1537–1539, 1999.

[113] S Marksteiner, CM Savage, P Zoller, and SL Rolston. Coherent atomic waveguides from hollow optical fibers: quantized atomic motion. *Physical Review A*, 50(3):2680, 1994.

[114] Michael J Renn, D Montgomery, O Vdovin, DZ Anderson, CE Wieman, and EA Cornell. Laser-guided atoms in hollow-core optical fibers. *Physical Review Letters*, 75(18):3253, 1995.

[115] Michael J Renn, Elizabeth A Donley, Eric A Cornell, Carl E Wieman, and Dana Z Anderson. Evanescent-wave guiding of atoms in hollow optical fibers. *Physical Review A*, 53(2):R648, 1996.

[116] VI Balykin, DV Laryushin, MV Subbotin, and VS Letokhov. Increase of the atomic phase density in a hollow laser waveguide. *Journal of Experimental and Theoretical Physics Letters*, 63(10):802–807, 1996.

[117] Fetah Benabid, JC Knight, and P St J Russell. Particle levitation and guidance in hollow-core photonic crystal fiber. *Optics express*, 10(21):1195–1203, 2002.

[118] OA Schmidt, MK Garbos, TG Euser, and P St J Russell. Metrology of laser-guided particles in air-filled hollow-core photonic crystal fiber. *Optics Letters*, 37(1):91–93, 2012.

[119] Vivek Venkataraman, Kasturi Saha, and Alexander L Gaeta. Phase modulation at the few-photon level for weak-nonlinearity-based quantum computing. *Nature Photonics*, 7(2):138, 2013.

[120] P St J Russell, Philipp Hölzer, Wonkeun Chang, Amir Abdolvand, and JC Travers. Hollow-core photonic crystal fibres for gas-based nonlinear optics. *Nature Photonics*, 8(4):278, 2014.

[121] Michal Bajcsy, Sebastian Hofferberth, Vlatko Balic, Thibault Peyronel, Mohammad Hafezi, Alexander S Zibrov, Vladan Vuletic, and Mikhail D Lukin. Efficient all-optical switching using slow light within a hollow fiber. *Physical Review Letters*, 102(20):203902, 2009.

[122] Caleb A Christensen, Sebastian Will, Michele Saba, Gyu-Boong Jo, Yong-Il Shin, Wolfgang Ketterle, and David Pritchard. Trapping of ultracold atoms in a hollow-core photonic crystal fiber. *Physical Review A*, 78(3):033429, 2008.

[123] Stefan Vorrath, SA Möller, Patrick Windpassinger, Kai Bongs, and Klaus Sengstock. Efficient guiding of cold atoms through a photonic band gap fiber. *New Journal of Physics*, 12(12):123015, 2010.

[124] NK Wilkin and JMF Gunn. Instabilities and" phonons" of optical lattices in hollow optical fibers. *arXiv preprint arXiv:1310.6771*, 2013.

[125] Mihai Ibanescu, Steven G Johnson, Marin Soljačić, JD Joannopoulos, Yoel Fink, Ori Weisberg, Torkel D Engeness, Steven A Jacobs, and M Skorobogatiy. Analysis of mode structure in hollow dielectric waveguide fibers. *Physical Review E*, 67(4):046608, 2003.

[126] Pochi Yeh, Amnon Yariv, and Emanuel Marom. Theory of bragg fiber. *JOSA*, 68(9):1196–1201, 1978.

[127] MA Ol'Shanii, Yu B Ovchinnikov, and VS Letokhov. Laser guiding of atoms in a hollow optical fiber. *Optics communications*, 98(1-3):77–79, 1993.

[128] Maria Langbecker, Ronja Wirtz, Fabian Knoch, Mohammad Noaman, Thomas Speck, and Patrick Windpassinger. Highly controlled optical transport of cold atoms into a hollow-core fiber. *New Journal of Physics*, 20(8):083038, 2018.

[129] Eugene P Gross. Structure of a quantized vortex in boson systems. *Il Nuovo Cimento (1955-1965)*, 20(3):454–477, 1961.

[130] LP Pitaevskii. Vortex lines in an imperfect bose gas. *Sov. Phys. JETP*, 13(2):451–454, 1961.

[131] John David Jackson. Classical electrodynamics, 1999.

[132] Joseph A Burns, Philippe L Lamy, and Steven Soter. Radiation forces on small particles in the solar system. *Icarus*, 40(1):1–48, 1979.

[133] Lorenzo Niccolai, Alessandro A Quarta, and Giovanni Mengali. Electric sail elliptic displaced orbits with advanced thrust model. *Acta Astronautica*, 138:503–511, 2017.

[134] Theodor W Hänsch and Arthur L Schawlow. Cooling of gases by laser radiation. *Optics Communications*, 13(1):68–69, 1975.

[135] T Takekoshi and RJ Knize. Optical guiding of atoms through a hollow-core photonic band-gap fiber. *Physical Review Letters*, 98(21):210404, 2007.

[136] Tom Garlington, Joel Babbitt, and George Long. Analysis of free space optics as a transmission technology. *WP No. AMSEL-IE-TS-05001*, 2005.

[137] Shoichi Okaba, Tetsushi Takano, Fetah Benabid, Tom Bradley, Luca Vincetti, Zakhar Maizelis, Valery Yampol'Skii, Franco Nori, and Hidetoshi Katori. Lamb-dicke spectroscopy of atoms in a hollow-core photonic crystal fibre. *Nature communications*, 5:4096, 2014.

[138] Robert E Collin. *Field Theory of Guided Waves*. McGraw-Hill, 1960.

[139] Corning SMF-28 ULL optical fiber. `https://www.corning.com/worldwide/en/products/communication-networks/products/fiber.html`. Accessed: 14/10/19.

[140] Yuri S Kivshar and Govind Agrawal. *Optical Solitons: from Fibers to Photonic Crystals*. Academic press, 2003.

[141] Bruce A Garetz. The kerr effect. *Optics News*, 12(10):28–31, 1986.

[142] Stellios Tzortzakis, Lionel Sudrie, Michel Franco, Bernard Prade, André Mysyrowicz, Arnaud Couairon, and Luc Bergé. Self-guided propagation of ultrashort ir laser pulses in fused silica. *Physical Review Letters*, 87(21):213902, 2001.

[143] Gadi Fibich and Alexander L Gaeta. Critical power for self-focusing in bulk media and in hollow waveguides. *Optics Letters*, 25(5):335–337, 2000.

[144] Boris Grigorevich Korenev. *Bessel Functions and their Applications*. CRC Press, 2002.

[145] VN Melekhin and AB Manenkov. Dielectric tube as a low-loss waveguide. *SOVIET PHYSICS TECHNICAL PHYSICS-USSR*, 13(12):1698, 1969.

[146] Philip Russell. Photonic crystal fibers. *Science*, 299(5605):358–362, 2003.

[147] Burak Temelkuran, Shandon D Hart, Gilles Benoit, John D Joannopoulos, and Yoel Fink. Wavelength-scalable hollow optical fibres with large photonic bandgaps for co 2 laser transmission. *Nature*, 420(6916):650, 2002.

[148] Yoel Fink, Daniel J Ripin, Shanhui Fan, Chiping Chen, John D Joannopoulos, and Edwin L Thomas. Guiding optical light in air using an all-dielectric structure. *Journal of Lightwave Technology*, 17(11):2039, 1999.

[149] K Saitoh, NA Mortensen, and M Koshiba. Air-core photonic band-gap fibers: the impact of surface modes. *Optics Express*, 12(3):394–400, 2004.

[150] Christopher J Pethick and Henrik Smith. *Bose–Einstein Condensation in Dilute Gases*. Cambridge university press, 2008.

[151] KP Nayak, PN Melentiev, M Morinaga, Fam Le Kien, VI Balykin, and K Hakuta. Optical nanofiber as an efficient tool for manipulating and probing atomic fluorescence. *Optics express*, 15(9):5431–5438, 2007.

[152] G Sagué, E Vetsch, W Alt, D Meschede, and A Rauschenbeutel. Cold-atom physics using ultrathin optical fibers: Light-induced dipole forces and surface interactions. *Physical Review Letters*, 99(16):163602, 2007.

[153] SM Spillane, GS Pati, K Salit, M Hall, Prem Kumar, RG Beausoleil, and MS Shahriar. Observation of nonlinear optical interactions of ultralow levels

of light in a tapered optical nanofiber embedded in a hot rubidium vapor. *Physical Review Letters*, 100(23):233602, 2008.

[154] KP Nayak, Fam Le Kien, M Morinaga, and K Hakuta. Antibunching and bunching of photons in resonance fluorescence from a few atoms into guided modes of an optical nanofiber. *Physical Review A*, 79(2):021801, 2009.

[155] E Vetsch, D Reitz, G Sagué, R Schmidt, ST Dawkins, and A Rauschenbeutel. Optical interface created by laser-cooled atoms trapped in the evanescent field surrounding an optical nanofiber. *Physical Review Letters*, 104(20):203603, 2010.

[156] Yasuhiro Harada and Toshimitsu Asakura. Radiation forces on a dielectric sphere in the rayleigh scattering regime. *Optics Communications*, 124(5-6):529–541, 1996.

[157] Arthur Ashkin. Acceleration and trapping of particles by radiation pressure. *Physical Review Letters*, 24(4):156, 1970.

[158] JE Bjorkholm, RR Freeman, A Ashkin, and DB Pearson. Observation of focusing of neutral atoms by the dipole forces of resonance-radiation pressure. *Physical Review Letters*, 41(20):1361, 1978.

[159] I Golub and R Tremblay. Light focusing and guiding by an axicon-pair-generated tubular light beam. *JOSA B*, 7(7):1264–1267, 1990.

[160] M Florjańczyk and R Tremblay. Guiding of atoms in a travelling-wave laser trap formed by the axicon. *Optics communications*, 73(6):448–450, 1989.

[161] PJ Roberts, F Couny, H Sabert, BJ Mangan, DP Williams, L Farr, MW Mason, A Tomlinson, TA Birks, JC Knight, et al. Ultimate low loss of hollow-core photonic crystal fibres. *Optics express*, 13(1):236–244, 2005.

[162] Michal Bajcsy, S Hofferberth, Thibault Peyronel, Vlatko Balic, Qiangrong Liang, AS Zibrov, Vladan Vuletic, and Mikhail D Lukin. Laser-cooled atoms inside a hollow-core photonic-crystal fiber. *Physical Review A*, 83(6):063830, 2011.

[163] Saikat Ghosh, Amar R Bhagwat, C Kyle Renshaw, Shireen Goh, Alexander L Gaeta, and Brian J Kirby. Low-light-level optical interactions with rubidium vapor in a photonic band-gap fiber. *Physical Review Letters*, 97(2):023603, 2006.

[164] Taehyun Yoon and Michal Bajcsy. Laser-cooled cesium atoms confined with a magic-wavelength dipole trap inside a hollow-core photonic-bandgap fiber. *Physical Review A*, 99(2):023415, 2019.

[165] Frank Blatt, Thomas Halfmann, and Thorsten Peters. One-dimensional ultracold medium of extreme optical depth. *Optics Letters*, 39(3):446–449, 2014.

[166] Ashby P Hilton, Christopher Perrella, Fetah Benabid, Ben M Sparkes, Andre N Luiten, and Philip S Light. High-efficiency cold-atom transport into a waveguide trap. *Physical Review Applied*, 10(4):044034, 2018.

[167] SN Bose. Planck's law and light quantum hypothesis. *Z. Phys*, 26(1):178, 1924.

[168] Albert Einstein. Quantum theory of the monatomic ideal gas. *Sitzungsberichte der Preussischen Akademie der Wissenschaften, Physikalisch-mathematische Klasse*, pages 261–267, 1924.

[169] WJ Mullin. Bose-einstein condensation in a harmonic potential. *Journal of Low Temperature Physics*, 106(5-6):615–641, 1997.

[170] Pierre C Hohenberg. Existence of long-range order in one and two dimensions. *Physical Review*, 158(2):383, 1967.

[171] L Pitaevskii and S Stringari. Uncertainty principle, quantum fluctuations, and broken symmetries. *Journal of Low Temperature Physics*, 85(5-6):377–388, 1991.

[172] K. B. Davis, M. O. Mewes, M. R. Andrews, N. J. van Druten, D. S. Durfee, D. M. Kurn, and W. Ketterle. Bose-einstein condensation in a gas of sodium atoms. *Phys. Rev. Lett.*, 75:3969–3973, Nov 1995.

[173] Alban Urvoy, Zachary Vendeiro, Joshua Ramette, Albert Adiyatullin, and Vladan Vuletić. Direct laser cooling to bose-einstein condensation in a dipole trap. *Physical Review Letters*, 122(20):203202, 2019.

[174] Lev Pitaevskii and Sandro Stringari. *Bose-Einstein Condensation and Superfluidity*, volume 164. Oxford University Press, 2016.

[175] Herman Feshbach. Unified theory of nuclear reactions. *Annals of Physics*, 5(4):357–390, 1958.

[176] Ugo Fano. Effects of configuration interaction on intensities and phase shifts. *Physical Review*, 124(6):1866, 1961.

[177] S Inouye, MR Andrews, J Stenger, H-J Miesner, DM Stamper-Kurn, and W Ketterle. Observation of feshbach resonances in a bose–einstein condensate. *Nature*, 392(6672):151, 1998.

[178] Simon L Cornish, Neil R Claussen, Jacob L Roberts, Eric A Cornell, and Carl E Wieman. Stable 85 rb bose-einstein condensates with widely tunable interactions. *Physical Review Letters*, 85(9):1795, 2000.

[179] M Kira. Coherent quantum depletion of an interacting atom condensate. *Nature Communications*, 6:6624, 2015.

[180] G Theocharis, DJ Frantzeskakis, PG Kevrekidis, Boris A Malomed, and Yuri S Kivshar. Ring dark solitons and vortex necklaces in bose-einstein condensates. *Physical Review Letters*, 90(12):120403, 2003.

[181] Catherine Sulem and Pierre-Louis Sulem. *The Nonlinear Schrödinger Equation: Self-Focusing and Wave Collapse*, volume 139. Springer Science & Business Media, 2007.

[182] Naomi S Ginsberg, Sean R Garner, and Lene Vestergaard Hau. Coherent control of optical information with matter wave dynamics. *Nature*, 445(7128):623, 2007.

[183] Victor M Perez-Garcia, Humberto Michinel, and Henar Herrero. Bose-einstein solitons in highly asymmetric traps. *Physical Review A*, 57(5):3837, 1998.

[184] Elefterios Lidorikis, Marin Soljačić, Mihai Ibanescu, Yoel Fink, and JD Joannopoulos. Cutoff solitons in axially uniform systems. *Optics Letters*, 29(8):851–853, 2004.